IRCCS, Integrated Research Consortium on Chemical Sciences

統合物質創製化学研究推進機構

平成30年度 事業報告書

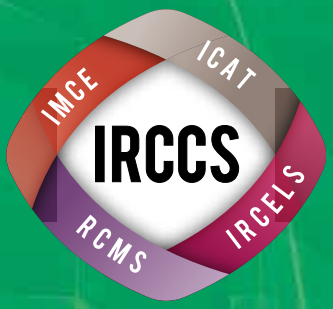

IRCCS, Integrated Research Consortium on Chemical Sciences

統合物質創製化学研究推進機構

平成30年度 事業報告書

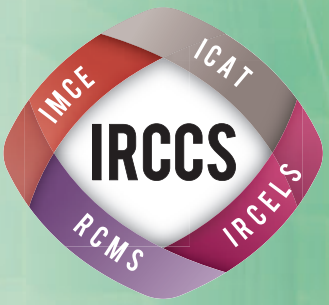

目　次

1

統合物質創製化学研究推進機構について

1-1

本機構の背景

１−１．本機構の背景

革新的な機能性物質の発見と創造が、科学と科学技術に飛躍的な発展をもたらしてきた。その根幹を担ってきたのが、原子・分子レベルで物質を探求し、創造しつづけてきた「ものづくり」の化学、すなわち物質創製化学である。豊かな物質に彩られた現代社会の恒常的発展を維持し、我が国の科学技術立国としての地位を揺るぎないものとするためにも、次世代の飛躍を約束する新たな機能性物質群を創造していかねばならない。特に、緊迫するエネルギー・環境問題の解決や最先端バイオ・情報技術の進展を図り、科学技術全般の国際的競争力を高めるためにも、革新的な機能性物質群の創造と、それらの合理合成法の開拓に向けた新学術基盤の構築が急務である。化学者に課せられた任務は極めて重い。

次世代の機能性物質創製の鍵を握るのが、物質を構成する元素、分子、分子集合体という階層性の理解と制御であると考えられている。元素により特徴づけられる多種類の原子が結合を作ることにより分子が形成され、さらに分子が集積することにより分子集合体へと組織化され、それぞれの階層に特有の性質や機能がある。生体物質の構造に例えると、個々の原子の特性を基礎とし（元素）、その機能を発揮する最小単位となるタンパク質や核酸が構成され（分子）、これらがさらに集積してウイルスや細胞内組織であるミトコンドリア（分子集合体）となる。高度に機能化された革新的な物質を創製するためには、全ての階層における構成単位を創製する術を学び、その機能を解明しなければならない。

本事業に参画する京都大学・名古屋大学・九州大学・北海道大学の４研究組織は、それぞれ「元素」「分子」「集合体」「触媒」をキーワードとした強力な中核的国際研究拠点として認知されている。本事業の前身となる「統合物質創製化学推進事業 − 先導的合成の新学術基盤構築と次世代中核研究者の育成（H22〜27 年度）」においては、４研究組織のそれぞれがストロング・ポイントをもつ各物質階層を中心に、個別に蓄積されてきた物質合成における知識と知恵を融合・深化させるとともに、物質合成概念の統合にも取り組んだ。すなわち、古典的な化学反応を利用した「化学的物質合成」ともに、高温超伝導体や発光材料、半導体などの開発に利用されてきた「物理的物質合成」や、生命体が穏和な条件下に日常的に行っている精巧かつ高効率な「生命物質合成」にも学ぶことによって、持続型経済社会を実現する、環境に調和した新たな「物質創製概念」の創出を実践した。「物質階層の統合」と「物質合成概念の統合」を合

言葉として、各研究機関の知識と経験を融合・深化させて新たな物質創製化学を遂行した結果、天然窒素還元酵素における機能中心構造の全合成、カーボンナノチューブ構造の化学合成、低環境負荷の鉄触媒による液晶材料の合成、強誘電性と強磁性が共存するマルチフェロイック物質の開発など、革新的な研究成果が生まれた。さらに、若手研究者に自由闊達な研究環境と、大学の垣根を越えた共同研究や情報交換の機会を与えたことによって、物質創製化学の未来を切り開く力量ある次世代中核研究者の育成を実現した。本事業は、この 4 大学間連携事業をさらに組織化・システム化した「新機構」を設立し、社会のニーズに応える「統合物質創製化学」を推進する。

1-2

本機構の目的

１－２．本機構の目的

新物質創製は、化学結合の形成のための新しい方法論や、機能の発現のための物質構築論などを探求する極めて基礎的な基盤学術である一方、その成果は、新触媒や新材料開発はもちろん、イノベーション創成を通じてエネルギー・資源から環境・創薬に至る極めて広い範囲に適用される。ここでは、基礎と応用が直結し（縦糸）、また化学を中心として物理から生命科学までの多くの研究分野の協力が必須である（横糸）。すなわち、物質と情報そして人が集結することが何より重要な分野と言えよう。しかしながら、我が国の物質創製研究は極めて高い国際競争力をもつにもかかわらず、新物質創製を総合的かつ戦略的に進める機関・組織は、残念ながら我が国には存在しない。基礎と応用を結ぶ縦糸と多様な分野を結ぶ横糸を組み合せ、近年長足の進歩を遂げたナノ計測や計算化学を取り込んだ統合的な研究組織の構築が急務である。その一方で、現在のひっ迫した財政の下では、多くの面積とポストを必要とする新研究所設立のような事業は現実的ではない。物質創製の学術を継承・発展させ、迫りくる環境問題などの重点課題を解決し、また新産業創出を成すためには、産官学連携や国際

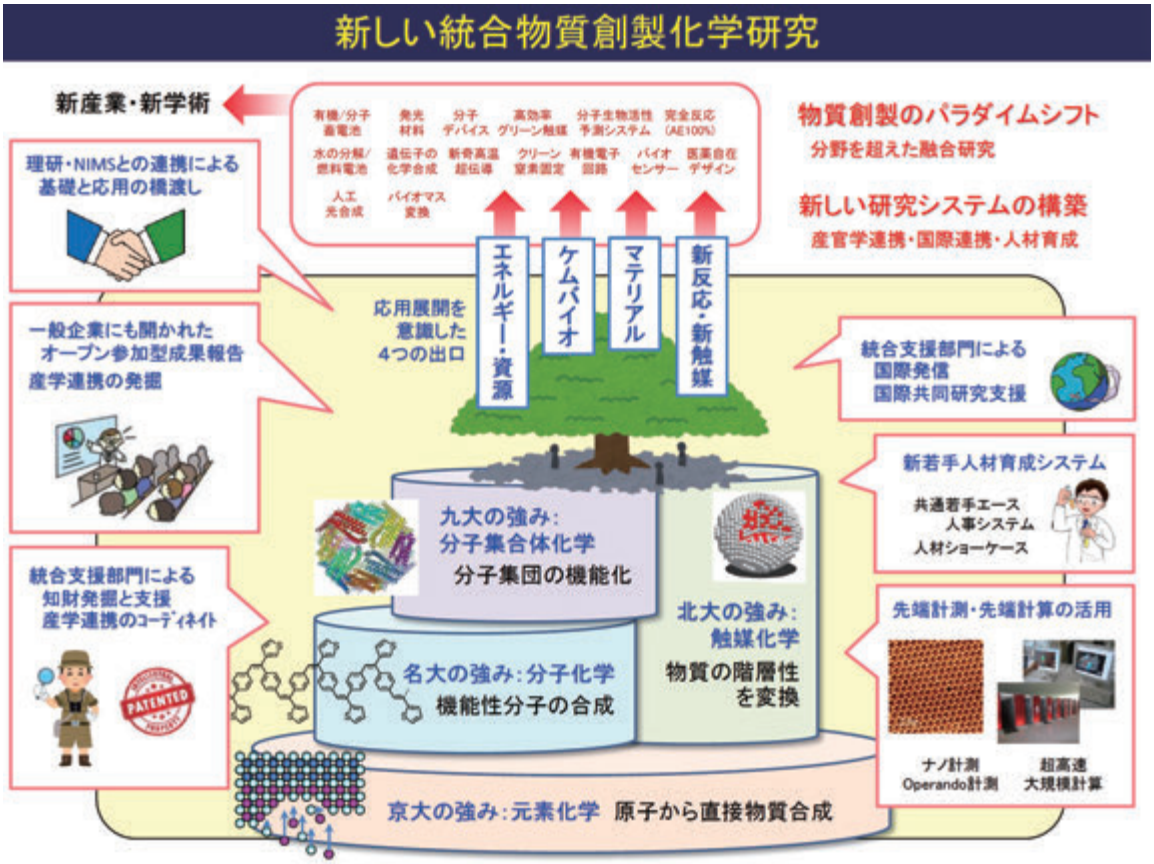

図１

連携を前面に出し、責任あるマネージメント体制を持ちながらも、最小限の面積とポストの獲得で遂行できる、大学間連携を基盤とした「統合物質創製化学研究推進機構」は、必要かつタイムリーな事業である。

図１に統合物質創製化学研究推進機構の概念図を示す。本機構事業に参画する名古屋大学・京都大学・九州大学・北海道大学の４研究組織は、「分子」、「元素」、「集合体」、「触媒」の化学研究において、それぞれに特色ある強力な中核的国際研究拠点として認知されているが、以下に示すそれぞれのストロング・ポイントを活かしながら、物質の階層構造を縦断する研究連携を実現する。

名古屋大学：無機化学から有機化学にわたる分子性物質の合成と機能の発現、さらには不斉反応を含む分子触媒の開発研究において卓越した成果をあげてきた。最近では、生物無機化学やナノ炭素科学分野においても世界をリードする。

京都大学：元素の特性の解明と、それに基づく機能創出の化学において先導的な研究成果をあげている。機能性元素科学という新しい研究パラダイムを提唱し、分子性物質から凝縮系物質に至る様々な革新的新物質群の出現を促してきた。

九州大学：複雑な分子集合体・集積体を構築する新概念を提出し、多くの機能性集積体の合成研究を通してナノサイエンス・テクノロジー研究に先鞭をつけた。最近では、核酸ナノマシンやナノハイブリッド材料の創出などで顕著な成果を挙げる。

北海道大学：触媒化学において世界を先導する中核的研究拠点である。触媒元素・分子のナノ・ミクロ集積・集合化学の研究を推進し、資源高度利用触媒、環境触媒、バイオ利用触媒、燃料電池・電極触媒、光触媒などで多くの成果を挙げる。

さらに本研究推進機構では、基礎研究を中心とする一方、「新反応・新触媒」、「マテリアル」、「エネルギー・資源」、「ケムバイオ」という、応用展開を意識した４つの出口を設定して基礎と応用を直結させる。その上で、産官学連携や国際連携を組織的に取り込み、新しい研究システムや研究支援体制、人材育成システムを取り入れた、社会に開かれた新組織である。物質創製における我が国の研究の厚みを継承し、新学術・新産業の創出と後継人材の育成を両立させながら、持続可能な社会の発展を導く。

1-3

本機構の組織

１－３．本機構の組織

本機構事業では、１－２で説明した機構研究の概念を実現するため、全く新しい大学間連携のフレームワークを構築する。一般論だが、これまでの大学間ネットワーク事業が抱える問題点としは、

① 高い大学間の壁
② 出口設定が難しく、研究目標を立てにくい
③ 平等主義によるガバナンス不足
④ 縦割り（大学別）の研究支援と人材育成支援
⑤ 外部意見が反映されにくい
⑥ 連携のメリットがネットワーク内に閉じる

などが挙げられる（図２(a)）。最大の問題点は⑥で、連携のメリットが社会発信されず、また社会の要請による事業という意識も希薄であった。ネットワーク形成のような大学強化事業は、社会からの認知によってはじめて達成されるもので、本研究推進機構事業においては、成果、情報、人材がネットワークの外側に輩出される外部発信型の連携を目指している。研究推進機構の組織図を図３に示すが、以下、運営体制、統括研究部門、研究支援部門についてその概要を説明する。

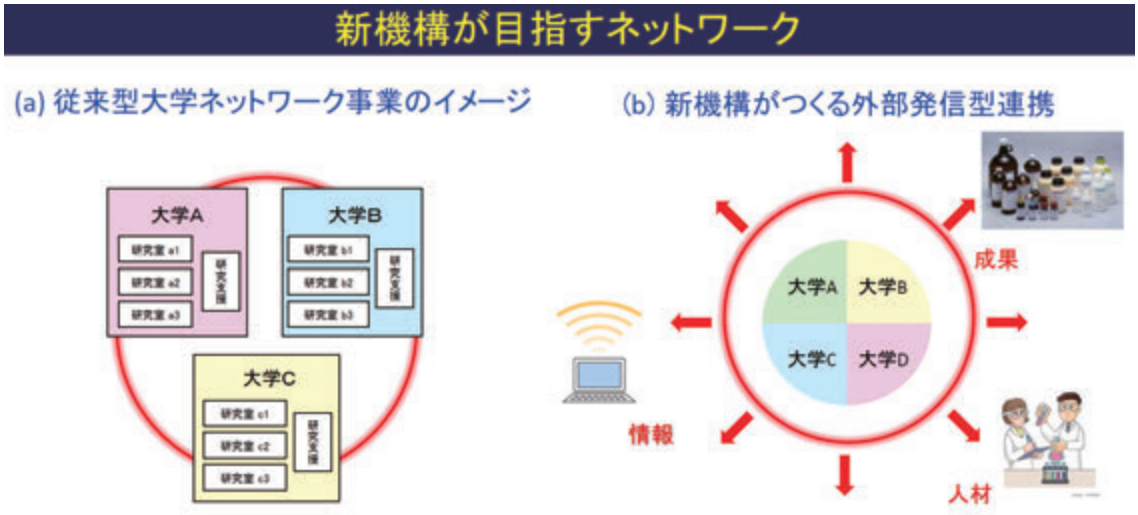

図２

運営体制

本事業推進に全責任を負う機構長を置く。機構長は、国内の学識経験者（4〜6 名）や理化学研究所などの連携機関から派遣された委員、本事業の実行委員から構成される運営委員会を組織する。運営委員会は、連携事業計画の策定と成果の取纏めを行う。運営委員会で制定された事業計画は、研究統括部門の研究プラットホーム・リーダーから構成される実行委員会によって遂行される。

統合研究部門

機構長および運営委員会のリーダーシップの下、応用という研究の出口を意識した統合研究部門（新反応・新触媒、マテリアル、エネルギー・資源、ケムバイオの４研究プラットホーム）を設置する。各プラットホームには、連携大学から１研究室ずつ選抜した４研究室と、産官学・海外から招聘した連携客員研究室を設置して共同研究を実施する。各プラットホームにおける研究内容は以下の通りである。

新反応・新触媒研究：連携４大学の固体触媒（北大）、分子触媒（名大）、元素触媒（京大）、分子集合体触媒（九大）の研究チームの共同研究によって、ゼロエミッション・カップリング反応の開発など、必要なものを必要なだけグリーンにつくりだす化学を発展させ、炭素ナノ材料や医薬品の革新的合成に展開する。

マテリアル研究：炭素材料、ナノ粒子、有機物、無機固体、金属錯体、高分子に至る物質群の開発は、機構４大学が世界を先導している分野である。その研究は多岐にわたるが、例えば４大学が開発する新規光機能性分子を超分子化することによって、既存の細胞イメージングから、分子イメージングや更には機能イメージングへと発展させる。

エネルギー・資源研究：エネルギー・資源問題は化学が取り組むべき緊急課題である。金属ナノ粒子・界面の機能化（北大、名大）や革新的ナノカーボン材料開発（名大）を通じて、新しい燃料電池や太陽電池を開発する（北大、京大、九大）。X 線吸収スペクトル計測（北大、名大）などによって反応機構を押さえながら、ユビキタス元素が生み出すグリーンエネルギーを創製する。

ケムバイオ研究：人工酵素を実現するための基本設計の確立は、生命科学における主題の一つである。生体分子合成（九大）とナノクラスター導入技術（京大）、ミューテーション技術（名大）を組み合わせ、計算シミュレーション（九大）を道しるべとしながら、機能をつくりこんだ人工酵素の合成にまで発展させる。

各研究プラットホームの構成は以下の通りである。

プラットホーム名	リーダー	コア研究室メンバー
新反応・新触媒	中野環（北大）	唯美津木・伊丹健一郎（名大）、中村正治（京大）、永島英夫・國信洋一郎（九大
マテリアル	島川祐一（京大）	清水研一（北大）、山口茂弘（名大）、高原淳・友岡克彦（九大）
エネルギー・資源	阿波賀邦夫（名大）	福岡淳（北大）、小澤文幸・村田靖次郎（京大）、佐藤治（九大）
ケムバイオ	吉澤一成（九大）	長谷川淳也（北大）、阿部洋（名大）、二木史朗（京大）

各プラットホームにグループリーダーを置き、各分野の連携研究の推進に責任をもつ。さらに、各プラットホームでは若手研究者を特任助教や博士研究員として雇用する。これらの若手研究は、共通若手エース人事システムにより採用される。若手研究者の登竜門として機構を位置づけ、切磋琢磨による人材育成によって外部のパーマネント・ポジションに送り出す。

本機構内に限定せず、統合的な共同研究を促進するため、**融合創発研究**を実施する。共同研究提案を行い、運営委員会の審査を経て採択課題を決定し、実施する。また、年度末に研究成果について報告書を作成し、運営委員のレビューを受けるものとする。概ね毎年 10 件程度を実施する。

統括支援部門

名古屋大学物質科学国際研究センター内に設置し、センターに付設の化学測定機器室を用いて本事業の研究を支援するとともに、国際シンポジウム等の開催に必要な外国人研究者招聘に関わる事務手続き、本事業の研究成果の取纏め、ポスターの作成、ホームページの管理などの広報活動を担当する。具体的には、以下の支援を行う。

① **外部発信・国際発信**：機構の研究成果を、HP や種々のメディアなどを通じて国際的に広報する。
② **共同研究コーディネート**：機構研究全体を見渡して、新しい共同研究を萌芽させる。
③ **知財発掘と管理**：機構研究全体を見渡して、知財獲得を支援する。
④ **若手キャリアパス支援**：求職情報を若手に流布し、キャリアパスセミナーを実施する。
⑤ **会議・シンポジウム開催支援**：オープン参加型シンポなどを広報、支援する。

1-4

本機構の組織

１－４．本機構の特長

社会に開かれた新機構は、以下の５つの特長を持つ。

① **戦略的なガバナンスに基づく融合研究**：機構長のリーダーシップの下、応用という研究の出口を意識した統合研究部門（新反応・新触媒、マテリアル、エネルギー・資源、ケムバイオの４研究プラットホーム）を設置し、各プラットホームには、連携大学から１研究室ずつ選抜した４研究室と、産官学・海外から招聘した連携客員研究室を設置して共同研究を実施する。更に融合研究部門を設置し、産官学や国際連携の場とする。大学間の壁を乗り越え、かつ開かれた研究組織を構築する。

② **イノベーション創出とグローバル化**（図４）：研究部門を横断的に支援するため統括支援部門を設置し、マネージメント教員、プロジェクト支援員などを配置する。共同研究コーディネート、知財獲得、国際発信、若手人材育成などを、大学間の壁を取り払って行う。理化学研究所などを連携機関として加え、イノベーション創出などを活性化する。

③ **外部発信型連携**：新しい産官学連携と国際連携のパラダイムを構築する。オープン参加型の成果報告会などを開催することによって、研究成果・研究情報・人材を、産業界、官界、学界、海外に対して外向きに発信・輩出する。

④ **共通若手エース人事システム**（図５）：大学院生から若手研究者まで、各階層のニーズに合わせた人材育成を行う。特任助教や研

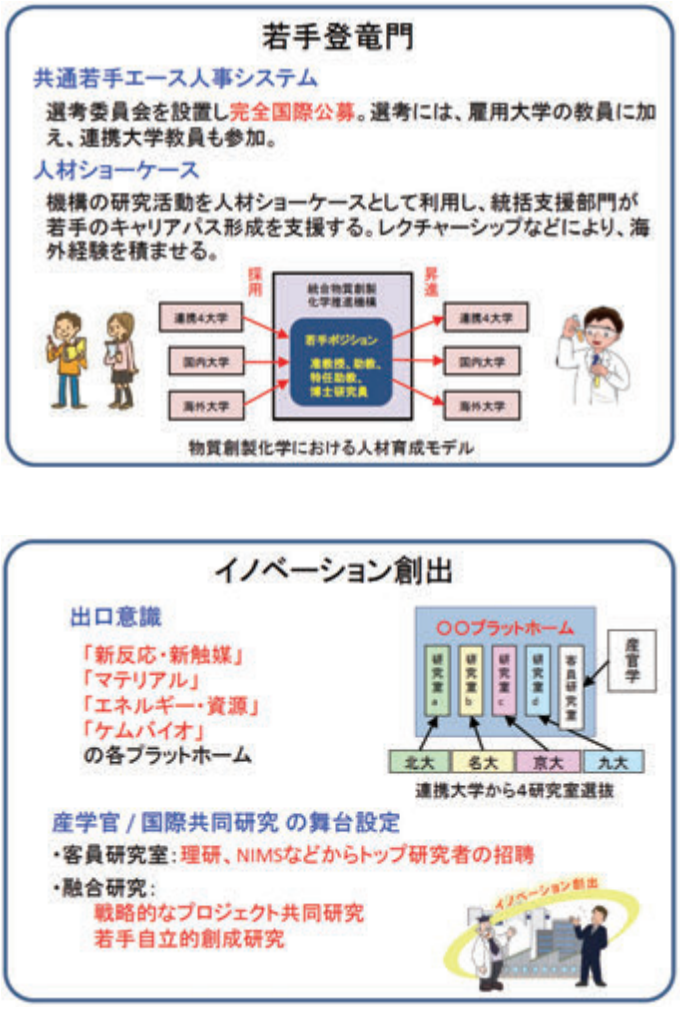

図４

究員の人事ついては、共通若手エース人事システムを採用する。すなわち、連携大学共通の選考委員会を設置して人選する。機構の研究活動を人材ショーケースとして利用して若手のキャリアパス形成を支援すると共に、レクチャーシップ派遣や招聘により国際的人脈形成を促す。若手研究者の登竜門として機構を位置づけ、切磋琢磨による人材育成によって外部のパーマネント・ポジションに送り出すことにより、物質創製分野における新たな人材育成モデルを実現する。

⑤ **ナノ計測と計算化学の支援**：ナノ計測と計算化学の支援の下、合理的な物質創製研究を展開する。

以上、基礎研究を重視しながらも、応用という研究の出口を意識した４テーマに各大学から１研究室を送り込む形で統合研究部門を形成することによって、互いの研究の強みを補完する研究体制を敷く。ガバナンスを効かした機構運営によって招聘される、理化学研究所などからの客員研究室の存在は、産官学との結びつきを強化すると共に、機構組織の流動性を高めるだろう。この上で、大学の壁を越えた統括支援部門による効率的な知財発掘や国際発信によって、新機構のビジビリティは必然的に高まる。このように、社会を意識した機構の研究活動は、院生や若手研究者の人材ショーケースとして作用し、前述した共通若手エース人事システムは人材の流動性を必然的に生み出す。

1-5

事業計画

１－５．事業計画

本事業のロードマップを図６に示す。

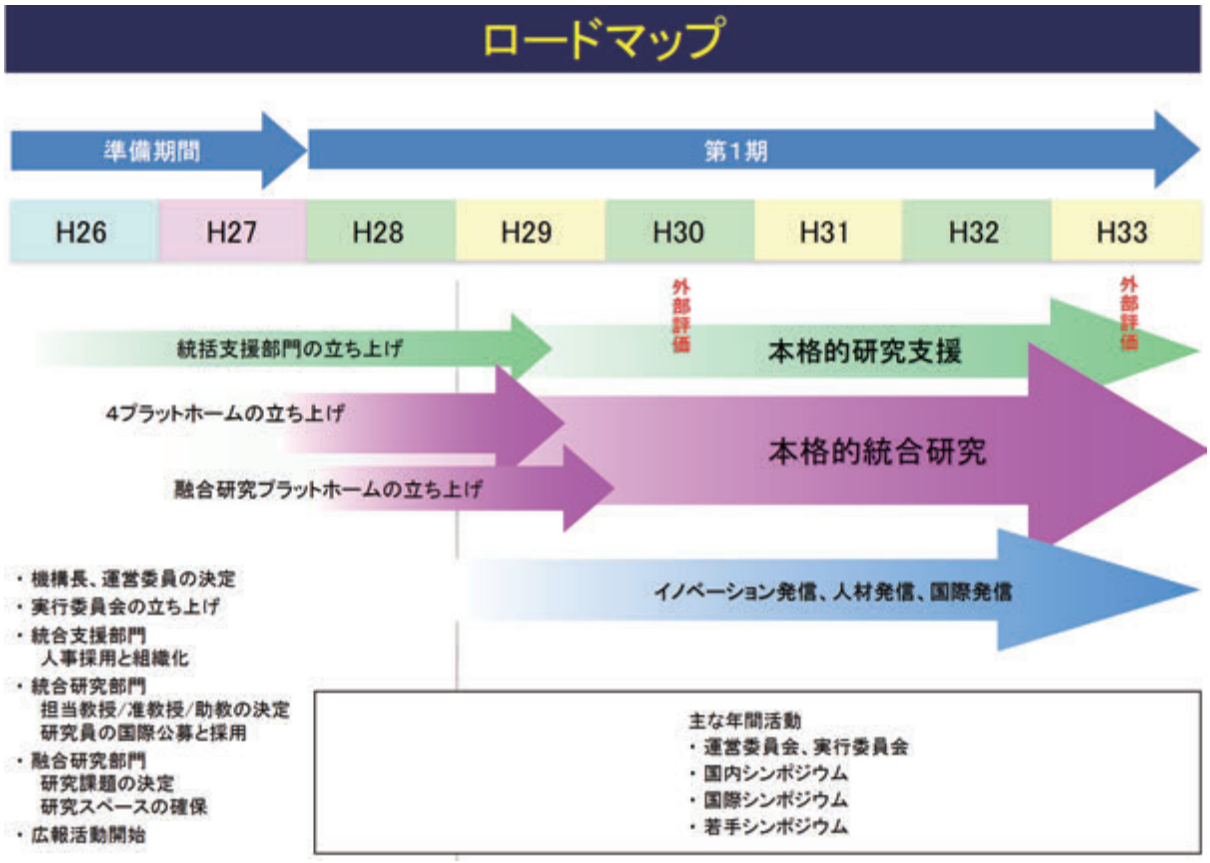

図６

1-6

本機構の期待される成果と波及効果

１－６．本事業の期待される成果と波及効果

１）本事業がめざす物質階層の統合と物質合成概念の統合により、総合的な物質観に基づく多彩な物質創製法が創出される。それらは、生体機能、電子機能、光機能、触媒機能などの有用機能をもつ機能性物質群を創造するための新学術基盤の構築へと展開される。

２）革新的な機能性物質群の創製は、材料科学分野に革新をもたらす。これまでの物質合成では、ナノテクノロジーで多用される熱力学支配による自己組織化が指導原理として用いられてきた。これに対して、本事業では、準安定物質の合成法の開拓により、自己組織化を超えた新規機能性物質群の創製法が開発されるものと期待される。これにより、高圧合成と薄膜技術の融合による非平衡物質群の創製、人工超格子をもつ特異な高次構造体の合成、光磁気特性を示す新規錯体や有機発光素子の開発、酵素反応の解明と生命機能の理解に資する人工酵素の合成などが達成され、最先端のバイオ・情報技術へと応用・展開される。

３）縦糸（基礎と応用）と横糸（多様な分野）が結ばれ、産官学及び国際的に開かれた物質創製化学研究が実施され、物質創製化学の新しい学術基盤が構築される。その結果、環境に優しい新触媒開拓、新規機能電子物質に基づく骨太イノベーション、更には新医薬品や生体活性物質開発が成される。これらは持続可能な文明社会の構築に大きく貢献する。

４）高度な研究機能をもつ国際研究拠点の有機的連携により、多くの若手研究者に広範な学問領域を統合した卓越した研究環境を提供することができる。このような環境は、幅広い知識と複眼的思考力を備えた中核研究者の養成に必要不可欠な要件である。本事業では、若手研究者を統合研究フェローとして処遇し、自由で創造的な研究環境を提供する。これにより、物質創製化学の将来を担う中核研究者を多数育成できるものと期待される。また、国際研究拠点の連携は、我が国の学術的先進性と国際競争力を確保するためにも重要であり、多くの若者に、海外の一流研究者と切磋琢磨する機会を提供し、国際的な研究者として成長するためのインセンティブを与える。

５）本申請が提案する新機構のスキームの有効性は、物質創製化学分野にだけ限定されない。このスキームにより、参加大学の強みを生かして我が国の学術を結集できるほか、大学間連携のメリットが産官学連携や国際連携を通じて外向きに発信されることにより、社会からの支持も得られる。この効果は、新国立研究所の設立にも匹敵す

る。このような外向きリンクの大学間連携事業のパイロットプログラムとして、他分野への波及効果やインパクトも大きい。

６）事業計画終了後は、新物質創製を総合的かつ戦略的に進める研究システムという枠組みは残しながらも、統括研究部門における研究テーマや参加研究室を全面的に見直し、また現在の連携 4 大学以外からの参加を促してオールジャパン体制をつくり、更に進んだ物質創製最先端研究を進める。

2

メンバー

2-1

コア研究室メンバー、連携研究室メンバー
リサーチフェロー

● 機構長

巽 和行

名古屋大学物質科学国際研究センター 特任教授

● 北海道大学

新反応・新触媒研究プラットホーム　メンバー一覧

＜コア・連携研究室＞

朝倉清高　教授（基礎研究系・触媒表面研究部門）

長谷川淳也　教授（基礎研究系・触媒理論研究部門）

福岡　淳　教授（基礎研究系・物質変換研究部門）

清水研一　教授（基礎研究系・触媒材料研究部門）

大谷文章　教授（基礎研究系・光触媒科学研究部門）

高橋　保　教授（基礎研究系・分子触媒研究部門）

中野　環　教授（基礎研究系・高分子機能科学研究部門）

西田まゆみ　教授（実用化推進系・研究開発部門）

＜リサーチフェロー＞ …平成 31 年 3 月末現在

SIDDIKI, S. M. A. Hakim 特任助教（基礎研究系・触媒材料研究部門）

佐川拓矢　研究員（基礎研究系・物質変換研究部門）

● 名古屋大学

エネルギー・資源研究プラットホーム　メンバー一覧

＜コア・連携研究室＞

阿波賀邦夫 教授（物性化学）
山口茂弘 教授（機能有機化学）
伊丹健一郎 教授（有機化学）
唯美津木 教授（無機化学）
阿部洋 教授（生物有機化学）
野依良治 特別教授・斎藤進 教授（分子触媒化学）
田中健太郎 教授（分子組織化学）
菱川明栄 教授（光物理化学）
篠原久典 教授（物理化学）
渡辺芳人 教授（生物無機化学）

＜リサーチフェロー＞ …平成 31 年 3 月末現在

Wu Yang（物性化学）
Dattatraya B. Bagal（有機合成化学）
阿部奈保子（生物有機化学）
王晨光（機能有機化学）
Xian-Kai Wan（無機化学）

● 京都大学

マテリアル研究プラットホーム　メンバー一覧

＜コア・連携研究室＞

中村 正治 教授（有機分子変換化学）
島川 祐一 教授（先端無機固体化学）
小澤 文幸 教授（錯体触媒変換化学）
金光 義彦 教授（光ナノ量子物性化学）
村田 靖次郎 教授（構造有機化学）
二木 史朗 教授（生体機能設計化学）
時任 宣博　教授（有機元素化学）
若宮 淳志　教授（分子集合解析）

＜リサーチフェロー＞…平成 31 年 3 月末現在

GELDSETZER, Jan 特定研究員（有機分子変換化学）
後藤 真人 研究員（先端無機固体化学）
阿波連 知子 研究員（光ナノ量子物性科学）
GUO, Jing-Dong 研究員（有機元素化学）

● 九州大学

ケムバイオ研究プラットホーム　メンバー一覧

＜コア・連携研究室＞

吉澤　一成　教授（反応・物性理論分野・先導物質化学研究所）
佐藤　治　教授（分子物質化学分野・先導物質化学研究所）
國信　洋一郎　教授（機能分子化学分野・先導物質化学研究所）
友岡　克彦　教授（集積分子機能分野・先導物質化学研究所）
永島　英夫　教授（クラスター分子化学分野・先導物質化学研究所）
高原　淳　教授（複合分子システム分野・先導物質化学研究所）

＜リサーチフェロー＞ …平成 31 年 3 月末現在

塩田　淑仁　准教授（反応・物性理論分野・先導物質化学研究所）
金川　慎治　助教（分子物質化学分野・先導物質化学研究所）
SU, Shengqun　特任助教（分子物質化学分野・先導物質化学研究所）
河崎　悠也　特任助教（集積分子機能分野・先導物質化学研究所）

2-2

外部評価委員

● 外部評価委員

岩村 秀
　東京大学 名誉教授

岩澤康裕
　電気通信大学 燃料電池イノベーション研究センター長 特任教授

上村大輔
　神奈川大学 特別招聘教授

江崎信芳
　放送大学京都学習センター 所長

大峰 巌
　分子科学研究所 名誉教授

新海征治
　九州大学高等研究院 特別主幹教授

玉尾皓平
　理化学研究所グローバル研究 クラスタ長

3

平成30年度事業報告

3-1

第２回 統合物質若手の会

統合物質創製化学研究推進機構（IRCCS）
第二回　若手の会

開催日：平成 30（2018）年 6 月 15 日(金) ～16 日(土)
会場：北海道千歳市「休暇村支笏湖」
主催：統合物質創製化学研究推進機構

プログラム / Program

平成 30 年 6 月 15 日(金)

14:00-14:25　参加登録 / Regstration
14:25-14:30　開会の挨拶・趣旨説明 / Opening
古川森也（Shinya FURUKAWA, 北海道大学 清水研准教授）

研究発表 / Oral Session
座長 / Chair　辻　雄太（Yuta TSUJI, 九州大学　吉澤研助教）
14:30-14:45　OP-1　愛場　雄一郎（Yuichiro AIBA, 名古屋大学 渡辺研助教）
「ゲノム DNA 認識に向けたペプチド核酸（PNA）の開発」

14:45-15:00　OP-2　菅　大介（Daisuke KAN, 京都大学 島川研准教授）
「エピタキシャル成長した遷移金属酸化物をモデル電極とした酸素還元反応触媒活性の評価」

15:00-15:15　OP-3　齋藤　雅明（Masaaki SAITO, 名古屋大学 柳井研助教）
「大規模実在系に適用可能な高精度電子状態理論の開発と応用」

15:15-15:25　休憩 / Break
座長/ Chair　橋川　祥史（Yoshifumi HASHIKAWA, 京都大学 村田研助教）
15:25-15:40　OP-4　古川　森也（Shinya FURUKAWA, 北海道大学　清水研准教授）
「金属間化合物を用いた高効率触媒系の構築と新奇な表面効果」

15:40-15:55　OP-5　脇岡　正幸（Masayuki WAKIOKA, 京都大学　小澤研助教）
「直接的アリール化重合：π共役系高分子の簡便かつ高精度な合成法」
15:55-16:00　休憩 / Break

招待講演 / Invited Lecture　座長/ Chair　古川　森也（北海道大学）
16:00-17:00　北野　政明　先生
（Masaaki KITANO, 東京工業大学 元素戦略研究センター　准教授）
「非酸化物を利用した低温アンモニア合成触媒の開発」

17:00-18:30　写真撮影後、フリータイム / Group photo, Free time

18:30-19:15　夕食 / Dinner

19:30-21:00　ポスターセッション / Poster Session

21:00-23:00　懇親会 / Mixer

平成 30 年 6 月 16 日(土)

研究発表 / Oral Session
座長 / Chair　愛場　雄一郎 (Yuichiro AIBA, 名古屋大学 渡辺研助教)

9:00-9:15　OP-6　宮崎　玲 (Ray Miyazaki, 北海道大学 長谷川研D2)
「シリカ担持白金触媒によるエチレンの完全酸化反応機構の解析: C=C 結合活性化メカニズムに関する理論的研究」

9:15-9:30　OP-7　中西　勇介 (Yusuke NAKANISHI, 名古屋大学 篠原研特任助教)
「ナノチューブ鋳造法による一次元遷移金属カルコゲナイドの創製と物性評価」

9:30-9:45　OP-8　河野　健一 (Kenichi KAWANO, 京都大学 二木研助教)
「高曲率小胞指向性を有する曲率感知ペプチドの開発」

9:50-10:00　休憩 / Break

座長 / Chair　古川　森也 (北海道大学)

10:00-10:15　OP-9　辻　雄太 (Yuta TSUJI, 九州大学 吉澤研助教)
「IrO_2 表面でのメタン活性化についての理論的研究」

10:15-10:30　OP-10　山田　泰之 (Yasuyuki YAMADA, 名古屋大学　田中研准教授)
「超分子会合体形成反応を利用した低級アルカン酸化触媒活性化」

10:30-10:40　休憩 / Break

招待講演 / Invited Lecture　座長 / Chair　古川　森也 (北海道大学)

10:40-11:40　猪熊　泰英　先生
(Yasuhide INOKUMA, 北海道大学大学院工学研究院　准教授)
「カルボニルひも ～着想と合成、これからの展開～」

12:00-12:30　閉会の挨拶 / Closing
中野　環 (Tamaki NAKANO, 北海道大学 教授, オブザーバー)
総括　古川　森也 (北海道大学)

解散

ポスターセッション / Poster Session

平成 30 年 6 月 15 日(金)　19:30-21:00

PP-1　河崎　悠也 (Yuuya KAWASAKI, 九州大学　友岡研特任助教)
「クリック反応素子 DACN を用いた多分子連結法の開発」

PP-2　Jan GELDSETZER (PD, Nakamura Lab, Kyoto University)
“Iron-Catalysed Asymmetric Carbometalation of Azabicyclic Alkenes”

PP-3　河野　慎一郎 (Shin-ichiro KAWANO, 名古屋大学, 田中研講師)
「巨大な内部空孔サイズを持つカラムナー液晶性大環状化合物の開発」

PP-4　戴　河双 (Heshuang DAI, 北海道大学, 中野研 D2)
「(R)-1,1’-Bi(2-naphthol)を用いた光学活性ポリウレタンの合成」

PP-5　田原　淳士 (Atsushi TAHARA, 九州大学, 永島研助教)
「Ir 触媒を用いたアミド化合物の化学選択的ヒドロシラン還元反応による D-A 型 π 共役エナミンの合成及び機能評価」

PP-6　行本　万里子 (Mariko YUKIMOTO, 京都大学, 時任研助教)
「トリプチシル基骨格を導入したテトラアルキルジシレンの合成と構造」

PP-7　友池　史明 (Fumiaki TOMOIKE, 名古屋大学, 阿部研助教)
「GSTP 共有結合性阻害剤の開発」

PP-8　張　照明 (Zhaoming ZHANG, 北海道大学, 中野研 D3)
「(R)-1,1’-Bi(2-naphthol)を用いた光学活性ポリウレタンの合成」

PP-9　池田　京 (Kei IKEDA, 九州大学, 吉澤研 M2)
「芳香族性と伝導性の相関に関する理論的研究」

PP-10　橋川　祥史 (Yoshifumi HASHIKAWA, 京都大学, 村田研助教)
「フラーレン C_{60} の疎水性内部空間にとりこまれた水分子の動的挙動」

PP-11　鄭　知恩 (Jieun JUNG, 名古屋大学, 野依研助教)
「PNNP 型四座配位子を有するイリジウム錯体を用いた二酸化炭素の　光還元反応」

PP-12　王　ヤン (Yue Wang, 北海道大学, 中野研助教)
「近赤外色素分子の会合体およびキラル複合体の形成」

PP-13　Sheng-qun SU (Resercher, Sato Lab, Kyushu University)
“Large Anisotropic Thermal Expansion in a crystalline Cobalt(II) Complex”


K+
Na+
ゲノムDNA認識に向けた
ペプチド核酸（PNA）の開発


SrTiO3
KYOTO


Nanoscale casting


Self Introduction

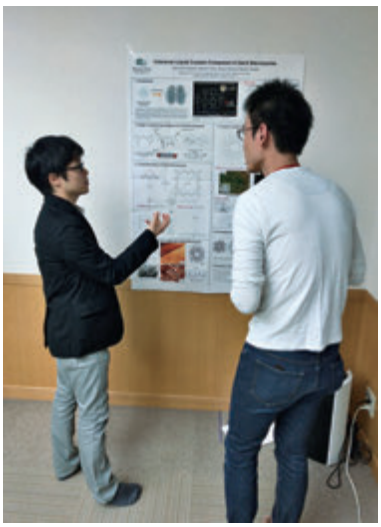

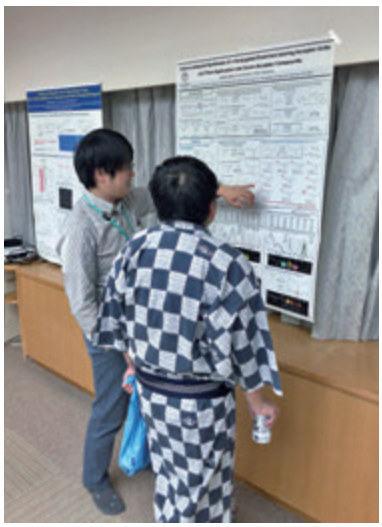

若手会集合写真

3-2

第４回 統合物質国内シンポジウム

Integrated Research Consortium on Chemical Sciences

統合物質創製化学研究推進機構
第4回国内シンポジウム

物質創製化学の多様化と深化

2018 10.29 月・30 火

▶13:00〜18:20　▶9:30〜15:00

会場／九州大学 筑紫キャンパス
総合研究棟（C-CUBE） 1F 筑紫ホール

招待講演

石原 達己 九州大学大学院工学研究院、カーボンニュートラルエネルギー国際研究所 教授
「Pd系ナノコロイドの合成と直接法による過酸化水素合成への応用」

土居 久志 理化学研究所 生命機能科学研究センター チームリーダー
「臨床研究を目指したPET分子プローブの開発：高速化学反応と迅速化学合成」

吉川 浩史 関西学院大学理工学部 准教授
「分子および分子集積体の蓄電機能開拓」

研究報告

北海道大学	名古屋大学	京都大学	九州大学
朝倉 清高	柳井 毅	島川 祐一	高原 淳
中島 清隆	伊藤 英人	田原 弘量	Su Shengqun

問合せ先
九州大学先導物質化学研究所
友岡 克彦
〒816-8580 福岡県春日市春日公園6-1
Phone: 092-583-7806, Fax: 092-583-7810
E-mail: ktomooka@cm.kyushu-u.ac.jp

統合物質創製化学研究推進機構
第4回国内シンポジウム

物質創製化学の多様化と深化

北海道大学　触媒科学研究所

名古屋大学　物質科学国際研究センター

京都大学　化学研究所

九州大学　先導物質化学研究所

日時：2018 年 10 月 29 日（月）13:00~18:20
2018 年 10 月 30 日（火） 9:30~15:00
会場：九州大学 筑紫キャンパス
総合研究棟（C-CUBE）1F 筑紫ホール

プログラム

研究報告 (A：30 分，B：20 分)，招待講演 (IL)

10 月 29 日（月）

13:00~13:10　開会の辞

13:10~13:40　研究報告 (A-1)　柳井 毅
名古屋大学・教授
「高速量子多体アルゴリズムを用いた量子化学計算」

13:40~14:10　研究報告 (A-2)　高原 淳
九州大学・教授
「量子ビームによるポリマーブラシの水界面での構造解析」

14:10~14:30　研究報告 (B-1)　伊藤 英人
名古屋大学・准教授
「縮環π拡張重合によるグラフェンナノリボンの精密合成」

14:30~14:50　休憩

14:50~15:10　研究報告 (B-2)　中島 清隆
北海道大学・准教授
「固体触媒を利用したバイオポリエステル原料の高効率合成」

15:10~16:00　招待講演 (IL-1)　石原 達己
九州大学大学院工学研究院,
カーボンニュートラル エネルギー国際研究所・教授
「Pd 系ナノコロイドの合成と直接法による
過酸化水素合成への応用」

16:00~16:10　休憩

16:10~16:50　ショートプレゼンテーション

16:50~18:20　ポスターセッション
会場：総合研究棟（C–CUBE）３階　ピロティー

18:30~20:30　交流・フリーディスカッション
会場：レストラン ぞんね

10 月 30 日（火）

9:30~10:00　研究報告 (A-3)　島川 祐一
京都大学・教授
「イオン結晶モデルによる遷移金属酸化物の
構造安定性予測と物質設計」

10:00~10:20　研究報告 (B-3)　Shengqun Su
九州大学・特任助教
「An effective way to switch the orbital magnetic momentum」

10:20~10:40　休憩

10:40~11:20　招待講演 (IL-2)　吉川 浩史
関西学院大学理工学部・准教授
「分子および分子集積体の蓄電機能開拓」

11:20~13:00　昼食

13:00~13:50　招待講演 (IL-3)　土居 久志
理理化学研究所生命機能科学研究センター
標識化学研究チーム・チームリーダー
「臨床研究を目指したPET分子プローブの開発：
高速化学反応と迅速化学合成」

13:50~14:00　休憩

14:00~14:20　研究報告 (B-4)　田原 弘量
京都大学・助教
「半導体ナノ粒子におけるマルチエキシトンの
コヒーレントダイナミクス」

14:20~14:50　研究報告 (A-4)　朝倉 清高
北海道大学・教授
「奇妙な発光分光XAFS」

14:50~15:00　閉会の辞

ポスター発表

*ショートプレゼンテーションの発表者

P-01* 金属酸化物表面でのC–H結合活性化に関する理論的研究
○辻 雄太，吉澤 一成 【九大】

P-02 含窒素多環芳香族化合物の新規一段階構築反応の開発
○川原 巧，松岡 和，伊藤 英人，伊丹 健一郎 【名大】

P-03 鉛フリーハライドペロブスカイトの光学特性および太陽電池特性
○阿波連 知子，若宮 淳志，金光 義彦 【京大】

P-04 イノラート/アライン３連続環化付加反応を用いたイプチセンの合成
○岩田 隆幸，深見 拓人，吉永 達郎，新藤 充 【九大】

P-05 光強度依存性解析にもとづく
白金担持酸化タングステン系光触媒反応機構の解明
○山田 千晴，高島 舞，大谷 文章 【北大】

P-06* 環化カップリングによる八員環構造を含む多環芳香族炭化水素の合成
○松原 聡志，古賀 義人，村上 慧，伊丹 健一郎 【名大】

P-07 イリジウム触媒によるC–Hボリル化に基づく
形式的なメタ位選択的C-H変換
○鳥越 尊，王 杰，國信 洋一郎 【九大】

P-08 PdIn金属間化合物を用いた高選択的NO還元触媒の開発
○古川 森也，全 載完，清水 研一 【北大】

P-09* General Method for the Synthesis of
Transition-metal Dichalcogenide Nanoribbons Inside Carbon Nanotubes
○相崎 元希，Ellne Park，Zheng Liu，末永 和知，中西 勇介，
篠原 久典 【名大】

P-10 DACN含有ポリマーの合成とそのクリック反応
○井川 和宣，山中 祐貴，青山 慎，河崎悠也，友岡 克彦 【九大】

P-11 Electronic Structure Origin of
Mechanochemically Activated Chitin Depolymerization
○Danjo De Chavez，Atsushi Fukuoka，Jun-ya Hasegawa 【北大】

P-12 2 色強レーザー場におけるメタン C–H 結合の非対称切断:
レーザー場強度依存性
○長谷川 景郁，藤瀬 光香，松田 晃孝，菱川 明栄 【名大】

P-13 Activation of methane at metal-support interface of Ni_4-CeO_2 (111) catalyst:
A Theoretical study
○Rajib Kumar Singha，Yuta Tsuji，M. Haris Mahyuddin,
Kazunari Yoshizawa 【九大】

P-14 環境応答性基によるオリゴ核酸の細胞内機能制御
○吉永 静也，友池 史明，木村 康明，阿部 洋 【名大】

P-15 原子価異性錯体結晶の分極制御
○佐藤 治 【九大】

P-16* 温度制御 X 線回折による酸化チタン(IV)の
アナターススールチル結晶相転移挙動の解析
○高島 舞，Bob John，大谷 文章 【北大】

P-17 X線吸収分光による鉄触媒クロスカップリング反応の機構研究
高谷 光，縣 亮介，青木 雄真，岩本 貴寛，中谷 直輝，
シャルマ アキレッシ，本間 徹男，○中村 正治 【京大】

P-18 プロトン移動が協奏するスピンクロスオーバー鉄(II)錯体の理論的研究
○堀 優太，中西 匠，塩田 淑仁，佐藤 治，吉澤 一成 【九大】

P-19 円偏光強レーザー場中 D_2 分子からの光電子垂直運動量分布の計測
○池谷 大夢，仲村 武瑠，山本 将央，長尾 優，藤瀬 光香，
松田 晃孝，伏谷 瑞穂，菱川 明栄 【名大】

P-20 銅-酸素錯体によるカルボニル化合物の
触媒的炭素–炭素結合形成反応の理論的研究
○阿部 司，堀 優太，塩田 淑仁，吉澤 一成 【九大】

P-21　Effects of Surfactants on the Oxidative Degradation of Single-wall Carbon Nanotubes
○岡 優果，山岸 美保，大町 遼，篠原 久典　【名大】

P-22　スピン転移とプロトン移動が協奏する鉄二価錯体における光誘起プロトン移動
○中西 匠，佐藤 治　【九大】

P-23*　異常高原子価鉄イオンを有するペロブスカイト酸化物の酸素脱離及び結晶構造変化
○後藤 真人，齊藤 高志，島川 祐一　【京大】

P-24*　酵素活性化分子の新規設計とスクリーニング
○米村 開，有安 真也，荘司 長三，渡辺 芳人　【名大】

P-25*　アニオン交換樹脂を用いた2-(メタクリロイルオキシエチルコリンリン酸)の新規分離法
○向井 理，高原 淳　【九大】

P-26　高選択的直接的アリール化重合によるベンゾジチオフェン含有 DA ポリマーの合成
○鳥居 直宏，脇岡 正幸，斎藤 慎彦，尾坂 格，小澤 文幸　【京大】

P-27　レブリン酸とニトリルの水素化によるラクタムの直接合成
○清水 研一，SMA Hakim Siddiki，Abeda S. Touchy，鳥屋尾 隆　【北大】

P-28　光触媒が駆動するベンジル位選択的酸化反応の開発
○宮内 紗久良，榊原 陽太，村上 慧，伊丹 健一郎　【名大】

P-29　Pd 触媒による六員環ケイ素化合物のケイ素−ケイ素結合活性化を伴う環状有機ケイ素化合物の合成
○田原 淳士，投野 竣亮，灰毛 遼平，砂田 祐輔，永島 英夫【九大】

P-30　金クラスター触媒によるピペリドンの脱水素機構に関する理論的研究: 荷電状態と触媒活性の関連性について
○宮崎 玲，金 雄傑，吉井 大地，谷田部 孝文，山口 和也，水野 哲孝，長谷川 淳也　【北大】

P-31　絶縁体の分極電流を介した交流光電変換
○富松 明宏，横倉 聖也，松下 未知雄，阿波賀 邦夫　【名大】

P-32　メタ位選択的な C–H ボリル化反応における
反応の加速と基質特異性の発現
○盧 旭，吉越 裕介，井田 悠，西 光海，金井 求，
國信 洋一郎　【九大】

P-33　カーボンナノチューブの内部空間を利用した
シェブレル相 Mo_6Te_6 ナノワイヤーの精密合成
○永田 雅貴，中西 勇介，Shivani Shukla，Zheng Liu，Yung-Chang Lin，
末永 和知，篠原 久典　【名大】

P-34*　立体保護基の活用と新規高反応性化学種への応用
○行本 万里子，時任 宣博　【京大】

P-35　金属酸化物ナノワイヤ・セルロースナノファイバーが融合した
ナノペーパーセンサの創成
○長島 一樹，古賀 大尚，高橋 綱己，Guozhu Zhang，能木 雅也，
柳田 剛　【九大】

P-36　担体–担持金属間相互作用の表裏両面直接観察への挑戦
○城戸 大貴，朝倉 清高　【北大】

P-37　ホスフィン酸を架橋部位に有する水溶性ラダー型スチルベンの
合成と光物性
○中島 菜月，深澤 愛子，小笠原 宏亮，山口 茂弘　【名大】

P-38　多官能基化されたキラルシラシクロペンタン類の不斉合成
○黒尾 明弘，井川 和宣，友岡 克彦　【九大】

P-39　Development of Transparent Organic Hole-Transporting Materials Containing
Partially Oxygen-bridged Triphenylamine Skeletons
○Minh Anh Truong，Richard Murdey，Atsushi Wakamiya　【京大】

P-40　Preparation and Redox Behavior of Ce-Cr-Rh Mixed Oxides
○Satoru Ikemoto，Xiubing Huang，Shoko Nagase，Gen-ichi Yokota，
Hirosuke Matsui，Satoshi Muratsugu，Mizuki Tada　【名大】

P-41* h-BN/Au(111)に担持金クラスターの
安定性と水素発生反応に関する理論的研究
○高 敏，中原 真希，Andrey Lyalin，武次 徹也 【北大】

P-42 DFT Exploration of Active Site Motifs in Methane Hydroxylation by Ni-ZSM-5 Zeolite
○Muhammad Haris Mahyuddin，Kazunari Yoshizawa 【九大】

P-43 Synthesis and properties of phenanthroline polymers having a pi-stacked, helical conformation
○Jiyue Luo，Weixi Yang，Zhiyi Song，Tamaki Nakano 【北大】

P-44 シトクロム P450BM3 を用いた高圧条件下エタンの直接水酸化
○有安 真也，児玉 侑朔，笠井 千枝，愛場 雄一郎，荘司 長三，
渡辺 芳人 【名大】

P-45 アルケンの光異性化を鍵とする面不斉中員環分子の合成
○吉田 祐樹，町田 康平，井川 和宣，友岡克彦 【九大】

P-46* π 共役ポリマーの精密合成のための
高性能直接的アリール化重合触媒
○脇岡 正幸，山下 菜摘，森田 葉月，市原 暢子，小澤 文幸【京大】

P-47 電荷分離層のモルフォロジー制御を目指した
ペンダント型ジブロック共重合体の開発
○牧野 貴明，高野 敦志，松下 裕秀，阿波賀 邦夫 【名大】

P-48 複数の分子連結部位を有する新規クリック反応素子の開発と応用
○河崎 悠也，瀬戸 祐樹，河原 慎太朗，井川 和宣，
友岡 克彦 【九大】

P-49 触媒反応のための高分子配位子の開発
○中野 環，木村 彰宏，長谷川 淳也，ナゲ ハッサン，王ヤン，
宋 志毅，西田 まゆみ，永 直文 【北大】

P-50 TiN 上の Pt 合金触媒の調製と酸素還元反応活性評価
○庄司 麻子，松井 公佑，唯 美津木 【名大】

P-51　Oxidation of Trace Ethylene at 0 ºC over
Platinum Nanoparticles Supported on Silica
○Shazia Sharmin Satter，Jun Hirayama，Kiyotaka Nakajima，
Atsushi Fukuoka　【北大】

P-52　動的面不斉を有する10員環ジアリルアミドの設計と合成
○林 純一，堀川 真太郎，井川 和宣，友岡 克彦　【九大】

P-53　フラーレン C60 の疎水性内部空間に取り込まれた水分子の動的挙動
橋川 祥史，○村田 靖次郎　【京大】

P-54*　非共有結合性相互作用による分極制御を利用した
マルチカラー蛍光分子の開発
○森 敏彰，吉越 裕介，山川 健司，金井 求，國信 洋一郎　【九大】

P-55　リン酸フロリド基の医薬化学への応用
○田辺 航，友池 史明，村上 優子，木村 康明，阿部 洋　【名大】

P-56　金属酸化物粉末の電子トラップ密度エネルギー分布解析の
高エネルギー対応と高精度化
○村上 雄馬，高島 舞，大谷 文章　【北大】

P-57　アザビシクロアルケンの鉄触媒不斉カルボメタル化反応
○ゲルトセッツァー ヤン，磯崎 勝弘，アダク ラクスミカンタ，
齋藤 奨太，ガワー ニコラス J，コグスウェル ポール，川端 辰弥，
神 将吉，伊藤 拓馬，伊藤 慎庫，中村 正治　【京大】

P-58　ゼロ価コバルト及び鉄–イソシアニド触媒を用いる
ヒドロシロキサンによるアルケンのヒドロシリル化反応
○真川 敦嗣，永島 英夫　【九大】

P-59*　Re/TiO_2 触媒を用いた CO_2 の水素化による低温メタノール合成
○鳥屋尾 隆，陳 家偉，清水 研一　【北大】

P-60　アミノ酸ジアミドの時間発展的超分子重合に及ぼす二量化の効果
○高松 愛子，大城 宗一郎，松本 健太郎，山口 茂弘　【名大】

P-61　単結晶ナノワイヤ表面に対する分光分析を用いた
酸化物表面におけるアルデヒドの化学変換経路の解明
○細見 拓郎，王 琛，長島 一樹，高橋 綱己，張 国柱，金井 真樹，
水上 渉，塩谷 暢貴，下赤 卓史，玉岡 武泰，吉田 秀人，
竹田 精治，安井 隆雄，馬場 嘉信，青木 百合子，寺尾 潤，
長谷川 健，柳田 剛　【九大】

P-62　Photocatalytic CO_2 reduction using an iridium complex with
PNNP-type tetradentate ligand
○Kenji Kamada，Manami Muraki，Jieun Jung，Kieta Sekizawa，
Shunsuke Sato，Takeshi Morikawa，Shunichi Fukuzumi，
Ryoji Noyori　【名大】

P-63　Efficient and Reproducible Lead-free Perovskite Solar Cells Based on Purified Precursor Materials and Modified Solution Process
○Jiewei Liu，Masashi Ozaki，Shinya Yakumaru，Taketo Handa，
Yoshihiko Kanemitsu，Takashi Saito，Yuichi Shimakawa，Yasujiro Murata，
Tomoya Nakamura，Richard Murdey，Atsushi Wakamiya　【京大】

P-64　Metal-loaded TiO_2 photocatalysts for dehydrogenation of methanol under flow conditions
○Kensuke Kobayashi，Ryoko Nagata，Ryoji Noyori，Susumu Saito，
Hiroshi Naka　【名大】

集合写真

3-3

第２回 統合物質国際シンポジウム

Integrated Research Consortium on Chemical Sciences

IRCCS The 2nd International Symposium

New Future by Chemical Synthesis and Energy Materials

Jan. 25th–26th, 2019

Kihada Hall, Uji Campus, Kyoto University, Uji, Japan

Invited Lectures

Prof. James Durrant
Imperial College London, UK

Prof. Wen-Yann Yeh
National Sun Yat-sen University, Taiwan

Prof. Yasuhiro Tachibana
RMIT University, Australia

Prof. Kyungkon Kim
Ewha Womans University, Korea

Contributions from IRCCS members

Kyoto University, Japan
Prof. Atsushi Wakamiya
Prof. Takashi Hirose

Hokkaido University, Japan
Prof. Bunsho Ohtani
Dr. Takashi Toyao

Kyushu University, Japan
Prof. Shigeto Okada
Dr. Kazunobu Igawa

Nagoya University, Japan
Prof. Shigehiro Yamaguchi
Dr. Zhongyue Zhang

Contact

Prof. Yuichi Shimakawa
Prof. Yasujiro Murata
Institute for Chemical Research,
Kyoto University
Uji, Kyoto 611-0011, Japan

Secretary office

E-mail: yasujiro@scl.kyoto-u.ac.jp
Phone: +81-774-38-3172
Fax: +81-774-38-3178
http://jointproject-cscri.rcms.nagoya-u.ac.jp

ICR Institute for Chemical Research

IRCCS The 2nd International Symposium

"New Future by Chemical Synthesis and Energy Materials"

Jan. 25th–26th, 2019

Kihada Hall, Uji Campus, Kyoto University, Uji Japan

January 25th (Fri.)

12:30–13:30	Registration
13:30–13:40	Opening Remarks
	(Chair: Masaharu Nakamura, Kyoto University)
13:40–14:00	[YR-1] **Zhongyue Zhang** (*Nagoya University, Japan*) "Triptycene-Derived Metal-Organic Frameworks: Unusual Topologies, Connectivites and Physical Properties"
14:00–14:30	[SR-1] **Shigeto Okada** (*Kyushu University, Japan*) "High Voltage Sodium-Ion Battery by Concentrated Aqueous Electrolyte"
14:30–14:50	[YR-2] **Takashi Hirose** (*Kyoto University, Japan*) "Development of Molecular Functions Based on Helically Twisted Polycyclic Aromatic Hydrocarbons"
14:50–15:10	Coffee break
	(Chair: Yasujiro Murata, Kyoto University)
15:10–15:40	[SR-2] **Atsushi Wakamiya** (*Kyoto University, Japan*) "Purified Materials for Highly Efficient Perovskite Solar Cells"
15:40–16:30	[IL-1] **Wen-Yann Yeh** (*National Sun Yat-sen University, Taiwan*) "Metal Complexation and C–C Bond Activation with Fullerenes"
16:30–18:00	Poster session at 2nd floor The former half: odd numbers, the latter half: even numbers.
18:00–20:00	Banquet (Kihada restaurant, 2nd floor)

January 26th (Sat.)

(Chair: Hideki Hirori, Kyoto University)

09:20–09:50 [SR-3] **Bunsho Ohtani** (*Hokkaido University, Japan*)
"Identification and Detailed Characterization of Metal-Oxide Powders with Their Energy-Resolved Distribution of Electron Traps"

09:50–10:30 [IL-2] **Yasuhiro Tachibana** (*RMIT University, Australia*)
"Interfacial Charge Transfer and Transport Dynamics in Lead Halide Perovskite Solar Cells"

10:30–10:50 Coffee break

(Chair: Yoshiyuki Mizuhata, Kyoto University)

10:50–11:10 [YR-3] **Kazunobu Igawa** (*Kyushu University, Japan*)
"Stereoselective Synthesis of Asymmetric Silicon Molecules"

11:10–11:40 [SR-4] **Shigehiro Yamaguchi** (*Nagoya University, Japan*)
"Phosphorus-Containing Photostable and NIR Fluorophores for Bio-Imaging"

11:40–12:00 [YR-4] **Takashi Toyao** (*Hokkaido University, Japan*)
"Statistical Analysis and Design of Heterogeneous Catalysis Using Machine Learning"

12:00–13:20 Lunch

(Chair: Atsushi Wakamiya, Kyoto University)

13:20–14:00 [IL-3] **Kyungkon Kim** (*Ewha Womans University, Korea*)
"Strategies to Enhance the Performance and Stability of Organic Photovoltaics"

14:00–14:50 [IL-4] **James Durrant** (*Imperial College London, UK*)
"Charge Carrier Dynamics in Conjugated Polymers for Organic Solar Cells and Solar to Fuels"

14:50–15:00 Closing Remarks

Poster Session

At 2nd floor, from 16:30 to 18:00 on January 25th (Fri.).
The posters with odd numbers will be presented in the former half and even numbers in the latter half.
After this session, please remove posters by 12:00 on January 26th (Sat.).

[P-1] Hiroe Kubota, Takehiro Amada, Takashi Toyao, Zen Maeno, Ken-ichi Shimizu
"Spectroscopic and Theoretical Investigations of the Mechanism of NH_3-SCR Reactions over Cu-Zeolite Catalysts"

[P-2] Shunsaku Yasumura, Liu Chong, Takashi Toyao, Zen Maeno, Ken-ichi Shimizu
"Theoretical Investigation of 13-Group Metal Clusters in CHA Zeolite by Ab Initio Thermodynamics Analysis"

[P-3] Fitri Rizki Amalia, Mai Takashima, Bunsho Ohtani
"Development of a Simple but Reliable Method for Photocatalytic-Activity Evaluation"

[P-4] Pradudnet Ketwong, Shugo Takeuchi, Mai Takashima, Bunsho Ohtani
"Light Intensity-Dependence Study for Titania Photocatalysis with Multielectron Transfer Processes"

[P-5] Tharishinny Raja Mogan, Mai Takashima, Ewa Kowalska, Bunsho Ohtani
"Synthesis of Gold-Nanoparticle/silica Colloidal Crystal to Form Highly Ordered Titania Inverse-Opal Structures"

[P-6] Nabin Ch. Maity, Maximilian Krämer, Jun-ya Hasegawa, Tamaki Nakano
"Synthesis and Characterization of a Novel Fluorenone Derivative with Intramolecular Charge Transfer Properties"

[P-7] Maia Merlani, Vakhtang Barbakadze, Zhiyi Song, Tamaki Nakano
"Studies on Synthetic Analogues of Comfrey-Based, Wound-Healing Natural Biopolymer"

[P-8] Nino Zavradashvili, Yue Wang, Zhiyi Song, Ramaz Katsarava, Tamaki Nakano
"Synthesis and Physicochemical Properties of Chiral Cationic Polymers"

[P-9] Kashaboina Upendar, Natee Sirisit, Hiroko Ariga-Miwa, Satoru Takakusagi, Yuta Nishikawa, Fumiya Kuriyama, Arnoldus lambertus Dipu, Hitoshi Ogiwara, Shoji Iguchi, Ichiro Yamanaka, Takahiro Wada, Kiyotaka Asakura
"Operando EXAFS Analysis of In/SiO_2 Catalyst during NMC"

[P-10] Min Gao, Andrey Lyalin, Satoshi Maeda, Tetsuya Taketsugu
"Theoretical Study on Geometry Effect on the Catalytic Activity of Gold Clusters"

[P-11] Toshiyuki Sugiyama, Akira Nakayama, Jun-ya Hasegawa
"Reaction Mechanism of the Direct Synthesis of Dimethyl Carbonate from CO_2 and Methanol over Metal-Oxide Catalysis: a Theoretical Study"

[P-12] Liming Zhao, Akira Nakayama, Koji Oohora, Hiroyuki Meichin, Takashi Hayashi, Jun-ya Hasegawa
"Controlled Intersystem Crossing in Iron Porphycene Substituted Myoglobin for Cyclopropanation Reaction: a Theoretical Study"

[P-13] Pengru Chen, Abhijit Shrotri, Atsushi Fukuoka
"Selective Synthesis of Cello-Oligosaccharides by Hydrolysis of Cellulose over Carbon Catalyst in a Semi-Flow Reactor"

[P-14] Kyohei Tomita, Shin-ichiro Kawano, Kentaro Tanaka
"Development of Columnar Liquid Crystals of Macrocycles toward Anisotropic Transport of Lithium Ion"

[P-15] Masaaki Saitow
"Accurate Wave Function Theories for Large, Real-life Molecules"

[P-16] Ryosuke Y. Shimizu, Takeshi Yanai, Yuki Kurashige, Daisuke Yokogawa
"Calculating Bioimaging Probes with RISM(-DMRG)-CASPT2"

[P-17] Ayaka Yoshikawa, Masaaki Saitow, Takeshi Yanai
"A Hybrid Solvation Model Using CPCM in CASSCF Framework for Real-Life Molecules"

[P-18] Ayano Yamada, Masaaki Saitow, Takeshi Yanai
"Development of Fast and Accurate Self-Consistent Field Method Based on Local Resolution-of-the-Identity Approximation"

[P-19] Ayaka Ueda, Hiroyuki Kitano, Jaehoon Choi, Hideto Ito, Shinya Hagihara, Toshiyuki Kan, Hirokazu Kawagishi, Kenichiro Itami
"Discovery of Plant Growth Stimulants by C–H Arylation of 2-Azahypoxanthine"

[P-20] Shusei Fujiki, Akiko Yagi, Kenichiro Itami
"Solid-Phase Synthesis of Unsubstituted Poly(*para*-phenylene)"

[P-21] Asuka Naraoka, Tomoya Kanda, Hiroshi Naka
"Palladium-Catalyzed Transfer Hydration of Cyanohydrins"

[P-22] Shota Yoshioka, Masayuki Naruto, Ke Wen, Susumu Saito
"Development of Bidentate Diphosphine Ligands of Highly Active Ru Catalysts for Practical Hydrogenation of Carboxylic Acids"

[P-23] Yuma Sasaki, Hikaru Fujise, Yoshitaka Kawabe, Kasumi Hashigaya, Akitaka Matsuda, Yasumasa Hikosaka, Mizuho Fushitani, Akiyoshi Hishikawa
"Formation of Xe 4d Double-Core-Hole States in Strong XUV-FEL Fields Studied by Electron-Ion Coincidence Spectroscopy"

[P-24] Kouhei Wakamatsu, Hirosuke Matsui, Nozomu Ishiguro, Satoshi Muratsugu, Mizuki Tada
"*In situ* XAFS Imaging of Redox-Active Ceria Particles with Transition Metals"

[P-25] Kodai Ishihara, Yuna Araki, Mizuki Tada, Yoichi Sakai, Yasuhiro Ohki
"Synthesis of Dinuclear Mo-Fe Hydride Complexes for the Catalytic Silylation of N_2"

[P-26] Yusaku Kodama, Shinya Ariyasu, Osami Shoji, Yoshihito Watanabe
"Direct Hydroxylation of Gaseous Alkane by Cytochrome P450 under High-Pressure Condition"

[P-27] Yuichiro Aiba, Masaki Hibino, Gerardo Urbina, Yuuki Ochiai, Naomi Kochi, Masanari Shibata, Osami Shoji, Yoshihito Watanabe
"Chemically-Modified Peptide Nucleic Acids for *in cellulo* Applications"

[P-28] Hideo Katakura, Yushi Niimi, Fumiaki Tomoike, Yasuaki Kimura, Hiroshi Abe
"Development of 2′-Modified Nucleoside Analogues as Antiviral Agents"

[P-29] Haruka Fujikawa, Yuko Shishido, Keiko Kuwata, Yasuaki Kimura, Fumiaki Tomoike, Hiroshi Abe
"A Covalent Inhibitor for Glutathione *S*-Transferase Pi (GSTP1-1) in Human Cells"

[P-30] Qing Wang, Marek Grzybowski, Masayasu Taki, Shigehiro Yamaguchi
"Phospha-Rhodamine based Glutathione Fluorescent Probes"

[P-31] Yoshiaki Sugihara, Shigehiro Yamaguchi
"Donor–π–Acceptor-Type Boron-Containing NIR-Fluorophores"

[P-32] Yoshiaki Shuku, Kunio Awaga
"Honeycomb Crystal Structures Formed by 3-Fold Symmetric Triptycene Derivatives"

[P-33] Dongwan Yan, Yang Wu, Kunio Awaga
"Highly-Porpous Heteroatom-Doped Carbons Prepared by Salt-Assisted Pyrolysis of Covalent Organic Frameworks for High-Performance Supercapacitors"

[P-34] Tomoko Aharen, Taketo Handa, Takumi Yamada, Atsushi Wakamiya, Yoshihiko Kanemitsu
"Lead-Free Halide Perovskites: Effect of Additive Choice and Solvent Engineering on Optical Properties and Cell Performance"

[P-35] Yasuyuki Sanari, Tomohito Otobe, Yoshihiko Kanemitsu, Hideki Hirori
"Nonlinear Interaction of Strong Laser Fields with Semiconducting Materials in the Nonperturbative Regime"

[P-36] Takumi Yamada, Tomoko Aharen, Yoshihiko Kanemitsu
"Anti-Stokes Photoluminescence Properties of Lead-Halide Perovskite Semiconductors"

[P-37] Keiichi Ohara, Takumi Yamada, Hirokazu Tahara, Tomoko Aharen, Hideki Hirori, Yoshihiko Kanemitsu
"Nonlinear Optical Properties of Lead Halide Perovskite Single Crystals"

[P-38] Sojiro Masada, Naoki Yarita, Hirokazu Tahara, Masaki Saruyama, Tokuhisa Kawawaki, Ryota Sato, Toshiharu Teranishi, Yoshihiko Kanemitsu
"Photoluminescence Properties of Lead Bromide Perovskites Nanocrystals Revealed by Single-Dot Spectroscopy"

[P-39] Satoshi Nakahara, Hirokazu Tahara, Go Yumoto, Tokuhisa Kawawaki, Masaki Saruyama, Ryota Sato, Toshiharu Teranishi, Yoshihiko Kanemitsu
"Mechanism of Trion Generation in $CsPbBr_3$ Perovskite Nanocrystals"

[P-40] Hirokazu Tahara, Masanori Sakamoto, Toshiharu Teranishi, Yoshihiko Kanemitsu
"Coherent Spectroscopy of Multiple Excitons in Semiconductor Nanocrystals"

[P-41] Taketo Handa, Tomoko Aharen, Atsushi Wakamiya, Yoshihiko Kanemitsu
"Fundamental Optical Responses of Lead-Free Tin Iodide Perovskites"

[P-42] Hideki Hirori
"Crystallization of Phase-Change Materials Induced by Strong THz Pulses"

[P-43] Jing-Dong Guo, Tomohiro Sugahara, Takahiro Sasamori, Shigeru Nagase, Norihiro Tokitoh
"Mechanistic Studies on Reversible Addition of Terminal Alkene to Digermynes"

[P-44] Tomohiro Sugahara, Takahiro Sasamori, Norihiro Tokitoh
"Synthesis and Properties of 2,5-Digermaselenophene"

[P-45] Shiori Fujimori, Yoshiyuki Mizuhata, Norihiro Tokitoh
"Synthesis and Structure of Heavier Group 14 Element Analogues of Aryl Anions"

[P-46] Jiewei Liu, Masashi Ozaki, Shinya Yakumaru, Taketo Handa, Ryosuke Nishikubo, Yoshifumi Hashikawa, Yasujiro Murata, Takashi Saito, Yuichi Shimakawa, Yoshihiko Kanemitsu, Akinori Saeki, Richard Murdey, Atsushi Wakamiya
"Simple Approaches to Realize Efficient and Reproducible Lead-free Perovskite Solar Cells: Purification of Precursor Materials and Modification of Solution Process"

[P-47] Minh Anh Truong, Richard Murdey, Atsushi Wakamiya
"Transparent Hole-Transporting Materials Containing Partially Oxygen-Bridged Triphenylamine Skeletons: Synthesis and Properties"

[P-48] Sheng Zhang, Yoshifumi Hashikawa, Yasujiro Murata
"Cage-Expansion of Fullerene from C_{60} to $C_{65}N$ and $C_{64}N$ Skeletons"

[P-49] Shota Hasegawa, Yoshifumi Hashikawa, Yasujiro Murata
"Dynamic Behavior of a Single H_2O Molecule Induced by Hydrogen-Bondings inside an Open-Cage Fullerene C_{60} Derivative"

[P-50] Francesca Pincella, Katsuhiro Isozaki, Hikaru Takaya, Masaharu Nakamura
"Magnetic Iron Oxide Nanoparticles as Green and Recyclable Catalysts for the Selective Microwave-Assisted Oxidation of Secondary Alcohols"

[P-51] Atsushi Hosokawa, Takahiro Iwamoto, Masaharu Nakamura
"Light-Driven Entropically Unfavourable Coupling between *N*-Methylamine and Aromatic Ketone"

[P-52] Takafumi Shanoh, Hikaru Takaya, Masato Ito, Masaharu Nakamura
"Synthetic Resolution of Wood Lignin by Iron-Catalyzed Oxidation"

[P-53] Anucha Koedtruad, Taketo Handa, Tomoya Nakamura, Takashi Saito, Daisuke Kan, Yoshihiko Kanemitsu, Atsushi Wakamiya, Yuichi Shimakawa
"Crystal Structures and Properties of Ag-Bi-I Compounds"

[P-54] Yooun Heo, Daisuke Kan, Yuichi Shimakawa
"Dynamics of Oxygen Ions in $SrFeO_{2.5+\delta}$ Thin Films"

[P-55] Zhenhong Tan, Takashi Saito, Fabio Denis Romero, Midori Amano Patino, Masato Goto, Yuichi Shimakawa
"Novel Hexagonal Perovskite $Ba_4Fe_3NiO_{12}$ Containing Tetravalent Fe and Ni Ions"

[P-56] Pritam Sadhukhan, Shengqun Su, Shinji Kanegawa, Osamu Sato
"Directional Electron Transfer Coupled Spin-Crossover in the Crystals of [FeCo] Di-Nuclear Complexes Facilitating Ultrafast Polarization Switching"

[P-57] Sheng-qun Su, Shu-qi Wu, Shinji Kanegawa, Osamu Sato
"Tetrahydrofuran-Triggered Magnetic Coupled with Vapochromism Switching in a Cobalt(II)-Based Single-Ion Magnet"

[P-58] Tsukasa Abe, Yuta Hori, Yoshihito Shiota, Kazunari Yoshizawa
"Aldol Reaction Type C–C Bond Formation Catalyzed by a Mononuclear Copper(II)-Superoxide Complex"

[P-59] Yuuya Kawasaki, Yuuki Seto, Shintarou Kawahara, Kazunobu Igawa, Katsuhiko Tomooka
"Development and Application of Multi-Molecule Connectable DACN"

[P-60] Takayuki Iwata, Takuto Fukami, Tatsuro Yoshinaga, Takumi Fujiwara, Mitsuru Shindo
"Synthesis of Iptycenes Using Ynolate-Aryne Triple Cycloaddition"

[P-61] Shinji Kanegawa, Osamu Sato
"Polarity Switching Crystals Prepared by Pseudo-Racemic Crystallization"

[P-62] Takumi Nakanishi, Osamu Sato
"Proton Coupled Spin Transition in Fe(II) Coordination Compounds"

[P-63] Takuro Hosomi, Kazuki Nagashima, Tsunaki Takahashi, Nobutaka Shioya, Takafumi Shimoaka, Guozhu Zhang, Masaki Kanai, Takeshi Hasegawa, Takeshi Yanagida
"Regioselective Oxidation of Aliphatic Ketones on ZnO Single-Crystal Nanowires"

[P-64] Kei Ikeda, Yuta Hori, Yoshihito Shiota, M. Haris Mahyuddin, Aleksandar Staykov, Takahiro Matsumoto, Kazunari Yoshizawa, Seiji Ogo
"Theoretical Study of H_2O Oxidation by a Half-Sandwich Iridium Complex"

[P-65] Kazuki Nagashima, Hirotaka Koga, Tsunaki Takahashi, Masaya Nogi, Takeshi Yanagida
"Robust Nanowire-Nanocellulose Composite Network Structure for One-Time Use Disposable Paper Molecular Sensor"

[P-66] Takeru Torigoe, Ryuhei Muta, Yoichiro Kuninobu
"Regioselective Trifluoromethylthiolation of *N*-Heteroaromatic Compounds"

[P-67] Yuta Tsuji, Kaunzari Yoshizawa
"Effects of Electron-Phonon Coupling on Quantum Interference in Polyenes"

[P-68] Atsushi Tahara, Yuto Ii, Yusuke Sunada, Mitsunobu Kawamura, Hideo Nagashima
"Reverse ATRP of St and MMA Catalyzed by $Me_3TACNFeX_3$ (X = Cl, Br)"

[P-69] Yuta Hori, Takumi Nakanishi, Yoshihito Shiota, Osamu Sato, Kazunari Yoshizawa
"Theoretical Study of Proton-Coupled Spin Crossover Fe(II) Complexes"

[P-70] Yuki Yoshida, Kouhei Machida, Mariko Okamoto, Yusuke Ano, Kazunobu Igawa, Katsuhiko Tomooka
"Photochemical Isomerization Approach to Planar Chiral Medium-Sized Cyclic Molecules"

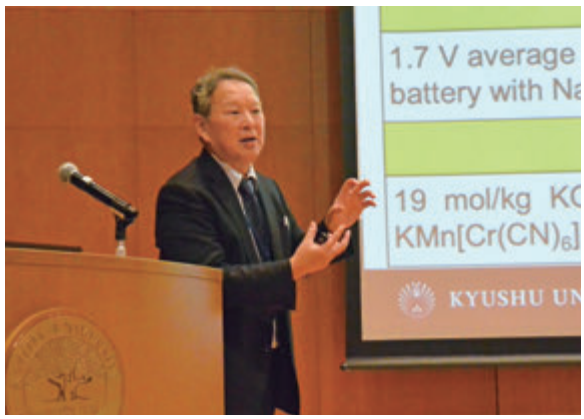
1.7 V average
battery with Na
19 mol/kg KC
KMn[Cr(CN)6]
KYUSHU UN

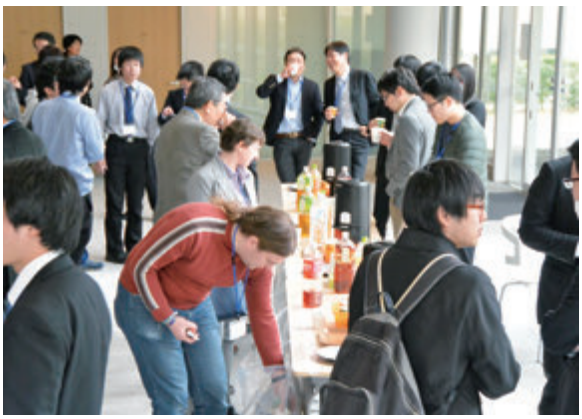


Weight / %

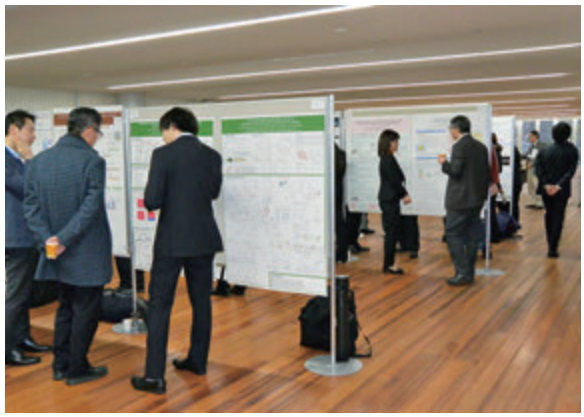

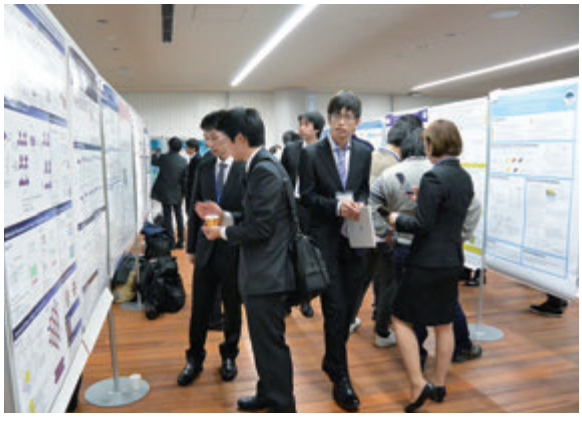


GSS

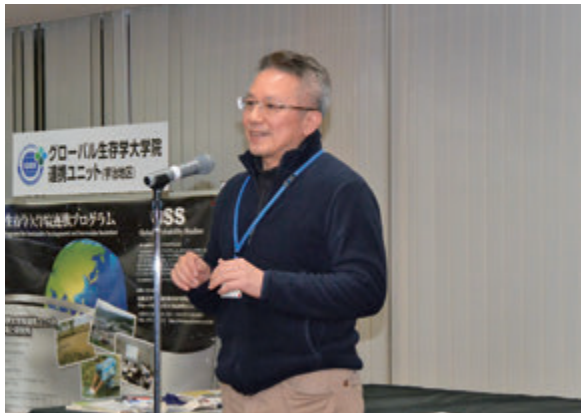
グローバル生存学大学院
連携ユニット


グローバル生存学大学院
連携ユニット


グローバル生存学大学院
連携ユニット


A fingerprint of
metal oxide powders:
Characterization and
identification with energy-
resolved distribution of
electron traps
organic
compounds

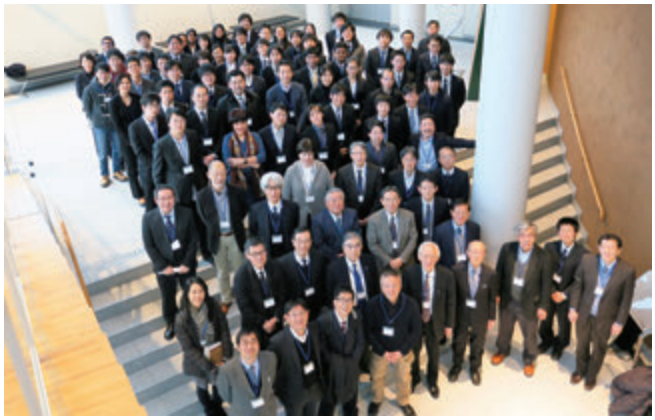

Spectroscopic and Theoretical Investigations of the Mechanism of NH_3-SCR Reactions over Cu-Zeolite Catalysts

Hiroe Kubota[1], Takehiro Amada[1], Takashi Toyao[1,2], Zen Maeno[1], Ken-ichi Shimizu[1,2]

[1] Institute for Catalysis, Hokkaido University, N-21, W-10, Sapporo 001-0021, Japan

[2] Elements Strategy Initiative for Catalysts and Batteries, Kyoto University, 615-8520, Kyoto, Japan

Introduction

NH_3–SCR (Selective Catalytic Reduction)

Standard SCR $4NH_3 + 4NO + O_2 \longrightarrow 4N_2 + 6H_2O$

Fast SCR $4NH_3 + 2NO + 2NO_2 \longrightarrow 4N_2 + 6H_2O$

Slow SCR $8NH_3 + 6NO_2 \longrightarrow 7N_2 + 12H_2O$

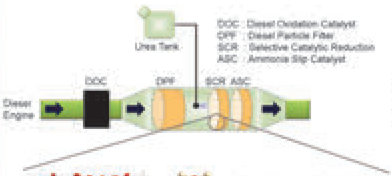

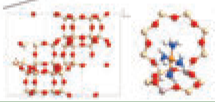

Small pore Cu-CHA catalysts has practically been used as very efficient and robust catalysts to meet the EuroVI requirements for removal of NOx from mobile diesel engine exhaust gases, also under real driving emissions (RDE).

Proposed mechanisms

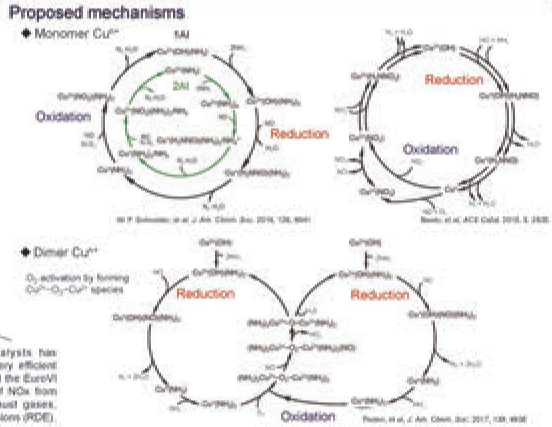

This study

We have investigated reaction mechanisms of NH_3–SCR over Cu-exchanged zeolites by using various operando spectroscopic techniques including XAFS, FT-IR, and UV-vis, as well as DFT calculations. In particular, special attention has been paid to the reoxidation of Cu^{1+}.

It is believed that the reoxidation of Cu species requires both NO and O_2. However, our combined spectroscopic and theoretical investigations indicate that the reoxidation of Cu^{1+} can be achieved by only O_2.

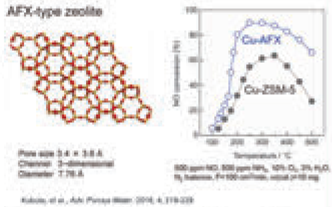

Kubota, et al., Adv. Porous Mater. 2016, 4, 219-229

Sample	Si/Al	Cu wt%	Cu/Al
Cu-AFX	8.3	4.1	0.32
		2.1	0.16
		0.4	0.03

Results and discussion

Operando UV-vis

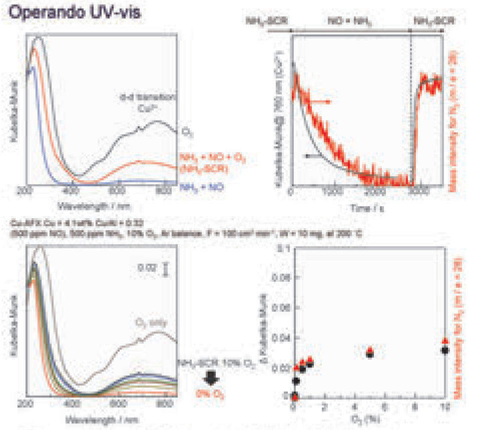

The reoxidation of Cu^{1+} by only O_2 (Effect of Cu/Al ratio)

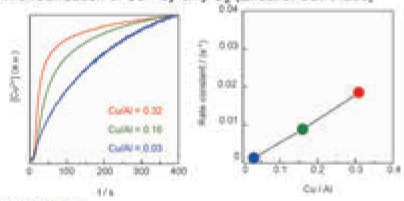

In situ XAFS

Reduction of Cu^{2+} — Reoxidation of Cu^{1+}

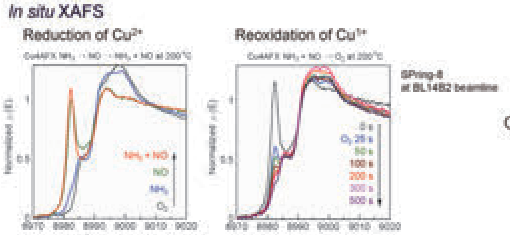

Temperature dependence on NH_3-SCR reaction (Steady state)

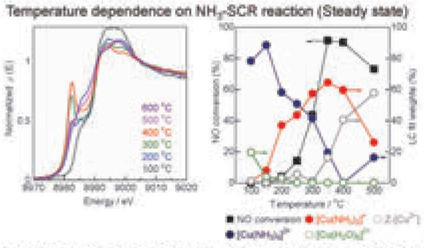

F = 1000 ml/min, W = 3.8 mg, 1000 ppm NH_3, 1000 ppm NO, 10% O_2, with a balance of He

In situ FT-IR

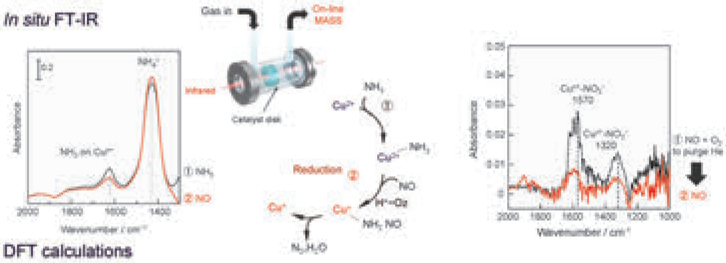

DFT calculations

Structure model — O_2 activation of $[Cu(NH_3)_2]^+$

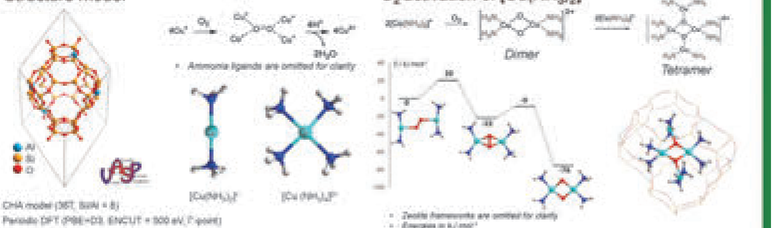

Cu tetramer decomposition

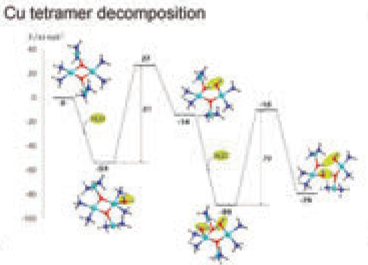

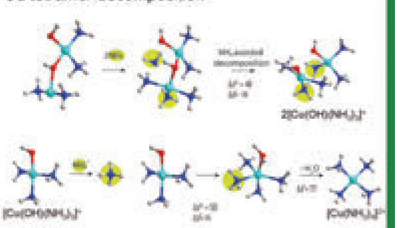

O_2 + NO activation

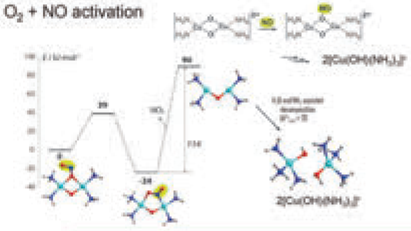

Diffusion of $[Cu(NH_3)_2]^+$

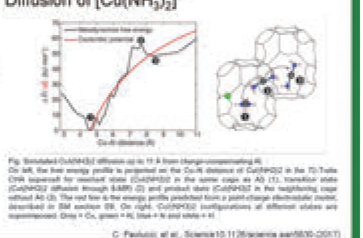

Conclusions

Reaction mechanisms of NH_3–SCR over Cu-exchanged zeolites have been investigated by using various operando spectroscopic techniques including XAFS, FT-IR, and UV-vis, as well as DFT calculations. The obtained results indicate that the reoxidation of Cu^{1+} can be achieved by only O_2.

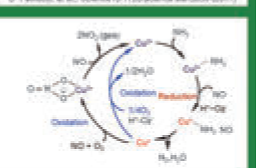

Theoretical Investigation of 13-Group Metal Clusters in CHA Zeolite by Ab Initio Thermodynamics analysis

Shunsaku Yasumura[1], Takashi Toyao[1,2], Zen Maeno[1], Ken-ichi Shimizu[1,2]

[1] Institute for Catalysis, Hokkaido university, N-21, W-10, Sapporo 001-0021, Japan

[2] Elements Strategy Initiative for Catalysts and Batteries, Kyoto University, 615-8520, Kyoto, Japan

Introduction

13-group metal loaded zeolite

Promising candidate for CH_4 activation

Ga-loaded zeolite

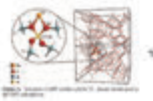

Activation of hydrocarbons

In-loaded zeolite

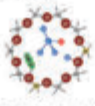

- Transformation of CH_4 and C_2H_6 to Higher hydrocarbons

- Selective catalytic reduction of NO by CH_4

H/D exchange reaction of CH_4 (453-573 K)

- The local structure of In-species in zeolite is still unknown.
- The activation of CH_4 in the range of low temperature is unrevealed.

This work

Speciation

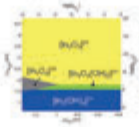

Ab initio thermodynamics

CH_4 activation

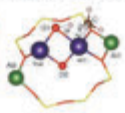

Transition state calculation

Local structure of 13-group metal cluster depends on …

- Partial pressure of O_2 and H_2O
- Temperature

Ab initio thermodynamics analysis

Each effects are inserted as chemical potentials

Calculation method

Methods

- Package : VASP
- Functional : PBE
- cutoff : 500 eV
- k-point : Γ point
- Spin polarized
- Chemical potential : NIST
- Temperature : 800 K
- Lattice parameter is fixed

Formulas for ab initio thermodynamics

$$x\ln(OH)/CHA + (1-x)CHA\_2H + \frac{(2m-3x-n+2)}{4}O_2 + \frac{(x+n-2)}{2}H_2O \approx In_xO_mH_n/CHA \quad (1)$$

$$\Delta E = E_{In_xO_mH_n/CHA} - xE_{In(OH)/CHA} - (1-x)E_{CHA\_2H} - \frac{(2m-3x-n+2)}{4}E_{O_2} - \frac{(x+n-2)}{2}E_{H_2O} \quad (2)$$

$$\Delta F(T,p) = \frac{1}{A}\left[\Delta E - \frac{(2m-3x-n+2)}{2}\Delta\mu_O - \frac{(x+n-2)}{2}\Delta\mu_{H_2O}\right] \quad (3)$$

$$\Delta\mu_O(T,p) = \frac{1}{2}\left[\Delta\mu_{O_2}(T,p^0) + RT\ln\left(\frac{p_{O_2}}{p^0}\right)\right] \quad (4)$$

$$\Delta\mu_{H_2O}(T,p) = \Delta\mu_{H_2O}(T,p^0) + RT\ln\left(\frac{p_{H_2O}}{p^0}\right) \quad (5)$$

Structure models

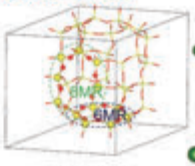

CHA Zeolite

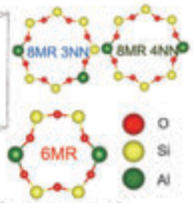

a = b = 13.675 Å, c = 14.767 Å

α = β = 90.0° and γ = 120°

Results and discussion

Ab initio thermodynamics analysis

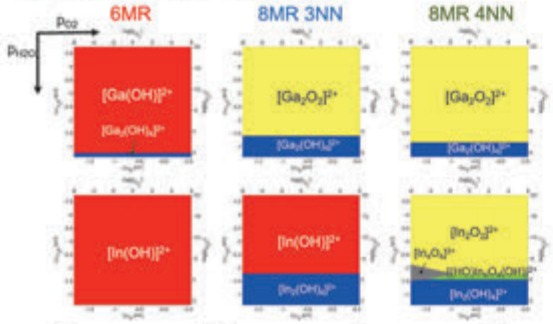

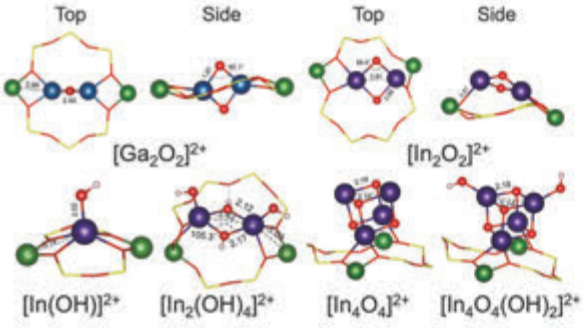

Ga

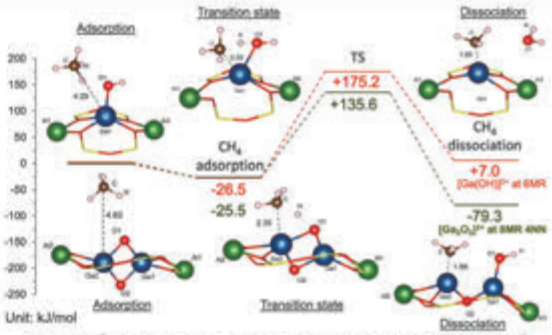

$[Ga_2O_2]^{2+}$ has lower activation energy than $[Ga(OH)]^{2+}$

In

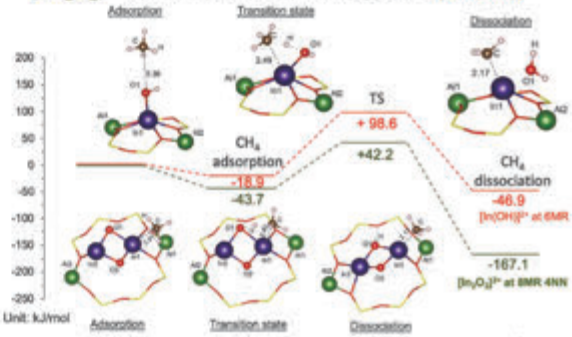

$[In_2O_2]^{2+}$ has lower activation energy than $[Ga_2O_2]^{2+}$

Dissociation of CH_4 molecule

Ga

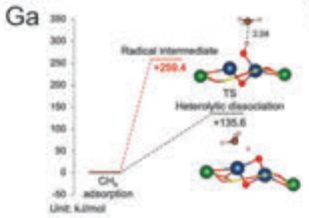

In

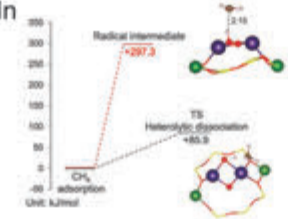

Orbitals of TS state

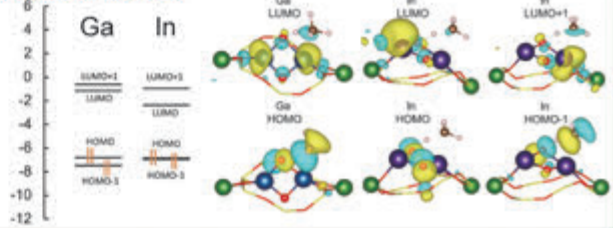

Synthesis of gold-nanoparticle/silica colloidal crystal to form highly ordered titania inverse-opal structures

Tharishinny Raja Mogan[1],Mai Takashima[1,2],Ewa Kowalska[1,2] and Bunsho Ohtani[1,2*]
[1]*Graduate School of Environmental Science, Hokkaido University, Sapporo 060-0810, Japan*
[2]*Institute for Catalysis, Hokkaido University, Sapporo 001-0021, Japan*
*Corresponding author: ohtani@cat.hokudai.ac.jp

Titania (TiO_2) as photocatalyst

- Lack of photochemical activity under visible light
- Only 3-5% of sunlight is UV

Theories behind the proposed idea

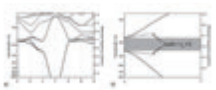

optical stop-band effect of TIO_2-IO structure

localized surface plasmon resonance (LSPR) of Au-NP

give rise to visible light absorption

ACS Appl.Mater.Interfaces **2016**,8, 31738-31745

Our proposed idea

TITANIA INVERSE OPAL (TIO_2-IO) CONTAINING SINGLE GOLD NANOPARTICLE (AU-NP) PER VOID

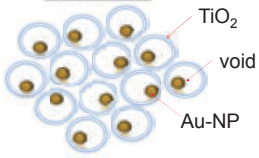

Schematic procedure to synthesize TiO_2-IO containing Au-NP per void

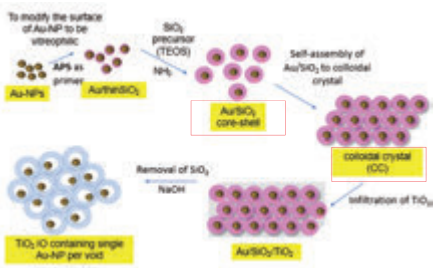

Synthesis of Au/SiO_2 colloidal crystal is VITAL STEP to form highly ordered TiO_2-IO structure as the desired photocatalyst!

Formation of Au/SiO_2 core-shell ⇨ **Self-assembly of Au/SiO_2 core-shell** ⇨ **Au/SiO_2 colloidal crystal**

FACTORS AFFECTING FORMATION OF Au/SiO_2 CORE-SHELL PARTICLES

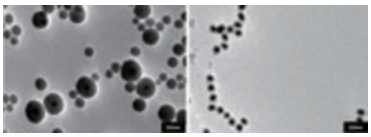

Number of particles present in $Au/thinSiO_2$

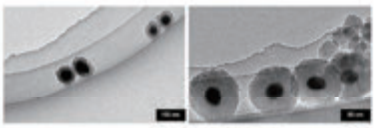

Amount of catalyst used (NH_3)

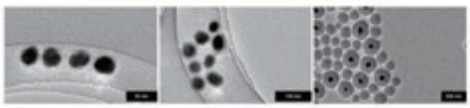

Amount of SiO_2 precursor)

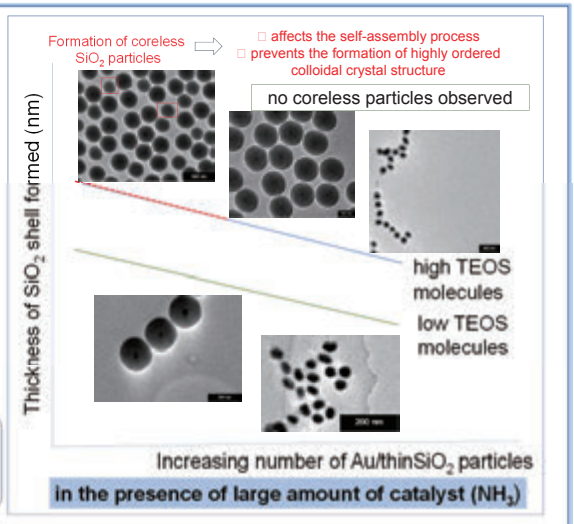

SELF-ASSEMBLY BY Au/SiO_2 CORE-SHELL PARTICLES TO FORM COLLOIDAL CRYSTAL

Au/SiO_2 core-shell particles

Sedimentation assisted via centrifugation

Vertical deposition

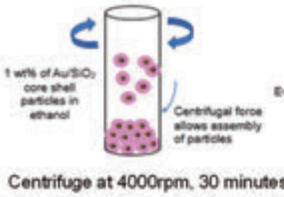

Centrifuge at 4000rpm, 30 minutes

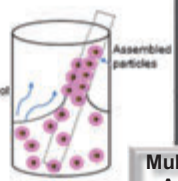

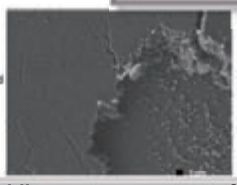

Multilayers arrangement of Au/SiO_2 colloidal crystal

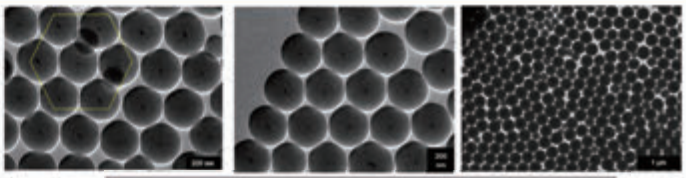

Highly ordered arrangement by self-assembled Au/SiO_2 particles

FUTURE WORK/IN PROGRESS

- Infiltration of TiO_2 onto the self-assembled particles
- Selective etching of the SiO_2 template to form void

Development of a Simple but Reliable Method for Photocatalytic-activity Evaluation

Fitri Rizki Amalia,1 Mai Takashima,1,2 and Bunsho Ohtani1,2
1Grad. School of Env. Science, Hokkaido University
2Institute for Catalysis, Hokkaido University

Introduction

Evaluation of Photocatalytic-activity test

1.Gas chromatography (GC) and liquid chromatography (LC)

+ ✓accurate
✓reliable

− ✓expensive
✓complicated

2.Spectrophotometer

+ ✓ affordable
✓ simple

− ✓ unreliable for some analysis (photodecomposition)

Developing simple and reliable method without dye by only using spectrophotometer

Formaldehyde detection

HCHO

+

Nash reagent (ammonium acetate, acetylacetone, and acetic acid)

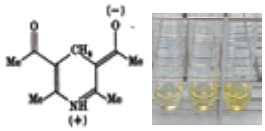

Diacetyldihydrolutidine (DDL)

spectrophotometer

T. Nash, Biochem J., 55, 416-421 (1953)

Conclusion

1. Spectrophotometer as the only instrument for photocatalyrtic activity
2. Formaldehyde as the main compound in photocatalytic activity-test

Future plan

1. Shorten irradiation time
2. Check dissolved CO_2
3. Checking the possibility of other compound

Methanol dehydrogenation procedure

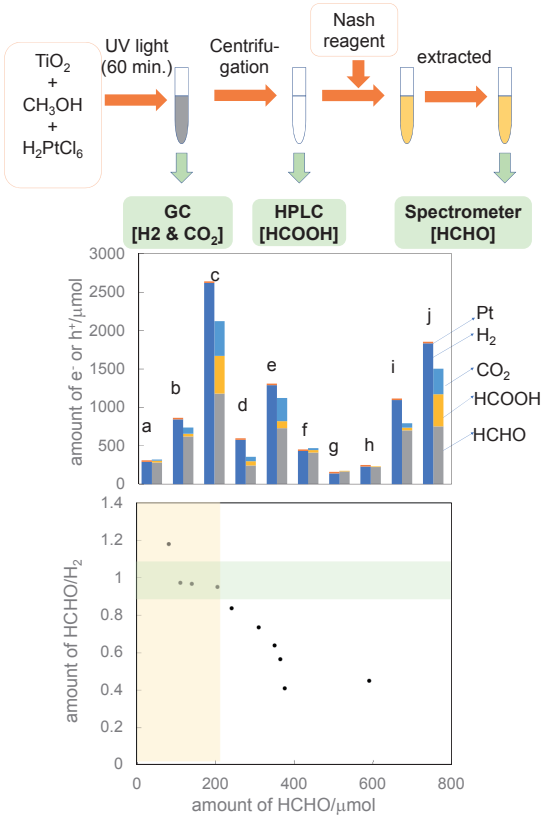

$CH_3OH + 2h^+ \rightarrow HCHO + 2H^+$

$CH_3OH + 4h^+ + H_2O \rightarrow HCOOH + 4H^+$

$CH_3OH + H_2O + 6h^+ \rightarrow CO_2 + 6H^+$

$2H^+ + 2e^- \rightarrow H_2$

Oxidative decomposition of formaldehyde procedure

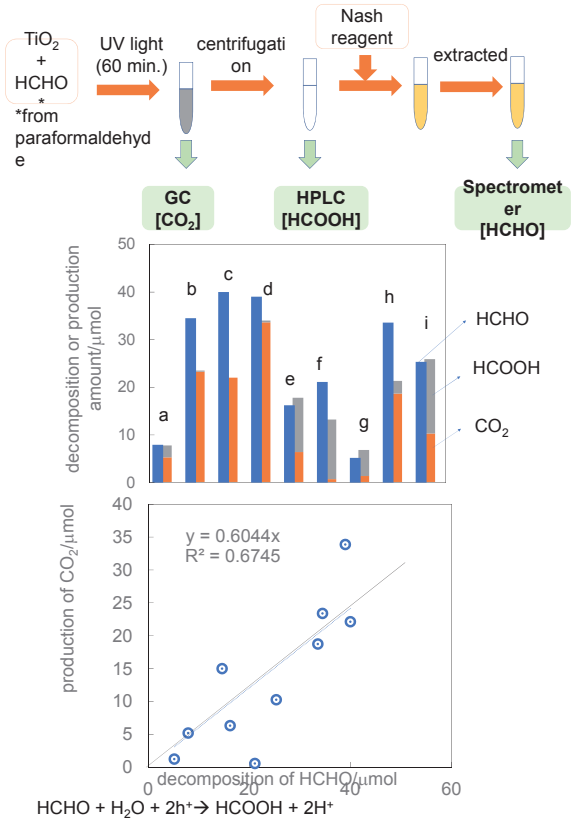

$HCHO + H_2O + 2h^+ \rightarrow HCOOH + 2H^+$

$\frac{1}{2} O_2 + 2^+ + 2^- \rightarrow H_2O$

$HCHO + 4h^+ \rightarrow CO_2 + 4H^+$

$O_2 + 4^+ + 4e^- \rightarrow 2H_2O$

Light intensity-dependence study for titania photocatalysis with multielectron transfer process

Pradudnet Ketwong, Shugo Takeuchi, Mai Takashima, and Bunsho Ohtani

Institute for Catalysis, Hokkaido University, Japan

Photocatalytic oxygen evolution

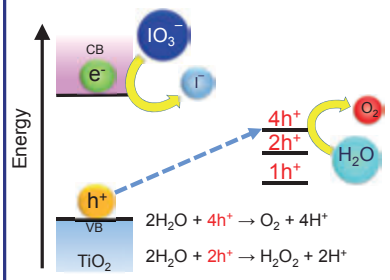

$2H_2O + 4h^+ \rightarrow O_2 + 4H^+$ (+ 1.23 V)

$2H_2O + 2h^+ \rightarrow H_2O_2 + 2H^+$ (+ 1.76 V)

$H_2O + h^+ \rightarrow {}^{\cdot}OH + H^+$ (+ 2.8 V)

Order of reaction rate was changed

1 ⇨ 4 ⇨ 1

by increasing Light Intensity

Experimental

Photocatalyst : Small anatase titania (Ishihara ST01)
Electron acceptor: Iodate ion (sodium iodate solution 0.05 mol L^{-1})
Lamp: High-intense UV-LED NS Lighting ULEDN-101
Wavelength: 365 nm

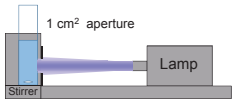

Scheme of experiment set up

Light power = 500.4 mW
$Area_{95}$ = 0.15 cm^2
Light intensity (I_L) = 0.95 × 500.4 / 0.15
= 3.17 W cm^{-2}

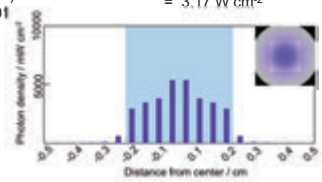

Light-intensity distribution of a UV-LED lamp

Results and Discussion

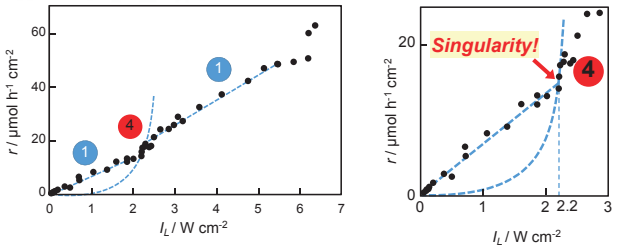

Fig. 1 Light-intensity dependence of photocatalytic oxygen evolution rate

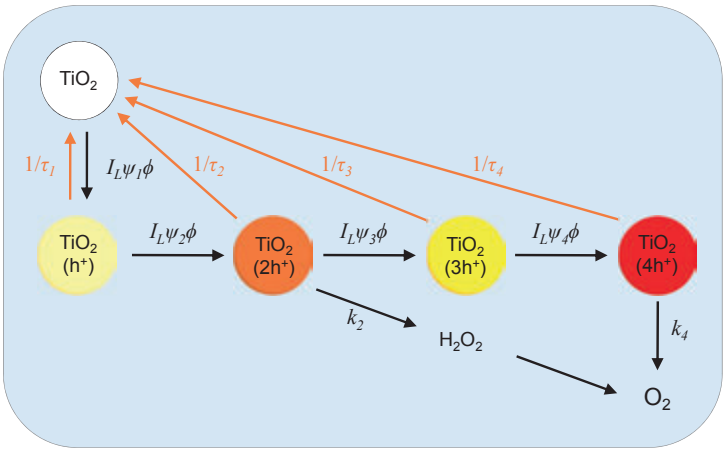

Multielectron-transfer model for photocatalytic oxygen evolution

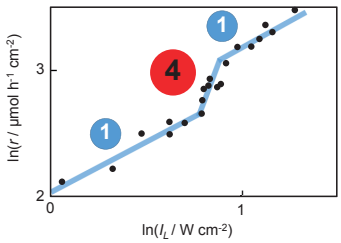

Fig. 2 Double logarithmic plot of light intensity and oxygen evolution rate

Based on steady-state approximation, the model suggests that photocatalytic oxygen evolution is strongly depended on **photoabsorption of each particle** and **accumulation of generated holes**

Two-electron transfer process

low light-intensity limit : second order

$$r = \psi_1\psi_2\phi^2\tau_1 I_L^{\,2}$$

high light-intensity limit : first order

$$r = \psi_1\phi I_L$$

Four-electron transfer process

low light-intensity limit : fourth order

$$r = k_4\psi_1\psi_2\psi_3\psi_4\phi^4\tau_1\tau_2\tau_3 I_L^{\,4}/(k_4 + 1/\tau_4)$$

high light-intensity limit : first order

$$r = k_4\psi_1\phi I_L/(k_4 + 1/\tau_4)$$

Where

- r = Reaction rate
- I_L = Light intensity
- Ψ = Photoabsorption efficiency
- Φ = Quantum efficiency of electron capture
- τ = Lifetime
- k = Rate constant

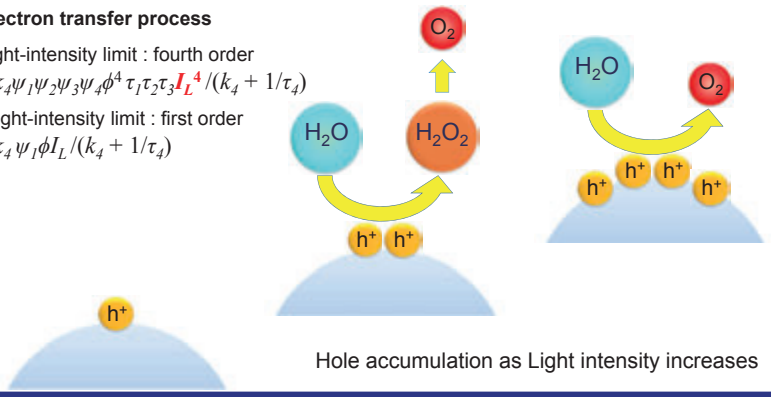

Hole accumulation as Light intensity increases

Studies on Synthetic Analogues of Comfrey-based, Wound-healing Natural Biopolymer

Maia Merlani,[1,2] Vakhtang Barbakadze[2], Zhiyi Song[1], Tamaki Nakano[1,*]

[1]*Institute for Catalysis (ICAT), Hokkaido University, N 21, W 10, Kita-ku, Sapporo 001-0021, Japan*
[2]*Kutateladze Institute of Pharmacochemistry, Tbilisi State Medical Uiniversity, 36 P. Sarajishvili str., 0159 Tbilisi, Georgia*
∗tamaki.nakano@cat.hokudai.ac.jp

Abstract: Poly[3-(3,4-dihydroxyphenyl)glycderic acid] (PDPGA), isolated from different species of comfrey (Boraginacea family), is a biologically active, water soluble polymer with antioxidant, antilipoperoxidant, antiinflammatory and wound healing properties. Molecular mass of these regular polymers is >1000 kDa and the repeating unit is 3-(3',4'-dihydroxyphenyl)-glyceric acid residue (fig.1.). In this work, 2-methoxycarbonyl-3-(3,4-dimethoxyphenyl)oxirane (MCDMPO) as an unsymmetrically 2,3-disubstituted oxirane monomer was synthesized and polymerized using a cationic initiator under various conditions. Under all conditions examined, the monomer was almost completely consumed to afford methylated analogue of PDPGA - poly(MCDMPO) (*Mn* 2900-12800).

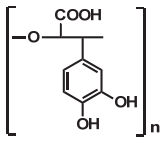

Fig.1. PDPGA

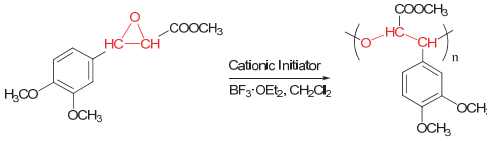

Scheme 1. Cationic polymerization of **MCDMPO**

Run	T/°C	M/I	Y^c/%	$M_n^d \times 10^{-3}$	M_w/M_n^e	α^f	k^f
1	23	20	83	3.8	1.18	0.90	3.2×10^{-5}
2	0	20	88	5.7	1.21	0.79	5.8×10^{-5}
3	-20	20	68	3.5	1.16	1.1	6.8×10^{-6}
4	-40	20	72	2.9	1.18	1.1	8.3×10^{-6}
5	0	10	93	4.5	1.76	0.44	1.7×10^{-3}
6	0	50	93	6.1	1.55	0.59	4.7×10^{-4}
7	0	100	95	8.7	2.48	0.82	7.2×10^{-5}
8	0	200	96	12.8	1.79	0.66	1.5×10^{-4}

Table 1. Polymerization of MCDMPO with $BF_3{\cdot}OEt_2$ in CH_2Cl_2 for 5 h [a,b]

[a] Monomer 200 mg, $[monomer]_0$ 0.84 M (runs 1–3, 5–8) or 0.60 M (run 4). [b] The monomer conversion ratio >99% as determined from ^{1}H NMR spectra of the crude mixture. [c] The yield of the hexane-insoluble part. [d] Estimated by SEC with right-angle laser light scattering and viscometric detectors. [e] Estimated by SEC using standard polystyrenes. [f] Mark–Houwink–Sakurada coefficients.

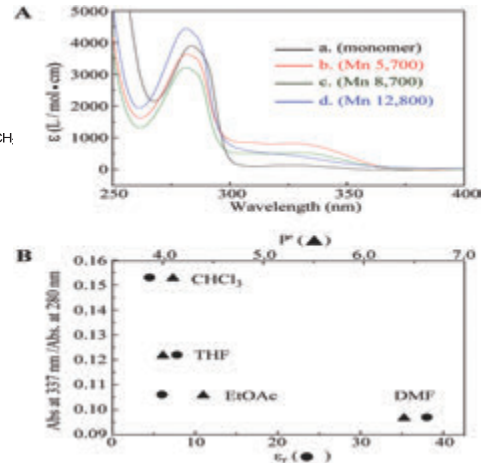

Fig. 3. UV spectra of the MCDMPO monomer (a) and poly(MCDMPO)s of *Mn* 5700 (b), 8700 (c), and 12 800 (d) (A) and a plot of the ratio of absorbance at 330 nm (ICT) to that at 280 nm (π–π*) of the polymer of *Mn* 12 800 against the dielectric constant (ε_r) and Rohrschneider polarity parameter (P') of the solvent used for measurements (B). The spectra in A were obtained in $CHCl_3$ at 1.7×10^{-4} M (a), 2.4×10^{-4} M (b), 2.4×10^{-4}M (c), and 2.0×10^{-4} M (d) at 23 °C in a 1 mm quartz cell, and the data points in B were obtained from $CHCl_3$ (ε 4.5; *P'* 4.1), EtOAc (ε 6; *P'* 4.4), THF (ε 7.8; *P'* 4.0), and DMF (ε 38, *P'* 6.4) solutions at 1.0×10^{-5} M at 23 °C.

^{1}H NMR and MALDI-TOF mass spectra of poly(MCDMPO)

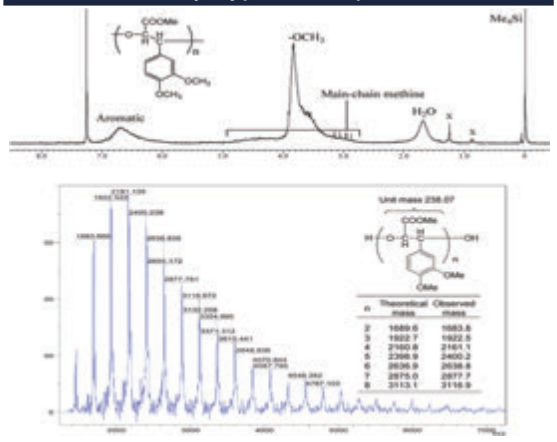

Fig.2. 1H NMR spectrum of poly(MCDMPO) (run 7 in Table 1) (400 MHz, CDCl3, at 23 °C) (top) and the MALDI-TOF mass spectrum of the polymer using α-cyano-4-hydroxycinnamic acid along with a chemical structure deduced from the spectrum and tabulated theoretical and observed mass numbers corresponding to the structure (bottom).

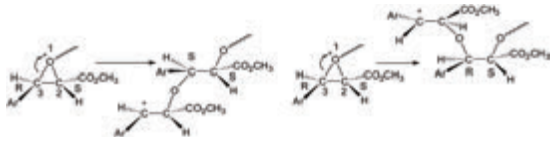

Scheme 2. Head-to-tail growth with inversion (left) and retention (right) of the C(2) configuration in MCDMPO polymerization.

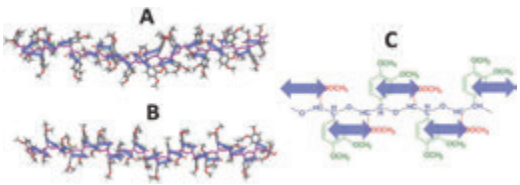

Fig. 4. Structures obtained through MD simulations for 5 ns at 297 K (S,S)-20-mer (A), (S,S)/(R,R)-20-mer (B), and a schematic drawing of a chain (C). In A and B, white, gray, and red correspond to H, C, and O, respectively, and pink corresponds to the main chain. Blue arrows indicate carbonyl–aromatic combinations that may contribute to ICT interactions

Conclusions

2-Methoxycarbonyl-3-(3,4-dimethoxyphenyl)oxirane was synthesized and polymerized using a cationic initiator to afford a polymer having a rather stiff, stretched conformation. The side-chain methoxycarbonyl group and 3,4-dimethoxyphenyl group of neighboring monomeric unity form a hetero π-stacked structure between side-chain carbonyl and aromatic groups which leads to intramolecular charge transfer (ICT) interactions.

Synthesis and Switching between Emitting and Non-emitting Intramolecular Charge Transfer Stated of a Donor-Acceptor-Donor Triad Molecule

Nabin Ch. Maity,[1] Maximilian Krämer,[1] Shichibu Yukatsu,[2] Jun-ya Hasegawa,[1,3] Katsuaki Konishi,[2] Song Zhiyi,[1] and Tamaki Nakano[1,3*]

[1]Institute for Catalysis, Hokkaido University, N20W10, Kita-ku, Sapporo 001-0021, Japan
[2]Faculty of Environmental Earth Sciences, Hokkaido University, N10, W5, Kita-ku, Sapporo 060-0810, Japan[3]Integrated Research Consortium on Chemical Sciences (IRCCS), Institute for Catalysis, Hokkaido University, N21W10, Kita-ku, Sapporo 001-0021, Japan
*tamaki.nakano@cat.hokudai.ac.jp**

Abstract: A molecule having a donor and acceptor moieties connected through electronic conjugation can exhibit ICT-based properties in the ground state and excited states. Our recently developed novel 9-fluorenone derivative showed switchable ICT behavior. The switching behavior was controlled by the addition of the base or the acid. Additionally, a detail computational studies had been carried out to rationalize the ICT behaviors.

Synthesis

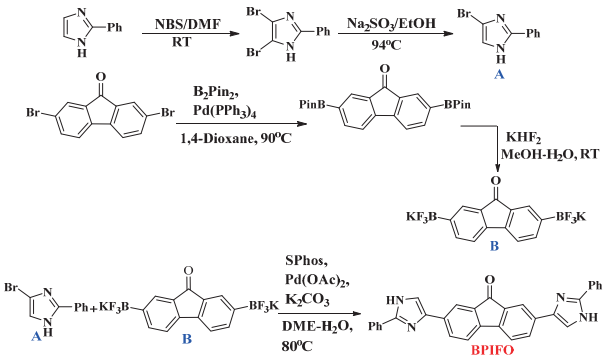

Scheme 1. Synthesis of the 2,7-bis(2-phenyl-1H-imidazol-4-yl)fluorenone (**BPIFO**) *via* Suzuki-Miyaura cross Coupling reaction.

UV-Vis in various solvent

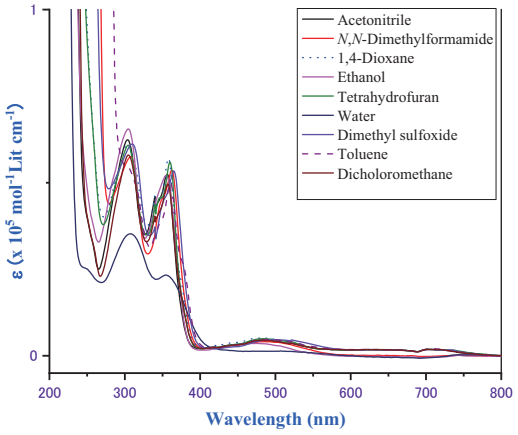

Figure 1. Absorbance spectra of **BPIFO** in various solvents

Emission spectra

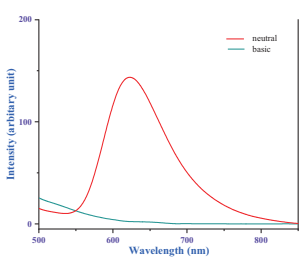

Figure 2. Emission spectra of the neutral and basic state of the **BPIFO**

Excitation spectra

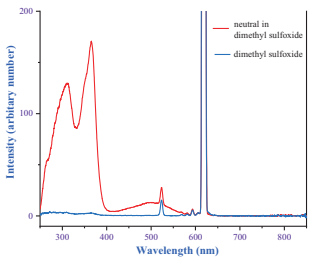

Figure 3. Excitation spectra of **BPIFO** (red) with concentration of 6.45 x 10^{-6}

ICT switching

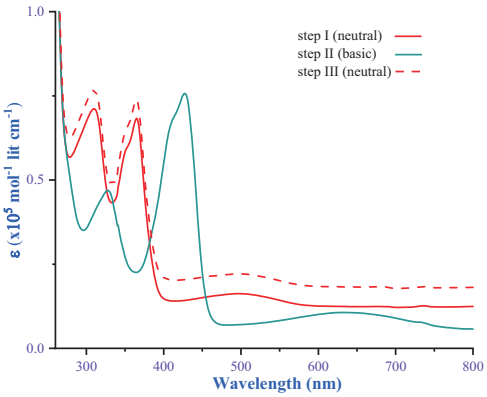

Figure 4. UV-Vis spectra of the **BPIFO** at various conditions; neutral state (red solid line), after addition of the aqueous K_2CO_3 (green line) and after addition of the aqueous HCl (red dotted line).

NMR titration

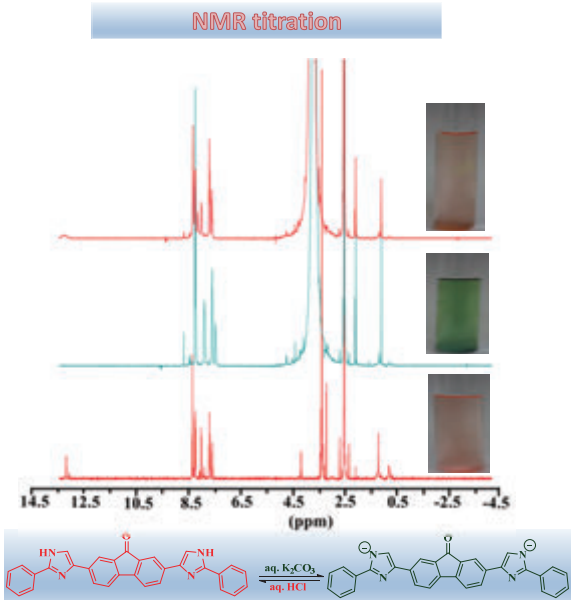

Figure 5. ^{1}H NMR of the **BPIFO** at various conditions; neutral state (red), after addition of aqueous K_2CO_3 of strength 1 (M) (green) and after addition of aqueous HCl (red) (400 MHz, DMSO-d_6, Room Temperature).

Conclusions

The novel fluorenone derivative, BPIFO is successfully synthesized

Synthesis and Physicochemical Properties of Chiral Cationic Polymers

Nino Zavradashvili,[1,2] Yue Wang,[1] Zhiyi Song,[1] Ramaz Katsarava,[2] Tamaki Nakano[1,*]

[1]*Institute for Catalysis (ICAT) and Integrated Research Consortium on Chemical Sciences (IRCCS), Hokkaido University, N 21, W 10, Kita-ku, Sapporo 001-0021, Japan*
[2]*Institute of Chemistry and Molecular Engineering, Agricultural University of Georgia, Kakha Bendukidze University Campus, 240 David Aghmashenebeli Alley, Tbilisi 0159, Georgia*
**tamaki.nakano@cat.hokudai.ac.jp*

Abstract: Cationic polymers (CPs) have been intensively utilized for nucleic acid drug delivery owing to their charge condensing capability [1, 2]. We herein report the synthesis and physicochemical properties of novel CPs comprising of L-arginine and spermine units. The new CPs were found to form chiral complexes with methyl orange whose structures were investigated by circular dichroism (CD) and ultra violet (UV) spectroscopic analyses. Appropriate biological studies of the new CPs are under way.

Monomer Synthesis

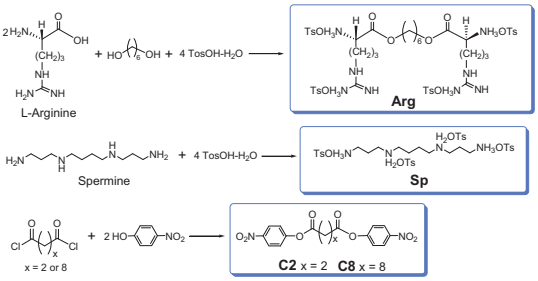

Scheme 1. Synthesis of monomers.

NMR Analysis

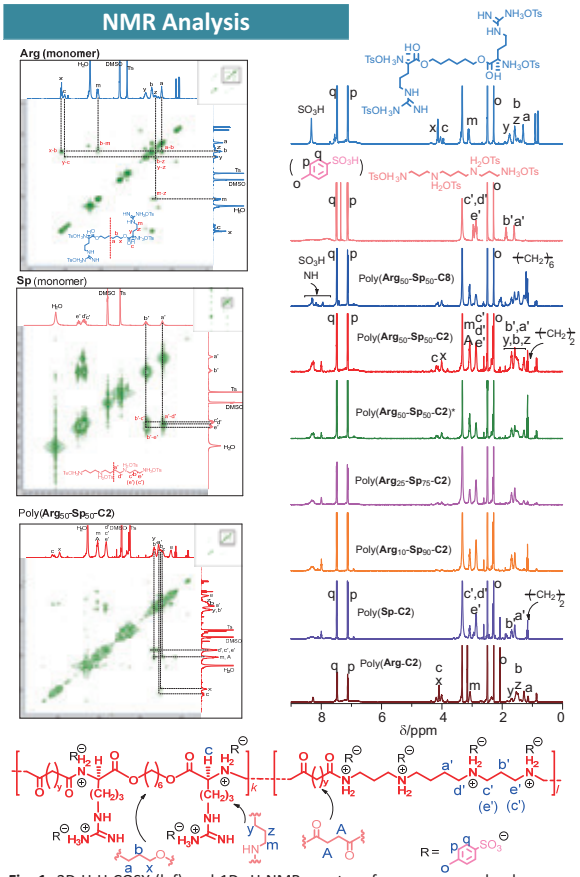

Fig. 1. 2D H-H COSY (lef) and 1D $_1$H NMR spectra of monomers and polymers (400 MHz, DMSO-d_6, r.t.).

(1) Whitehead, K.A.; Langer, R.; Anderson, D.G. *Nat Rev Drug Discov.* **2009**, *8*,129.
(2) Samal, S. K.; Dash, M., Van Vlierberghe, S.; Kaplan, D. L.; Chiellini, E.; Van Blitterswijk, C.; Moroni, L.; Dubruel, P. *Chem. Soc. Rev.* **2012**, *41*, 7147.

Conclusions

The novel, chiral polyelectrolytes were successfully prepared and found to form chiral complex with methyl orange possibly through ionic interaction or (partial) anion exchange.

Polymerization

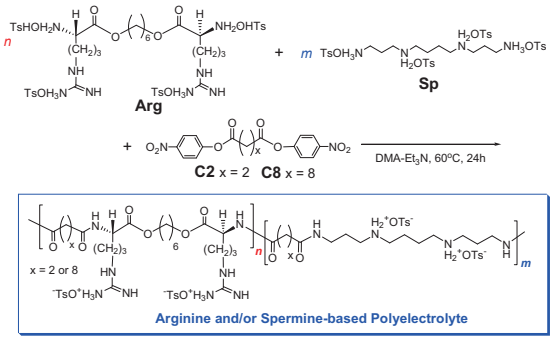

*Poly(**Arg**$_{50}$-**Sp**$_{50}$-**C2**) was reacted with a small amount of 1,6-diisocyanatohexane leading to poly(**Arg**$_{50}$-**Sp**$_{50}$-**C2**) *.*

Scheme 2. Synthesis of polyelectrolytes.

Polymer-Methyl Orange Complexation

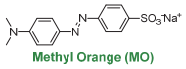

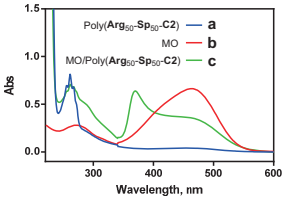

Fig. 2. Absorbance spectra of poly(**Arg**$_{50}$-**Sp**$_{50}$-**C2**) (0.01 M) (a), MO (0.0003 M) (b), and a mixture of the polymer and MO ([unit]/[MO] = 1/1) (c) in H_2O (1-mm cell).

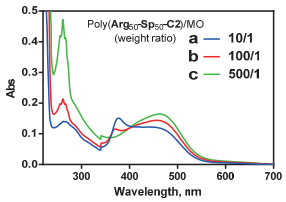

Fig. 3. Absorbance spectra of mixtures of poly(**Arg**$_{50}$-**Sp**$_{20}$-**C2**) and MO where [MO] = 0.01 g/L at [polymer]/[MO] = 10/1 (a), 100/1 (b), and 500/1 (c) (weight ratio) in H_2O (1-mm cell).

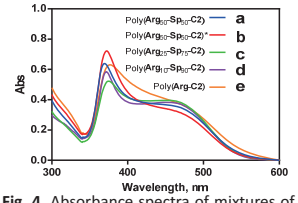

Fig. 4. Absorbance spectra of mixtures of MO and polymers at [MO] = 0.1 g/L and [polymer] = 1.0 g/L in H_2O (1-mm cell).

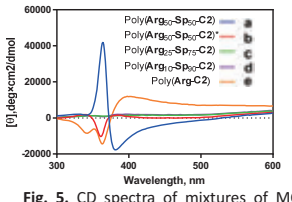

Fig. 5. CD spectra of mixtures of MO and polymers at [MO] = 0.1 g/L and [polymer] = 1.0 g/L in H_2O (1-mm cell).

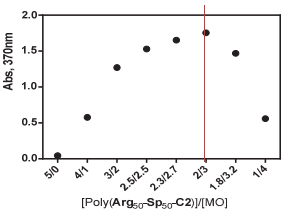

Fig. 6. Job's plot for mixtures of poly(**Arg**$_{50}$-**Sp**$_{50}$-**C2**) and MO at [**Arg** and **Sp** units] + [MO] = 0.0016 M in H_2O (1-mm cell).

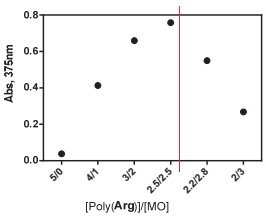

Fig. 7. Job's plot for mixtures of poly(**Arg-C2**) and MO at [**Arg** unit] + [MO] = 0.0016 M in H_2O (1-mm cell).

Theoretical study on geometry effect on the catalytic activity of gold clusters

○Min GAO[1,3], Andrey Lyalin[3], Satoshi Maeda[2], Tetsuya Taketsugu[2,3]

1 Institute for Catalysis, Hokkaido University, Sapporo 060-0810, Japan
2 Department of Chemistry, Faculty of Science, Hokkaido University
3 GRREN, NIMS, Japan

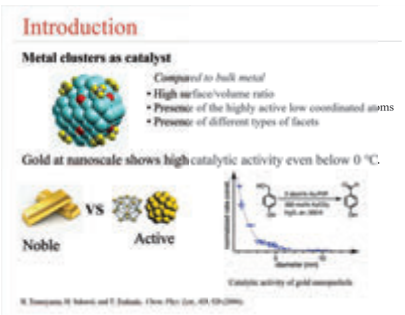

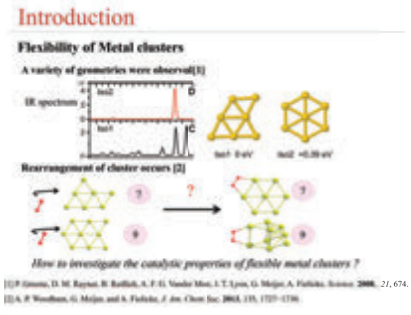

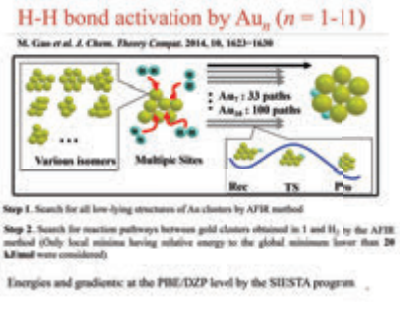

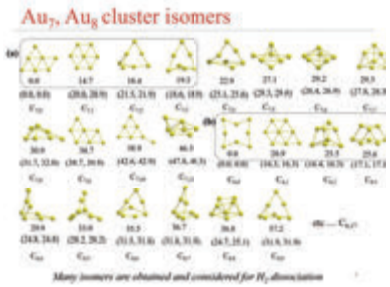

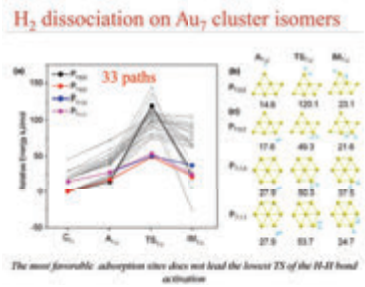

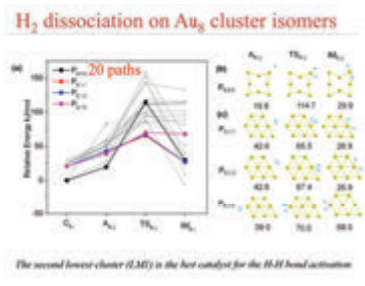

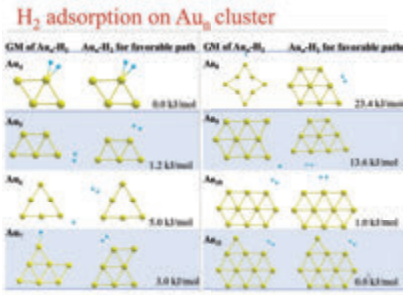

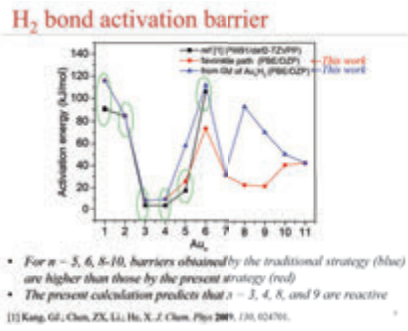

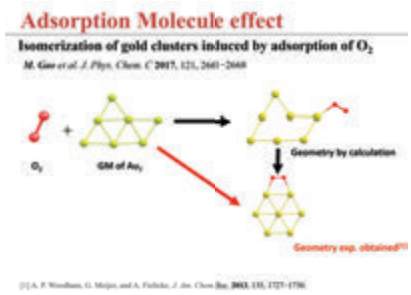

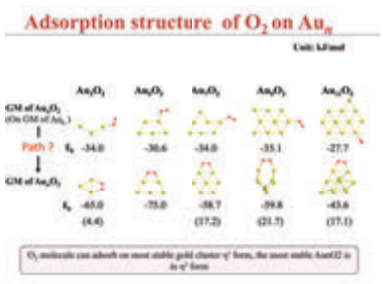

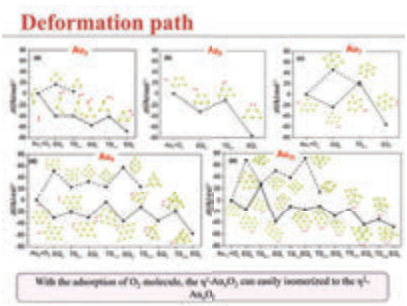

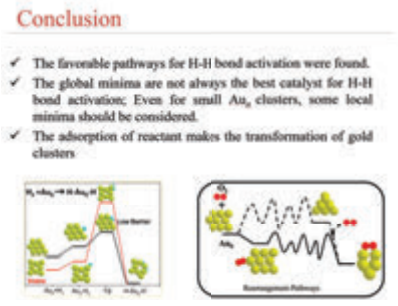

Controlled intersystem crossing in iron porphycene substituted myoglobin for cyclopropanation reaction: a theoretical study

Liming Zhao[1], Akira Nakayama[2], Koji Oohora[3], Hiroyuki Meichin[3], Takashi Hayashi[3], Jun-ya Hasegawa[2],
[1] *Graduate School of Chemical Sciences and Engineering, Hokkaido University*
[2] *Institute for Catalysis, Hokkaido University*
[3] *Department of Applied Chemistry, Graduate School of Engineering, Osaka University*

Introduction:

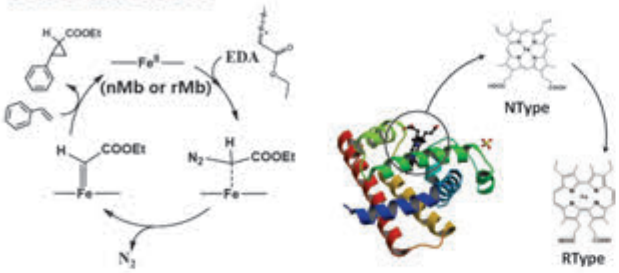

- In the experiment, comparing with wild-type myoglobin, iron porphycene base myoglobin has a much higher catalytic efficiency in the cyclopropanation reaction.[1]
- The step that EDA adduction to myoglobin to form carbene was found important in this reaction.

Results and Discussion:

1 No Protein Effect

Method: ub97d
*Basis: Fe/SDD others/6-31g**

Code: G09 and the package developed by our group to find intersystem crossing point.

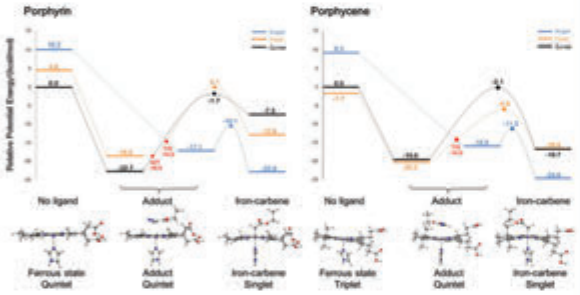

Fig. 1 Potential energy diagrams for the reactions of (left) the native heme-imidazole complex with EDA and (right) the FePc-imidazole complex withEDA. Optimized structures of stable intermediates in different spin states at each step in the reaction are shown below the diagrams.

- Q/T crossing point is very close to triplet minimum. So the quenching to quintet state is easily to occur.
- Intersystem crossing is happened twice in the case of porphyrin while only once in porphycene.
- Total energy barrier is lower in porphycene than the case of porphyrin.

In conclusion, Fe-porphycene is much easier to form Fe-carbene than Fe-porphyrin.

2 With Protein

Model and Method

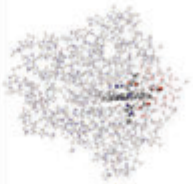

Method: QM/MM (ub97d/amber)
Basis set: Fe SDD; others 6-31g*

- Software: Amber16 and Gaussian16
- The way to optimize structures: optimize only QM regions to get different points along reaction pathway. Then, optimize each point of MM region and QM region in an iterative way. [2]

Potential Energy Surface

NType

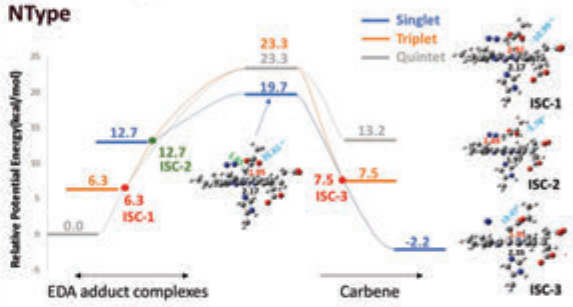

RType

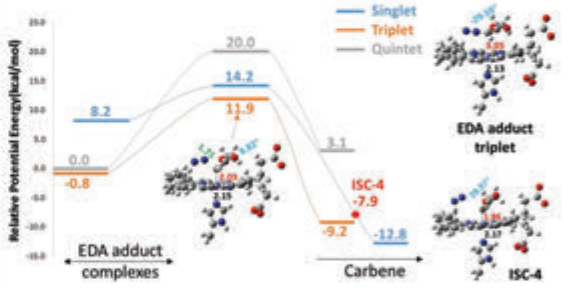

- The geometries of transition states and carbenes are very alike if the protein there is or not. The geometric difference was only found in the EDA addcut complexes of singlet, where the Fe-EDA distance become larger with protein there.
- There is no interaction can be found between the EDA and nearby histidine residue.
- The protein environment changes the potential surface where the ISC points of singlet and triplet (S/T) was found near the triplet carbene minimum in the case of porphycene. Also, in the case of porphyrin, one extra ISC point was found betwee S/T states.

Conclusions and Next:

- Fe-porphycene is more easy to form carbene structure basing on two facts. First, for the porphyrin, since the most stable spin states of EDA adduct complex and carbene are quintet and singlet, respectively, two intersystem crossing will take place while only one is needed for Fe-porphycene. Second, the location of ISC points in the Fe-porphyrin case makes the quenching easily to happen.
- The QM/MM calculations till now indicates that, the geometries of active sites were not significantly changed. But the potential energy surface is actually different.
- Next, free energy perturbation method will be used to calculate the free energy of the reaction and more protein effects will be investigated.

References:

[1] K. Oohora, H. Meichin, L. Zhao, M. Wolf, A. Nakayama, J. Hasegawa, N. Lehnert, and T. Hayashi. *J. Am. Chem. Soc.*, 139, 17265–17268 (2017)
[2] Y. Zhang, H. Liu, W. Yang. *J. Chem. Phys.* 112, 3483(2000)

Reaction Mechanism of the direct synthesis of dimethyl carbonate from CO_2 and methanol over metal-oxide catalysis : a theoretical study

北海道大学 HOKKAIDO UNIVERSITY

○Toshiyuki Sugiyama, Akira Nakayama, and Jun-ya Hasegawa

Institute for Catalysis, Hokkaido University, Sapporo 001-0021, Japan

Institute for Catalysis CAT

Background

$CO_2 + 2CH_3OH \rightleftharpoons H_3CO(C=O)OCH_3 + H_2O$ (catalyst)

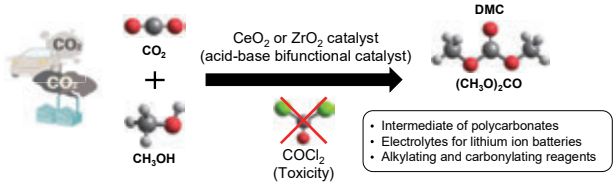

- Intermediate of polycarbonates
- Electrolytes for lithium ion batteries
- Alkylating and carbonylating reagents

A green and sustainable process to replace conventional methods

CeO_2 catalyst

- Acid-base sites (Lewis acid-base pairs)
- Redox properties

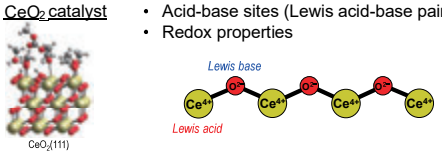

In this work

We investigate reaction mechanisms of DMC formation over CeO_2 and clarify the role of active sites.

Ref : Tomishige, K.; Sakaihori, T.; Ikeda, Y.; Fujimoto, K. *Catal. Letters* **1999**, *58*, 225–229.
Yoshida, Y.; Arai, Y.; Kado, S.; Kunimori, K.; Tomishige, K. *Catal. Today* **2006**, *115*, 95–101.

Computational details

- DFT+U (PBE functional)
- NVT ensemble (T = 360 K)
- Blue-moon ensemble approach (Free energy calculation)
- Slab model for CeO_2(111) surface
  $p(3\times3)$ with 3 O-C-O tri-layers (27 CeO_2 units)
  11.56 × 11.56 × 25.0 Å

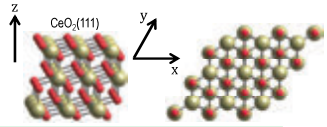

Adsorption structures of the reactants

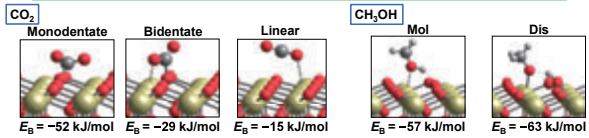

STEP1 $CO_2 + CH_3OH \rightarrow H_3CO(C=O)OH$

STEP2 $H_3CO(C=O)OH + CH_3OH \rightarrow H_3CO(C=O)OCH_3 + H_2O$

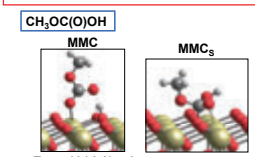

- Adsorption structures of CO_2
  - ◊ Surface carbonate species
    - — Monodentate / Bidentate → MMC_S
  - ◊ Molecular adsorption
    - — Linear → MMC
- Adsorption structures of CH_3OH
  - ◊ Dissociated adsorption
  - ◊ Molecular adsorption
    - → Both structures exhibit similar E_B

Reaction mechanism

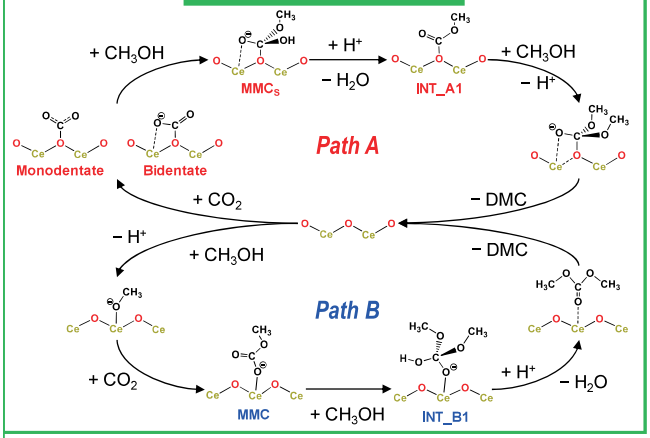

Analysis : Free energy profile

Problems of conventional first-principle calculations ($T = 0$, $P = 0$)

- Numerous local minima on the potential energy surface due to the complex interactions between molecules and metal-oxide surface.
- Neglects of the thermal (entropic) effects.

First-principle molecular dynamics simulations at finite temperature

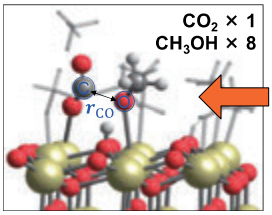

Integration of the mean force leads to the free energy profile along a reaction coordinate.

Conformational sampling by fixing r_{CO} at certain distances

=

Obtaining the mean force acting on r_{CO}.

Blue moon ensemble approach

$$W(\xi) = \int_{\xi_0}^{\xi_1} \frac{\partial W}{\partial \xi'} d\xi'$$

$W(\xi)$: free energy

$\frac{\partial W}{\partial \xi'}$: mean force

$\xi = r_{CO}$

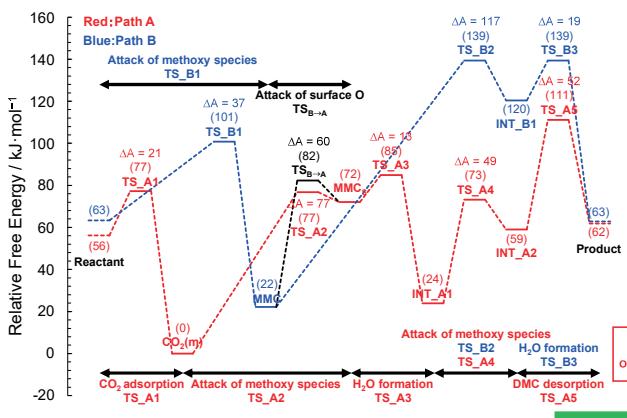

Reaction mechanism

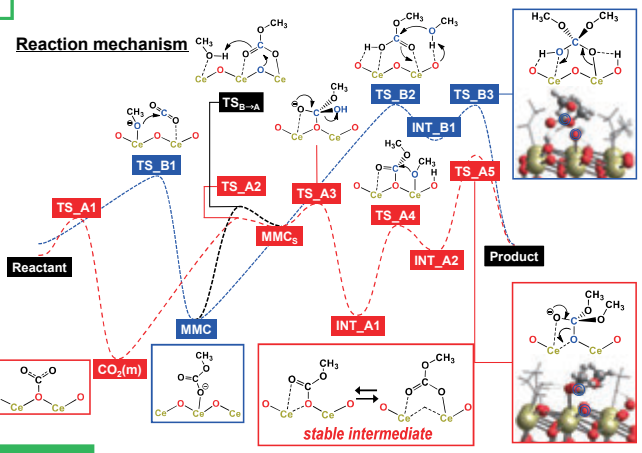

Conclusion

- The reaction mechanisms of DMC formation over CeO_2 were theoretically investigated.
- The reaction mechanism via a stable intermediate accompanying an oxygen vacancy is a preferable pathway.

Selective synthesis of cello-oligosaccharides by hydrolysis of cellulose over carbon catalyst in a semi-flow reactor

Pengru Chen,[1,2] Abhijit Shrotri,[1] Atsushi Fukuoka[1]
[1]Institute for catalysis, [2]Graduate School of Chemical Sciences and Engineering, Hokkaido University
email: chenpr@cat.hokudai.ac.jp

Introduction

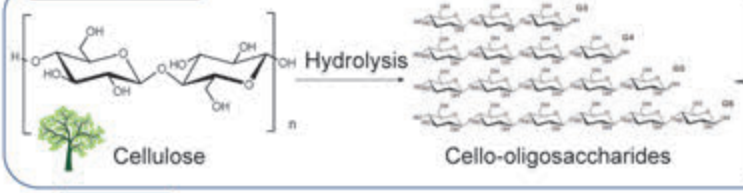

- Food additive: prevents lifestyle-diseases
- Improves the growth of calves
- Elicitor: reinforces plant immunity

Methods

Pre-treatment

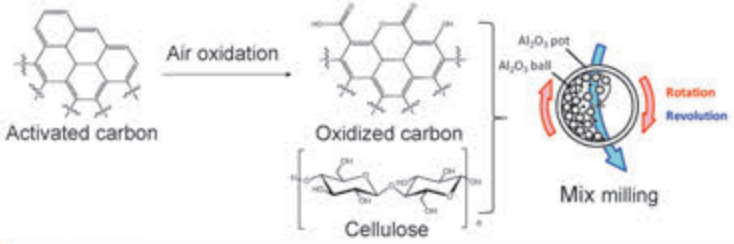

Hydrolysis in semi-flow reactor

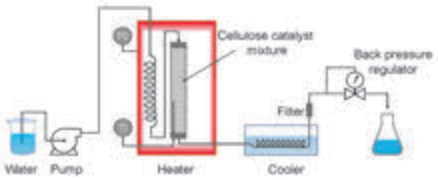

Results

Hydrolysis result

Time course of hydrolysis reaction

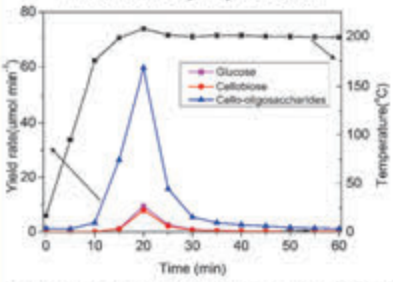

The yield of products

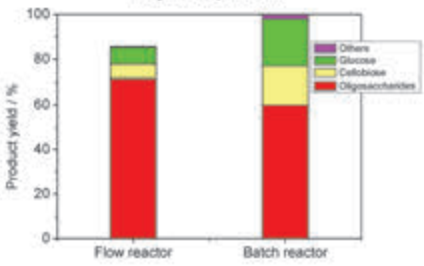

- Cellulose hydrolysis was complete within 20 min.
- High yield of cello-oligosaccharides was generated with glucose and cellobiose as the main byproducts in semi-flow reactor.

The effect of temperature

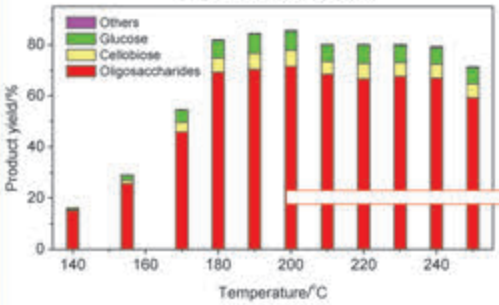

MALDI-TOF MS of oligosaccharides

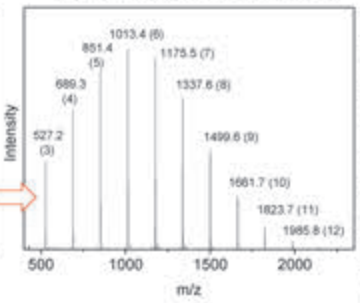

- The secondary hydrolysis of cello-oligosaccharides was limited even at high temperature.
- Formation of cello-oligosaccharides with DP as high as 13 monomer units was observed by MALDI-TOF MS.

Characterization

FT-IR spectra

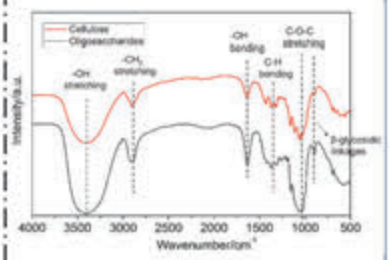

^{1}H NMR spectra

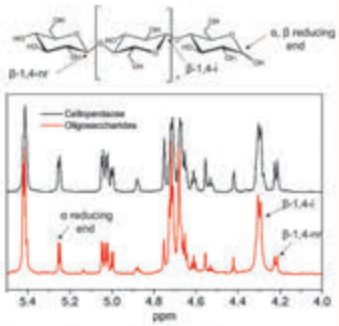

- ^{1}H NMR and FT-IR confirmed the structure of β-1,4 linked straight chain oligosaccharides without the presence of branching and impurities.

Conclusions

- Cello-oligosaccharides yield of 72% with DP as high as 13 was generated from cellulose hydrolysis in a semi-flow reactor.
- ^{1}H NMR and FT-IR of oligosaccharides confirmed the absence of any other glycosidic bonds except the β-1,4 linkages.

Development of Columnar Liquid Crystals of Macrocycles toward Anisotropic Transport of Lithium Ion

Kyohei TOMITA, Shin-ichiro KAWANO, Kentaro TANAKA
Department of Chemistry, Graduate School of Science, Nagoya University, Nagoya 464-8601, Japan
kentaro@chem.nagoya-u.ac.jp

1. Introduction

Lithium ion transport in 1-D pores or liquid crystal

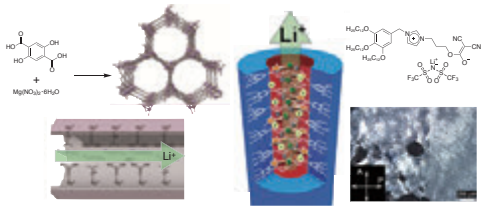

J. R. Long, *et. al.*, *J. Am. Chem. Soc.*, **133**, 14522 (2011)

- Lithium ion transport in 1-D honeycomb-type pores in MOF.

T. Kato, *et al.*, *J. Mater. Chem. A.*, **3**, 11232 (2015)

- Lithium ion transport in liquid crystal formed by self-assembly of wedge-shaped zwitterions.

Our liquid-crystalline macrocycle

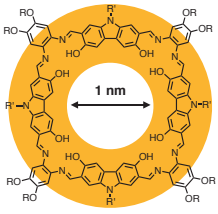

H_8**1**

K. Tanaka, *et. al.*, *J. Am. Chem. Soc.*, **137**, 2295 (2015)

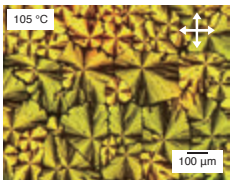

Phase Diagram Col$_r$: Rectangular columnar phase; Iso: Isotropic liquid

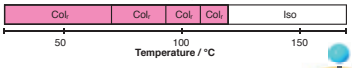

This work

- Formation of a conjugate of the macrocycle and lithium ions.
- Liquid-Crystalline behavior of the conjugate.

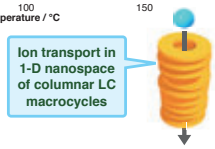

2. Synthesis of nLi⁺•H_{8-n}**1**$^{n-}$

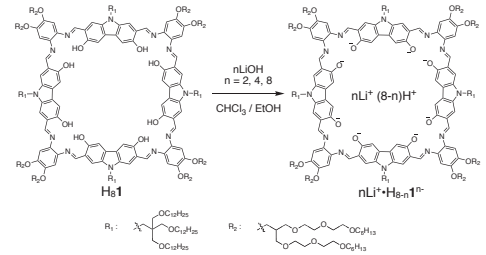

3. ^{1}H NMR and ^{7}Li NMR of nLi⁺•H_{8-n}**1**$^{n-}$

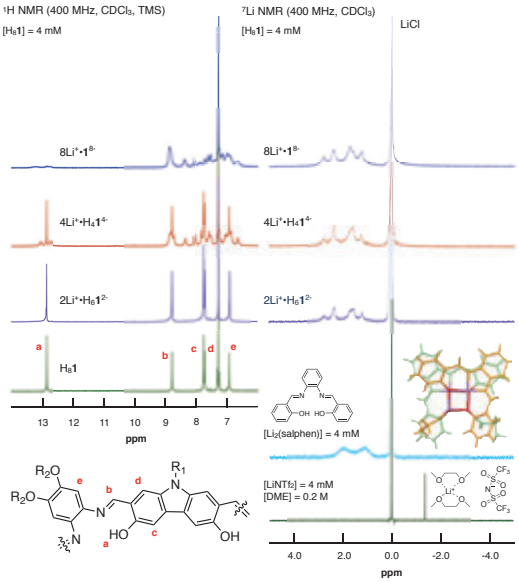

➔ ^{1}H NMR spectrum of 8Li⁺•**1**$^{8-}$ was different from that of H_8**1**. However, in the spectra of 2Li⁺•H_6**1**$^{2-}$ and 4Li⁺•H_4**1**$^{4-}$, the set of signals derived from H_8**1** were still observed, indicating disproportionation of the conjugates and H_8**1** in the solutions. On the other hand, in the ^{7}Li NMR spectra, the signals indicate lithium ions interact with salphen moieties inside the macrocycle rather than with ethers outside the macrocycle.

4. Liquid-Crystalline Properties of 2Li⁺•H_6**1**$^{2-}$

Table 1. Thermal properties

Compound	Phase		
2Li⁺•H_6**1**$^{2-}$	Col$_r$	150 °C →	Iso
4Li⁺•H_4**1**$^{4-}$	M	270 °C →	Dec
8Li⁺•**1**$^{8-}$	M	300 °C →	Dec

GIXRD

CuKα, 45 kV, 45 mA

Table 2. Observed XRD data of liquid crystal phase of 2Li⁺•H_6**1**$^{2-}$ and H_8**1**

Compound	Phase	2D cell parameters	
2Li⁺•H_6**1**$^{2-}$	Col$_r$	a = 50 Å	b = 37 Å
H_8**1**	Col$_r$	a = 45 Å	b = 36 Å

Structural Analysis by GIXRD

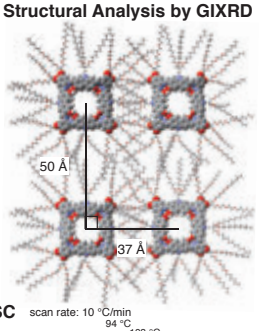

POM

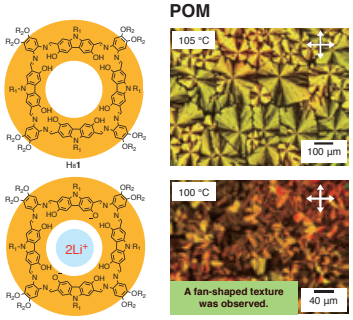

DSC

scan rate: 10 °C/min

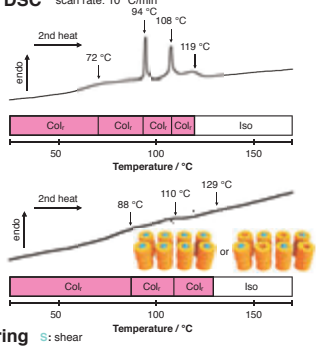

Orientation of columnar structure by Shearing

S: shear

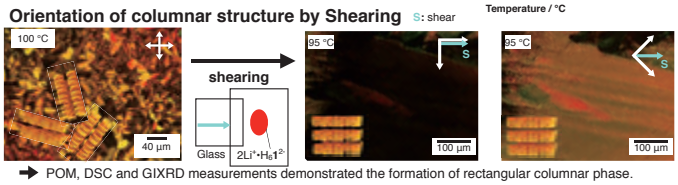

➔ POM, DSC and GIXRD measurements demonstrated the formation of rectangular columnar phase.

5. Summary and Perspectives

- Lithium ions were conjugated with the columnar liquid-crystalline macrocycle in its hollow.
- POM, DSC and GIXRD measurements revealed the complex 2Li⁺•H_6**1**$^{2-}$ showed a rectangular columnar liquid-crystalline phase.
- Ionic conductivity will be investigated.

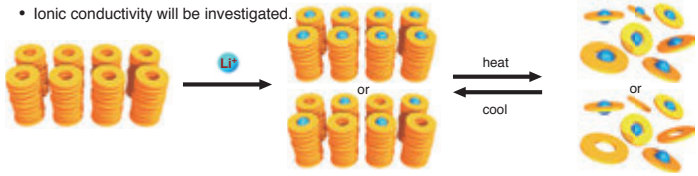

Accurate Wave Function Theory for Large, Real-life Molecules

NAGOYA UNIVERSITY

Masaaki Saitow

masa.saitow@chem.nagoya-u.ac.jp

DEPARTMENT OF CHEMISTRY NAGOYA UNIVERSITY

Introduction

Accurate *ab initio* computation of the electronic wave function in a linear-scaling scheme opens an unprecedented possibility for modelling chemical reactions for large, real-life molecules:

- Semi-empirical and DFT methods often give qualitatively wrong results. [1]
- Sub-linear scaling Domain-based Local Pair-Natural Orbital Coupled-Cluster (DLPNO-CC) theory for open-shell systems [2] and its extension to various magnetic and electronic properties [4] *(in collaboration with Prof. Frank Neese)*
- Reduced-scaling multireference perturbation theory in the local PNO framework using density-matrix renormalization scheme (DMRG-PNO-CASPT2) for large, strongly-correlated systems *(in collaboration with Prof. Takeshi Yanai)*

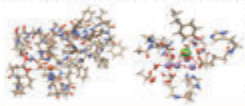

Figure 1: Quinone-Iron cluster (593 atoms) and oxygen evolving complex (243 atoms) active site models which are the large, real-life open-shell systems and are possible to treat with the DLPNO-CC method. [2,4]

Theory

The Linear-scaling Coupled-Cluster Theory:

The DLPNO-CCSD total electronic energy is given as

$$E_{\mathrm{CC}} = E_0 + \sum_i \sum_{a_i} F_i^{a_i} t_{a_i}^i + \frac{1}{4} \sum_{ij}^{\mathrm{occ.}} \sum_{ab}^{\mathrm{virt.}} \left(K_{ab}^{ij} - K_{ba}^{ij} \right) \left(t_{ab}^{ij} + t_a^i t_b^j \right)$$

where the second and third terms represent the electron correlation energy. The t_1 and t_2 amplitudes are determined by solving the cluster equations:

$$R_a^i = \langle \Psi_a^i | \exp(-T_1 - T_2) H \exp(T_1 + T_2) | \Psi \rangle \to 0$$
$$R_{ab}^{ij} = \langle \Psi_{ab}^{ij} | \exp(-T_1 - T_2) H \exp(T_1 + T_2) | \Psi \rangle \to 0$$

In the DLPNO scheme, we introduce virtual natural orbitals specific to *{i}* and *{ij}* which are constructed using the first-order perturbation theory and transform the energy and the cluster equations into DLPNO basis:

$$E_{\mathrm{DLPNO\text{-}CC}} = E_0 + \sum_i \sum_{a_i} F_i^{a_i} t_{a_i}^i + \frac{1}{4} \sum_{ij} \sum_{a_{ij} b_{ij}} \left(K_{a_{ij} b_{ij}}^{ij} - K_{b_{ij} a_{ij}}^{ij} \right) \left(t_{a_{ij} b_{ij}}^{ij} + t_{a_{ij}}^i t_{b_{ij}}^j \right)$$

When occupied MOs are localized, the average number of PNOs per pair becomes asymptotically independent of the molecular size. By solving the DLPNO-CC Λ-equations, one can calculate various molecular properties such as hyperfine coupling constants (HFCs) and electric field gradients (EFGs) in a linear-scaling computational time. [3,4]

The Reduced-scaling CASPT2 Formalisms:

In CASPT2 formalism, the wave function is defined as

$$|\Psi_{\mathrm{CASPT2}}\rangle = \sum_{ijab} t_{ab}^{ij} |\Psi_{ij}^{ab}\rangle + \sum_{\rho ab} t_{ab}^{\rho} |\Psi_{\rho}^{ab}\rangle + \sum_{ipab} t_{ab}^{ip} |\Psi_{ip}^{ab}\rangle$$
$$+ 5 \text{ more excitations}$$

where the configurations with ρ indices are the spin-adapted, non-redundant internally-contracted basis (nr-ICB) which are generated by removing the linear-dependency of the redundant ICB:

$$|\Psi_{\rho}^{ab}\rangle = \frac{1}{2} \sum_{pq}^{\mathrm{active}} C_{pq}^{\rho} |\Psi_{pq}^{ab}\rangle = \frac{1}{2} \sum_{pq}^{\mathrm{active}} C_{pq}^{\rho} E_{pq}^{ab} |\Psi_0\rangle$$

The orthonormalization matrix is obtained by solving the following equations:

$$\sum_{rs}^{\mathrm{active}} \left(\langle \Psi_{ab}^{pq} | H_0 | \Psi_{rs}^{ab} \rangle - E_{\rho} \langle \Psi_{ab}^{pq} | \Psi_{rs}^{ab} \rangle \right) C_{rs}^{\rho} = 0$$

The first-order wave function is determined by solving the residual equations in nr-ICB basis:

$$R_{ab}^{\rho} = \langle \Psi_{ab}^{\rho} | H | \Psi_0 \rangle + \sum_{cd}^{\mathrm{virt.}} \sum_{\tau}^{\mathrm{nr\text{-}ICBs}} \langle \Psi_{ab}^{\rho} | H_0 | \Psi_{\tau}^{cd} \rangle t_{cd}^{\tau} + \cdots \to 0$$

The multireference PNOs are defined for each of nr-ICBs and the residua are transformed into the following form:

$$R_{a_\rho b_\rho}^{\rho} = \langle \Psi_{a_\rho b_\rho}^{\rho} | H | \Psi_0 \rangle + \sum_{\tau}^{\mathrm{nr\text{-}ICBs}} \sum_{c_\tau d_\tau} \langle \Psi_{a_\rho b_\rho}^{\rho} | H_0 | \Psi_{\tau}^{c_\tau d_\tau} \rangle t_{c_\tau d_\tau}^{\tau} + \cdots \to 0$$

Results

Performance to the open-shell systems: C_nH_{2n+2} (S=3/4)

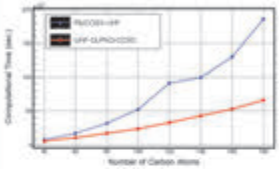

Figure 2: Computational times of RIJCOSX-UHF and UHF-DLPNO-CCSD for the linear alkene chains in triplet state def2-TZVPP basis. 4 CPU cores and 128with GB of memory were used without competing jobs. The identical geometries as the singlet alkane chains were used.

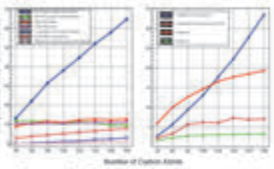

Figure 3: Timings of each computational steps in the UHF-DLPNO-CCSD method per atom. Despite the linear scaling behaviour for case of closed-shell systems, the RI 3-index integral generation does not reach plateau, scaling rather quadratically (the effective exponent is 1.93).

Accuracy of DLPNO-based HFCCs for *3d* Metals Complexes:

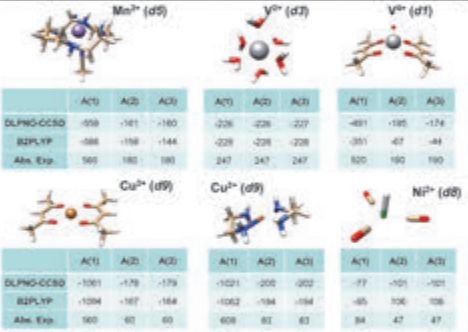

	A(1)	A(2)	A(3)
DLPNO-CCSD	-559	-161	-160
B2PLYP	-586	-158	-144
Abs. Exp.	560	180	180

	A(1)	A(2)	A(3)
DLPNO-CCSD	-226	-226	-227
B2PLYP	-229	-228	-228
Abs. Exp.	247	247	247

	A(1)	A(2)	A(3)
DLPNO-CCSD	-491	-195	-174
B2PLYP	-351	-67	-44
Abs. Exp.	520	190	190

	A(1)	A(2)	A(3)
DLPNO-CCSD	-1061	-179	-179
B2PLYP	-1094	-167	-164
Abs. Exp.	560	60	60

	A(1)	A(2)	A(3)
DLPNO-CCSD	-1021	-200	-202
B2PLYP	-1062	-194	-194
Abs. Exp.	608	83	83

	A(1)	A(3)	A(3)
DLPNO-CCSD	-77	-101	-101
B2PLYP	-85	106	106
Abs. Exp.	84	47	47

(Experimental and computational HFCCs are given in MHz)

Preliminary Results with PNO-CASPT2:

We have derived and implemented the PNO-CASPT2 residual equations for the external excitation (V(0), V(-1), V(-2)) subspaces using our code generator framework. [5]

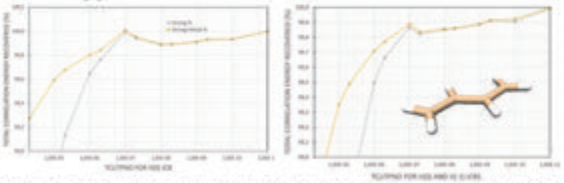

Figure 4: Total correlation energies recovered (%) for the C_4H_6 linear polyene calculated by PNO-CASPT2 code with respect to the canonical CASPT2 values. In the left plot, the TCutPNO threshold for V(0) subspaces are changed while setting those for the rests to zero. In the right plot, value of TCutPNO for V(-2) subspace is fixed to 1e-9 and those for the other subspaces which involve at least one DOMO indices are changed.

Summary

The open-shell DLPNO-CCSD has been implemented and available in ORCA package and has been shown faster then RI-SCF. The metal HFCCs are accurately calculated if the second-order SOC contribution is negligible e.g., *d1*, *d3* and *d5* configurations.

In the PNO-CASPT2, truncation of PNOs for those subspaces involving at least one LMO indices dominates the accuracy of the total correlation energy.

References

[1] F. Neese *et al.*, J. Am. Chem. Soc., **DOI:** 10.1021/jacs.8b13313

[2] M. Saitow *et al.*, J. Chem. Phys. **146**, 164105 (2017).

[3] D. Datta, S. Kossmann and F. Neese, J. Chem. Phys. **145**, 114101 (2016).

[4] M. Saitow and F. Neese, J. Chem. Phys. **149**, 034104 (2018).

[5] M. Saitow, Y. Kurashige, T. Yanai, J. Chem. Phys. **139**, 044118 (2013).

Calculating Bioimaging Probes with RISM(-DMRG)-CASPT2

○Ryosuke Y. Shimizu[1], Takeshi Yanai[1,2,3], Yuki Kurashige[4], Daisuke Yokogawa[5]

[1]Department of Chemistry, Graduate School of Science, and [2]Institute of Transformative Bio-Molecules (WPI-ITbM), Nagoya University, Nagoya 464-8602

[3]Japan Science and Technology Agency, PRESTO, Kawaguchi 332-0012

[4]Department of Chemistry, Graduate School of Science, Kyoto University, Kyoto 606-8502

[5]Department of Basic Science, Graduate School of Arts and Sciences, The University of Tokyo, Tokyo 153-0041

I. Advances in Bio-Imaging

Fluorescent molecules are powerful tools for visualizing biological events.

Optical images of SKH mice injected with hyaluronan analogs modified with IR-783 dye.

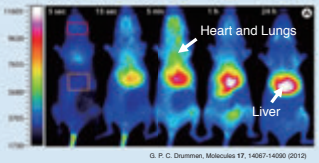

G. P. C. Drummen, Molecules **17**, 14067-14090 (2012)

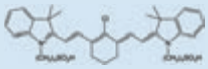

IR-783

With near-infrared (NIR) light, we are able to study "deeper" into biological systems.

① Why NIR?

NIR light has high permeability.

Reduced Scattering Coefficients

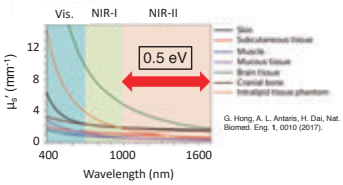

G. Hong, A. L. Antaris, H. Dai, Nat. Biomed. Eng. **1**, 0010 (2017).

The "second NIR window" has been gaining attention for improving the performance of bio-imaging.

To study theoretically, must consider excited state electronic structure and solvation effect.

② Can we theoretically predict photochemical properties?

We checked the absorption energies with a conventional method (PCM-TD-DFT).

Molecules with absorption in visible and NIR region

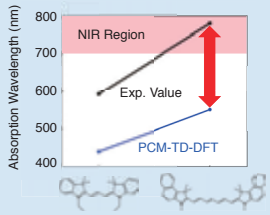

The accuracy of the widely used PCM-TD-DFT method was insufficient.

A new method is required for studying these molecules.

③ Which is important? Electronic structure vs. solvation effect

【Electronic Structure】

Error from experimental value (eV)

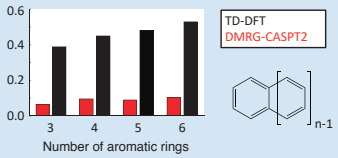

S. Grimme and M. Parac, ChemPhysChem **4**, 292 (2003).
Y. Kurashige and T. Yanai, Bull. Chem. Soc. Jpn. **87**, 1071 (2014).

【Solvation Effect】

Comparing calculated Stokes shifts

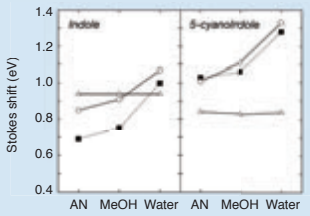

D. Yokogawa, J. Chem. Phys. **145**, 094101 (2016).

Improving accuracy of electronic structure and solvation effect is essential.

II. New Method: RISM-CASPT2

④ Formalization

We defined the Helmholtz free energy calculated with the CASPT2 method as:

$$\mathscr{A}_{\mathrm{CASPT2}} \equiv \langle \Psi | \hat{H} | \Psi \rangle + \Delta\mu + E_2.$$

The free energy is minimized by solving

$$\langle \delta\Psi | \hat{H}^{\mathrm{solv}} - E | \Psi \rangle = 0$$

subjected to the orthonormalization constraint.
$\hat{H}^{\mathrm{solv}}$ is the solvated Hamiltonian defined as:

$$\hat{H}^{\mathrm{solv}} \equiv \hat{H} + \sum_{pq} \mathbf{V}^t [\boldsymbol{\Xi} + (m-1)\boldsymbol{\Gamma}]^{-1} \mathbf{R}'_{pq} a_p^\dagger a_q$$

where

$$V_i = -\sum_s q_s \rho_s \int\int \frac{h_{\alpha s}(r) f_s(\mathbf{r}')}{|\mathbf{r}-\mathbf{r}'|} d\mathbf{r} d\mathbf{r}' \quad (i \in \alpha).$$

⑤ Program Development

【Flowchart of calculation】

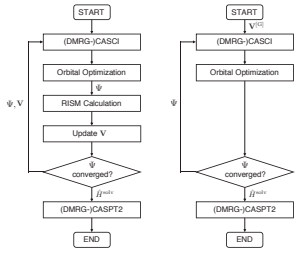

III. Assessment

⑥ Computational Details

Solvatochromism in Absorption

N-methyl-6-hydroxyquinolinium (12e,11o) (6HQ)

In DMSO, acetonitrile, methanol, water

Long π-Conjugated Systems

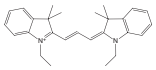

Modeled indocarbocyanine in DMSO (20e,19o) (CY3)

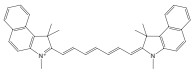

Modeled indocyanine green in water (32e,31o) (ICG)

Basis sets:
- aug-cc-pVDZ (N,O) and cc-pVDZ (other atoms)

⑦ Results and Discussion

【Solvatochromism in Absorption】

	Gas	ACN	DMSO	MET	WAT
PCM-TD-DFT					
CAM-B3LYP	1.30	3.34	3.33	3.34	3.38
PBE0	1.15	3.02	3.01	3.02	3.06
RISM-TD-DFT					
CAM-B3LYP	1.30	2.68	2.70	2.94	3.23
PBE0	1.15	2.44	2.46	2.66	2.91
PCM-MRMP2	1.14	2.44	2.44	2.43	2.45
RISM-CASPT2	1.04	2.38	2.38	2.73	3.21
Exp.	–	2.45	2.44	2.88	3.03

RISM successfully illustrated solvatochromism in absorption.

【Long π-Conjugated Systems】

Error in Absorption Energy (eV)

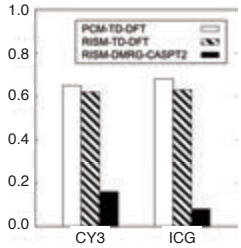

New method reduces error to within 0.2 eV.

⑧ Conclusion

- RISM and CASPT2 have been successfully combined.
- RISM-CASPT2 and its extension with the DMRG improved computed absorption energies.

R. Y. Shimizu, T. Yanai, Y. Kurashige, D. Yokogawa, *J. Chem. Theory Comput.* **14**, 5672 (2018).

Acknowledgement
- This work was supported by Grant-in-Aid for Scientific Research (C) and Fusion Emergent Research.

A hybrid solvation model using C-PCM in CASSCF framework for real-life molecules

○Ayaka Yoshikawa[1], Masaaki Saitow[2], Takeshi Yanai[2,3]
[1]Department of Chemistry, School of Science, [2]Department of Chemistry, Graduate School of Science, and [3]Institute of Transformative Bio-Molecules (WPI-ITbM), Nagoya University, Nagoya 464-8602, Japan

Introduction

1. Hybrid Solvation Model

Widely-used approaches:

- polarizable continuum model (PCM)[1] :
  - + Relatively low computational cost (Pro)
  - + Accuracy to describe solvent effect in non-polar solvents (Pro)
  - - Hydrogen bonding between solute and solvents (Con)
- explicit solvation model (explicit inclusion of solvent molecules) :
  - + High accuracy on various solvent effects including hydrogen bonding (Pro)
  - - Very high computational cost (Con)

→ **Combine advantages of above methods (Hybrid Solvation Model)** [2]

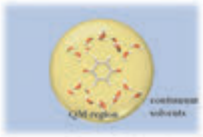

Figure 1: QM region: Solute molecule and first coordination sphere including hydrogen bonds.
Continuum solvents: Continuum solvents calculated with PCM where solvents are treated as polarizable media.

Current Status of the Development:

1.1 Full-scratch implementation of C-PCM model in ORZ package
1.2 Incremental scheme for speeding up the molecular integral computation [3]
1.3 PCM-CASSCF for strongly-correlated systems

Theory

1. Polarizable Continuum Model (PCM)

In PCM-SCF, the Gibbs energy of the solute molecule is given as

$$G = \langle\Psi|\hat{H}_0|\Psi\rangle + \frac{1}{2}\langle\Psi|\hat{V}|\Psi\rangle$$

where $\hat{H}_0$ and $\hat{V}$ represent Hamiltonian of the isolated solute and a solvent effect term calculated in PCM procedure, respectively. Conductor-like PCM (C-PCM) formalism is used in our implementation and treats solvents as a polarizable media.

① Generate cavities centered on each atoms in the solute using GEPOL algorithm:

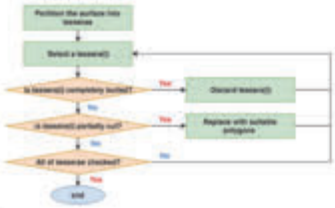

Figure2: Solute is embedded in a cavity constructed in GEPOL scheme and the surface is partitioned into small domains (tessellation). Surface points are defined on each center of tesserae. The flowchart describes the scheme of constructing tesserae.

② Calculate $\mathbf{V}_{\mathrm{MEP}}$ defined as

$$V_{\mathrm{MEP},i} = \sum_{A=1}^{\mathrm{Nnuclei}} \frac{Z_A}{|\mathbf{R}_A - \mathbf{s}_i|} + \sum_{\kappa\lambda} D_{\lambda\kappa} \int d\mathbf{r} \frac{-\chi_\kappa^*(\mathbf{r})\chi_\lambda(\mathbf{r})}{|\mathbf{r} - \mathbf{s}_i|}$$

assuming the Conductor-like boundary condition:

$$\mathbf{V}_{\mathrm{MEP}} + \mathbf{A}\mathbf{Q}_{\mathrm{ASC}} = 0, \quad \begin{cases} A_{ij} = \frac{1}{|s_i - s_j|} \\ A_{ii} = 1.07\sqrt{\frac{4\pi}{a_i}} \end{cases}$$

where $\mathbf{Q}_{\mathrm{ASC}}$ is the apparent surface charge of solvents.

③ Construct the correction term to the Fock matrix of solute as

$$(\Delta f_{\mathrm{PCM}})_{\kappa,\lambda} = \frac{\varepsilon - 1}{\varepsilon} \sum_{i \sim j} Q_{\mathrm{ASC},i} \int d\mathbf{r} \frac{-\chi_\kappa^*(\mathbf{r})\chi_\lambda(\mathbf{r})}{|\mathbf{r} - \mathbf{s}_i|}$$

where ε is the dielectric constant and the correction term is added to Fock matrix.

$$(F_{\mathrm{solute}})_{\kappa,\lambda} \leftarrow (F_{\mathrm{vac}})_{\kappa,\lambda} + (\Delta f_{\mathrm{PCM}})_{\kappa,\lambda}$$

④ The energy contribution of C-PCM is defined as

$$\Delta E_{\mathrm{PCM}} = \frac{\varepsilon - 1}{2\varepsilon} \left\{ \sum_i V_{\mathrm{MEP},i}\, Q_{\mathrm{ASC},i} - \sum_i D_{ii}\, Q_{\mathrm{ASC},i} \int d\mathbf{r} \frac{-\chi_i^*(\mathbf{r})\chi_\lambda(\mathbf{r})}{|\mathbf{r} - \mathbf{s}_i|} \right\}$$

and added to total SCF energy.

2. Incremental Construction Scheme

Introduction of incremental scheme for construction of MEP is defined as

$$\mathbf{V}_{\mathrm{MEP}}^{\mathrm{new}} = \mathbf{V}_{\mathrm{MEP}}^{\mathrm{old}} + \delta\mathbf{V}_{\mathrm{MEP}}$$

$$\delta V_{\mathrm{MEP},i} = \sum_{\kappa\lambda} \delta D_{\lambda\kappa} \int d\mathbf{r} \frac{-\chi_\kappa^*(\mathbf{r})\chi_\lambda(\mathbf{r})}{|\mathbf{r} - \mathbf{s}_i|} \quad \text{where} \quad \delta D_{\lambda\kappa} = D_{\lambda\kappa}^{\mathrm{new}} - D_{\lambda\kappa}^{\mathrm{old}}.$$

In the same way, the correction term to the Fock matrix is written as

$$(\Delta f_{\mathrm{PCM}})_{\kappa,\lambda}^{\mathrm{new}} = (\Delta f_{\mathrm{PCM}})_{\kappa,\lambda}^{\mathrm{old}} + \delta(\Delta f_{\mathrm{PCM}})_{\kappa,\lambda}$$

$$\delta(\Delta f_{\mathrm{PCM}})_{\kappa,\lambda} = \frac{\varepsilon - 1}{\varepsilon} \sum_{i \sim j} \delta Q_{\mathrm{ASC},i} \int d\mathbf{r} \frac{-\chi_\kappa^*(\mathbf{r})\chi_\lambda(\mathbf{r})}{|\mathbf{r} - \mathbf{s}_i|} \quad \text{where} \quad \delta Q_{\mathrm{ASC},i} = Q_{\mathrm{ASC},i}^{\mathrm{new}} - Q_{\mathrm{ASC},i}^{\mathrm{old}}.$$

Algorithm1: Avoiding computation of negligible molecular integrals leads to drastic acceleration up to 25.8 % and 30.9 % in construction of MEP and solvation correction to the Fock operator, respectively. The optimal incremental thresholds determined to be equal to SCF convergence threshold for density matrix in both cases.

```
for each density matrix element κ, λ
  if |MAX(δD)| <incremental threshold then
    skip the molecular integral calculation;
    (V^new_MEP,i)_κλ = (V^old_MEP,i)_κλ;
  else
    calculate (δV_MEP,i)_κλ;
    (V^new_MEP,i)_κλ = (V^old_MEP,i)_κλ + (δV_MEP,i)_κλ;
  end if
  V^new_MEP,i += (V^new_MEP,i)_κλ;
next element
```

```
for each surface point i
  if |δQ_ASC,i| <incremental threshold then
    skip the molecular integral calculation;
    (Δf_PCM)^new_κλ = (Δf_PCM)^old_κλ;
  else
    calculate δ(Δf_PCM)_κλ;
    (Δf_PCM)^new_κλ = (Δf_PCM)^old_κλ + δ(Δf_PCM)_κλ;
  end if
next point
```

3. PCM-CASSCF for strongly correlated systems

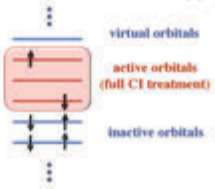

Figure 3: In CASSCF scheme, which is a multiconfigurational SCF (MC-SCF), the orbital space is divided into three classes. The CASSCF wave function is defined as

$$\Psi_{\mathrm{CASSCF}} = \sum_K C_K \Psi_K(\{c_K\})$$

$$\frac{\partial E}{\partial C_K} = \frac{\partial E}{\partial c_K} = 0.$$

In PCM-CASSCF procedure, the Hamiltonian of solute is modified by solvation correction in the same way as the PCM-SCF:

$$\mathbf{H}_{\mathrm{PCM}} = \mathbf{H}_{\mathrm{vac}} + \Delta\mathbf{f}_{\mathrm{PCM}},$$

Benchmarks

1. Checking correctness of our PCM-SCF implementation:

	SCF	PCM-SCF
MAD (kcal/mol)	0.0178	0.0448
RMSD (kcal/mol)	0.0154	0.0149

RMSD: Root Mean Square Deviation
MAD: Maximum Absolute Deviation

Table 1: MAD and RMSD in the radical stabilization energy for 43 reactions in RSE43 benchmark sets [4] with respect to the results by ORCA as a reference implementation.

2. Accuracy of hybrid solvation model for *p*-benzosemiquinone radical anion:

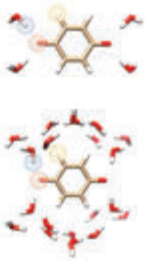

Figure 4: PCM-SCF and SCF calculations were carried out on the solvated models of *p*-benzosemiquinone radical anion surrounded by 4 and 20 water molecules, respectively.

Table 2: Convergence behavior of the isotropic hyperfine coupling constants (A_{iso}, [MHz]) on the bridging hydrogen, carbonyl oxygen and quinone hydrogen to fully-solvated model with 20 water molecules:

$$A_{\mathrm{iso},K} = \frac{8\pi}{3} \frac{g_e}{g_0} g_K \beta_e \beta_n \sum_{\kappa,\lambda} P_{\kappa,\lambda}^{\alpha-\beta} \langle\phi_\kappa|\delta(r_K)|\phi_\lambda\rangle$$

where g_K, β_n, g_e and g_0 represent the nuclear g-factor, the nuclear magneton, the electronic g-factors in the radical and in vacuum, respectively[6].

	Bridging hydrogen		Carbonyl oxygen			Quinone hydrogen		
H$_2$O	4	20	0	4	20	0	4	20
PCM-SCF	1.48	1.15	-162.71	-141.16	-138.12	-8.01	-7.70	-7.55
SCF	1.57	1.19	-183.77	-150.22	-142.04	-8.25	-7.98	-7.61
Exp6.		0.8		-22.1			-6.4	

3. Incremental construction scheme on real-life, bio-molecule:

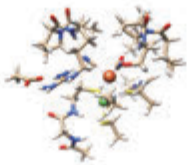

Table3: PCM-SCF calculations were carried out on an active site model of [NiFe] hydrogenase with various incremental thresholds ranging from $1.0E^{-02}$ to $1.0E^{-5}$. Setting both thresholds to $1.0E^{-3}$, the computational time for the PCM procedure is reduced to 28.9 %. Error in the energy caused by the incremental scheme is negligibly small (0.000076 kcal/mol).

Threshold (P_{MAX}, δV_{PCM})	Total time (s)	PCM time (s)	Ratio(PCM/Total) (%)	Energy error (kcal/mol)
(0, 0)	286176.7	89777.9	31.4	0.000076
($1.0E^{-3}$, $1.0E^{-3}$)	196722.8	25934.0	13.2	

Conclusion

We showed that our PCM-SCF implementation produces correct numbers and in combination with explicit inclusion of a few solvent molecules, the PCM-SCF gives quite similar results to fully-solvated models for anisotropic HFCCs which is very sensitive to the chemical environment of the nucleus. Incremental construction scheme in PCM skips unnecessary evaluation of molecular integrals and drastically reduces the computational costs while keeping the original accuracy.

References

[1] Barone, V.; Cossi, M. J. Am. Chem. Soc. 1998, 102, 1995-2001.
[2] Vetta, M. D. et al. J. Phys. Chem. B. 2018, 122, 2975-2975.
[3] Schwegler, E.; Challacombe, M.; Head-Gordon, M. J. Chem. Phys. 1997, 106, 9708-9717.
[4] Goerigk, L.; Grimme, S. J. Chem. Theory Comput. 2011, 7, 291-309.
[5] Sonnecker, S.; Reijerse, E.; Neese,F.; Lubitz, W. J. Am. Chem. Soc. 2004, 126, 3280-3290.
[6] Datta, D.; Gauss, J. J. Chem. Phys. 2015, 143, 011101.

Development of fast and accurate self-consistent field method based on local resolution-of-the-identity approximation

○Ayano Yamada[1], Masaaki Saitow[2], Takeshi Yanai[2,3]
[1]Department of Chemistry, School of Science, Nagoya University, Japan
[2]Department of Chemistry, Graduate School of Science, Nagoya University, Japan
[3]Institute of Transformative Bio-Molecules (WPI-ITbM), Nagoya University, Japan

Introduction

The Hartree-Fock (HF) method is considered to be a good approximation to the electronic wave functions and a starting point of the quantum chemical calculations. However HF method has a limitation in the size of molecules to calculate because of $O(N^4)$ computational costs for constructing the Fock matrix.

Our goal:
[1] Reduce the scaling of Fock matrix construction to speed up SCF and CASSCF
... Resolution-of-the-Identity (RI) approximation
... Local RI (LRI) approximation
[2] Combine fast LRI-CASSCF with DMRG algorism
[3] Reaction mechanisms of realistic bio-molecules (~1000 atoms)
... Within chemical accuracy (~1 kcal/mol)
... Protein, Enzyme

Figure 1: [NiFe]Hydrogenase active site model. Hydrogenases are attracting attention as an ideal building block of fuel cells.

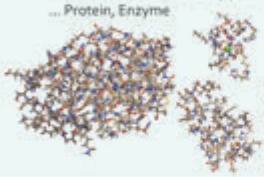

Figure 2: arsenate reductase (azurine), oxygen evolving complex (OEC) and bicarbonate ion (iron-quinone complex). These molecules are important catalytic centers in photosystem II.

Theory

In the conventional HF method, the computation of the two-electron integrals in the Fock matrix $F_{pq} = h_{pq} + J_{pq} - K_{pq}$ scales with the fourth power of the number of basis functions and becomes prohibitively expensive for large molecules.
→ **Hence, we employ the RI and LRI approximations to reduce the scaling of these calculations.**

1. RI approximation.

1.1. Coulomb (J) matrix.

In the RI approximation, the coulomb matrix is decomposed into a product of 2- and 3-center integrals over atomic orbital (AO) functions and the auxiliary basis:

$$J_{pq} = \sum_{r,s} D_{rs}(pq|rs) = \sum_{I} (pq|I) \sum_{J} (I|J)^{-1} \sum_{r,s} D_{rs}(J|rs)$$

The scaling of the coulomb integral calculation is at most cubic with respect to the number of basis functions.

1.2. Exchange (K) matrix.

The exchange matrix is also decomposed in the same way as the coulomb matrix:

$$K_{pq} = \sum_{r,s} D_{rs}(pr|qs) = \sum_{i} \sum_{r} (pr|I) \sum_{J} (I|J)^{-1} \sum_{s} D_{rs}(J|qs)$$

Exchange integral calculation scales still with the fourth power of the number of basis functions as in case of the conventional SCF procedure.

2. LRI approximation.

2.1. Exchange matrix.

The SCF density matrix is expressed using the molecular orbital (MO) coefficients

$$D_{rs} = 2 \sum_{i} C_{ri} C_{si}$$

and the index i refers to localized occupied MOs (LMOs):

$$\varphi_i = \sum_{r} C_{ri} \chi_r = \sum_{s} C_{si} \chi_s$$

In the LRI scheme, the exchange matrix is transformed into

$$K_{pq} \approx \sum_{i} \sum_{r} \sum_{s} C_{ri} (p_{[i]} r|q_{[i]} s) \sum_{J} (I_{[i]}|J_{[i]})^{-1} \sum_{s} C_{si} (J_{[i]}|q_{[i]} s_{[i]}).$$

Furthermore those molecular integrals are appropriately carved out in the atomic domains constructed for each of the LMOs, and thus the linear scaling is achieved.[1]

2.2. Domains.

The domains are subsets of AOs or atoms which make non-negligible contributions to the LMOs. Three types of domains (LMO, AO, and fitting domains) are determined by analyzing the sparsity in the localized occupied MOs. The degrees of the contributions are evaluated by screening thresholds of connecting matrix corresponding to each domains.

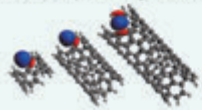

Figure 3: Localized occupied MOs of carbon nanotubes (C_{40},100 and 140). These orbitals expand almost in a constant size. Therefore the size of atomic domains is essentially independent of the system size, and hence the computational cost to construct the exchange integrals is asymptotically linear-scaling.

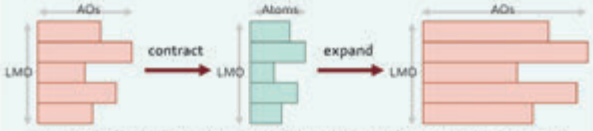

Figure 4: Contraction and expansion operations. (1) When contraction operation is carried out, those atoms at least one of whose orbitals are contained in the original LMO-AO map survive the screening. (2) When expansion operation is carried out, all the orbitals centered on the atoms in the LMO-Atom map survive.[1]

Domain	Connecting matrix
LMO domain	LMO coefficient C_{ri}
AO domain	differential overlap integral $\sqrt{\int dr\|\varphi_i(r)\|^2\|\chi_p(r)\|^2}$
Fitting domain	Mulliken population $\sum_{p\in X}\sum_q C_{ip}S_{pq}C_{iq}$

Figure 4: Connecting matrices corresponding to each domains.

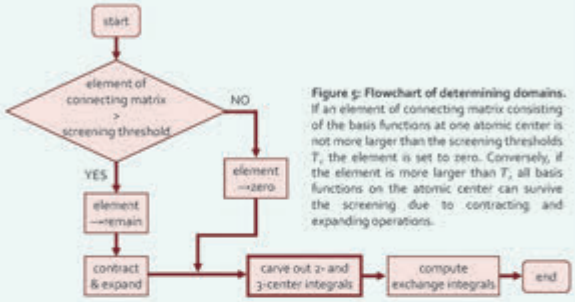

Figure 5: Flowchart of determining domains. If an element of connecting matrix consisting of the basis functions at one atomic center is not more larger than the screening thresholds T, the element is set to zero. Conversely, if the element is more larger than T, all basis functions on the atomic center can survive the screening due to contracting and expanding operations.

Pseudocode ---Building Exchange matrix
for localized occupied MOs i
  orbital coefficients $C_{\mu[i]} \leftarrow C_{\mu i}$
  calculate $Y \leftarrow \sum_{\alpha} C_{\alpha[i]} (J_{[i]}|q_{[i]} q_{[i]})$
  carve out Y_{loc} and $I|_{loc}$
  cholesky decomposition and solution $X_{loc} = \sum_J (I|J)^{-1}_{loc} Y_{loc}$
  calculate exchange matrix $K_{pq} \leftarrow \sum_I Y_{loc} X_{loc}$

Figure 6: Pseudocode.

Results

All calculations were performed using tzvp and def2-tzvpp/jkfit basis set. The screening threshold for fitting domains was set to 10^{-1}. The screening thresholds for LMO and AO domains were set to zero (implementations of these domains are not in progress).

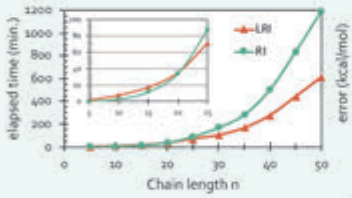

Figure 7: Total elapsed times in calculations of the exchange matrix with LRI (orange) and RI (green) approximations for linear alkane chains C_nH_{n+2} (n=5-50) as a function of chain length n.

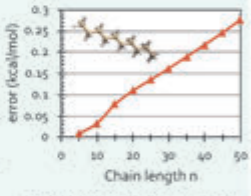

Figure 8: Error (in kcal/mol) in the total SCF energy with LRI approximation on C_nH_{n+2} (n=5-50) as a function of chain length n with respect to conventional RI values.

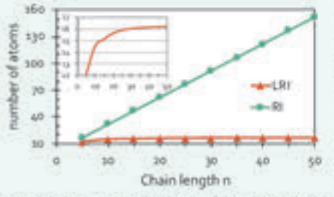

Figure 9: Average number of atoms in a fitting domain in the final iteration with LRI (orange) and RI (blue) approximations as a function of chain length n.

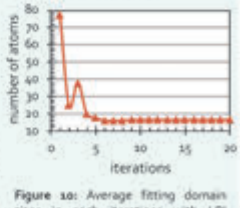

Figure 10: Average fitting domain sizes in each iterations with LRI approximations for $C_{50}H_{102}$.

Conclusions

- ✓ By truncating the auxiliary basis in the fitting domains, the a single construction of K integral was reduced to 51.3 % of the original computational time. The associated error error in the total energy is only up to 0.3 kcal/mol for $C_{50}H_{102}$.
- ✓ Implementation of AO and LMO domains and the extension of LRI scheme to CASSCF are in progress.

References

[1] Köppl, C.; Werner, H.-J. *J. Chem. Theory Comput.* **2016**, *12*, 3122-3134.
[2] Pinski, P.; Riplinger, C.; Valeev, E. F.; Neese, F. *J. Chem. Phys.* **2015**, *143*, 034108.

Synthesis of novel plant-growth stimulants by functionalization of 2-azahypoxanthine

Ayaka Ueda[1]; Hiroyuki Kitano[2]; Jaehoon Choi[3]; Hideto Ito[1,4]; Shinya Hagihara[1,2,5]; Toshiyuki Kan[6]; Hirokazu Kawagishi[3]; Kenichiro Itami[1,2,4]

[1)]Grad. Sch. Sci., Nagoya Univ.; [2)]WPI-ITbM, Nagoya Univ.; [3)]Grad. Sch. Sci. Technol., Shizuoka Univ.; [4)]ERATO, JST.; [5)]RIKEN CSRS; [6)] Sch. Pharm. Sci., Univ. Shizuoka.

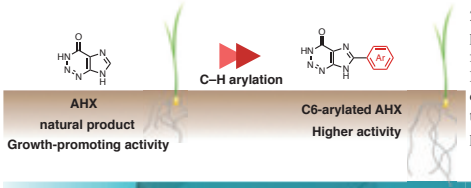

2-Azahypoxanthine (AHX) is a plant growth stimulator isolated from the fairy-ring-forming fungus *Lepista sordida*. Since plant growth regulators that enhance the crop production are in great demand, AHX has attracted considerable attention from agricultural and horticultural researchers. Herein, we report the synthesis of new AHX derivatives by Pd-catalyzed C–H functionalization of AHX. Their rice growth-promoting activity was evaluated in vivo. Among the synthesized compounds, C8 phenyl-substituted AHX showed remarkable growth-promoting activity on rice. The present study shows the power and significant opportunity of C–H functionalization chemistry to rapidly transform biologically active natural products into more active compounds.

("Discovery of Novel Plant Growth Stimulants by C–H Arylation of 2-Azahypoxanthine" *Org. Lett.* **2018**, *20*, 5684.)

Results & Discussion

1. Background

A story of fairy rings

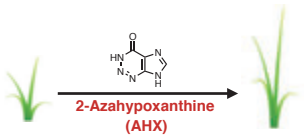

Fairy rings : naturally occurring rings of mushrooms or necrotic or stimulated growth of grasses.

Characteristics of 2-Azahypoxanthine (AHX)

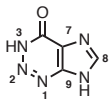

Biological activity

Growth promotion activity among varieties of plants

Structural feature

Very rare 1,2,3-triazine core as a natural product

Kawagishi. H. *et al. Chem. Bio. Chem.* **2010**, *11*, 1373.

New plant hormone…?

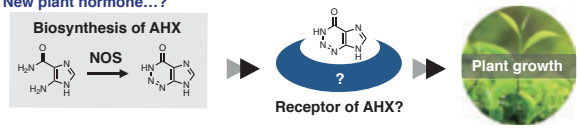

Kawagishi. H. *et al.* Angew. Chem., Int. Ed. **2014**, *53*, 1552. Kawagishi. H. *et al. Sci. Rep.* **2016**, *6*, 39087.

2. N–H functionalization

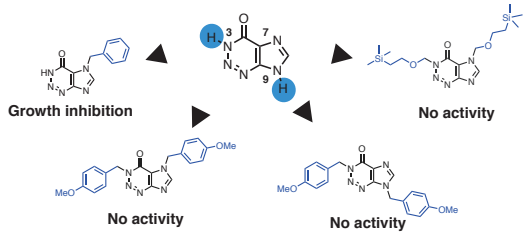

Functionalization of N–H bond decreases plant growth activity

3. C–H arylation of AHX

Strategy of arylation

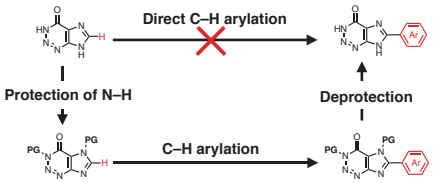

Protection of N–H bond

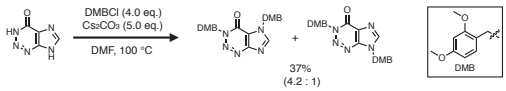

Optimized condition of C–H arylation

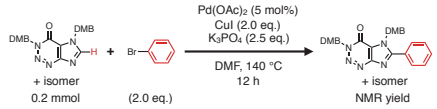

Solvent		Base		Additive	
DMF	**50%**	**K_3PO_4**	**50%**	**None**	**50%**
DMA	43%	Na_2CO_3	46%	$PCy_3{\cdot}HBF_4$ (10 mol%)	52%
1,4-dioxane	17%	K_2CO_3	21%	$P^tBu_3{\cdot}HBF_4$ (10 mol%)	49%
toluene	17%	Cs_2CO_3	44%	BINAP (5 mol%)	43%

1.1 mmol scale, reaction time 15 h **71% (Isolated yield)**

Miura, M. *Bull. Chem. Soc. Jpn.* **1998**, *71*, 467. Rossi, R. *Eur. J. Org. Chem.* **2006**, 1379.

C–H arylation and deprotection

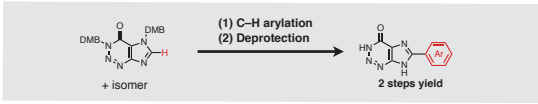

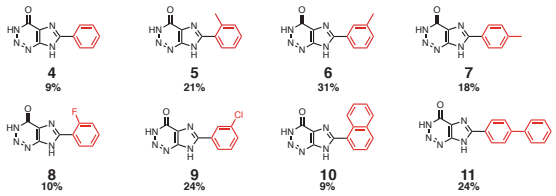

6. Plant growth assay

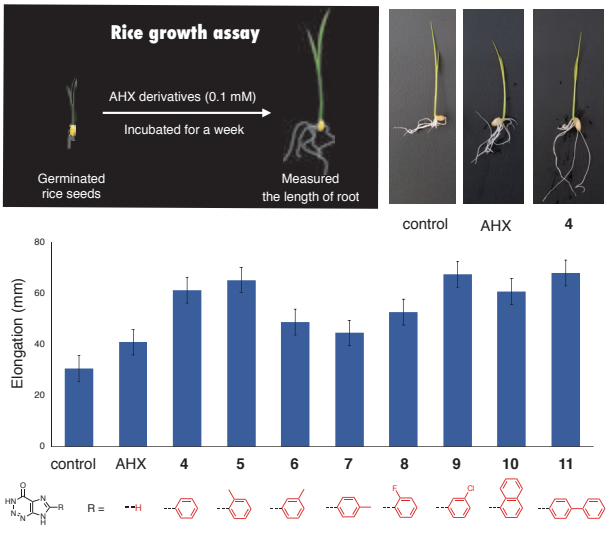

Solid-phase Synthesis of Unsubstituted Poly(*para*-phenylene)

Shusei Fujiki,[a] Akiko Yagi,[ab] Kenichiro Itami[abc]

[a]*Graduate School of Science, Nagoya University, Japan*
[b]*JST, ERATO, Itami Molecular Nanocarbon Project, Nagoya University, Japan*
[c]*Institute of Transformative Bio-Molecules (WPI-ITbM), Nagoya University, Japan*

ITAMI GROUP
RGANIC CHEMISTRY

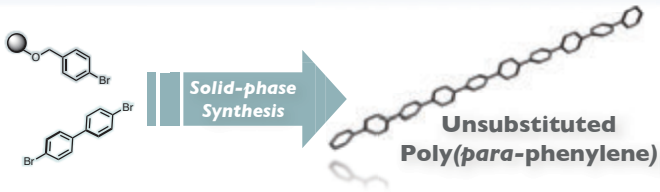

Polyarylenes, which are polymers solely composed of arenes, are promising candidates for electronic devices but insoluble because of their huge planer π-conjugated systems that cause intermolecular aggregation. In this study, we develop a new approach to dissolve such "solubility problem" through the synthesis of unsubstituted poly(*para*-phenylene) (PPP). We propose to apply solid-phase synthesis which is a technique to synthesize compounds on resin. Solid-phase synthesis allows efficient ligation of polymers by separating them on isolated sites on resin.

RESULTS

1 *Introduction*

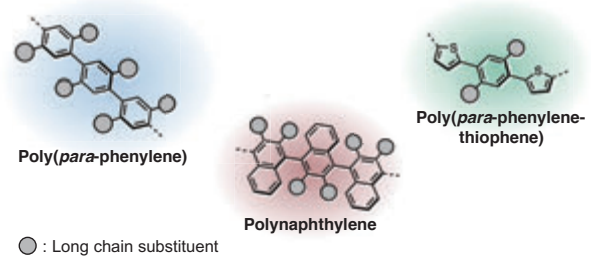

● : Long chain substituent

- *Increasing solubility*
- *Decreasing stability and carrier mobility*
- *Causing blue shift of luminescence*

2 *Successful Synthesis of Unsubstituted PPP*

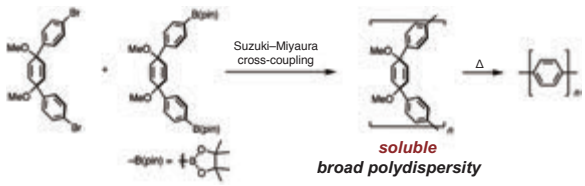

Müllen, K. *et al. J. Am. Chem. Soc.* **2016**, *138*, 16208.

3 *New Synthetic Methodology*

Synthesis of Unsubstituted Polyarylenes in Liquid-phase

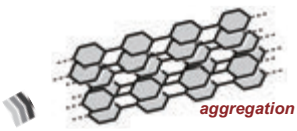

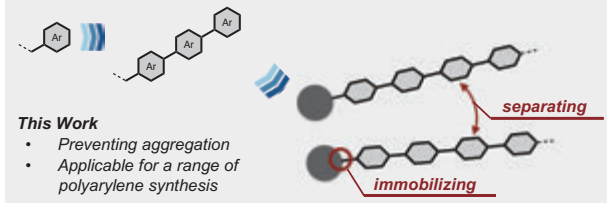

This Work

- *Preventing aggregation*
- *Applicable for a range of polyarylene synthesis*

Solid-phase Synthesis

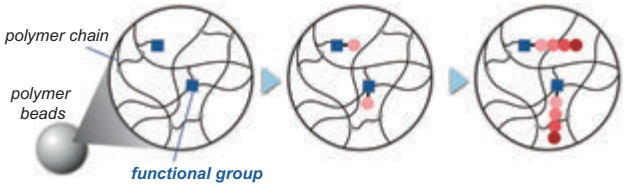

4 *Strategy toward Unsubstituted PPP*

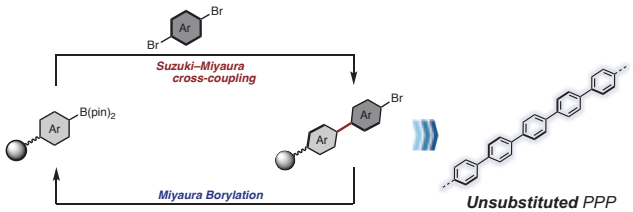

5 *Solid-phase Synthesis of PPP*

Reaction condition of Miyaura borylation

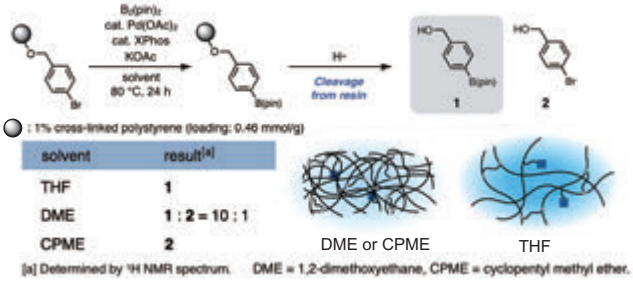

solvent	result[a]
THF	1
DME	1 : 2 = 10 : 1
CPME	2

[a] Determined by ^{1}H NMR spectrum. DME = 1,2-dimethoxyethane, CPME = cyclopentyl methyl ether.

Elongation of phenylene chain

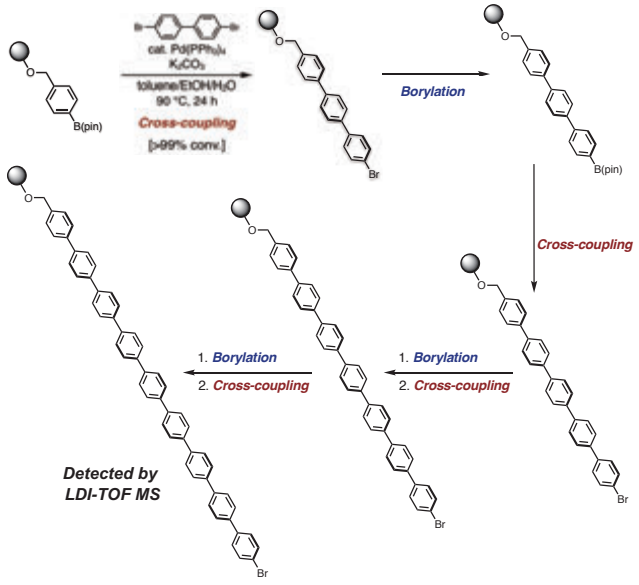

Palladium-Catalyzed Transfer Hydration of Cyanohydrins

Asuka Naraoka, Tomoya Kanda and Hiroshi Naka

Graduate School of Science and Research Center for Materials Science, Nagoya University

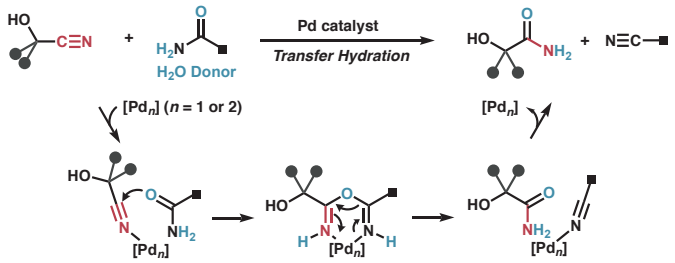

Abstract: We reported the palladium(II)-catalyzed transfer hydration of α-hydroxynitriles (cyanohydrins) to α-hydroxyamides by using carboxamides. This method enables selective hydration of various aldehyde- and ketone-derived cyanohydrins to afforded a series of α-mono- and α,α-disubstituted-α-hydroxyamides under mild conditions (50 °C, 10 min). The ^{18}O-labeling study revealed that the carboxamides work as water donors. The kinetic study indicated the p of two mechanistic periods in the catalytic profile.

J. Am. Chem. Soc. **2019** *ASAP.*

1. Background

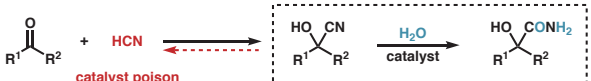

European Patent **EP 0412310 B1**.; United States Patent **US 8519187 B2**.; **Commeyras** *Tetrahedron Lett.* **1989**, *30*, 563.; **Tyler** *Inrog. Chem.* **2009**, *48*, 7828.; **Tyler** *Organometallics* **2012**, *31*, 2941. **Tyler** *Organometallics* **2013**, *32*, 824.;**Tyler** *Organometallics* **2013**, *32*, 3744.; **Cadierno** *Chem. Commun.* **2014**, *50*, 9661.; **Tyler** *ACS Catal.* **2014**, *4*, 3096.; **Tyler** *Inorg. Organomet. Polym.* **2015**, *25*, 73.; **Grubbs** *J. Am. Chem. Soc.* **2018**, *140*, 17782.

Issue: decomposition of cyanohydrins

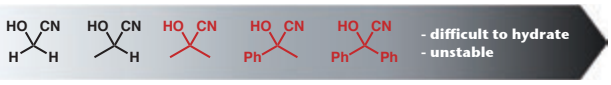

Cf. **Miller** *J. Am. Chem. Soc.* **1973**, *95*, 3729.

2. This Work

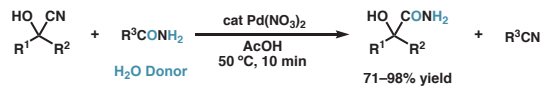

R^1, R^2 = H, alkyl, aryl; R^3 = CH_3, alkyl

Mild and Reversible Dehydration

Maffioli *Org. Lett.* **2005**, *7*, 5237.

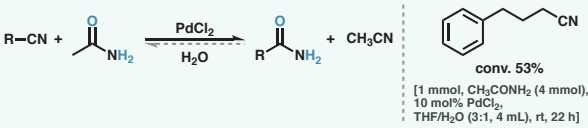

3. Optimization

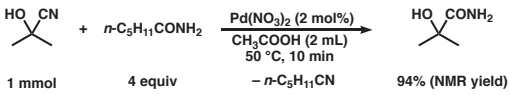

H_2O donor (4 equiv)
[1 mmol, 1 mol% $Pd(NO_3)_2$, 50 °C, 10 min]

n-$C_3H_7CONH_2$ 73%	n-$C_5H_{11}CONH_2$ 75%
CH_3CONH_2 46%	n-$C_7H_{15}CONH_2$ 65%
CF_3CONH_2 < 1%	$(CH_3)_2CCONH_2$ < 1%
H_2O < 1%	CH_3CH=NOH < 1%

Catalyst
[CH_3CONH_2]

$Pd(NO_3)_2$ 94%	$Pd(O_2CCF_3)_2$ 66%	
$Pd(O_2CCH_3)_2$ 47%	$PdSO_4$ 44%	$PdCl_2$ < 1%

Solvent
[CH_3CONH_2, 2–5 mol% $Pd(NO_3)_2$]

CH_3COOH > 99%	CH_3COOH/H_2O 25%
CH_3CN/H_2O 83%	C_2H_5COOH 74%

4. Substrate Scope

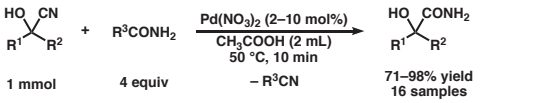

R^3 = n-C_5H_{11}

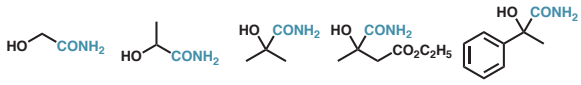

R^3 = CH_3

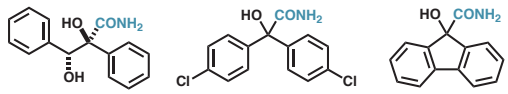

5. Mechanistic Studies

^{18}O-Labeling Experimet

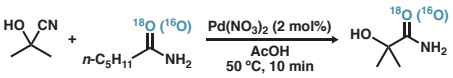

Kinetics

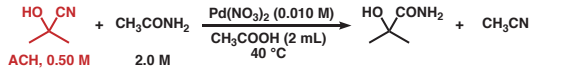

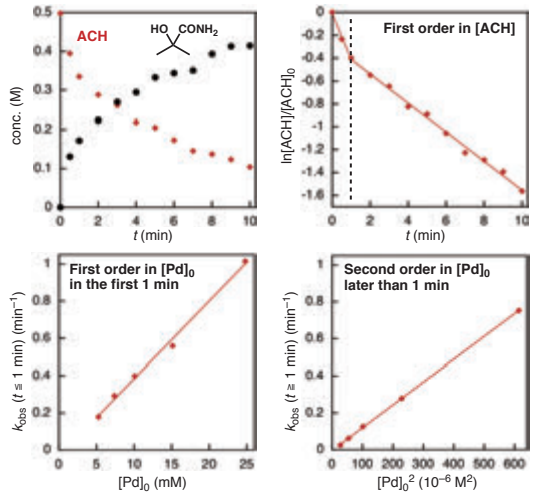

Acknowledgements: We sincerely thank Prof. J. Shimokawa (Kyoto U.) for his suggestions. We are grateful to support from Profs. R. Noyori and S. Saito.

Development of Bidentate Diphosphine Ligands of Highly Active Ru Catalysts for Practical Hydrogenation of Carboxylic Acids

Shota Yoshioka, Masayuki Naruto, We Ken, Susumu Saito*
Department of Chemistry, Graduate School of Science, Nagoya University

Abstract

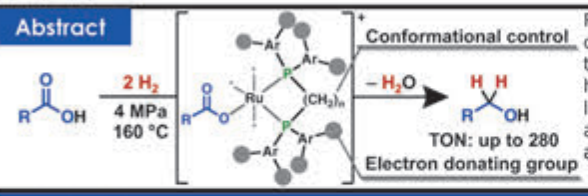

Recently, we have reported the carboxylic acid (CA)-derived cationic metal (M) carboxylate $[P_2M(OCOR)]^+$ (*P* denotes one phosphorous coordination) was found to be the catalyst prototype for *CA self-induced CA hydrogenation*. We report herein an improvement of catalytic activity by tuning the bidentate diphosphine ligands for Ru catalyst. After screening of the ligands, substituted Ar groups on P atoms and control of the conformation of alkyl chain connecting between two P atoms were found to be important for high catalytic activity.

Our recent feature article: S. Yoshioka, S. Saito, *Chem. Commun.* **2018**, *54*, 13319.

1. Introduction

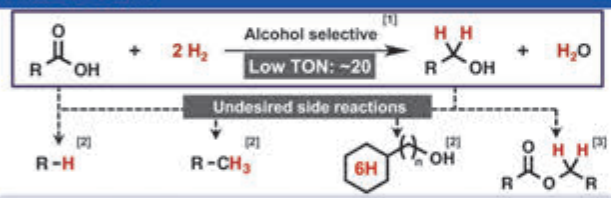

[1] Ru(triphos) (tmm)[a] Ru(acac)$_3$, Triphos, Sn(OTf)$_2$[b] $Co(BF_4)_2{\cdot}6H_2O$, Triphos[c] Re/TiO_2[d] Pd/Re/C[e]

[2] $Re_2O_7 + OsO_4$[a] ReO_4–Pd/SiO_2[b] and many patents etc.

[3] Pt/SnO_2[a] $Ru_4H_4(CO)_8(P^nBu_3)_4$[b] $[Cp^*Ir(bpy)(H_2O)][OTf]_2$[c]

[1] a) W. Leitner *et al. J. Am. Chem. Soc.* **2014**, *136*, 13217; b) M. Beller *et al. Angew. Chem. Int. Ed.* **2015**, *54*, 10596; c) B. de Bruin *et al. Science* **2015**, *350*, 298; d) K. Shimizu *et al. Chem. Eur. J.* **2017**, *23*, 1001; e) B. Breit *et al. ACS Catal.* **2018**, *8*, 785.
[2] a) J. Tsuji *et al. J. Am. Oil. Chem.* **1990**, *67*, 21; b) K. Tomishige *et al. ACS Catal.* **2015**, *5*, 7034.
[3] a) K. Shimizu *et al. Adv. Synth. Catal.* **2015**, *357*,1499; b) L. Rosi *et al. J. Organomet. Chem.* **2005**, *690*, 371; c) I. Goldberg *et al. J. Am. Chem. Soc.* **2013**, *135*, 16022.

2. Our catalysts for CA self-induced CA hydrogenation

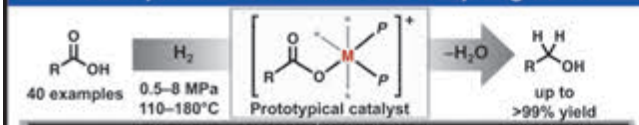

M = Ru^{II} (d^6, LOW-valent)	M = Re^{V} (d^2, HIGH-valent)
➢Milder reaction conditions ➢Low TON ~30 (24–48 h)	➢High functional group tolerance ➢α-C–H bond functionalization

R = H or Me

Ru system: M. Naruto, S. Saito, *Nat. Commun.* **2015**, *6*, 8140.
Re system: M. Naruto, S. Agrawal, K. Toda, S. Saito, *Sci. Rep.* **2017**, *7*, 3425.

Feature article: S. Yoshioka, S. Saito, *Chem. Commun.* **2018**, *54*, 13319.

3. Design of diphosphine ligands

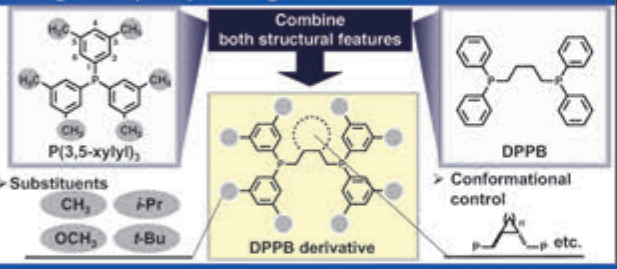

4. Effect of substituents of Ar groups on P atoms

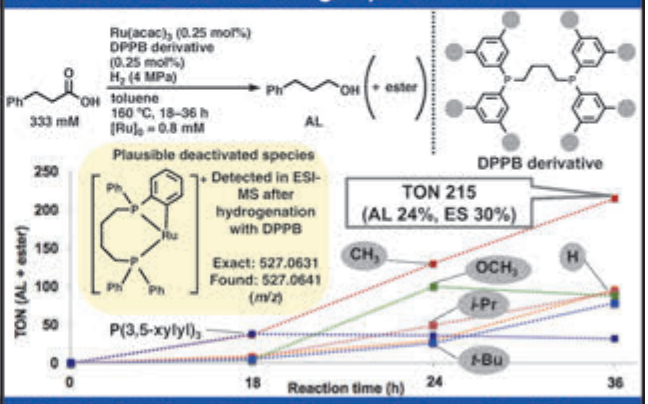

5. Effect of conformational change between two P atoms

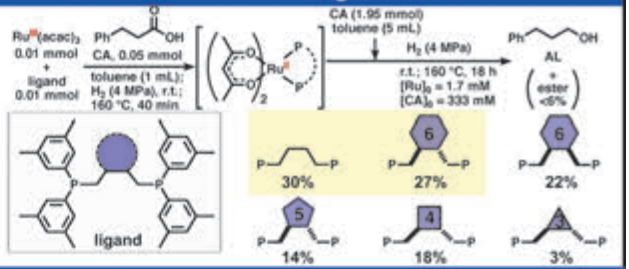

6. Hydrogenation using $Ru(OAc)_2(PP)$ as pre-catalyst

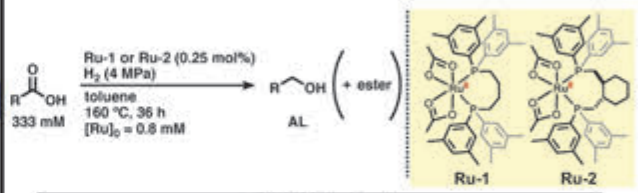

TON (AL + ester)	CA			
			H_2 (6 MPa)	(1.0 mol%, 18 h)
Ru-1	284	127	28	25
Ru-2	199	79	32	21

7. Plausible Mechanism of *CA Self-induced CA Hydrogenation*

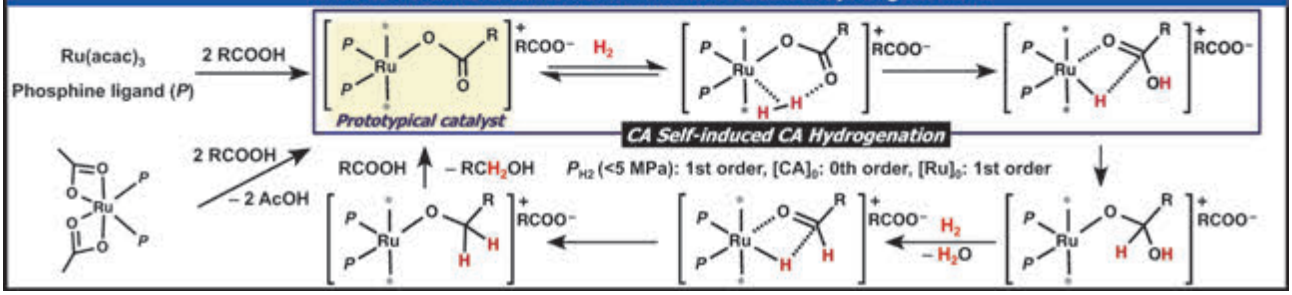

Formation of Xe 4d Double-Core-Hole States in Strong XUV-FEL Fields Studied by Electron-Ion Coincidence Spectroscopy

Y. Sasaki[1], H. Fujise[1], Y. Kawabe[1], K. Hashigaya[1], A. Matsuda[1], Y. Hikosaka[2], M. Fushitani[1], A. Hishikawa[1]
[1]*Nagoya University,* [2]*University of Toyama*

Introduction

Double-core-hole (DCH) states for chemical analysis

- Auger Electron Spectroscopy(AES)
  B. R. Stoner *et al.*, Phys. Rev. B. **45**, 11067(1992).

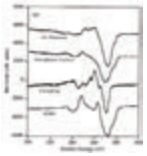

e.g. surface analysis

✓ Provides chemical bonding information

- Double-Core-Hole (DCH) states
  L. S. Cederbaum *et al.*, J. Chem. Phys. **85**, 6513 (1986).

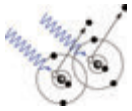

DCH { Single-site DCH (ssDCH) / Two-site DCH (tsDCH)

- Theory
  M. Tashiro *et al.*, J. Chem. Phys. **132**, 184302(2010).

Kinetic energy release of core hole relaxation

	SCH	ssDCH	tsDCH
C_2H_6	305.897 eV	651.265 eV	598.281 eV
C_2H_6	305.040 eV	649.714 eV	591.447 eV
Δ	0.857 eV	1.551 eV	6.834 eV

✓ High sensitivity to the nuclear arrangement

- Experiment
  P. Salén *et al.*, Phys. Rev. Lett. **108**, 153003(2012).
  N. Berrah *et al.*, PNAS 108, 41, 16912(2011).

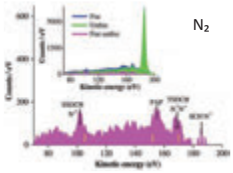

N_2

DCH signals are hidden

Electron-ion coincidence technique

Electrons labeled with corresponding ions

Detection of Xe 4d DCH states induced from two-photon absorption by electron-ion coincidence spectroscopy

This work

Experiment

Magnetic bottle type electron-ion coincidence spectrometer

A. Matsuda *et al.*, Rev. Sci. Instrum. **82**, 103105(2011).

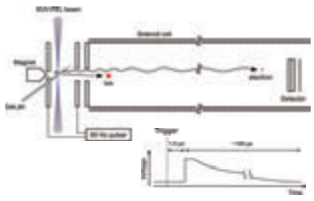

- ✓ High e^- collection efficiency suppress space charge effect
- ✓ e^- from small area reduce BG signal
- ✓ Long flight tube (1.5 m) $E/\Delta E \sim 50$

Event rate : 0.254 events/shot

- True coincidence rate (Xe^{4+})

$$\frac{N_C}{N_C + N_F} \sim 0.84$$

SACLA (SPring-8 Angstrom Compact free electron LAser)

- ✓ High coherence
- ✓ fs scale time resolution
- ✓ Soft X-ray ~ X-ray region

Experiment condition
Photon energy : 91 eV
Pulse energy : 65 μJ
Repetition frequency : 60 Hz
Pulse width : ~ 88 fs

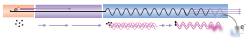

Pulse width measurement

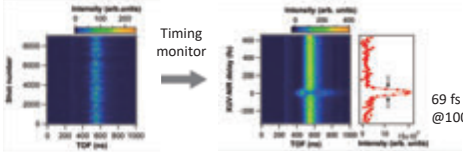

Timing monitor

69 fs (cross correlation) @100 eV

Results and discussion

Xe nonlinear ionization processes

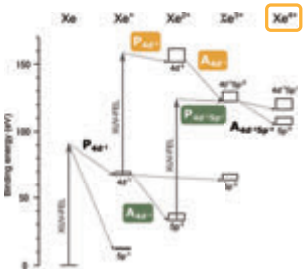

1st photon absorption
Xe 4d giant resonance (~ 20 Mb)
Xe + *hν* (91 eV) → $Xe^+(4d^{-1}) + e^-$

2nd photon absorption
DCH
$Xe^+(4d^{-1}) + h\nu \rightarrow Xe^{2+}(4d^{-2}) + e^-$
Sequential SCH
$Xe^{2+}(5p^{-2}) + h\nu \rightarrow Xe^{3+}(4d^{-1}5p^{-2}) + e^-$

Time of flight spectrum

$Xe^+ : Xe^{2+} : Xe^{3+} : Xe^{4+} = 0.11 : 1 : 0.37 : 0.038$
A. A. Sorokin *et al.*, Phys. Rev. Lett. **99**, 213002(2007).

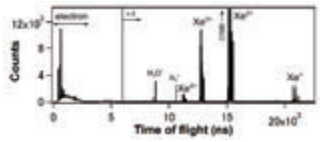

e^--ion coincidence map

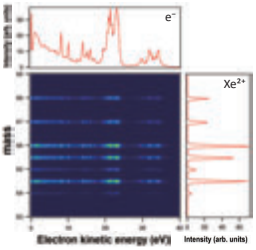

e^--ion coincidence

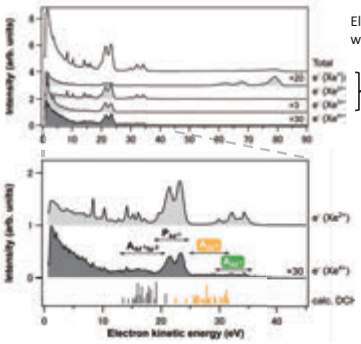

Electron spectra in coincidence with $Xe^+ \sim Xe^{4+}$ ions

Single-photon
Multi-photon

e^- (Xe^{2+})
Good agreement with synchrotron studies
J. Viefhaus *et al.*, J. Phys B. **38**, 3885(2005).

e^- (Xe^{4+})
Cannot be described only by sequential SCH processes
➡ Suggestion of 4d DCH states formation

e^--e^--ion coincidence

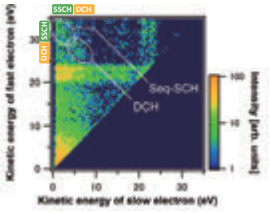

From count ratios,
(DCH) : (Sequential SCH) = 1 : 1.68(4)

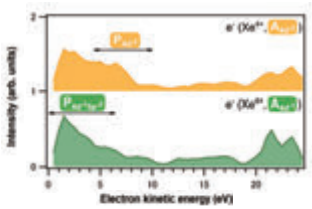

Correlation between electrons from DCH and Sequential SCH processes

Distinguished Xe 4d DCH states from sequential SCH

Simulations

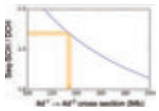

- Estimation of 2-photon DCH cross section
  Branching ratio (sequential SCH / DCH)
  ↓ Coupled rate equation
  σ(DCH) = 135(3) Mb
  Resonance to Rydberg states converging to DCH states?

U. Becker *et al.*, Phys. Rev. A. **39**, 8, 3902(1989).
P. Andersen *et al.*, J. Phys. B. **34**, 2009(2001).

Summary

- ✓ Observation of Xe 4d DCH states competing with sequential SCH processes
  ➡ Electron-ion coincidence spectroscopy
  Branching ratio (DCH) : (Sequential SCH) = 1 : 1.68(4)
  Outlook : Apply to molecular samples (e.g. CH_3I, $C_6H_4I_2$)

In situ XAFS imaging of redox-active ceria particles with transition metals

Kouhei Wakamatsu,[1,2] Hirosuke Matsui,[1,2] Nozomu Ishiguro,[2] Satoshi Muratsugu,[1,3] Mizuki Tada,[1,2]

[1]Nagoya University [2]RIKEN/SPring-8 [3]JST PRESTO

Introduction and purpose

Ceria (CeO_2): oxygen storage/release material

- Water gas shift reaction catalyst
- Three-way catalyst

$CeO_2 \leftrightarrow CeO_{2-\delta} + \delta/2\ O_2$ (more than 723 K)

Many candidates of metal-doped/supported ceria are proposed.

In our research group

$Ce_{0.80}Cr_{0.15}Rh_{0.05}O_X$

- Oxygen release at low temperature (373 K)
- Reversible oxygen storage and release

Purpose: For understanding redox mechanism of $CeCrRhO_X$ system at lower temperature, *in situ* spatial-resolved XAFS technique was applied to newly prepared micron-sized $CeCrRhO_X$ particles.

Preparation

$(NH_4)_2[Ce(NO_3)_6]$ 300 mg (550 μmol)
$Cr(NO_3)_3 \cdot 9H_2O$ 39.8 mg (99 μmol)
$RhCl_3 \cdot 3H_2O$ 1.22 mg (4.6 μmol)
dissolved in 30 mL distilled water

Diethanolamine aq. 2.6 M, 40 mL
Urea 0.6 g
stirring in ice bath (30 min.~)

hydrothermal synthesis 443 K, 72 K
autoclave

vacuum filtration → vacuum drying → calcination 773 K, 6 h

$Ce_{0.91}Cr_{0.093}Rh_{0.00046}O_X$
*determined by ICP-OES

Image of optical microscope

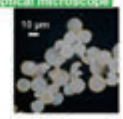

TEM

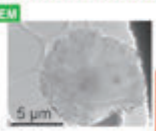

- micron-sized particles (>10 μm)
- disk-shaped morphology

Structural analysis

XRD

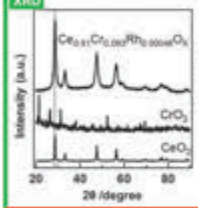

Raman

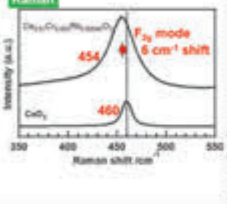

- $CeCrRhO_X$ had similar crystal structure of CeO_2 (XRD).
- Existence of oxygen defect was suggested by shifting CeO_2 F_{2g} mode (Raman spectroscopy).

TEM

FFT of TEM images

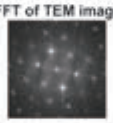

N_2-BET

	Specific surface area /$m^2\ g^{-1}$
$Ce_{0.91}Cr_{0.093}Rh_{0.00046}O_X$	112
Commercial CeO_2 (Aldrich) (particle size < 25 nm)	27

- (111) termination was confirmed by FT-TEM diffraction.
- However, polycrystalline structure was confirmed in part.
- Higher specific surface area

STEM-EDS

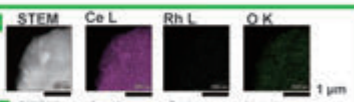

STEM-EELS

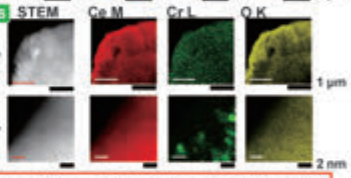

- Cr and Rh were highly dispersed in CeO_2 bulk.
- However, Cr forms domain within 1 nm size.

Redox performance

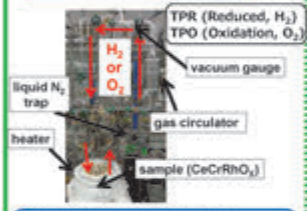

- Closed-batch reactor system
- Sample was heated from r.t. to 623 K at 5 K min^{-1} step.
- Consumption of O_2 or H_2 was monitored by vacuum gauge.

as-prepared → pretreatment TPR → 1st TPO → 1st TPR → 2nd TPO → 2nd TPR

H_2-TPR (oxygen release process)

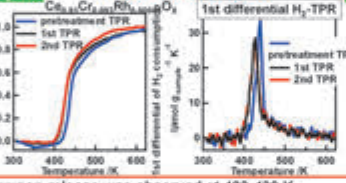

O_2-TPO

$Ce_{0.91}Cr_{0.093}Rh_{0.00046}O_X$

O_2 consumption [mmol g_{sample}^{-1}]

	293 K	< 623 K
1st TPO	0.42	0.48
2nd TPO	0.39	0.55
average	0.41	0.51

oxygen storage process

- Oxygen release was observed at 423-439 K.
- The temperature of oxygen release was lower than those of CeO_2 (more than 723 K) or $CeCrO_3$ (630 K).
- At least, two types of oxygen storage were found at r.t. and during heating within 623 K.
- Reversible oxygen storage and release was confirmed.

TPR results of $CeCrRhO_Y$ with different Cr and Rh doping amounts

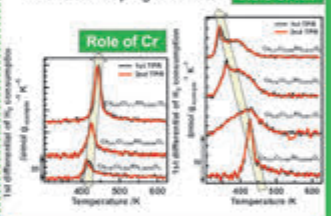

Cr controls the amount of redox amount while Rh decreased redox temperature.

Chemical state changes of Ce and Cr under Redox process

In situ Ce L_{III} and Cr *K*-edge quick-XAFS measurements were conducted during H_2-TPR and O_2-TPO reactions.

($Ce_{0.91}Cr_{0.093}Rh_{0.00046}O_X$, 100 mL min^{-1} H_2 or O_2 flow, Heating at 5K min^{-1} step from r.t. to 623 K)

as-prepared → pretreatment TPR, TPO
TPR: H_2 r.t.-623 K
TPO: O_2 r.t.-623 K

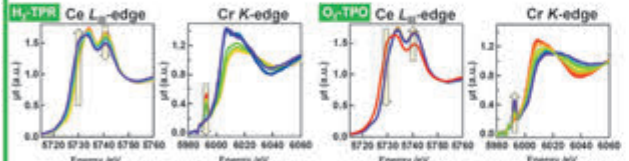

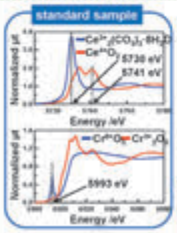

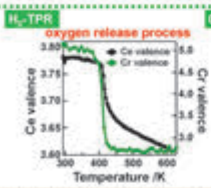

- In the oxygen release process, Cr and Ce were simultaneously activated at 400 K but the oxygen diffusion was selectively enhanced in Cr.
- In the oxygen storage process, the oxidation of Ce was completed at r.t. but that of Cr required higher temperature.

I_{Ce} fitting = $a \times I_{Ce3+} + (1-a) \times I_{Ce4+}$ (5737.5-5750 eV)
I_{Cr} fitting = $a \times I_{Cr3+} + (1-a) \times I_{Cr6+}$ (5989-5996.5 eV)

2D map of Ce valence in particles

Ce L_{III}-edge imaging-XAFS

- Focused X-rays were irradiated onto sample.
- Transmitted X-rays were imaged by FZP and 2D-X-ray detector.
- Measured at Ce L_{III}-edge E = 5650-5800 eV (154 pts)

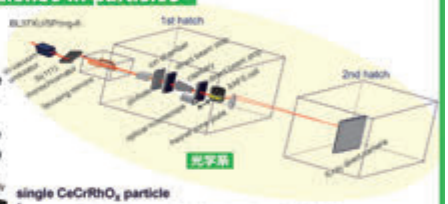

single $CeCrRhO_X$ particle

154 energy points at Ce L_{III}-edge

- Spatially-resolved Ce L_{III}-edge XANES spectra was obtained at each pixel.
- Ce valence was estimated by LCF method.

Ce L_{III}-edge μt images

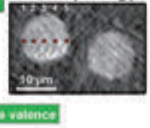

Ce morphology

XANES fitting at typical points

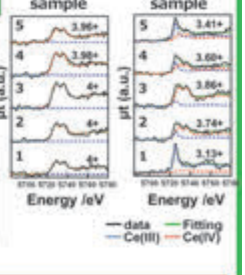

Mappings of Ce valence

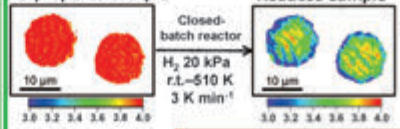

- Property of stoichiometric redox between Ce^{3+} and Ce^{4+} was observed near the surface.

Redox mechanism

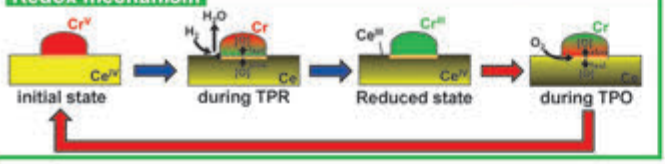

Conclusion

- Micron-sized ceria particle with Cr and Rh, which shows a high redox activity, was newly prepared and their oxygen release and storage mechanism were discussed.
- Through *in situ* XAFS measurements, it was found that Ce required a higher temperature to diffuse oxygen in TPR, but for TPO, the reaction was rapidly completed at r.t.
- Through Ce L_{III}-edge imaging-XAFS measurements, the activated area was limited near the CeO_x surface but the stoichiometric redox was observed.

Synthesis of Dinuclear Mo-Fe Hydride Complexes for the Catalytic Silylation of N_2

Kodai Ishihara,[1] Yuna Araki,[1] Mizuki Tada,[1] Yoichi Sakai,[2] Yasuhiro Ohki[1]

[1]Graduate School of Science and Research Center for Materials Science, Nagoya University, Furocho, chikusa-ku, Nagoya 464-8602, Japan,
[2]Department of Chemistry, Daido University, Takiharu-cho, Minami-ku, Nagoya 457-8530, Japan

Introduction

N_2 activation by dinuclear hydride complexes

Michael D. Fryzuk et al., J. Am. Chem. Soc. 2001, 123, 3960.

FeMo-cofactor

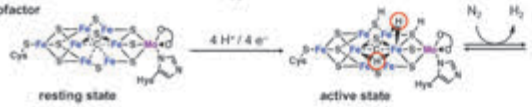

Fe, Mo, bridged hydride ligand

Previous work

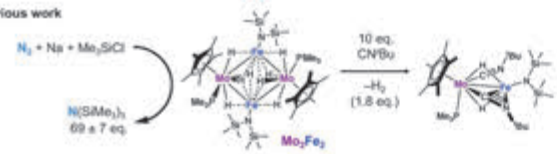

Synthetic strategy

Previous work
L = N(SiMe$_3$)$_2$

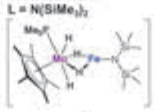

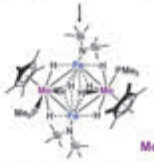

Y. Ohki et al., Chem. Eur. J. 2017, 23, 13240.

This work
L = C$_5$Me$_5$

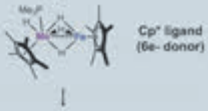

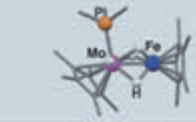

Synthesis and characterization of the Mo-Fe hydride complexes

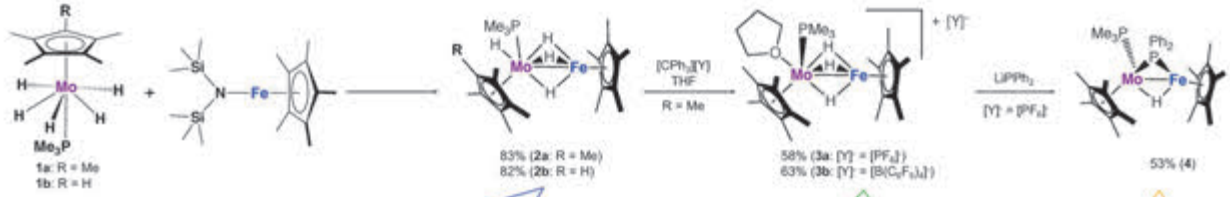

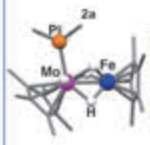

Bond lengths (Å)

Mo-Fe	2.4004(4)
Mo-P	2.4526(6)
Mo-H-Fe	1.76(4)-2.00(4)
Mo-H	1.79(3)
Mo-H-Fe	1.59(4)-1.67(3)

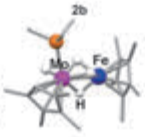

Bond lengths (Å)

Mo-Fe	2.3951(4)
Mo-P	2.4357(6)
Mo-H-Fe	1.82(2)-1.85(2)
Mo-H	1.65(2)
Mo-H-Fe	1.56(2)-1.64(2)

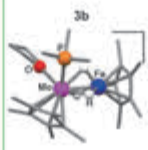

Bond lengths (Å)

Mo-Fe	2.4067(10)
Mo-P	2.5006(18)
Mo-H-Fe	1.81(6)-1.98(6)
Mo-H-Fe	1.41(8)-1.69(6)

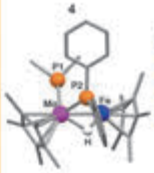

Bond lengths (Å)

Mo-Fe	2.4321(13)
Mo-P1	2.4021(19)
Mo-P2	2.3181(15)
Mo-H	1.87(10)
Fe-H	1.53(8)

^{1}H NMR spectrum

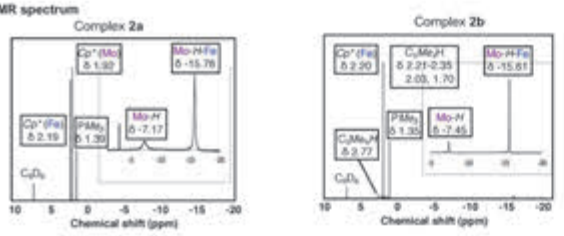

^{57}Fe Mössbauer spectrum

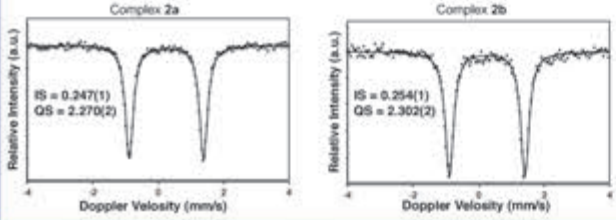

Mo-PMe$_3$ bond lengths (Å)
2a: 2.4526(6)
2b: 2.4357(6)
3b: 2.5006(18)

Mo(IV)-PMe$_3$: 2.4336(5)-2.546(5)

Oxidation states of complexes 2a, b and 3b: Mo(IV)Fe(II)

- ^{57}Fe Mössbauer spectrum: Low spin Fe(II) state
- Mo-PMe$_3$ bond length: Mo(IV)

Catalytic N_2 silylation

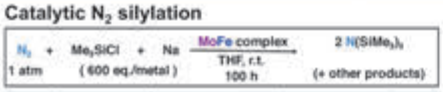

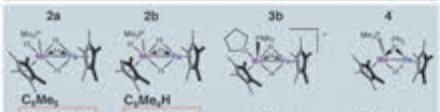

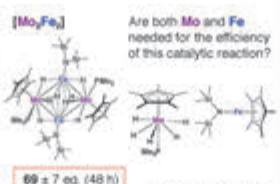

Are both Mo and Fe needed for the efficiency of this catalytic reaction?

Y. Ohki et al., Chem. Eur. J. 2017, 23, 13240.

Summary

- ✓ MoFe hydride complexes **2a, b** were obtained via deprotonation of a half-sandwich Mo(VI) pentahydride complex **1a, b** by Cp*Fe(N(SiMe$_3$)$_2$).
- ✓ Cationic complexes **3a, b** were obtained by removal of a hydride ligand from **2a** using trityl cation.
- ✓ Phosphide-bridged complex **4** was obtained by the reaction of **3a** with LiPPh$_2$.
- ✓ The oxidation states of clusters were analyzed as Mo(IV)Fe(II) based on the Mo-PMe$_3$ distances and the ^{57}Fe Mössbauer spectrum of **2a, b** and **3b**.
- ✓ MoFe complexes **2a, b - 4** were subjected to the dinitrogen silylation reactions, giving up to 128 equiv. of N(SiMe$_3$)$_3$ based on the dinuclear complex.

Direct Hydroxylation of Gaseous Alkane by Cytochrome P450 under High-pressure Condition

Yusaku Kodama[1], Shinya Ariyasu[1], Osami Shoji[1,2], Yoshihito Watanabe[3]
[1]Department of Chemistry, Graduate School of Science, Nagoya University, [2]CREST, Japan Science and Technology Agency, [3]Research Center for Materials Science, Nagoya University

Introduction

◆ **P450BM3**

Enzyme that efficiently hydroxylates fatty acids by consuming NADPH and O_2

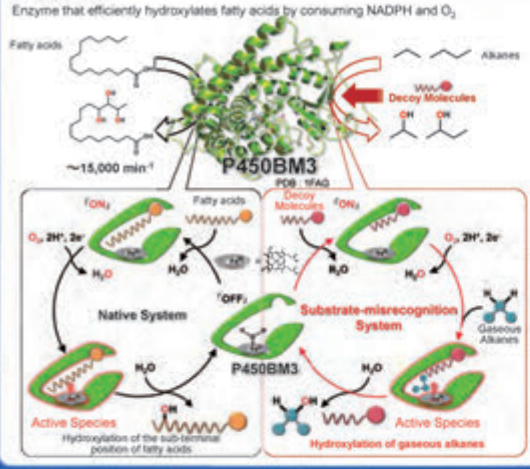

◆ **The Active Site of P450BM3**

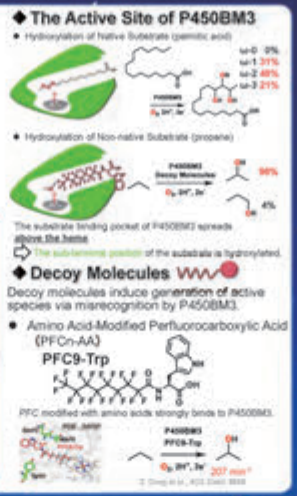

◆ **Decoy Molecules**

Decoy molecules induce generation of active species via misrecognition by P450BM3.

- Amino Acid-Modified Perfluorocarboxylic Acid (PFCn-AA)

PFC9-Trp

Motivation

Gaseous Alkane Hydroxylation under Mild Conditions using Enzymes

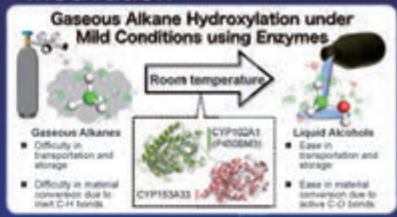

Research Aim

Improvement of hydroxylation activity by increasing the concentration of gaseous alkanes

The concentration of gaseous alkanes increases depending on its pressure.

Hydroxylation reaction system of gaseous alkanes under high pressure was constructed

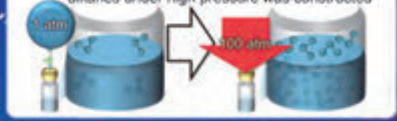

Experiments

◆ **Development of the High Pressure Reactor (HPR)**

Developed an equipment that can pressurize up to 100 atm easily and safely

- Construction of the HPR

- How to Pressurize

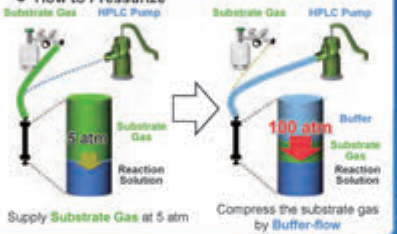

Conclusion

Hydroxylation of Propane by P450BM3

- Improvement of the reaction efficiency was achieved by high pressure condition using the high pressure reactor.
- The turnover frequency (TOF) of 2-propanol conversion reached 2193 min^{-1} under high-pressure condition.
- The total turnover number (TON) of 2-propanol conversion under high-pressure condition exceeded 10,000.

Hydroxylation of Propane by CYP153A33

- Application of substrate-misrecognition system to CYP153A33 was achieved.
- Depending on the structure of the substrate binding pocket of CYP153A33, 1-propanol was selectively produced.
- The propane hydroxylation activity will be improved by optimizing decoy molecules and high-pressure reaction conditions.

Results and Discussion

Hydroxylation of Propane by P450BM3

C-H Bond Dissociation Energy (BDE)

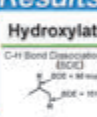

Concentration of Propane in Buffer: 1 atm, 2.8 mM → 100 atm, 12 mM* (*Saturation at 5 atm)

■ **Utility of High Pressure Reactor**

● Reaction Conditions

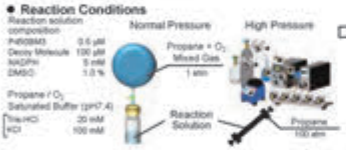

● Structure of Decoy Molecules

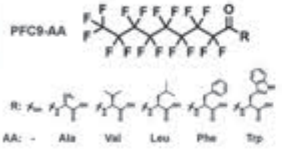

● Comparison of TOF of 2-Propanol Conversion at Normal Pressure (1 atm) and High Pressure (100 atm)

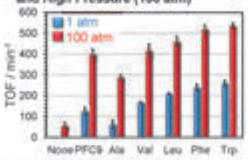

✓ The activity was improved about 2-folds at 100 atm using a novel high pressure reactor.

■ **Pressure Dependence of Hydroxylation Activity**

● Reaction Conditions

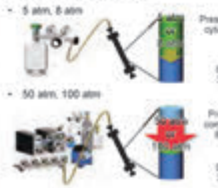

● TOF of 2-Propanol Conversion at Each Pressure Condition

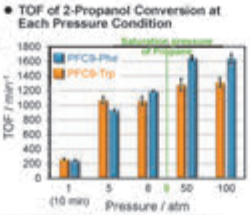

✓ Improvement of TOF was observed depending on the propane concentration in the reaction solution.

■ **The Time Course of the Reaction**

● 2-Propanol Concentration at Each Time Point

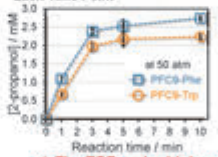

● The TOF Estimated by 1 min Reaction

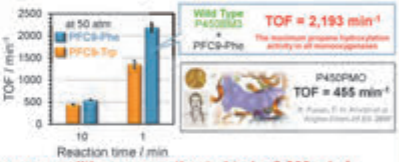

✓ The TOF under high-pressure conditions was estimated to be 2,200 min^{-1} by investigating the time course of the reaction.

■ **Optimization of the Long-time Reaction Conditions**

● Reaction Conditions & Total Turnover Number (TON)

P450BM3 / μM	Pressure / atm	NADPH / mM	PFC9-Phe / μM	Reaction time / h	TON
0.05	50	10	10	0.5	3,762
0.1	100	10	50	1.5	4,050
0.2	50	10	50	**0.5**	**11,227**
0.2	50	10	50	**1.5**	**10,220**
0.2	50	20	50	**12**	**10,655**

P450PMO TON = 45,800

TON is almost the same regardless of reaction time. ⇨ It is caused by depletion of NADPH.

✓ It is necessary to optimize the reaction conditions to exceed the TON of P450PMO.

Hydroxylation of Propane by CYP153A33

■ **The Active Site of CYP153A33**

● Hydroxylation of Native Substrate (lauric acid)

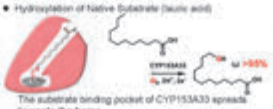

The substrate binding pocket of CYP153A33 spreads towards the heme.
The terminal position of the substrate is hydroxylated.

● Application of Substrate-misrecognition System to CYP153A33

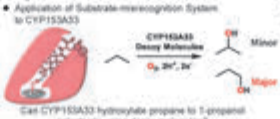

Can CYP153A33 hydroxylate propane to 1-propanol selectively using decoy molecules?

■ **Design and Expression of CYP153A33-BMR**

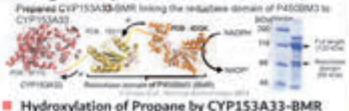

■ **Hydroxylation of Propane by CYP153A33-BMR**

GC Chromatogram

Decoy Molecule : PFC8-Trp
Pressure Condition : 1 atm

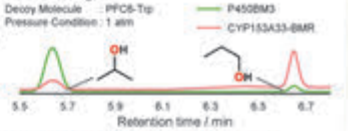

✓ Application of substrate-misrecognition system to CYP153A33 and 1-propanol selective hydroxylation were achieved.

Chemically -Modified Peptide Nucleic Acids for *in cellulo* Applications

○Yuichiro Aiba[a], Masaki Hibino[a], Gerardo Urbina[a], Yuuki Ochiai[a], Naomi Kochi[a], Masanari Shibata[a], Osami Shoji[a], Yoshihito Watanabe[b]

[a]Department of Chemistry, Graduate School of Science, Nagoya University; [b]ResearchCenter for Materials Science, Nagoya University

Research Goal

Controlling DNA function *in cell* or *in vivo*

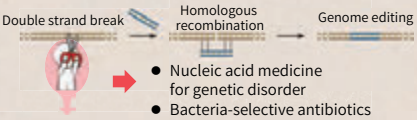

- Nucleic acid medicine for genetic disorder
- Bacteria-selective antibiotics

Efficient dsDNA recognition in cells is essential

Summary

- Optimization of Ru-complex introduction to PNA
- Enhanced invasion efficiency even under physiological conditions
- Photocleavage of dsDNA by Ru-PNA

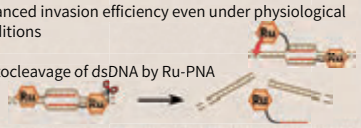

Background

PNA (Peptide Nucleic Acid)

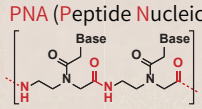

- peptide backbone
  - high DNA affinity due to the lack of electrostatic repulsion
- duplex stability: PNA/DNA >> DNA/DNA

DNA

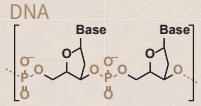

A pair of PNA can undergo a unique DNA recognition mode "**double-duplex Invasion**"

Invasion

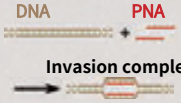

A pair of PNAs invade into dsDNA and form an invasion complex without a prior DNA denaturation

J. Lohse, *et al. Proc. Natl. Acad. Sci.*, **1999**, *96*, 11804.

Problem to solve

- Improvement of invasion efficiency under physiological conditions
  - high salt concentrations stabilize DNA/DNA duplex, but destabilize PNA/DNA duplex

Development of "Ru-PNA"

(Ru-complex/PNA conjugate)

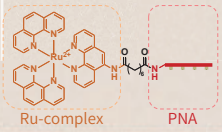

1. Improving DNA affinity
2. Photo cleavage of DNA

E. Yavin, *et al. J. Inorg. Biochem.*, **2004**, *98*, 1750.

Synthesis of Ru-PNA

Synthesis of Ru-complex

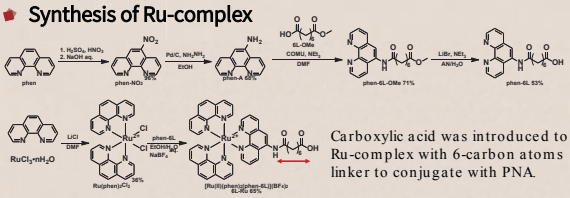

Carboxylic acid was introduced to Ru-complex with 6-carbon atoms linker to conjugate with PNA.

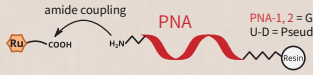

PNA-1, 2 = GUUDCUGDUG, CDUCDGUDDC (10-mer)
U-D = Pseudo-complementary A-T pair

Optimization of Ru-complex modification

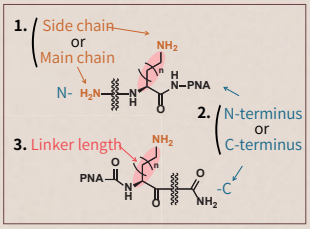

Optimization

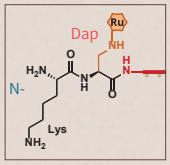

Ru-PNA

1. Side chain
2. N-terminus
3. Dap (n = 1)

The most effective Ru-complex modification for the PNA invasion

*Dap: 2,3-diaminopropionic acid

Results

Identification of Ru-PNA

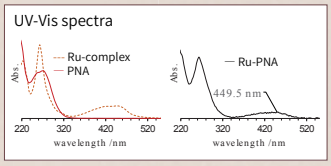

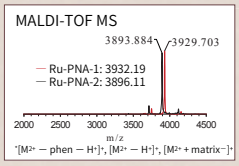

UV spectra: Ru-PNA ≈ Ru-complex + PNA

T_m (melting temperature of duplex)

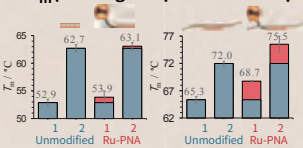

additional 10-mer DNAs at the both ends
→ + 3.4 °C increase

It is indicated that Ru-complex interacts with DNA on the outer region of PNA binding site.

Conditions: [DNA] = [PNA] = 1 μM, [HEPES (pH 7.0)] = 5 mM, [NaCl] = 12 mM, [KCl] = 139 mM, [$MgCl_2$] = 0.8 mM

Invasion under physiological conditions

- 130-bp DNA: 50 nM
- PNA: n eq. of DNA
- HEPES: 5 mM (pH7.0)

+ physiological conditions
- Na^+: 12 mM
- K^+: 139 mM
- Mg^{2+}: 0.8 mM

Overnight incubation at 37 °C

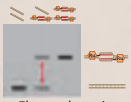

Electrophoresis mobility shift assay

physiological conditions

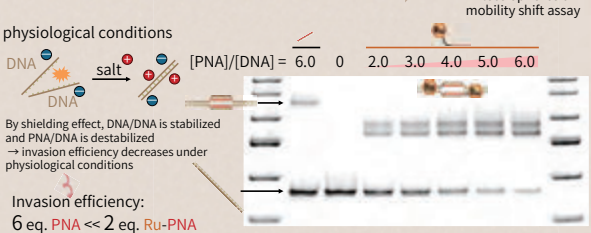

By shielding effect, DNA/DNA is stabilized and PNA/DNA is destabilized
→ invasion efficiency decreases under physiological conditions

Invasion efficiency:
6 eq. PNA << 2 eq. Ru-PNA

Ru-PNA showed more than 70% improvement of invasion efficiency

The conjugation of PNA with Ru-complex improved its invasion efficiency even under physiological conditions.

Photoreactivity of Ru-PNA to DNA

- 130-bp DNA: 50 nM
- PNA: *n* eq. of DNA
- HEPES(pH7.0): 5 mM
- 100 mM NaCl

Incubation at 50 °C for 2 h

In dark or 80 mW/cm² 450 nm at 4 °C for 2 h

Mismatch 130-bp DNA:
Single-base mismatch forming G-G base pair

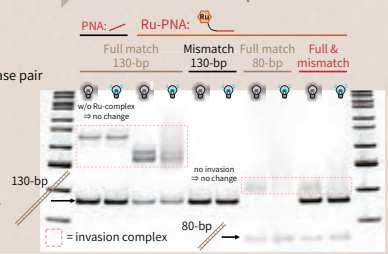

- No invasion with mismatch DNA
- Photocleavage only occurs to the invasion complex

Ru-PNAs discriminate single-base mismatch and cause the light-induced DNA damage sequence-specifically

References - M. Hibino, Y. Aiba,* Y. Watanabe, and O. Shoji* *ChemBioChem*, **2018**, *19*, 1601.

Development of 2′-modified Nucleoside Alalogs as Antiviral Agents

○ Hideo Katakura[1)], Yushi Niimi[1)], Tetsuro Suzuki[2)], Ayato Takada[3)], Tsutomu Murakami[4)], Eiichi Kodama[5)], Yasuaki Kimura[1)], Hiroshi Abe[1)]
[1)]Nagoya University, [2)]Hamamatsu University School of Medicine, [3)]Hokkaido University, [4)]National Institute of Infectious Diseases, [5)] Tohoku University

Introduction

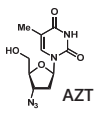

AZT

- conventional inhibitor
- competitive inhibition

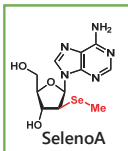

SelenoA

Pro SelenoA

Patent JP2018-043329

Design, synthesis and evaluation of a potential irreversible inhibitor for several virus polymerases

Possible mechanism

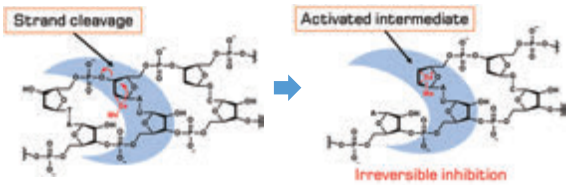

Target-specific and strong inhibitor for viral polymerases

Results

◇Inhibition of reverse transcription

5′-[FAM]- G G T G G A C T T T C G C -3′
3′- C C A C C U G A A A G C G U G C A G C A -5′

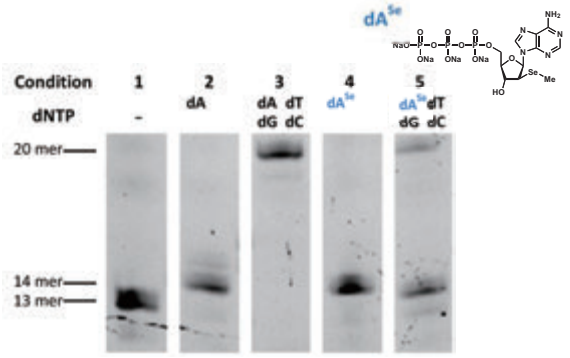

20% dPAGE (7.5 M Urea, 1×TBE, 7.5% formamide), Analysis by fluorescence
Reaction solution (template RNA 0.2 μM, primer DNA 0.2 μM, 100 μM each dNTP, Tris-HCl (pH 8.3) 2.5 mM, KCl 5 mM, DTT 0.2 mM, 0.5 mM $MgCl_2$, AMV RT 0.1 U/μL)

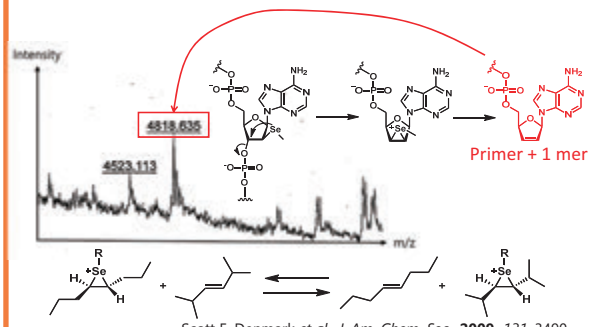

Scott E. Denmark *et al., J. Am. Chem. Soc.*, **2009,** *131*, 3490

◇Irreversible inhibition

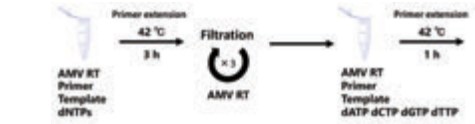

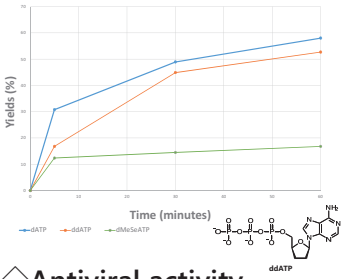

Reaction solution (template RNA 0.2 μM, primer DNA 0.2 μM, 100 μM each dNTP, Tris-HCl (pH 8.3) 2.5 mM, KCl 5 mM, DTT 0.2 mM, 0.5 mM $MgCl_2$, AMV RT 0.1 U/μL) was incubated for 3 hours and the enzyme was purified by Microcon 100K. After purification, the reaction was carried out on the same condition for 1 hour.

◇Antiviral activity

Anti-HBV activity

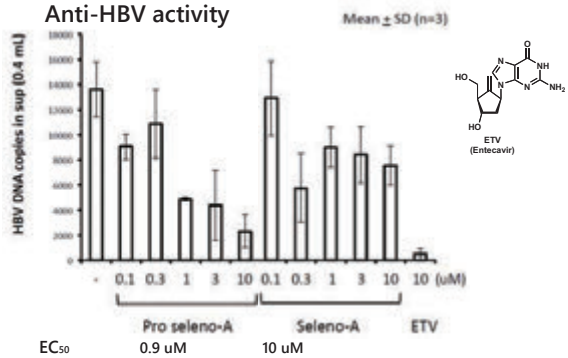

EC_{50} 0.9 uM 10 uM

Anti-HIV activity (MT4 cell MTT assay)

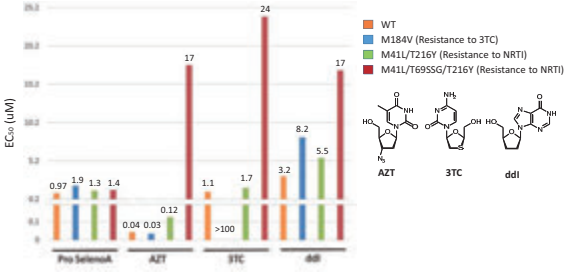

Pro SelenoA is durable to various durg-resistance mutants.

Prospect

- Investigation on inhibition mechanism
- Evaluation of other antiviral activity
- Synthesis and evaluation of analogues with other nucleobases

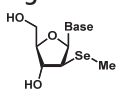

Base = Guanine, Cytosine, Thymine

化合物に関するお問い合わせ E mail : h-abe@chem.nagoya-u.ac.jp

Synthesis and Evaluation of Covalent GST Inhibitors with Improved Cell Permeability

Haruka Fujikawa[1,2], Yuko Shishido[1,3], Yasuaki Kimura[1], Fumiaki Tomoike[1], Yuko Murakami-Tonami[4], Masahiro Aoki[2,5], Hiroshi Abe[1]
[1] Nagoya University, [2] Nagoya City University, [3] Hokkaido University, [4] Juntendo University, [5] Aichi Cancer Center

1. Introduction

GST : Glutathione *S*-transferase

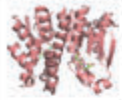

- Catalyze the conjugation of glutathione (GSH) to a wide variety of hydrophobic and electrophilic compounds in phase-II metabolism.
- Involved in detoxification of xenobiotics (Fig.1) and suppression of apoptosis, causing drug resistance and cell proliferation in cancer cells.

→GST inhibition is a promising approach to cancer.

- Since existing GST inhibitors are competitive inhibitors, high concentrations are required to obtain sufficient inhibitory activity.
- We have developed a covalent inhibitor GS-ESF which is expected to have potent inhibitory activity. (Fig. 2)
- A sulfonyl fluoride group was introduced as a reactive functional group for tyrosine, which is an active residue of GST, at the cysteine residue end of GSH.
- However, GS-ESF had poor cell membrane permeability. Therefore, in order to increase cell membrane permeability, covalent inhibitors based on small molecules were developed.

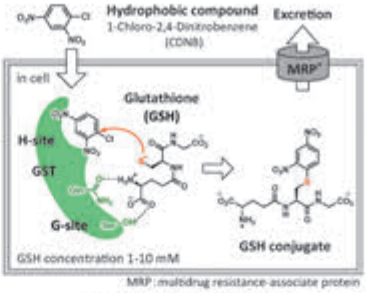

Fig. 1 Detoxification mechanism

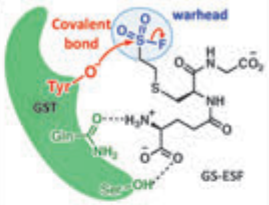

Fig. 2
Novel GST inhibitor

Ref.) Chem. Commun., 2017, 53, 11138.

2. Inhibitor design

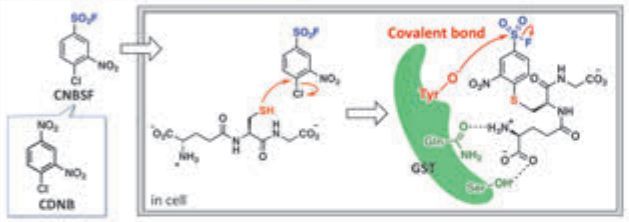

- We developed a covalent inhibitor based on CDNB.
- CNBSF reacts with GSH *in cell* to become GSH conjugate and occupys G-site. The sulfonyl fluoride group and tyrosine would form a covalent bond and inhibit GST activity.

3. Result of CDNB Derivative

IC_{50} assay

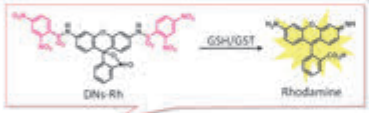

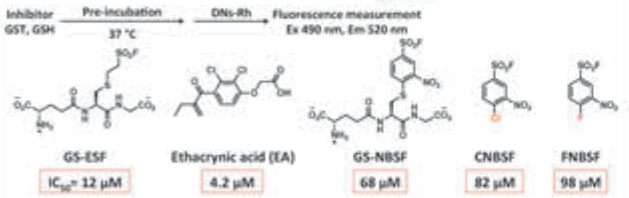

GS-ESF	Ethacrynic acid (EA)	GS-NBSF	CNBSF	FNBSF
IC_{50}= 12 μM	4.2 μM	68 μM	82 μM	98 μM

Reversibility assay

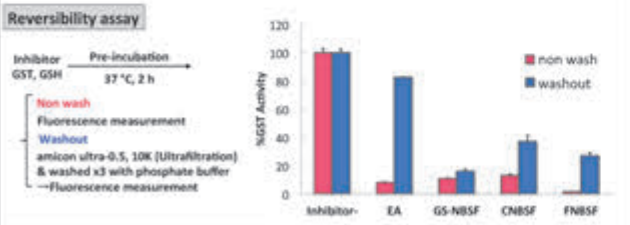

Intracellular GST inhibitory activity

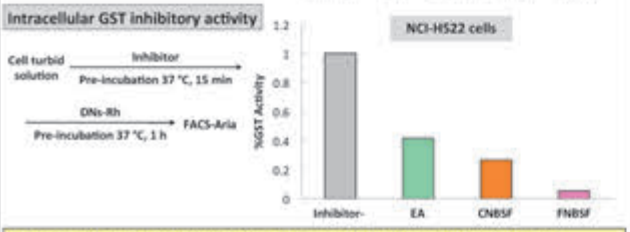

- The IC_{50} of the CDNB derivative was higher than that of EA and GS-ESF *in vitro*. However, their GST inhibitory activity greatly exceeded that of ethacrynic acid in cell.
- Both CNBSF and FNBSF were suggested to be irreversible inhibitors.

4. Result of CNBSF Derivative

- Derivatized CNBSF for further improvement of GST inhibitory activity.

IC_{50} assay

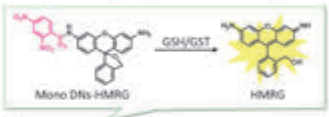

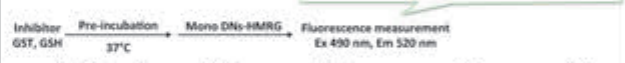

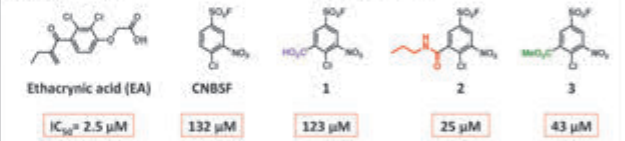

Ethacrynic acid (EA)	CNBSF	1	2	3
IC_{50}= 2.5 μM	132 μM	123 μM	25 μM	43 μM

Reversibility assay

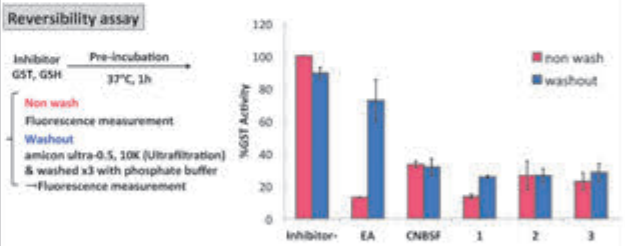

Cytocidal activity

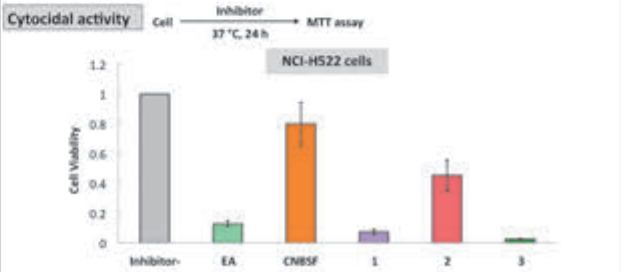

- The IC_{50} of compounds 2, 3 significantly exceeded that of CNBSF *in vitro*. It was also suggested that they were irreversible inhibitors.
- The cytocidal activity of compounds 1, 3 in cancer cells exceeded that of EA.

5. Conclusion

- We have developed small molecule based covalent inhibitor. Since the membrane permeability was improved, the inhibitory activity in cells was improved.
- The cytocidal activity of the CNBSF derivative exceeded that of EA. And it was suggested that all compounds were irreversible inhibitors.

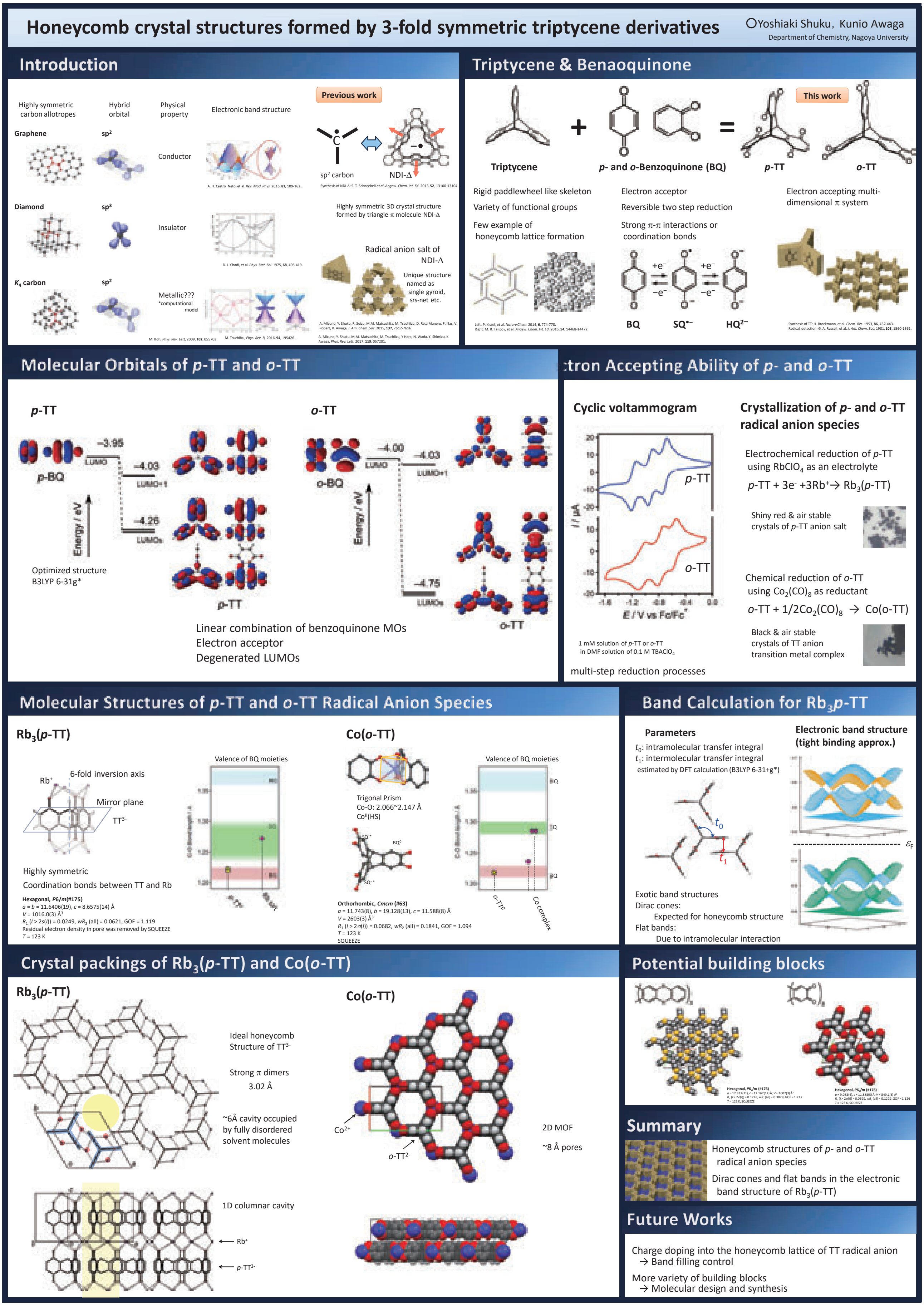
Honeycomb crystal structures formed by 3-fold symmetric triptycene derivatives
○Yoshiaki Shuku, Kunio Awaga
Department of Chemistry, Nagoya University
Introduction
Highly symmetric carbon allotropes
Hybrid orbital
Physical property
Electronic band structure
Previous work
Graphene
sp2
Conductor
sp2 carbon
NDI-Δ
Diamond
sp3
Insulator
Highly symmetric 3D crystal structure formed by triangle π molecule NDI-Δ
Radical anion salt of NDI-Δ
Unique structure named as single gyroid, srs-net etc.
K4 carbon
sp2
Metallic???
*computational model
Triptycene & Benaoquinone
Triptycene
p- and o-Benzoquinone (BQ)
This work
p-TT
o-TT
Rigid paddlewheel like skeleton
Variety of functional groups
Few example of honeycomb lattice formation
Electron acceptor
Reversible two step reduction
Strong π-π interactions or coordination bonds
Electron accepting multi-dimensional π system
+e−
−e−
BQ
SQ•−
HQ2−
Molecular Orbitals of p-TT and o-TT
p-TT
o-TT
p-BQ
o-BQ
LUMO
LUMO+1
LUMOs
Energy / eV
−3.95
−4.03
−4.26
−4.00
−4.75
Optimized structure
B3LYP 6-31g*
Linear combination of benzoquinone MOs
Electron acceptor
Degenerated LUMOs
Electron Accepting Ability of p- and o-TT
Cyclic voltammogram
I / μA
E / V vs Fc/Fc+
1 mM solution of p-TT or o-TT in DMF solution of 0.1 M TBAClO4
multi-step reduction processes
Crystallization of p- and o-TT radical anion species
Electrochemical reduction of p-TT using RbClO4 as an electrolyte
p-TT + 3e- +3Rb+→ Rb3(p-TT)
Shiny red & air stable crystals of p-TT anion salt
Chemical reduction of o-TT using Co2(CO)8 as reductant
o-TT + 1/2Co2(CO)8 → Co(o-TT)
Black & air stable crystals of TT anion transition metal complex
Molecular Structures of p-TT and o-TT Radical Anion Species
Rb3(p-TT)
Rb+
6-fold inversion axis
Mirror plane
TT3-
Highly symmetric
Coordination bonds between TT and Rb
Valence of BQ moieties
Co(o-TT)
Trigonal Prism
Co-O: 2.066~2.147 Å
CoII(HS)
Band Calculation for Rb3p-TT
Parameters
t0: intramolecular transfer integral
t1: intermolecular transfer integral
estimated by DFT calculation (B3LYP 6-31+g*)
Electronic band structure (tight binding approx.)
Exotic band structures
Dirac cones:
Expected for honeycomb structure
Flat bands:
Due to intramolecular interaction
Crystal packings of Rb3(p-TT) and Co(o-TT)
Rb3(p-TT)
Ideal honeycomb Structure of TT3-
Strong π dimers
3.02 Å
~6Å cavity occupied by fully disordered solvent molecules
1D columnar cavity
Rb+
p-TT3-
Co(o-TT)
Co2+
o-TT2-
2D MOF
~8 Å pores
Potential building blocks
Summary
Honeycomb structures of p- and o-TT radical anion species
Dirac cones and flat bands in the electronic band structure of Rb3(p-TT)
Future Works
Charge doping into the honeycomb lattice of TT radical anion
→ Band filling control
More variety of building blocks
→ Molecular design and synthesis

Highly-Porous Heteroatom-Doped Carbons Prepared by Salt-Assisted Pyrolysis of Covalent Organic Frameworks for High-Performance Supercapacitors

Dongwan Yan, Yang Wu, Kunio Awaga
Graduate School of Science, Department of Chemistry, Nagoya University, Japan

Introduction

Supercapacitors | Heteroatom-Doped Carbons | Method of Heteroatom-Doped Carbons | COFs

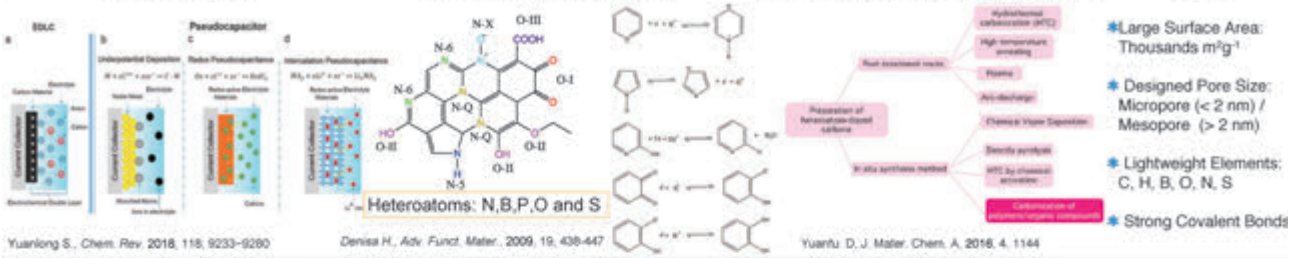

Yuanlong S., Chem. Rev. 2018, 118, 9233−9280 | Denisa H., Adv. Funct. Mater., 2009, 19, 438-447 | Yuanfu D, J. Mater. Chem. A, 2016, 4, 1144

Synthesis and Characteristic of Heteroatom-Doped Carbons

Synthesis of AQ-COF | Salt-Assisted Pyrolysis | 77K N_2 Sorption | Pore Distribution and Pore Volume

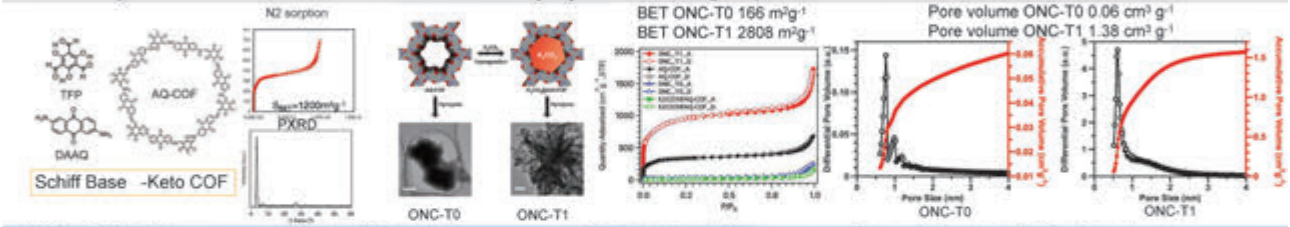

X-Ray Diffraction | Elemental analysis | Thermogravimetric | Energy Dispersive X-Ray Spectroscopy

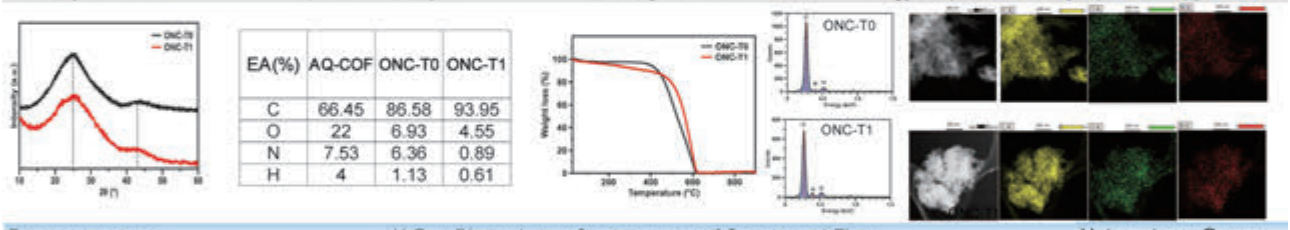

EA(%)	AQ-COF	ONC-T0	ONC-T1
C	66.45	86.58	93.95
O	22	6.93	4.55
N	7.53	6.36	0.89
H	4	1.13	0.61

Raman spectrum | X-Ray Photoeletron Spectroscopy of Survey and Fine | Heteroatoms Group

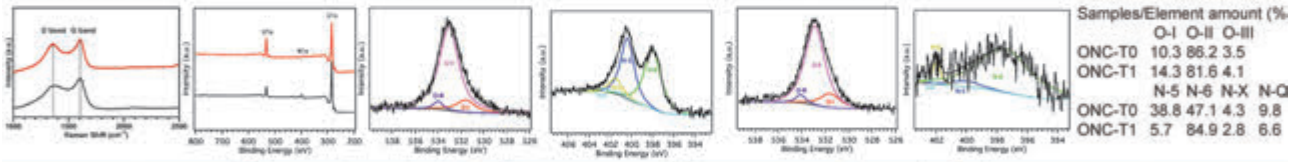

Samples/Element amount (%

	O-I	O-II	O-III	
ONC-T0	10.3	86.2	3.5	
ONC-T1	14.3	81.6	4.1	
	N-5	N-6	N-X	N-Q
ONC-T0	38.8	47.1	4.3	9.8
ONC-T1	5.7	84.9	2.8	6.6

Electrochemical Performance of Heteroatom-Doped Carbons

3-Electrode | Cyclic Voltammetry of different from 1mV s^{-1} to 1000 mV s^{-1} | EIS

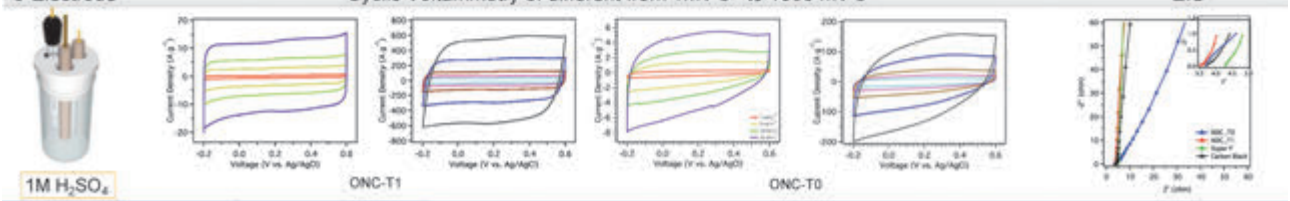

Galvanostatic Charge-Discharge GCD | Specific Capacitance and Cyclic Performance | Summary

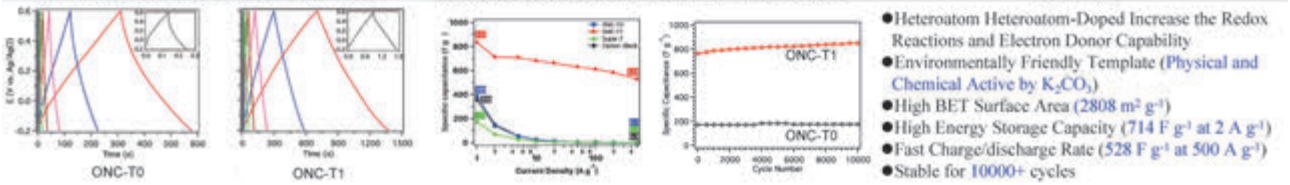

- Heteroatom Heteroatom-Doped Increase the Redox Reactions and Electron Donor Capability
- Environmentally Friendly Template (Physical and Chemical Active by K_2CO_3)
- High BET Surface Area (2808 $m^2 g^{-1}$)
- High Energy Storage Capacity (714 F g^{-1} at 2 A g^{-1})
- Fast Charge/discharge Rate (528 F g^{-1} at 500 A g^{-1})
- Stable for 10000+ cycles

Lead-Free Halide Perovskite: Effect of additive choice and solvent engineering on optical properties and solar cell performance

Tomoko Aharen, Taketo Handa, Takumi Yamada,
Atsushi Wakamiya, and Yoshihiko Kanemitsu
Institute for Chemical Research, Kyoto University

Introduction

C, Si, Ge, Sn, Pb

Pb Lead based perovskite solar cell
- Power Conversion Efficiency (PCE) >23%*
- Toxicity and Environmental impact

Primary solution to these problems:
Alternating with tin (Sn,Group14 element)
- similar ionic radii to lead ensures structural stability
- solubility to the major solvents such as DMF and DMSO

*https://www.nrel.gov/pv/assets/pdfs/pv-efficiencies-07-17-2018.pdf

Sn Lead free tin based perovskite solar cell
- Power Conversion Efficiency (PCE) <10 %
- Heavily doped nature of the perovskites

Driving back to favorable semiconductor
- Additive (SnF_2) assisted perovskite layer formation : excess tin and reducing

Approach to improving PCE :①Material quality ②Interfacial property etc.

For option ①: Use of other additives
$SnCl_2$: tin rich, moderate reducing, improving crystallinity (Cl ion)

Material Preparation and Characterization

One step spin-coating film fabrication (in N_2 filled glovebox)

$FAI + SnI_2 \xrightarrow[SnCl_2 \text{ additive}]{} FASnI_3$

Solvent: DMSO only or DMF/DMSO mixture
Annealing: Sequential 70℃→100℃

Antisolvent(tol) dripping assisted layer formation: ①Deposition → ②Tol drip → ③Anneal → ④Done!

Shiny mirror-like reflection (flat surface)

Spontaneous layer formation: ①Deposition → ②Anneal → ③Done!

Slow conversion from step 2 to 3, approx. a minute to convert fully to black film

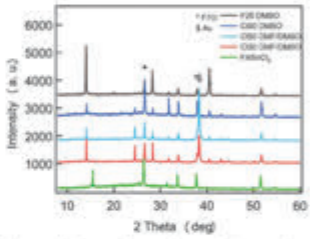

No impurity/secondary phases observed
→Iodide as ligand is stronger than chloride to form the halide perovskite

Optical Properties

<$FASnI_3$, SnF_2 20mol% or $SnCl_2$ 20,30 mol% addition>

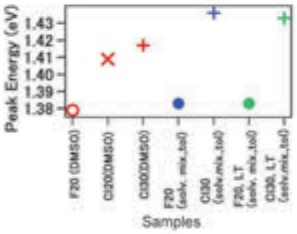

	Lifetime (ns)
F20 HT○	5.0
Cl30 HT×	6.2
Cl20 HT+	6.6
Cl30 HT+	8.8
Cl30 LT+	17.4
F20 HT●	10.6
F20 LT●	14.1

Longer life time is observed!

F20: 1.38 eV Cl30: 1.41~ 1.43 eV
→ blue shift in PL
→ Cl incorporation?

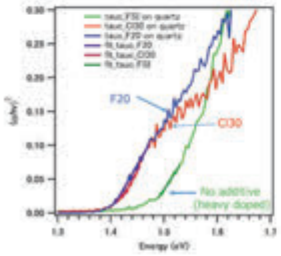

Absorbance:
F20 & Cl30≈1.40 eV
No additive ≈1.47 eV

Blue-shift is expected when the valence band maximum is occupied with doped carriers * (heavily doped condition)
→The absorbance shift observed for Cl30 is opposite

*T Handa, *et al*. J. Phys. Chem. C 2017, 121, 16158−16165

Device Characterization

<Performance screening>

$SnCl_2$ addition to DMSO solution

	Jsc (mA cm^{-2})	Voc (V)	FF	PCE (%)
Cl10	12.89	0.06	0.14	0.1
Cl20	17.2	0.19	0.44	1.4
Cl30	15.91	0.15	0.42	1
Cl40	16.45	0.23	0.45	1.8
Cl50	13.33	0.25	0.49	1.7

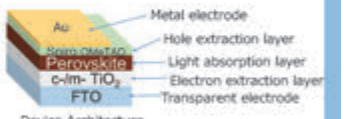

Device Architecture (standard type)

$SnCl_2$ addition to DMF/DMSO solution, tol dripping

Cl mol%	Jsc (mA cm^{-2})	Voc (V)	FF	PCE (%)
0	2.8	0.02	0	0
10	4.91	0.05	0	0
20	21	0.21	0.42	1.8
30	23.02	0.29	0.51	3.3
40	22.09	0.31	0.45	2.9
50	17.87	0.33	0.46	2.6
60	13.89	0.31	0.43	1.8
70	15.72	0.26	0.41	1.7

All the factors (Jsc, Voc and FF) are improved when using solvent mixure coupled with antisolvent dripping

<$FASnI_3$, 30 mol% $SnCl_2$ additive, DMF/DMSO, tol dripping>

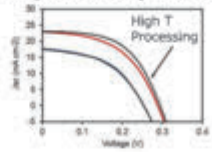

Device Performance comparison for processing T difference
→ Although lower T processing is better for the perovskite layer, device performance does not show same trend

Comparison between high T and low T processing

	Jsc (mA cm^{-2})	Voc (V)	FF	PCE (%)
HT	23.02	0.29	0.51	3.3
LT	17.64	0.25	0.46	2.1

→ Film formation on TiO2 or interfacial problem?

Summary

$SnCl_2$ as effective additive is demonstrated for improvement in optical properties of the thin films. The quality of the light absorber can be enhanced by lower T engineering. The solar cell performance could be improved by choosing suitable carrier extraction layers.

Acknowledgement

CREST (JPMJCR16N3) and IRCCS for funding
Shimakawa Lab for XRD facility

Nonlinear interaction of strong laser fields with semiconducting materials in the nonperturbative regime

Yasuyuki Sanari[1], Tomohito Otobe[2], Yoshihiko Kanemitsu[1], and Hideki Hirori[1]
[1]ICR, Kyoto University, [2]Kansai Photon Science Institute, QST

Abstract In semiconductor GaSe, the polarization properties and the crystal rotation angle dependence of the higher harmonics generated by two-color excitation lights (ω_1, ω_2) were investigated. As a result, by driving the electron to the high energy state with the excitation light of ω_1 and increasing the tensor component of the band curvature in the ω_2 direction, it is possible to obtain a large nonlinear current and harmonics which can not be obtained only by the weak ω_2.

High harmonic generation (HHG)

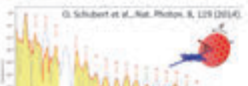

- High sensitivity to band structure
  →All optical band reconstruction
- Importance of motion of electrons in k space
  →Inter-band polarization
  →Inter-band current
- Many works by 1-color laser electric field
  →By using two-color laser field, adoption of parameter of motion control of electrons

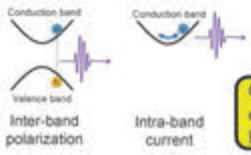

Clarify the relationship between the electronic motion of the k_x-k_y plane and HHG by using two-color electric fields

Comparison with the perturbative nonlinear optics.

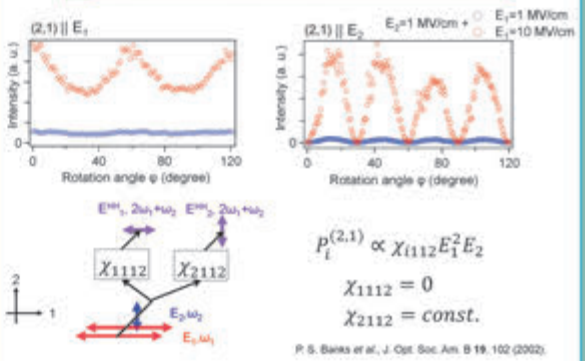

$$P_i^{(2,1)} \propto \chi_{i112} E_1^2 E_2$$

$$\chi_{1112} = 0$$

$$\chi_{2112} = const.$$

P. S. Banks et al., J. Opt. Soc. Am. B 19, 102 (2002)

Non-perturbative symmetry which can't be explained by nonlinear optics

Experimental setup

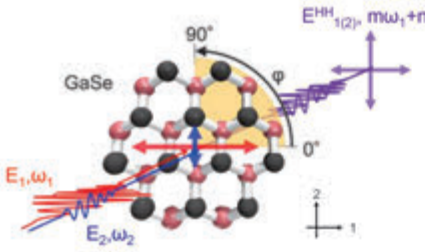

E_1 ~ 10 MV/cm
ω_1 = 0.52 eV
Wavelength:2400nm

E_2 ~ 1 MV/cm
ω_2 = 0.95 eV
Wavelength:1300nm

Rotate the crystal and measure the φ dependence of HHG

Cos-band model calculation

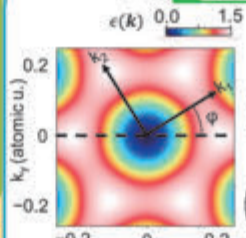

$$\epsilon(\boldsymbol{k}) = 1 - \frac{1}{3}\sum_{i=1}^{3}\cos(\boldsymbol{a}_i \cdot \boldsymbol{k})$$

$$\boldsymbol{a}_1 = \left(\cos(\pi/3), \sin(\pi/3)\right)$$
$$\boldsymbol{a}_2 = \left(\cos(\pi), \sin(\pi)\right)$$
$$\boldsymbol{a}_3 = \left(\cos(-\pi/3), \sin(-\pi/3)\right)$$

$$k_x = k_1\cos\varphi - k_2\sin\varphi$$
$$k_y = k_1\sin\varphi + k_2\cos\varphi$$

$$\begin{pmatrix} E_1^{HH}(t) \\ E_2^{HH}(t) \end{pmatrix} \propto \begin{pmatrix} \frac{\partial^2\epsilon(\boldsymbol{k})}{\partial k_1^2} & \frac{\partial^2\epsilon(\boldsymbol{k})}{\partial k_2 \partial k_1} \\ \frac{\partial^2\epsilon(\boldsymbol{k})}{\partial k_1 \partial k_2} & \frac{\partial^2\epsilon(\boldsymbol{k})}{\partial k_2^2} \end{pmatrix} \begin{pmatrix} E_1(t) \\ E_2(t) \end{pmatrix}$$

12 fold symmetry

6 fold symmetry

$E_1(t) = E_1\cos(\omega_1 t), E_2(t) = E_2\cos(\omega_2 t + \delta)$

$$\frac{\partial^2\epsilon(\boldsymbol{k})}{\partial k_1 \partial k_2} \propto \sum_{M,N=0}^{\infty} \cos(2M\omega_1 t)\cos(2N\omega_2 t + 2N\delta)$$

$(2M+1)\omega_1 + 2N\omega_2$

$2M\omega_1 + (2N+1)\omega_2$

(even,odd) component generated from the motion of electrons in E_2 direction

Rotation angle dependence

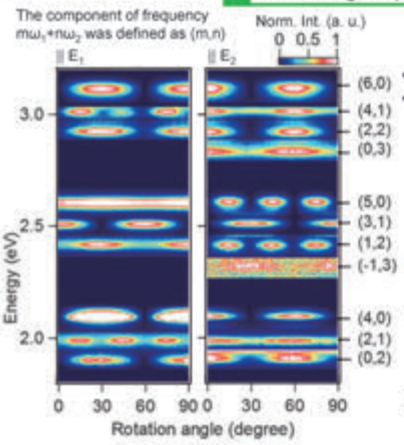

Classification

- (odd,odd) ⇒ Inter-band polarization
- (even,even) ⇒ Inter-band polarization

Explained by spatial symmetry

- (odd,even) ⇒ Intra-band current

|| E_1:6 fold symmetry
|| E_2:12 fold symmetry

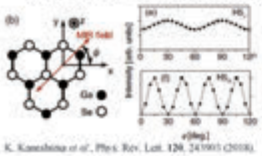

This symmetry is the same as a 1 color excitation Cf. (5,0)

Explained by the motion of electrons along the E_1 direction

- (even,odd) ⇒ Intra-band current

|| E_1:12 fold symmetry
|| E_2:6 fold symmetry

What is the generation mechanism of the component (even,odd)?

E_1 intensity dependence of band curvature tensor

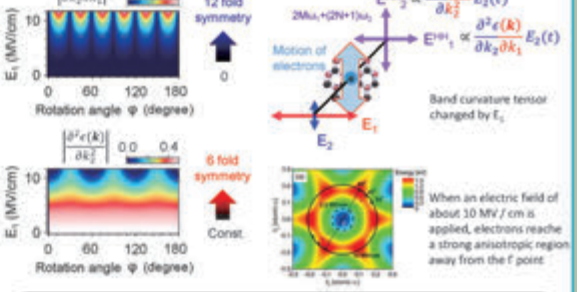

As E_1 increased, the electrons reached the non-perturbative region and changed the band curvature tensor

Conclusion

HHG in solids by an orthogonally polarized two-color laser field were investigated. In the (even, odd) component, non-perturbative symmetry that does not appear only with E_2 appears with E_1 because E_1 change the band curvature despite the fact that the vibration directions of the electrons are orthogonal to E_1 direction.

P-38

Anti-Stokes Photoluminescence Properties of Lead-Halide Perovskite Semiconductors

Takumi Yamada, Tomoko Aharen, Yoshihiko Kanemitsu
Institute for Chemical Research, Kyoto University, Uji, Japan

Lead-Halide Perovskite

Perovskite Structure

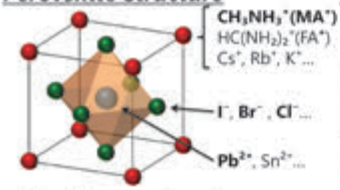

Various Samples

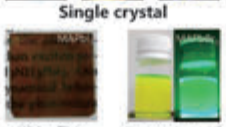

✓Band gap engineering

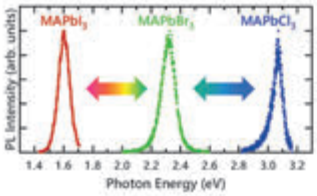

Applications

✓Solar cell ← 23.7%!!
✓Photodetector
✓Light emitting diode
✓Laser...

✓Sharp absorption : direct gap semiconductor

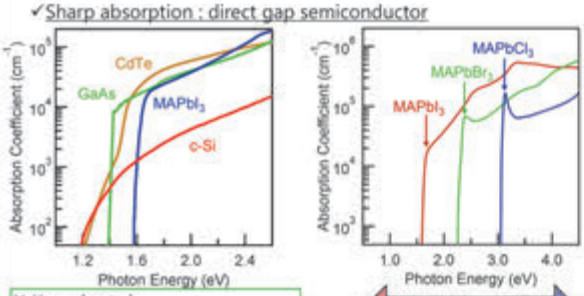

Y. Yamada *et al.*, *Bull. Chem. Soc. Jpn.* **90**, 1129 (2017).

Intrinsic properties still unclear... ⇨ **Study single crystals**

MAPbBr$_3$ Single Crystal

Time Resolved 2-Photon PL Microscopy

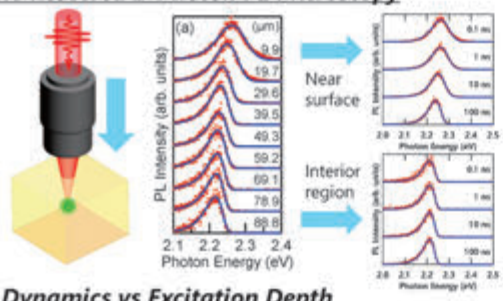

PL Dynamics vs Excitation Depth

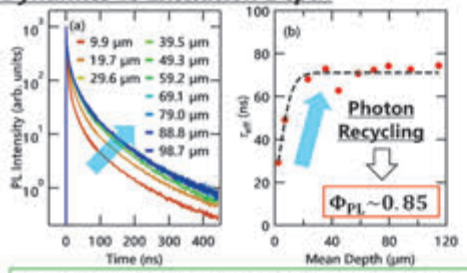

T. Yamada *et al.*, *Phys. Rev. Applied* **7**, 014001 (2017).

MAPbCl$_3$ Single Crystal

Two-Dimensional 1- and 2-PLE Spectra

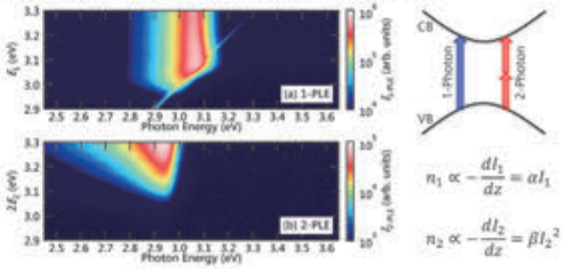

$$n_1 \propto -\frac{dI_1}{dz} = \alpha I_1$$

$$n_2 \propto -\frac{dI_2}{dz} = \beta {I_1}^2$$

Fundamental Optical Spectra

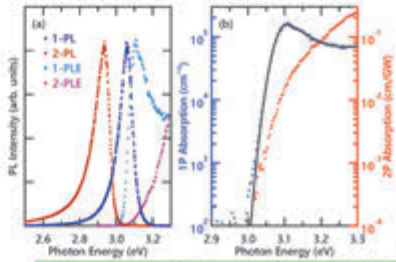

Excitonic Property & Photon Recycling

E_g = 3.15 eV
E_b = 41 meV

T. Yamada *et al.*, *Phys. Rev. Lett.* **120**, 057404 (2018).

MAPbI$_3$ Single Crystal and Thin Film

Resonant excitation by PLE Spectroscopy

✓ Experimental Setup

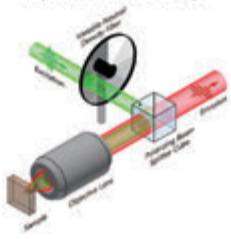

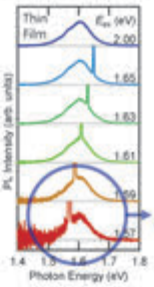

Y. Yamada *et al.*, *Bull. Chem. Soc. Jpn.* **90**, 1129 (2017).

FWHM ~ 90 meV
↓
Intrinsic Broadening

Anti-Stokes PL!

PL Peak vs Excitation Energy

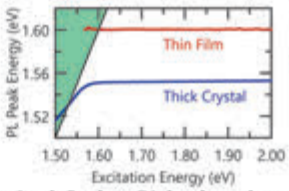

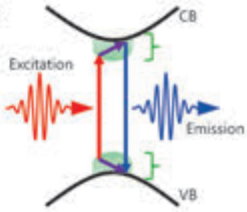

Anti-Stokes PL is also observed in thick crystal!

T. Yamada *et al.*, submitted for publication.

Conclusions

TRPL and PLE measurement for MAPbX$_3$ single crystals
✓ Excitation depth dependence of PL lifetime⇒ Φ_{PL}~0.85
✓ Detail analysis for PLE spectra with photon recycling
⇒ Determine 1- and 2-photon absorption spectra
✓ Efficient anti-Stokes PL from thick single crystal

Acknowledgement : JST-CREST (JPMJCR16N3), JSPS(17J07890), and IRCCS

Nonlinear Optical Properties of Halide Perovskite Single Crystals

Keiichi Ohara, Takumi Yamada, Hirokazu Tahara, Tomoko Aharen, Hideki Hirori, and Yoshihiko Kanemitsu
Institute for Chemical Research, Kyoto University, Uji, Japan

Introduction

Lead Halide Perovskites

- Less trap and defect tolerance
- Tunable band gap
- Easy fabrication at low cost

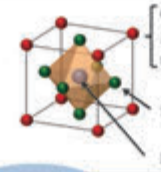

Linear Optical Response (~0.1 W/cm²)

- ✓ Strong absorption
- ✓ High luminescence efficiency

➢Solar cell
➢Light emitting diode etc...


Tan *et al.*, Nat. Nanotechnol. 9, 687 (2014)

Nonlinear Optical Response (~10^9 W/cm²)

- Potential for nonlinear optical device applications
  - ➢Laser
  - ➢Optical Switching
  - → **Not fully understood**


Tahara *et al.*, Adv. Optical Mater. 6, 1701366 (2018)

Third Order Nonlinear Optical Coeffitcients

Previous research: using polycrystalline thin films and nanocrystals

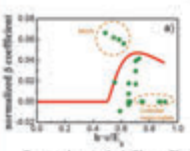
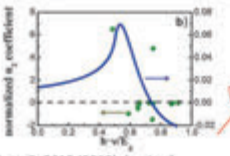
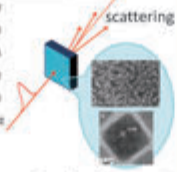

Ferrando *et al*,. J. Phys. Chem. Lett. 9, 5612 (2018) (review)

Various values was reported !

Extrinsic effects?

- grain structure
- interface
- concentration

Purpose

Elucidation of intrinsic factors for third order optical nonlinearity

- **Repetition rate dependence**
- **Intensity & Wavelength dependence**

using **Single crystal**

Experimental Method and Sample

Centrosymmetric Material ($\chi^{(2)} = 0$)

$$P(t) = \epsilon_0[\chi^{(1)}E(t) + \chi^{(2)}E^2 + \chi^{(3)}E^3(t) + \cdots]$$

Third Order Susceptibility

$$\chi_I^{(3)} = \frac{n_0^2\epsilon_0 c^2}{\omega}\beta \qquad \chi_R^{(3)} = 2n_0^2\epsilon_0 c\,\gamma$$

Z-scan Method

β and γ can be measured individually by transmission measurements

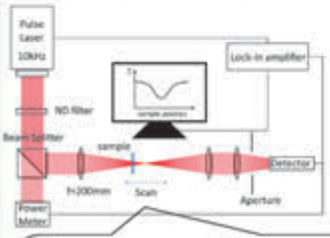

Sample

$MAPbCl_3$ Single Crystals

Sample Preparation

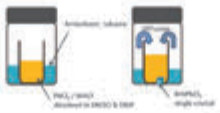

Open Aperture

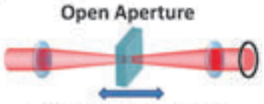

Two-photon absorption

$$\alpha(I) = \alpha + \beta I$$

Close Aperture

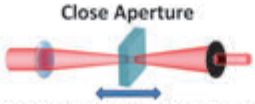

Optical Kerr effect (Self focusing)

$$n(I) = n_0 + \gamma I$$

Results and Discussion

What is the major effect in the observed nonlinear effects?

Third order nonlinearity vs Higher order vs Thermal effect

Repetition Rate Dependence

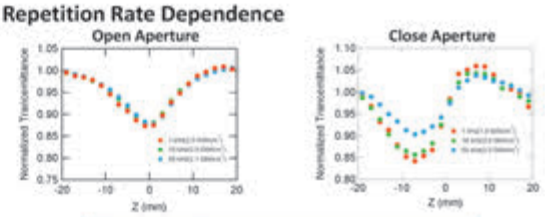

Thermal effect is negligible @10 kHz

Excitation Intensity and Wavelength Dependence

Open Aperture

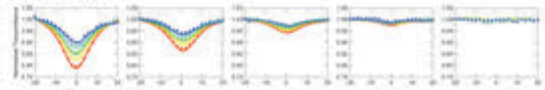

Fitting Function

$$T(x, S=1) = \frac{1+x^2}{\sqrt{\pi}q_0}\int_{-\infty}^{\infty}\ln\left(1+\frac{q_0}{1+x^2}e^{-\tau^2}\right)d\tau$$

Bahae *et al.*, IEEE J. Quantum Electron. 26, (1990)

$$\Rightarrow q_0 = \beta I_0 L + O(I_0^2)$$

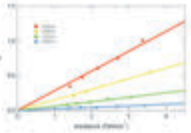

Close Aperture

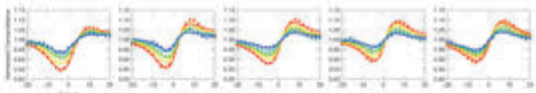

Fitting Function

$$T(x, S=0) \approx 1 - \frac{4x\Delta\Phi_0 - (x^2+3)q_0}{(x^2+9)(x^2+1)}$$

Gu *et al.*, Appl. Opt., 47, 1187 (2008)

$$\Rightarrow \Delta\Phi_0 = k\gamma I_0 L + O(I_0^2)$$

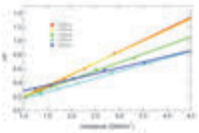

Higher order ($\chi^{(n)}(n \geq 4)$, Saturable absorption, Free carrier etc..) are all negligible

✓ Third order nonlinearity
Two-photon absorption & Optical Kerr effect are dominant

Wavelength Dependence of Third Order Nonlinear Optical Coefficients

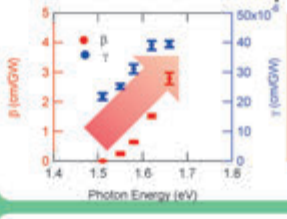

- ✓ Positive correlation with photon energy
- ✓ The absolute values are comparable to the conventional semiconductor

Conclusions

☛ **Z-scan measurement for $MAPbCl_3$ single crystals**

- ◆**third-order nonlinear optical response** is dominant (Higher order or thermal effect is negligible)
- ◆Third order nonlinear optical coefficients
  ⇒ β = 0~3 cm/GW, $\gamma = 2\sim4 \times 10^{-5}$ cm²/GW (800 nm~740 nm)
- ◆**Wavelength dependence** of β and γ
  ⇒ Positive correlation with photon energy

Acknowledgement : JST-CREST (JPMJCR16N3) and IRCCS

Photoluminescence properties of lead bromide perovskite nanocrystals revealed by single-dot spectroscopy

Institute for Chemical Research, Kyoto University
Sojiro Masada, Naoki Yarita, Hirokazu Tahara, Masaki Saruyama, Tokuhisa Kawawaki, Ryota Sato, Toshiharu Teranishi, and Yoshihiko Kanemitsu

Lead Halide Perovskite Nanocrystals

- High PLQY(90%)
- Narrow linewidth
- Tunable bandgap
- Application to LED etc.

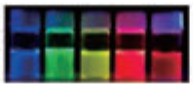

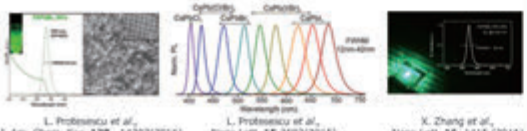

L. Protesescu et al., J. Am. Chem. Soc. **138**, 14202(2016)
L. Protesescu et al., Nano Lett. **15**,3692(2015)
X. Zhang et al., Nano Lett. **16**, 1415 (2016)

Purpose of This Study : A Site Cation

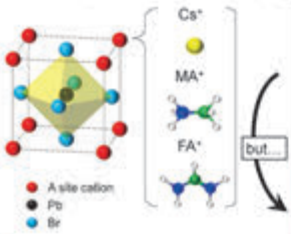

but...

Enhancement of chemical stability

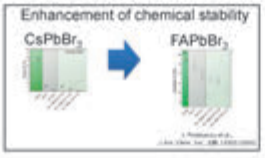

There are many unknown points as to what kind of difference occurs in the PL properties depending on A site cation

Sample

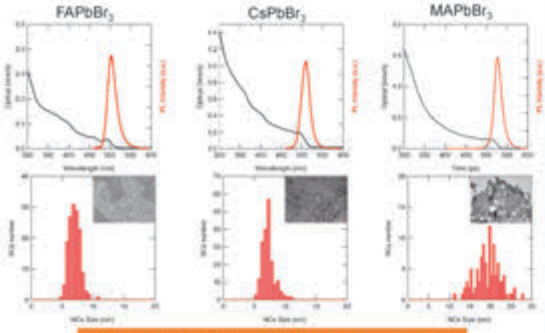

We prepared all three NCs with almost same size

Single-dot Spectroscopy

◆ Measurement system of single-dot spectroscopy

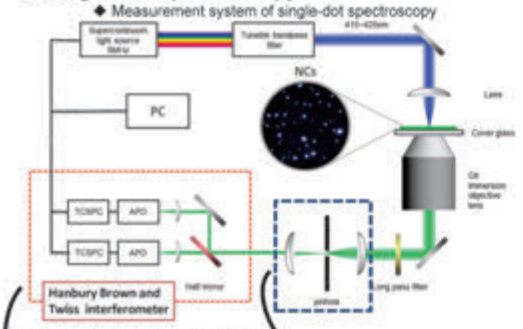

◆ Second order photon correlation

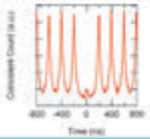

Using confocal system, we measured single NC PL

Clear antibunching
⇒ Single NC

Common PL Properties

◆ PL decay

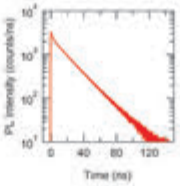

◆ PL intermittency

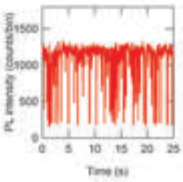

◆ PL spectrum

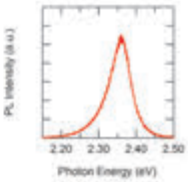

σ :Absorption cross section $\propto$ NCs volume V

$$\sigma = \frac{I_s}{F \cdot j_{ex} \cdot \eta_s \cdot \xi}$$

I_s : PL intensity (counts/s)
F : Excitation pulse frequency (5MHz)
j_{ex} : Excitation photon fluence (4.78794×10^{11} photon/cm^2)
η_s : PL quantum yield of neutral excitons (100%)
ξ : Detection efficiency (15.7%)

We measured 789 NCs in total (Cs:211 NCs, MA:195 NCs, FA: 383 NCs)

◆ PL Lifetime vs absorption cross section

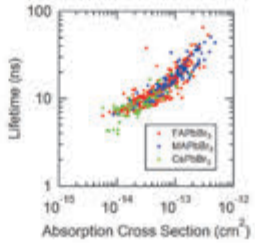

◆ PL peak energy vs absorption cross section

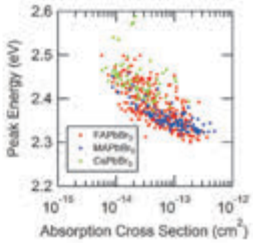

Regardless of A site cation
PL lifetime and PL peak energy are both influenced by quantum confinement effect (size reduction)

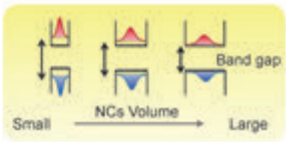

Difference in PL Properties

◆ PL spectrum from single $FAPbBr_3$ NC

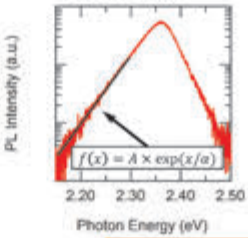

◆ Spectrum broadening of low energy side

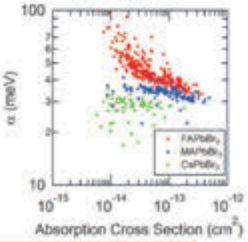

As the size of FAPbBr3 NCs decreased, the low energy side of PL broadened

Conclusion

- The spectral shape and size dependence of PL were observed in three different NCs
- In $FAPbBr_3$ as the size of the NCs decreased, the low energy side of the spectra broadened
- This effect was particularly conspicuous in $FAPbBr_3$, and almost not seen in $CsPbBr_3$

Acknowledgement: JST-CREST(JPMJCR16N3) and IRCCS

P-39

Mechanism of Trion Generation in $CsPbBr_3$ Perovskite Nanocrystals

Institute for Chemical Research, Kyoto University

Satoshi Nakahara, Hirokazu Tahara, Go Yumoto, Tokuhisa Kawawaki, Masaki Saruyama, Ryota Sato, Toshiharu Teranishi, and Yoshihiko Kanemitsu

Cesium Lead Halide Perovskite Nanocrystals (NCs)

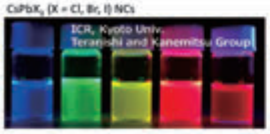

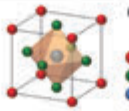

Light Emitting Diodes

Lasers

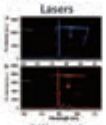

Superior optical properties

- ✓ High photoluminescence quantum yield (PLQY)
- ✓ Tunable emission wavelength
- ✓ Lasing

⇨ Implementation for light emitting devices

Introduction

Photogenerated Exciton Complexes in Perovskite NCs

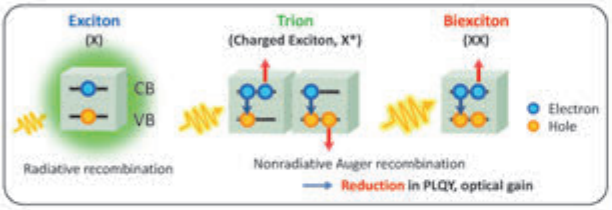

- Photoluminescence intermittency of $CsPbBr_3$ NCs

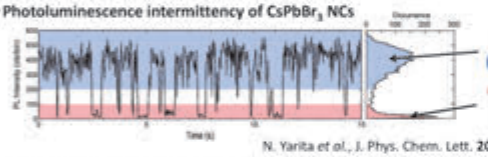

N. Yarita *et al.*, J. Phys. Chem. Lett. **2017**, *8*, 1413.

Trions cause the blinking and reduction of the PLQYs

⇨ Trion generation processes remain unclear

Clarify the trion generation mechanism in $CsPbBr_3$ NCs

Samples

◆ $CsPbBr_3$ NCs : Dispersed in octane

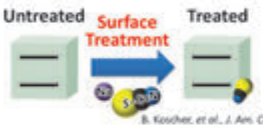

B. Koscher, *et al.*, J. Am. Chem. Soc. 2017, 139, 6566

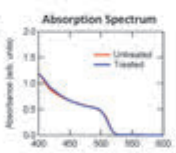

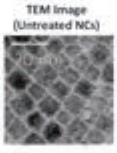

PLQY improvement : 65% → 80%

Band-gap Energy
E_g = 2.44 eV (508 nm)

Experimental

Transient Absorption (TA) Spectroscopy

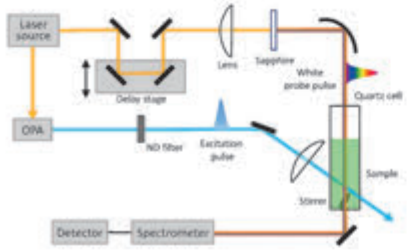

$CsPbBr_3$ NCs in a quartz cell

- ➢ Observation of ultrafast carrier dynamics → ✓ Pump-probe measurement
- ➢ Suppression of photo charging effect → ✓ Stirring
- ➢ Influence of NC surface condition → ✓ NaSCN surface treatment

Results and Discussion

Extraction of Exciton, Trion, and Biexciton Components

[Excitation : 440 nm (2.81eV)]

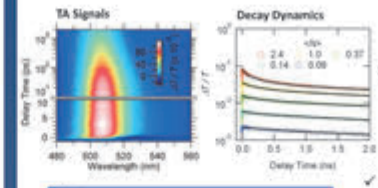

Strong bleaching signal (~ 508 nm)
→ **Occupation of band-edge states** by photoexcited carriers

$$\frac{\Delta T}{T}(t) = A_{XX}e^{-t/\tau_{XX}} + A_X e^{-t/\tau_X} + A_{X^*}e^{-t/\tau_{X^*}}$$

- ✓ Weak excitation regime : **Slow decay**
  → **Excitons** τ_X = 5.1 ns
- ✓ Strong excitation regime : **Fast decay**
  → **Trions** & **Biexcitons**
  τ_{X^*} = 280 ps τ_{XX} = 52 ps

$$\langle N \rangle = \sigma \cdot j$$

Average of absorbed photon number per NC

Trion Generation Mechanism

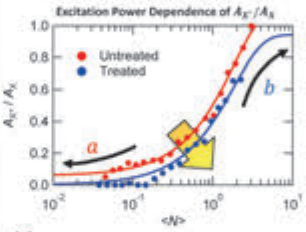

Assuming Poisson distribution in absorbed photon number : N
k-photon absorption : $p_k = e^{-\langle N \rangle}\frac{\langle N \rangle^k}{k!}$

Ratio between A_X and A_{X^*}
(Difference between samples is negligible)

$$\frac{A_{X^*}}{A_X} = a + b\frac{1 - e^{-\langle N \rangle} - \langle N \rangle e^{-\langle N \rangle}}{1 - e^{-\langle N \rangle}}$$

a : Charged NCs
b : Neutral NCs

- ✓ Untreated NCs
  a = 0.058 b = 1.1
- ✓ Surface-treated NCs
  a = 0.00 b = 0.94

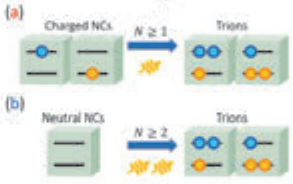

Trion generation is suppressed by surface treatment

Dominant trion generation pathways :
Surface Traps (under weak excitation)
Auger Recombination (under strong excitation)

S. Nakahara *et al.*, J. Phys. Chem. C 2018, *122*, 22188.

Generation of Charged NCs

[Excitation : 508 nm (2.44 eV = E_g)]

- Double Pump TA

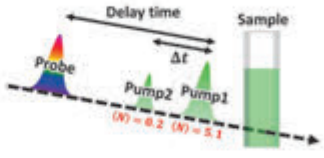

Δt Dependence of $A_{X^*}^{2nd}$

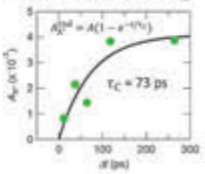

Pump1
→ Initial carrier generation

Pump2
→ Reconstruct carrier profile

✓ Extraction of $A_{X^*}^{2nd}$
(Trion component generated by pump2)

✓ $k_C = 1/\tau_C$:
Generation rate of **Charged NC**
~ $k_{XX} = 1/\tau_{XX}$ (τ_{XX} = 52 ps)
(**Biexciton** recombination rate)

Charged NCs generation via biexciton Auger recombination

Conclusions

We clarified the trion generation mechanism in $CsPbBr_3$ NCs.

- ➢ Surface treatment : Suppressing the trion generation
- ➢ Trion generation mechanism :
  Surface traps (weak excitation) & Auger recombination (strong excitation)
  S. Nakahara *et al.*, J. Phys. Chem. C 2018, *122*, 22188.

Acknowledgement : JST-CREST (JPMJCR16N3)

Coherent Spectroscopy of Multiple Excitons in Semiconductor Nanocrystals

Hirokazu Tahara, Masanori Sakamoto, Toshiharu Teranishi, and Yoshihiko Kanemitsu

Institute for Chemical Research, Kyoto University, Uji, Kyoto 611-0011, Japan

Introduction

Lead sulfide (PbS) nanocrystals

High-degeneracy
4-fold x 2 spins (L-point)

Similar effective mass
$m_e^* \sim m_h^* \sim 0.1 m_0$

Promising candidate for quantum dot solar cell

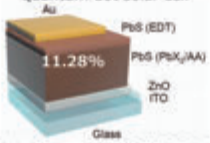

Nat. Mater. 16, 258 (2017)

Multiple carriers up to 8 excitons can be confined in one nanocrystal

Many-body interaction in multiple exciton dynamics

Auger recombination | Multiple exciton generation

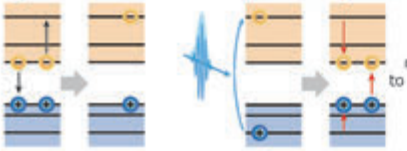

one hot exciton to multiple excitons

Carrier multiplication process improving photon-to-current conversion efficiencies in solar cells and photodetectors

Carrier multiplication and coherent dynamics of multiple excitons is not solved yet

In this study

- We developed a new method using phase-sensitive transient absorption measurement to observe the ultrafast multiple exciton dynamics.
- We successfully observed harmonic quantum coherence of multiple excitons.

Experimental Details

■ PbS/CdS core/shell nanocrystals

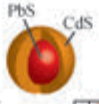

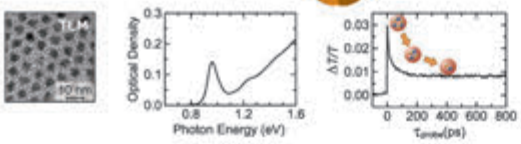

■ Phase-locked interference detection system of transient absorption measurement

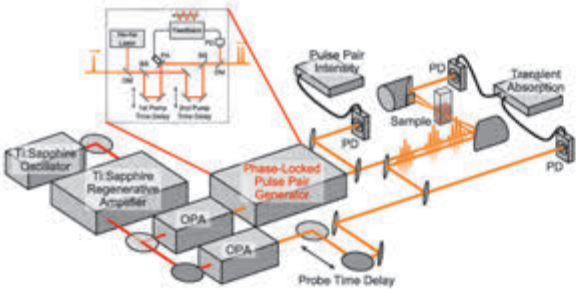

Synchronized detection of coherent optical field and excitonic dipole oscillations

Results and Discussion

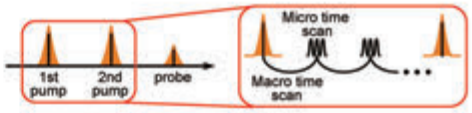

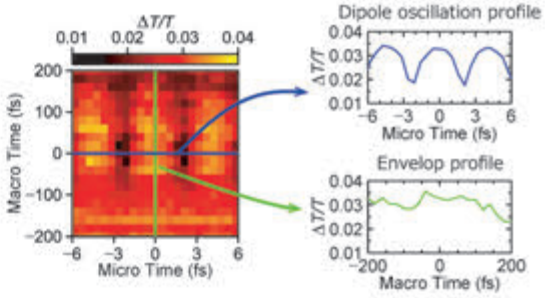

Expansion to harmonic dipoles

$\Sigma_{n=1,2,3} g A_n \cos(n\omega t)$ $A_n = n\omega$-oscillation, g = parity

■ Excitation power dependence of harmonic dipoles

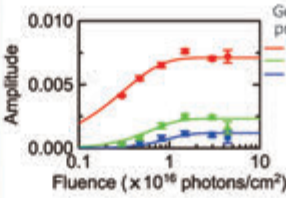

Amplitudes of harmonic dipoles correspond to the generation probabilities of multiple excitons

Harmonic dipoles = Multiple exciton dipole oscillations

■ Ultrafast envelop decay of harmonic dipoles

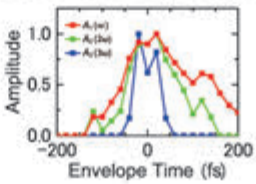

Envelop decay time decreases with increasing the harmonic order

Envelop decay = Free-induction decay of dipole oscillations

Decrease of decay time is the evidence of harmonic dipole oscillation due to multiple excitons

Conclusion

- We observed harmonic dipole oscillations in semiconductor nanocrystals.
- From our comprehensive analysis of multiple excitons using photon statistics and ultrafast envelope dynamics, we find that the harmonic dipole oscillations are originated from multiple excitons.

H. Tahara, M. Sakamoto, T. Teranishi, and Y. Kanemitsu, *Phys. Rev. Lett.* 119, 247401 (2017)

H. Tahara, M. Sakamoto, T. Teranishi, and Y. Kanemitsu, *Nat. Commun.* 9, 3179 (2018)

Acknowledgements: JST-CREST (JPMJCR16N3), JSPS KAKENHI (18K13481), and IRCCS

Fundamental optical responses of lead-free tin iodide perovskites

Institute for Chemical Research, Kyoto University

Taketo Handa, Tomoko Aharen, Atsushi Wakamiya, and Yoshihiko Kanemitsu

Background

◆ Metal halide perovskites AMX_3, A= MA, FA, Cs, M= Pb, Sn, X= Br, I

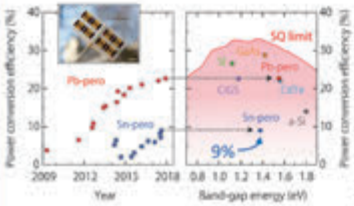

Kaltenbrunner et al., Nat. Mater. 14, 1032 (2015); NREL solar cell efficiency chart

■ Pb-perovskites show high efficiency, but they are toxic

■ Sn perovskites are potential Pb-free materials; however, their efficiency is lower

Stoumpos et al., Inorg. Chem. 52, 9019 (2013)
Hao et al., Nat. Photonics 8, 489 (2014)
Shao et al., Adv. Ener. Mater. 8, 1702019 (2018)

◆ Working principles of solar cells

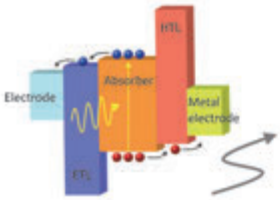

1. Optical properties of absorber layer
2. Losses in actual device

■ Spectroscopic evaluation in device structure is needed

◆ Conversion eff. vs PLQY

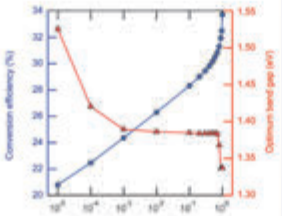

Zhu et al., Opt. Express 24, A740 (2016)
Shockley et al., J. Appl. Phys. 32, 510 (1961)

■ Fundamental optical properties (Eg, PLQY) determine upper limit of conversion efficiency;
But in Sn perovskites, these are unknown

We investigated the band-edge optical responses of Sn perovskites

Experimental

◆ $CH_3NH_3SnI_3$ ($MASnI_3$) thin films

・Spin-coating method

Liao et al., Adv. Mater. 28, 9333 (2016)

・Addition of SnF_2

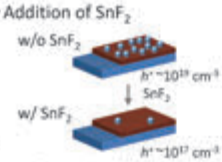

Suppression of hole density

・Choice of antisolvent

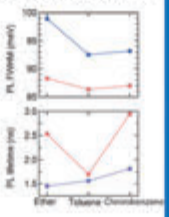

◆ $MASnI_3$ solar cell

・Device structure

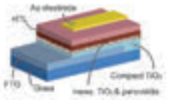

・$MASnI_3$ as absorber layer

・J-V characteristics

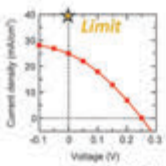

η = 1.94 %
J_{SC} = 26.1 mA/cm²
V_{OC} = 0.25 V
FF = 0.30
× 0.67
J_{SC}^{Limit} = 39.0 mA/cm²

Handa et al., J. Phys. Chem. C 121, 16158 (2017)

◆ PL measurements

・Resonantly excited PL:
Excitation: monochromatic light; Detection: InGaAs spectromator

・Time-resolved PL:
Excitation: fs-laser (650 nm); Detection: streak camera

・Temperature dependence of PL:
Excitation: ps-laser (688 nm); Detection: InGaAs spectromator

Steady-state PL: Electron-phonon coupling

◆ Resonantly excited PL

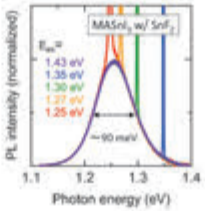

◆ Temperature dependence of PL

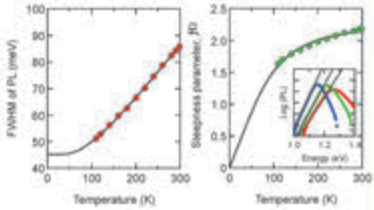

■ Temperature dependence of PL width is explained with electron-LO phonon interaction

・PL FWHM = $\Gamma_0 + \frac{\Gamma_{LO}}{(e^{\hbar\omega_{LO}/k_BT}-1)}$ Γ_0 = 45.2 meV, Γ_{LO} = 53.8 meV, $\hbar\omega_{LO}$ = 21.6 meV

■ PL tail is described with electron-LO phonon coupling with $\hbar\omega_{ph}$ = 22.3 meV

・PL low energy tail $\propto E^2 \exp\left(\frac{\sigma(T)-1}{k_BT}E\right)$, $E_U(T) = \frac{k_BT}{\sigma(T)}$ $E_U(298\ K) = 12$ meV

Steady-state PL responses of $MASnI_3$ are similar to Pb perovskites

→ **Potential for solar cells**

Handa et al., Phys. Rev. Materials 2, 075402 (2018)

Carrier dynamics: Hole doping & energy loss

◆ Optical absorption: Effect of SnF_2

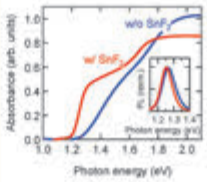

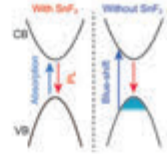

■ Absorption onset of $MASnI_3$ (w/o SnF_2) is at higher energy

→ **Band-filling effect due to high hole doping density**

Impact of doping on photocarrier recombination/transport dynamics

◆ Time-resolved PL: Hole density & energy loss mechanism in device

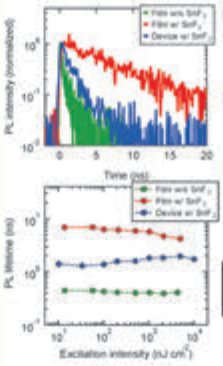

■ Comparison b/w films:
PL lifetime is longer for $MASnI_3$ film w/ SnF_2
→ **Prolonged carrier lifetime due to suppressed hole density**
(※But, still shorter than $MAPbI_3$, which shows > 100 ns)

■ Comparison b/w film and device:
PL lifetime is shorter for device sample
→ **Indicative of charge extraction**

■ Charge extraction efficiency: $\eta_{ex} = 1 - \frac{\tau_{device}}{\tau_{film}} = 79\%$

→ J_{SC}^{calc} = 39.0 mA/cm² × 0.9 × 0.79 = 27.7 mA/cm²
(Theoretical limit · Surface reflection · η_{ex})
Same as electrically measured J_{SC}

Short carrier lifetime because of hole doping is the origin of the decreased photocurrent

Handa et al., J. Phys. Chem. C 121, 16158 (2017)

◆ Recent collaborative work:

Improved preparation methods enabled longer PL lifetime, leading to efficient Sn solar cells with eff. > 7%

Liu,... Handa et al., Angew. Chem. Int. Ed. 57, 13221 (2018)

Conclusion

◆ Steady-state PL responses of $MASnI_3$ are governed by electron-LO phonon coupling and similar to Pb perovskites → Potential for solar cell application
◆ However, residual holes shorten carrier lifetime and decrease device performance
→ With improved preparation and suppressed doping, better performance is expected

Acknowledgement: JST-CREST (JPMJCR16N3), KAKENHI (17J09650), IRCCS

Crystallization of phase-change materials induced by strong THz pulses

Yasuyuki Sanari[1], Takehiro Tachizaki[2], Yuta Saito[3], Kotaro Makino[3], Paul Fons[3], Alexander V. Kolobov[3], Junji Tominaga[3], Koichiro Tanaka[1]
Yoshihiko Kanemitsu[1], Muneaki Hase[4], and Hideki Hirori[1]
[1]*Kyoto University,* [2]*Tokai University,* [3]*National Institute of Advanced Industrial Science and Technology,* [4]*University of Tsukuba*

We have systematically investigated the spatial and temporal dynamics of crystallization that occurs in the phase-change material $Ge_2Sb_2Te_5$ upon irradiation with an intense terahertz (THz) pulse. The electric field causes a temperature increase via Joule heating, which in turn leads to nanometer-scale crystal growth parallel to the field and the formation of filamentary conductive domains across the sample.

Light/electric induced structural change

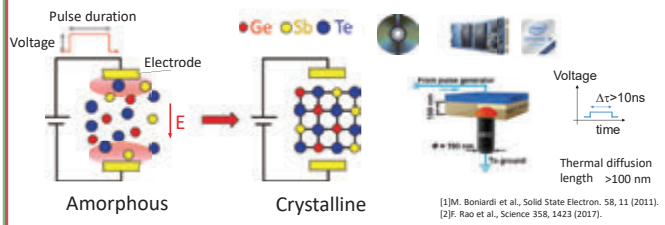

[1]M. Boniardi et al., Solid State Electron. 58, 11 (2011).
[2]F. Rao et al., Science 358, 1423 (2017).

- Obscuring the complex mechanisms of resistive switching, where the effects of both heating and electrical fields contribute to the phase change.
- The use of ultrashort THz pulses helps to suppress heat diffusion and may enable the study of crystallization mechanisms in which the lattice temperature exceeds the crystallization temperature on picosecond time scales.

Experiment

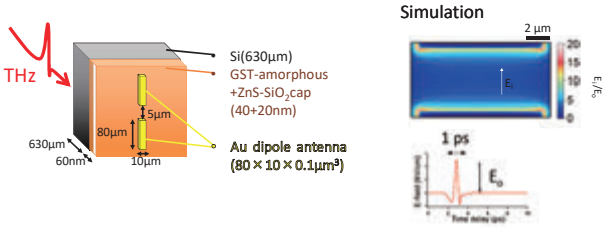

Allowing field induced phase change with the extremely short time duration (1 ps=0.001 ns).

THz induced phase change

Visible reflectivity change

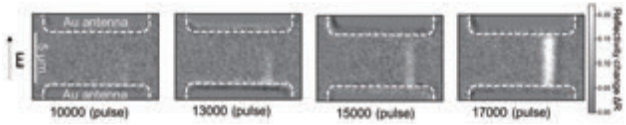

E_o =175 kV/cm

Raman spectra

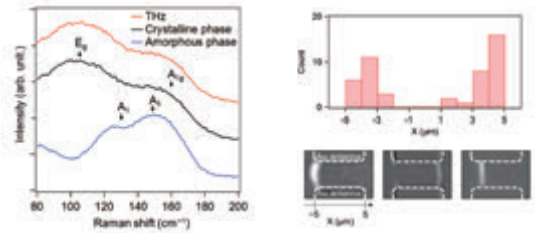

- Crystal growth along the electric field direction
- One dimensional crystal growth
- Crystallization speed: nm/pulse

Y. Sanari, HH et al., Phys. Rev. Lett. **121**, 165702 (2018)

What happens in the crystalized area?

Transient reflectivity change measurement

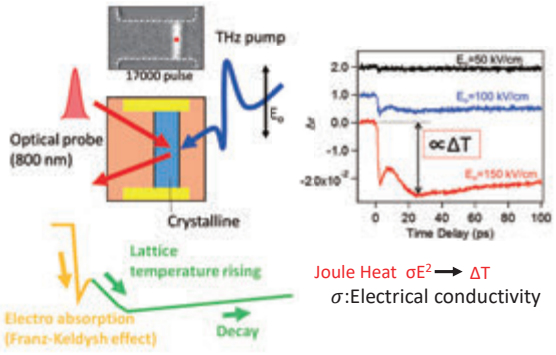

Joule Heat $\sigma E^2 \rightarrow \Delta T$
σ:Electrical conductivity

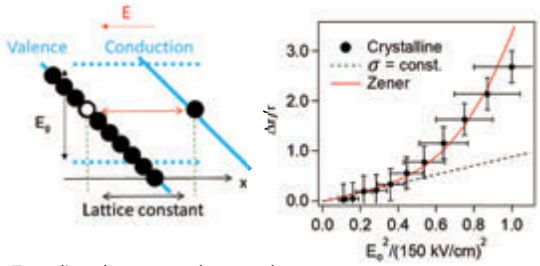

Tunneling electron number n under electric field E

$$n(E) = \frac{E^2 m_r^{\frac{1}{2}}}{18\pi\hbar^2 E_g^{\frac{1}{2}}} \exp\left(-\frac{\pi m_r^{\frac{1}{2}} E_g^{\frac{3}{2}}}{2\hbar E}\right)$$

Drude model

$$\sigma(t) = \sigma_0 + \sigma_{zener}(t,\omega)$$

$$\sigma_{zener}(t,\omega) = \frac{n(t)q^2}{m_r\tau(\omega^2+\frac{1}{\tau^2})}$$

E_g:bandgap energy, m_r:effective mass, τ:relaxation time, σ_0:Initial conductivity

High electric field causes Zener-tunneling

Mechanism

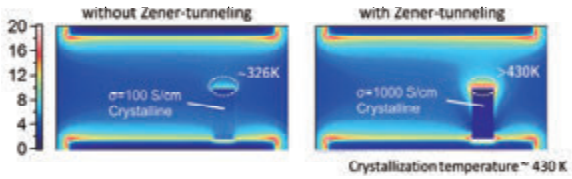

1. Crystallization occurs at the edge of Au antenna
2. Nonlinear increase of conductivity induced by Zener-tunneling
3. Preferential crystallization at the edge of crystalized area

The observed nonlinear increase in the conductivity of the crystalized region is a result of Zener tunneling; the tunneling leads to local heating which causes a one-dimensional crystal growth.

Mechanistic Studies on the Reactions of Digermynes with Styrene

Jing-Dong Guo,[a,d] Tomohiro Sugahara,[a] Takahiro Sasamori,[b] Shigeru Nagase,[c] Norihiro Tokitoh[a,d]

[a]*Institute for Chemical Research, Kyoto Univ., Gokasho, Uji, Kyoto 611-0011, Japan*
[b]*Graduate School of Natural Sciences, Nagoya City University, Yamanohata 1, Mizuho-cho, Mizuho-ku, Nagoya, Aichi 467-8501, Japan*
[c]*Fukui Institute for Fundamental Chemistry, Kyoto Univ., Kyoto, Kyoto 606-8103, Japan*
[d]*Integrated Research Consortium on Chemical Sciences, Kyoto Univ., Gokasho, Uji, Kyoto 611-0011, Japan*

Introduction

- In organic synthesis, olefins can be efficiently modified for introduction of various functional groups in many reaction processes.
- In such reaction, catalysts with transition metal are well established under mild experimental conditions.
- In recent years, catalysts with heavier group-14 atoms have received great attention. *[1,2]*
- Here, we focus on the reactivity of digermynes toward terminal alkene and the detailed catalytic mechanisms are investigated with hybrid density functional theory methods.

Reactions of Digermynes with Ethylene

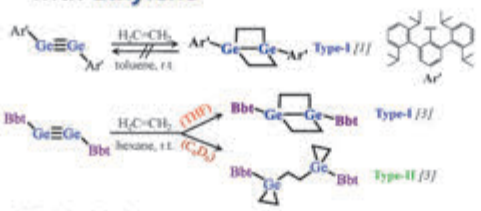

Experimental results

- Two types of product (**Type-I** and **Type-II**) generated under different conditions.

This Work: Reactions of Digermynes with Terminal Alkene (Styrene)

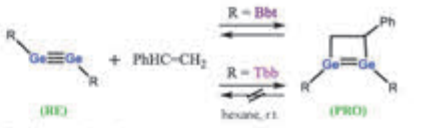

Experimental results

- **Type-I** and **Type-II**: not observed;
- R = Bbt: reversible ⇔ RE : PRO = 28 : 72 when 1 equiv. $PhHC{=}CH_2$ applied)
- R = Tbb: irreversible

Computational Models for Digermynes

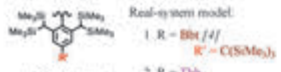

Real-system model:
1. R = Bbt *[4]*
R' = $C(SiMe_3)_3$
2. R = Tbb
R' = CMe_3

Computational methods

- Density functional theory (DFT) calculations at B3PW91 level, Gaussian 09 package. *[5]*
- Basis sets for optimization: 3-21G* for all atoms.
- Methods for single point calculations: TPSSTPSS-D3(BJ)
6-311+G(2d)<Ge,Si><6-31G(d,p)<C,H>.
- Potential energy surfaces (PES): constructed in terms of imaginary frequency and intrinsic reaction coordinate (IRC).

Validity of Computational Methods

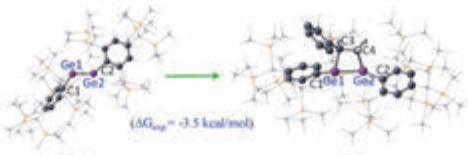

- Calculated geometric parameters (B3PW91): in good agreement with exp. values.
- Calculated reaction free energy:
1. ΔG_{calc} = -13.0 (B3PW91-D3(BJ));
2. ΔG_{calc} = -7.7 (TPSSTPSS-D3(BJ))⇒ closer to experimental result.

Geometric parameters (R = Bbt)	Calc. (gas) (RE/PRO)	EXP. (RE)/PRO)
Ge1-Ge2 (Å)	2.240/2.388	2.226/2.414
Ge1-C1 (Å)	1.974/1.990	1.966/1.977
Ge1-C3 (Å)	-- /2.016	-- /2.008
Ge2-C2 (Å)	1.962/1.999	1.942/2.004
Ge2-C4 (Å)	-- /2.047	-- /2.041
C3-C4 (Å)	-- /1.560	-- /1.539
C1-Ge1-Ge2 (°)	124.0/147.2	123.6/143.7
Ge1-Ge2-C2(°)	137.7/141.0	138.7/136.9
C1-Ge1Ge2-C2 (°)	179.2/-132.6	-168.9/-134.1
Total-A at Ge1 (°)	-- /333.4	-- /330.8
Total-A at Ge2 (°)	-- /330.3	-- /325.2

Selectivity with Ph Position

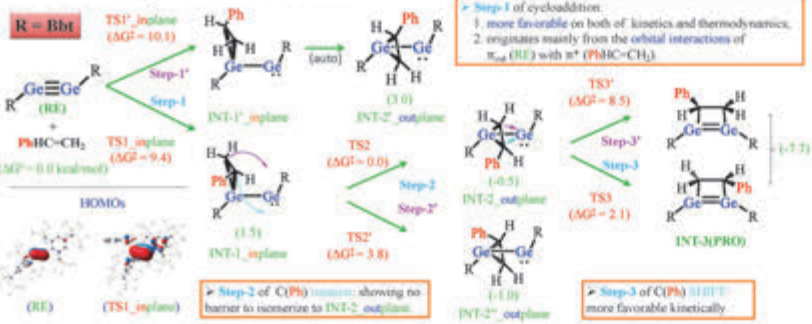

- Step-1 of cycloaddition:
1. more favorable on both of kinetics and thermodynamics;
2. originates mainly from the orbital interactions of π_{vdd} (RE) with π^* ($PhHC{=}CH_2$).
- Step-2 of C(Ph) isomer: showing no barrier to isomerize to INT-2' outplane.
- Step-3 of C(Ph) SHIFT: more favorable kinetically.

Selectivity with Ph Position

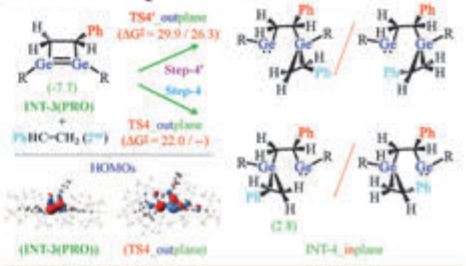

- Step-4 of cycloaddition at $Ge(CH_2)$ side:
1. more favorable kinetically;
2. originates mainly from the orbital interactions of π (INT-3) with π^* ($PhHC{=}CH_2$).

Selectivity toward Type-I and Type-II

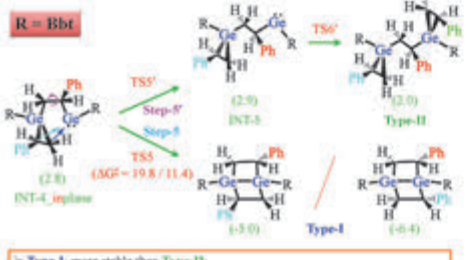

- **Type-I**: more stable than **Type-II**;
- Step-5 of C(Ph) SHIFT: more favorable kinetically than that of $C(H_2)$ SHIFT.

Free Energy Profiles

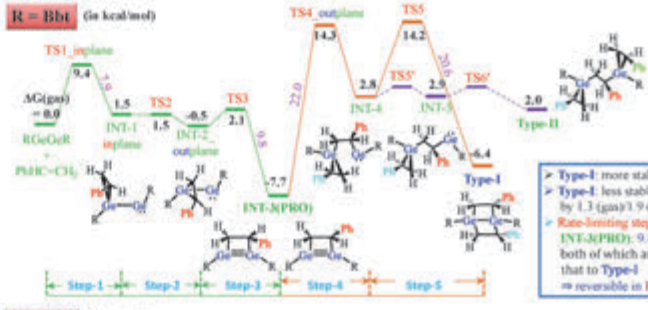

- **Type-I**: more stable than **Type-II**;
- **Type-I**: less stable than INT-3(PRO) by 1.3 (gas)/1.9 (n-hexane<CPCM>);
- Rate-limiting step between Reactants and INT-3(PRO): 9.4 (forward)/9.8 (backward), both of which are much smaller than that to **Type-I**
⇒ reversible in Bbt case.

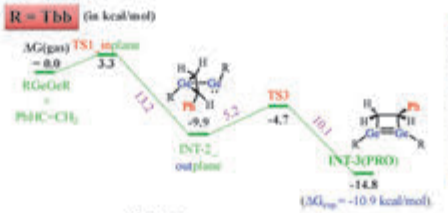

- Initial step: shows a decrease from 9.4 (Bbt) to 3.3 kcal/mol (Tbb), probably due to different electronic and steric effects from different substituents.
- Rate-limiting steps between Reactants and INT-3(PRO):
1. associated with INT-2_outplane which shows stronger stability [-0.5 (Bbt) → -9.9 (Tbb)], probably due to less steric effect in Tbb case;
2. 5.2 (forward)/13.2 (backward) ⇒ maybe irreversible in Tbb case.

Summary

(Ir)reversible reaction of digermynes with $PhHC{=}CH_2$:

- Unlike the reaction with ethylene, both of **Type-I** and **Type-II** not observed in experiments, probably due to their stability less than INT-3(PRO);
- In Bbt case, similar barriers [9.4 (forward)/9.8 (backward)] for rate-limiting steps between Reactants and INT-3(PRO), combined with much larger barrier (22.0 kcal/mol) to **Type-I** ⇒ maybe reversible in Bbt case.
- In contract, Tbb case shows that very different barriers [5.2 (forward)/13.2 (backward)] for rate-limiting steps between Reactants and INT-3(PRO) ⇒ maybe irreversible in Tbb case.

References

[1] V. Peng, D. D. Ellis, X. P. Wang, J. C. Fettinger, P. P. Power, *Science*, **2009**, *323*, 1608; T. Ohashi and W. Ando, *Organometallics*, **1998**, *13*, 3163.
[2] R. C. Fischer, P. P. Power, *Chem. Rev.* **2010**, *110*, 3877; S. Nagase, *Bull. Chem. Soc. Jpn.* **2014**, *87*, 167.
[3] T. Sasamori, T. Sugahara, T. Agou, K. Sugamata, J.-D. Guo, S. Nagase, N. Tokitoh, *Chem. Sci.*, **2015**, *6*, 3526.
[4] Y. Sugiyama, T. Sasamori, Y. Hosoi, Y. Furukawa, N. Takagi, S. Nagase, N. Tokitoh, *J. Am. Chem. Soc.* **2006**, *128*, 1023.
[5] Gaussian 09, Revision E.01, Gaussian, Inc., Wallingford CT, 2013.

Acknowledgements

This work was supported by JSPS KAKENHI grants JP15H03777 and 15K13640, as well as by Grants for Excellent Graduate Schools from MEXT (Japan). T. Sugahara gratefully acknowledges support from a JSPS grant-in-aid for JSPS fellows (JP16J05501). The authors would like to thank Mr. Toshiaki Noda and Ms. Hideko Natsume at Nagoya University for the expert manufacturing of custom-tailored glassware.

Synthesis and Properties of 2,5-Digermaselenophene

Tomohiro Sugahara,[1] Takahiro Sasamori,[2] and Norihiro Tokitoh[1]

[1]Institute for Chemical Research, Kyoto University, Uji, Kyoto 611-0011, Japan.

[2]Graduate School of Natural Sciences, Nagoya City Univ., Yamanohata 1, Mizuho-ku Nagoya, Aichi 467-8501, Japan.

1. Introduction～Functional material～

Polythiophene / selenophene

Physical properties (Ch = S, Se…)

- Low LUMO level
- High HOMO level
- Corresponding small HOMO-LUMO gap

O, S, Se, Te — Group 16

Examples

Oligomer type — Ladder type

Building blocks for organic optoelectronic materials

Modifying thiophenes via extension of π-conjugated system and introduction of π-conjugated functional substituents in order to diminish the HOMO-LUMO gap.

2. Introduction～Heavier triply bonded compounds～

Alkenes — Stable; Large overlap

Dimetallenes — M = Si, Ge, Sn, Pb; Highly reactive; Small overlap

heavier triply bonded compounds bearing bulky substituents

disilene West (1981) — *digermene* Lappert (1976) — *distannene* Lappert (1973)

- New π-bonded speicies
- Highly reactive
- Small HOMO-LUMO gap

Cyclic digermene

Ph–C≡C–Ph (1 equiv.), hexane, r.t.

Selected Structural Parameters	
Ge–Ge	2.4160(5) Å
Ge–C	2.022(2) Å
C–C	1.362(5) Å

Cf.

Ge=Ge	2.21-2.46 Å
Ge–C (avg.)	*ca.*1.95 Å
Ge=C (avg.)	*ca.*1.83 Å

Structural features

- Ring Strain
- Trans-bent Geometry

Large Contribution

Bull. Chem. Soc. Jpn. **2017**, *89*, 1375.

3. This Work ～Chalcogenation of 1,2-Digermacyclobutadiene～

Chalcogenation

Chem. Lett. **2018**, *47*, 7139.; *J. Am. Chem. Soc.* **2018**, *140*, 11206.

4. Chalcogenation of 1,2-Digermacyclobutadiene I

1 —(S_8 or Se (excess), THF, r.t.)→ —($P(NMe_2)_3$, Solvent, T °C)→

2a: Ch = S (38%)* **2b**: Ch = Se (75%)* **3a**: Ch = S (29%)* **3b**: Ch = Se (21%)*

	$P(NMe_2)_3$	Solvent	T °C	*1a*-Ch	*1b*-Ch
Ch = S_8	excess	toluene	110 °C	38%*	29%*
Ch = Se	---	THF	40 °C	80%*	20%*
Ch = Se	excess	toluene	110 °C	0%	57%**

* Estimated by ^{1}H-NMR spectroscopy.

Selected Structural Parameters (Side View)

Compound 2a — Compound 2b — Compound 3a — Compound 3b

5. Theoretical Calculations (Compound 1)

NBO6.0: B3PW91/6-311G(3d)<Ge,Si,Se>, 6-31G(d)<C,H>

Side View

Selected Structural Parameters

	1a-Se(obs.)	*1a*-Se (cal.)
Ge1-Se2	2.4214(8)	2.4474
Ge2-Se3	2.4345(8)	2.4455
Ge1-Se1	2.3467(5)	2.3674
Ge2-Se1	2.3399(7)	2.3731
Se2-Se3	2.3558(7)	2.3706

BD(2) C1-C2 → BD*(1) Ge1-Se2, BD*(1) Ge2-Se3: 7.3 kcal/mol

LP(2) Se1 → BD*(1) Ge1-Se2, BD*(1) Ge2-Se3: 15.0 kcal/mol

6. Chalcogenation of 1,2-Digermacyclobutadiene II

1 —(Ch=P(NMe$_2$)$_3$ (1 equiv.), C_6D_6, r.t.)→

4a: Ch = S (Not isolated) **4b**: Ch = Se (quant.)**

** Isolated yield.

Structural Parameters

	3 (Exp.)	**3** (C_1, Calc.)[a]	**3'** (C_2, Calc.)[a]	**4** (C_2, Calc.)[b]
Ge–Se [Å]	2.3176(14) 2.2730(14)	2.325 2.325	2.330	-----
Ge–C [Å]	1.919(7) 1.910(8)	1.918 1.918	1.922	-----
C1–C2 [Å]	1.363(10)	1.390	1.366	1.443
Ge–Se–Ge [°]	91.57(5)	92.48	90.08	88.55
α [°]	8.8	7.0	6.8	-----
WBI(Ge/C–Se)	-----	1.03 / 1.03	1.05	1.14
WBI(Ge/C–C)	-----	1.00 / 1.00	0.97	1.59
WBI(C1–C2)	-----	1.52	1.65	1.17
NICS (0) / NICS (1)	-----	–11.20/ –7.96	–12.33/ –9.86	–11.12/ –8.88
^{13}C NMR (C1/C2)	176.8	188.3	189.9	140.9
^{77}Se NMR	481.2	520.6	535.8	548.3

[a] B3PW91/6-311G(3df)<Ge,Si,Se>, 6-311G(d)<C,H>, [b] B3PW91/6-311G(3df)<Se>, 6-311G(d)<C,H>

(Simple model) 3'

(Tetramethylselenophene) 4

Flatness

7. Molecular Orbitals (Compounds 3' and 4)

Compound 3'		Compound 4	
LUMO (–2.63 eV)		LUMO (–0.21 eV)	
HOMO (–5.02 eV)		HOMO (–5.76 eV)	
HOMO-1 (–6.69 eV)		HOMO-1 (–6.10 eV)	
HOMO-2 (–7.33 eV)		HOMO-3 (–8.88 eV)	

Small HOMO-LUMO gap

3': B3PW91/6-311G(3df)<Ge,Si,Se>, 6-311G(d)<C,H>
4: B3PW91/6-311G(3df)<Se>, 6-311G(d)<C,H>

8. Reactions of 2,5-Digermaselenophene (Compound 3)

3 —(Se (excess), C_6D_6, 60 °C)→ 75%* + 21%*

—(H_2 (1 atm), hexane, r.t.)→ 39%**

* ^{1}H-NMR yield, ** Isolated yield.

Acknowledgement

This work was partially supported by the following grants: Grants-in-Aid for Scientific Research (B) (Nos. 22350017, 15H03777), Challenging Exploratory (15H13640), Scientific Research on Innovative Areas, "New Polymeric Materials Based on Element-Blocks" [#2401] (Nos. 25102519, 15H00738), "Stimuli-Responsive Chemical Species for the Creation of Functional Molecules" [#2408] (No. 24109013), and the MEXT Project of Integrated Research on Chemical Synthesis from the Ministry of Education, Culture, Sports, Science and Technology (MEXT), Japan, as well as the "Molecular Systems Research" project of the RIKEN Advanced Science Institute and the Collaborative Research Program of Institute for Chemical Research, Kyoto University. We would like to thank Mr. Toshiaki Noda and Ms. Hideko Natsume at Nagoya University for the expert manufacturing of custom-tailored glassware.

Synthesis and Structure of Heavier Group 14 Element Analogues of Aryl Anions

Shiori Fujimori, Yoshiyuki Mizuhata, and Norihiro Tokitoh*

Institute for Chemical Research, Kyoto University, Gokasho, Uji, Kyoto 611-0011, Japan

fujimori@boc.kuicr.kyoto-u.ac.jp

Introduction

Multiply bonded systems of heavier group 14 elements

Second row elements — large overlap, short bond; Group 14: C, Si, Ge, Sn, Pb; *stable multiple bond*

Heavy elements — small overlap, long bond; Group 14: C, Si, Ge, Sn, Pb; M = Si, Ge, Sn, Pb/ Ch = S, Se, Te; *extremely reactive multiple bond*

Germabenzenes

Kinetic stabilization by a bulky aryl group, Tbt, has been recognized to be efficient to stabilize germabenzene.

Previous Work

Stabilization by charge repulsion — E = Si, Ge, Sn, Pb

Benzene skeleton — germabenzenyl anion (M = Li, Na, K)

a) Y. Mizuhata, S. Fujimori, T. Sasamori, N. Tokitoh, *Angew. Chem. Int. Ed.*, **2017**, *56*, 4588. b) S. Fujimori, Y. Mizuhata, N. Tokitoh, *Chem. Lett.*, **2018**, *47*, 708.

C — aromatic character ↔ divalent species

Ge, Sn — aromatic character ↔ divalent species

S. Fujimori, Y. Mizuhata, N. Tokitoh, The 97th CSJ Annual Meeting, **2017**, 3G1-29.

This Work

Anthracene skeleton

☆ The reaction of *9-germaanthracene* with KC_8 afforded *trianion* and *dianion* depending on the reaction conditions.

Reaction with KC_8 (2 eq.)

trianion A (40% yield) — **purple crystals**, insoluble in hexane, benzene, soluble in THF

possible mechanism of *trianion* A — *germaanthracenylpotassium*, *high germylene character*

M. Weidenbruch, *J. Am. Chem. Soc.* **2003**, *125*, 10172. S. Masamune, *J. Am. Chem. Soc.* **1965**, *87*, 6390.

Reaction with KC_8 (1 eq.)

dianion B — **orange crystals**, insoluble in hexane, benzene

possible mechanism of *dianion* B — *radical anion of the 9-germaanthracene*

Formation of the *dianion* B suggested the generation of the radical anion of the 9-germa-*anthracene* as an intermediate.

Y. Mizuhata, S. Fujimori, T. Sasamori, N. Tokitoh, *Angew. Chem. Int. Ed.*, **2017**, *56*, 4588.

Structure of *Trianion* A

Selected bond lengths (Å), angles (deg), and sums of the interior angles (deg)

- Planar structure
- Ge–C single bond
- Almost similar C–C bond lengths

Delocalized anion on the whole ring except Ge atom

- Non-planar structure
- Ge–C bond lengths and C–Ge–C angle are equivalent to these of germole anion

Localized anion on Ge atom

Thermal ellipsoid plots (50% probability)

Cf. Ge–Ge single bond lengths — Ge–Ge: 2.5690(10) Å — R. West, *J. Am. Chem. Soc.*, **2002**, *124*, 12174.

Cf. germole anion — A. L. Rheingold, *J. Am. Chem. Soc.*, **1996**, *118*, 10457.

Cf. Ge–C bond lengths — Ge–C *single bond lengths* 1.944–1.966 Å — D. Seyferth, *J. Organomet. Chem.*, **1986**, *306*, 183.

aromatic compounds — N. Tokitoh, *Organometallics*, **2006**, *25*, 3536.

Structure of *Dianion* B

Selected bond lengths (Å) and angles (deg)

Thermal ellipsoid plots (50% probability)

Localized anion on Ge atom

Ge–K distance : 7.821 Å

separated ion pair

Cf. sum of van der Waals radii: Ge (2.11 Å) + K (2.75 Å) = 4.86 Å

D. G. Truhlar, *J. Phys. Chem.*, **2009**, *113*, 5806.

NMR Spectrum of *Trianion* A

^{1}H NMR Spectrum (THF-d_8)

Retain of the trimeric structure even in THF solution.

Acknowledgements

This work was supported by Grants-in-Aid for Scientific Research on Innovative Areas (No. 24109013), Scientific Research (B) (Nos. 16H04130, 21280021), Scientific Research (C) (No. 26410044), from the Ministry of Education, Culture, Sports, Science and Technology, of Japan. S. F. thanks Research Fellowships of the Japan Society for the Promotion of Science for Young Scientists.

Simple Approaches to Realize Efficient and Reproducible Lead-free Perovskite Solar Cells: Purification of Precursor Materials and Modification of Solution Process

[1]Institute for Chemical Research, Kyoto University, [2]Department of Applied Chemistry, Graduate School of Engineering, Osaka University
○Jiewei Liu,[1] Masashi Ozaki,[1] Shinya Yakumaru,[1] Taketo Handa,[1] Ryosuke Nishikubo,[2] Yoshifumi Hashikawa,[1]
Yasujiro Murata,[1] Takashi Saito,[1] Yuichi Shimakawa,[1] Yoshihiko Kanemitsu,[1] Akinori Saeki,[2] Richard Murdey,[1] Atsushi Wakamiya[1,*]

Introduction and Background

Tin-based Perovskite Solar Cells from SnI_2 Complexes

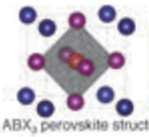

ABX_3 perovskite structure

✓ Environmentally friendly
✕ Low efficiency
✕ Low stability

H. J. Snaith, et al., *Energy Environ. Sci.* **2014**, *7*, 3061.
M. A. Lee et al., *Adv. Energy Mater.* **2017**, 1702019.

- We synthesized high purity [SnI_2(dmf)] complex as a precursor for fabricating tin perovskites with better electrical performance.
- We developed a hot antisolvent treatment (HAT) and solvent vapor annealing (SVA) methods to achieve mixed-cation $FA_{0.75}MA_{0.25}SnI_3$ perovskite films with improved morphology.
- We acheived lead-free perovskite solar cells with 7.2% power conversion efficiency.

Device Structure and Problems

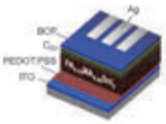

Z. Liu and Z. Bian et al., *Adv. Sci.* **2017**, 1700204.

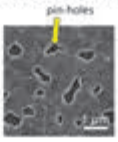

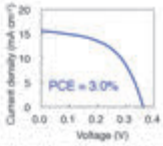

- Following reported method, perovskite films with poor coverage were obtained, leading to shunted devices with poor reproducibility.
- Only moderate PCE (3.0%) was obtained for the best solar cell device.

Results and Discussion

[SnI_2(dmf)] Complex

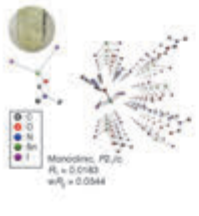

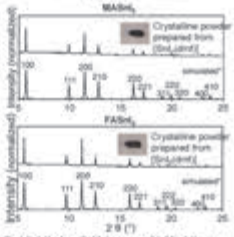

M. Ozaki, Y. Katsuki, J. Liu, T. Handa, R. Nishikubo, S. Yakumaru, Y. Hashikawa, Y. Murata, T. Saito, Y. Shimakawa, Y. Kanemitsu, A. Saeki, A. Wakamiya, *ACS Omega* **2017**, *2*, 7016-7021.

The high purity SnI_2(dmf) complex is a promising material as $MASnI_3$ and $FASnI_3$ precursor

Optimization Process for Sn Perovskite Film Formation

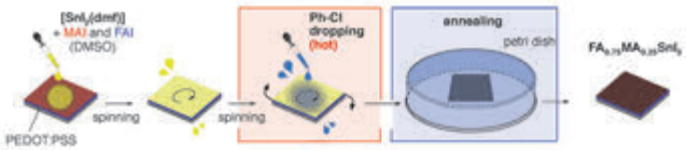

① Hot Antisolvent Treatment (HAT)
② Solvent Vapor Annealing (SVA)

We carefully examined the Sn perovskite film formation process at both the spin-coating and thermal annealing stages, developing two techniques which optimize these stages separately.

① Hot Antisolvent Treatment (HAT)

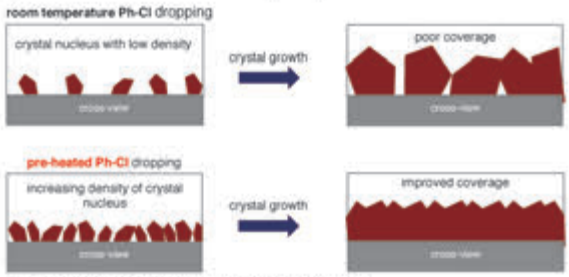

Hot antisolvent increase the number density of crystallization nucleus, leading to full coverage film.

Top-View SEM Images

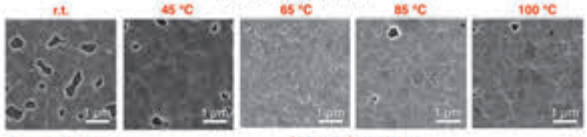

J–V Curves

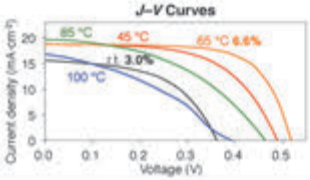

Photovoltaic Parameters

	J_{SC} (mA·cm⁻²)	V_{OC} (V)	FF	PCE (%)
r.t.	15.6	0.36	0.52	3.0
45 °C	18.8	0.49	0.59	5.4
65 °C	18.8	0.51	0.69	6.6
85 °C	19.7	0.46	0.45	4.1
100 °C	16.9	0.39	0.36	2.4

② Solvent Vapor Annealing (SVA)

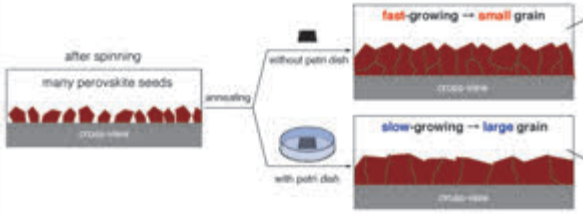

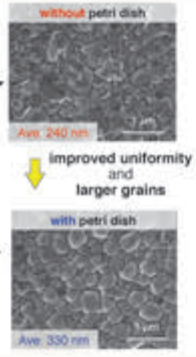

J–V Curves and Statistics of PCE

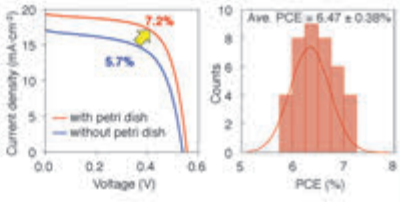

	J_{SC} (mA·cm⁻²)	V_{OC} (V)	FF	PCE (%)
—	17.2	0.54	0.61	5.7
—	19.4	0.55	0.67	7.2

A mild DMSO-rich atmosphere during film annealing retards film growth, leading to larger grains and better film uniformity.

Summary

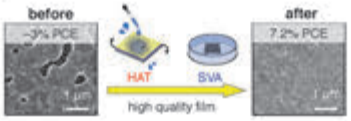

The film quality and device performance were improved by the combined HAT and SVA process optimization.

J. Liu, M. Ozaki, S. Yakumaru, T. Handa, R. Nishikubo, Y. Kanemitsu, A. Saeki, Y. Murata, R. Murdey, A. Wakamiya, *Angew. Chem., Int. Ed.* **2018**, *57*, 13221–13225.

Acknowledgements

- We thank Prof. Toshiharu Teranishi, Prof. Masanori Sakamoto, Dr. Ryota Sato, and Dr. Tokuhisa Kawawaki (Kyoto Univ.) for help with the SEM measurements.
- Financial Support from **IRCCS**, **ALCA**, and **COI**.

Transparent Hole-Transporting Materials Containing Partially Oxygen-Bridged Triphenylamine Skeletons: Synthesis and Properties

Institute for Chemical Research, Kyoto University
Minh Anh Truong, Richard Murdey, Atsushi Wakamiya

Introduction

❖ Transparent Hole-Transporting Materials

Transparency in the visible light region is an important factor for organic semiconducting materials used in tandem solar cells due to the requirement of light penetration in semiconducting layer.

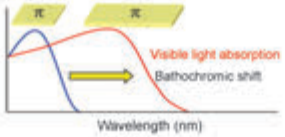

❖ Previous Work

Quasiplanar skeletons were connected through the meta-position of a benzene ring.

- Transparent ($\lambda_{edge,film}$ = 425 nm)
- Good mobility (μ_{SCLC} = 2.2×10^{-5} cm^2/Vs)

The absorption edge still in the visible region due to the partly connected π-conjugated system.

Ref:
1.A. Wakamiya, Y. Murata et al. *Chem. Lett.* **2017**, *46*, 817.
2.A. Wakamiya, L. T. Scott, Y. Murata et al. *J. Am. Chem. Soc.* **2015**, *137*, 15656.
3.A. Wakamiya, H. Kaji, Y. Murata et al. *Angew. Chem. Int. Ed.* **2014**, *53*, 5800.

The Problem: Although extended π-conjugation is desirable for effective transport of holes, it also results in reduced transparency.

How to Solve: A combination of strong donor like quasiplanar structure with weak donor can make electrons distribute separately on HOMO and LUMO, leading to weak (or forbidden) absorption.

❖ This Work

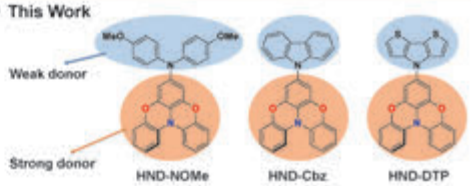

Three new transparent hole-transporting materials containing quasiplanar structures were synthesized and characterized.

Results and Discussion

❖ Synthesis

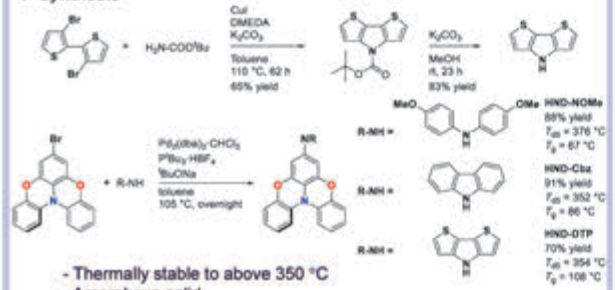

- Thermally stable to above 350 °C
- Amorphous solid

❖ Optical Absorbance, Energy Levels, and Hole-transporting Properties

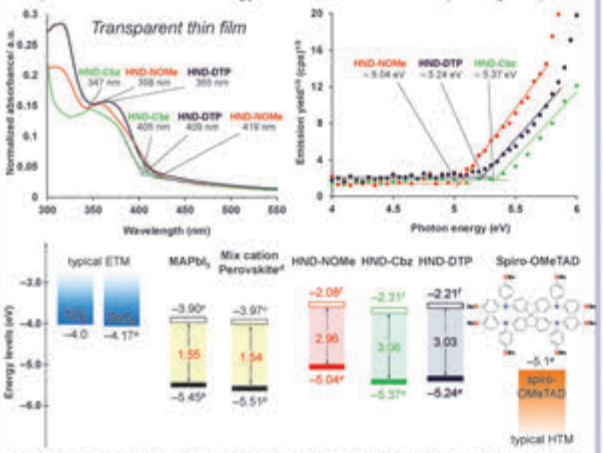

[a]H. Wang, F. Gao et al. *J. Mater. Chem. C*, **2018**, *6*, 6996. [b]Valence band of perovskite layer. [c]Conduction band of perovskite layer. [d]$Cs_{0.05}MA_{0.15}FA_{0.80}PbI_{2.55}Br_{0.25}$. MA^+ = $(CH_3NH_3^+)$, FA^+ = $((NH_2)_2CH^+)$. [e]HOMO energy levels in vacuum deposited films, determined by photoelectron spectroscopy. [f]LUMO energy levels were calculated by using HOMO energy levels and optical band gaps determined from the absorption spectra of the vacuum deposited films.

	HND-NOMe	HND-Cbz	HND-DTP	Spiro-OMeTAD[a]
μ_{SCLC} (cm^2/Vs)	1.3×10^{-5}	1.3×10^{-5}	2.4×10^{-5}	2.1×10^{-4}

[a]A. Wakamiya, L. T. Scott, Y. Murata et al. *J. Am. Chem. Soc.* **2015**, *137*, 15656.

❖ DFT Calculations (DFT: B3LYP/6-31G(d), TD-DFT: CAM- B3LYP/6-31G(d))

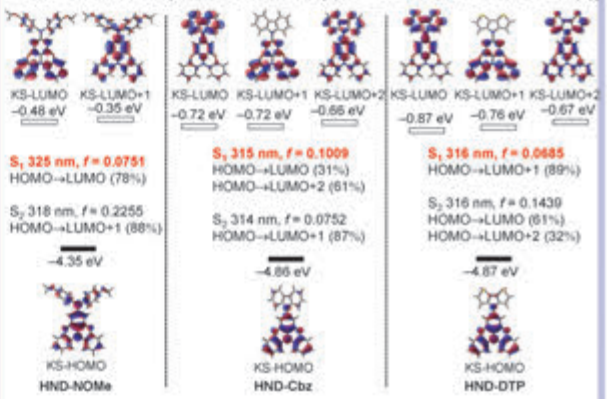

HOMOs localized on quasiplanar structures, while LUMOs localized on diarylamine structures. In addition to the S_1 absorption, π-π* transitions from nearby LUMO+1 and LUMO+2 are also significant.

❖ Device Performances

Method 1. Spin-coating:
$ITO/SnO_2/Cs_{0.05}MA_{0.15}FA_{0.80}PbI_2Br_{0.25}$ (~500 nm)/HTM/Au (80 nm)
HTM layer:
HTM [HND-NOMe (0.18 M), HND-Cbz (0.06 M), or Spiro-OMeTAD (0.06 M)] + LiTFSI (0.03 M), FK209 Co (III) dopant (9.0 mM), TBP (0.20 M) in PhCl was spin-coated.

Method 2. Vacuum-deposition:
$ITO/SnO_2/Cs_{0.05}MA_{0.15}FA_{0.80}PbI_2Br_{0.25}$ (~500 nm)/HTM (15 nm)/MoO_3 (10 nm)/Au (80 nm)
HTM layer:
HTM and MoO_3 was vacuum-deposited at a rate of 0.2 Å/s and 0.1 Å /s, respectively.

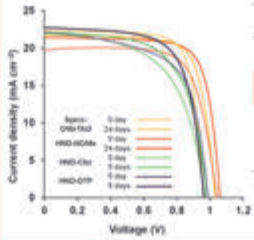

HTM	Time[a]	J_{sc}[b] (mA cm^{-2})	V_{oc}[b] (V)	FF[b]	PCE[b] (%)
Spiro-OMeTAD[c]	0 day	21.72	1.03	0.75	16.7
	24 days	22.32	0.96	0.76	16.4
HND-NOMe[c]	0 day	19.73	1.04	0.73	14.9
	24 days	21.43	1.06	0.76	17.2
HND-Cbz[d]	0 day	21.99	0.97	0.58	12.3
	5 days	22.02	0.98	0.63	13.7
HND-DTP[d]	0 day	22.15	0.98	0.63	13.8
	5 days	22.72	0.96	0.69	15.0

[a]Devices were kept in dry-box with the humidity around 20%. [b]Data in forward scan. [c]Devices were fabricated by spin-coating method. [d]Devices were fabricated by vacuum-deposition method.

Summary

- Three thermally stable, transparent, hole conducting materials were synthesized by connecting the partially oxygen-bridged triarylamine structure to carbazole , dithieno[3,2-*b*:2',3'-*d*]pyrrole, and 4,4'-dimethoxydiphenylamine through Buchwald-Hartwig C-N cross coupling reaction.
- The HOMO and LUMO levels lie higher than the corresponding VB and CB of typical perovskite layers, making them are suitable candidates for hole-transporting materials in perovskite solar cells. Moreover, these materials can be expected as promising materials for tandem solar cells due to their high transparency in the visible light region.
- The device using **HND-NOMe**, **HND-DTP** and **HND-Cbz** as HTM exhibits the best power conversion efficiency of 17.2%, 15.0% and 13.7%, respectively.

Acknowledgement

Financial supported from **IRCCS**, **NEDO**, **COI**, **JSPS**, and **ALCA**.

IRCCS The 2nd International Symposium @ Kyoto University, Uji campus on 25th–26th, January, 2019

Cage-Expansion of Fullerene from C_{60} to $C_{65}N$ and $C_{64}N$ Skeletons

Sheng Zhang, Yoshifumi Hashikawa, Yasujiro Murata*

Institute for Chemistry Research, Kyoto University, Uji, Kyoto 611-0011, Japan

INTRODUCTION

A cage expanded derivative

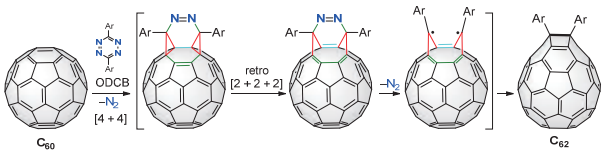

Rubin, Y. et al., *JACS* **2003**, *125*, 2066.

Only one example of chemical synthesis

THIS WORK & CONCLUSION

Novel method for synthesis of $C_{65}N$ and $C_{64}N$ cages

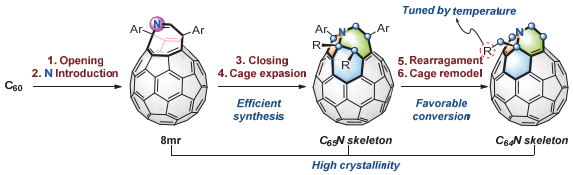

Rational strategy of cage expansion using open-cage derivatives

Restoration of open-cage fullerene derivatives

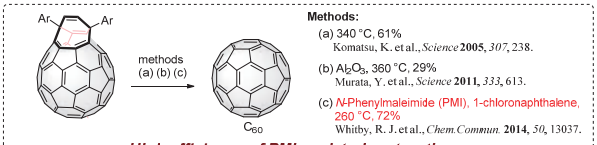

Methods:

(a) 340 °C, 61%
Komatsu, K. et al., *Science* **2005**, *307*, 238.

(b) Al_2O_3, 360 °C, 29%
Murata, Y. et al., *Science* **2011**, *333*, 613.

(c) *N*-Phenylmaleimide (PMI), 1-chloronaphthalene, 260 °C, 72%
Whitby, R. J. et al., *Chem. Commun.* **2014**, *50*, 13037.

High efficiency of PMI-assisted restoration

X-ray structures

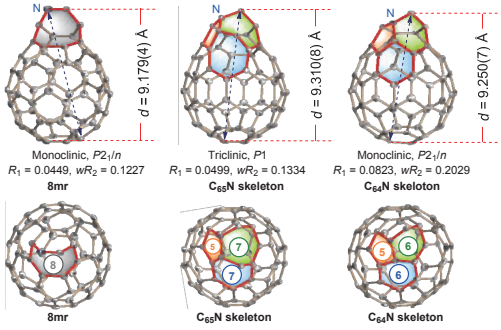

(The sutured regions are highlighted in red. Thermal ellipsoids are set in 50% probability levels. All of the substituents are omitted for clarify.)

Insertion of C_5N and C_4N units

Formation of pentagonal, hexagonal, and heptagonal rings

Enlargement of opening by PMI

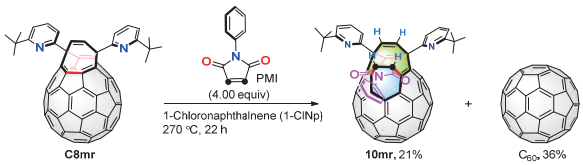

Successful insertion of a C_2 unit

Construction of $C_{65}N$ and $C_{64}N$ skeletons

Formation of expanded cages

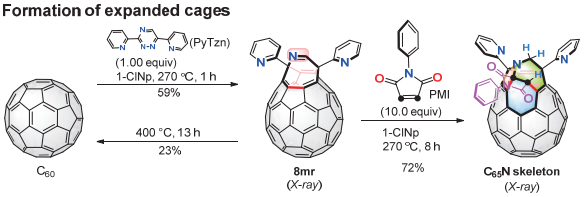

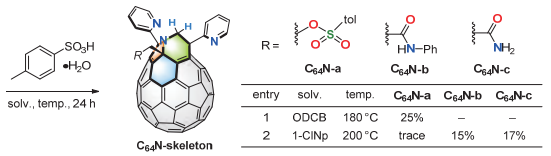

entry	solv.	temp.	$C_{64}N$-a	$C_{64}N$-b	$C_{64}N$-c
1	ODCB	180 °C	25%	–	–
2	1-ClNp	200 °C	trace	15%	17%

Construction of $C_{65}N$ and $C_{64}N$ cages

^{1}H NMR (CS_2 using a acetone-d_6 capillary, 500 MHz)

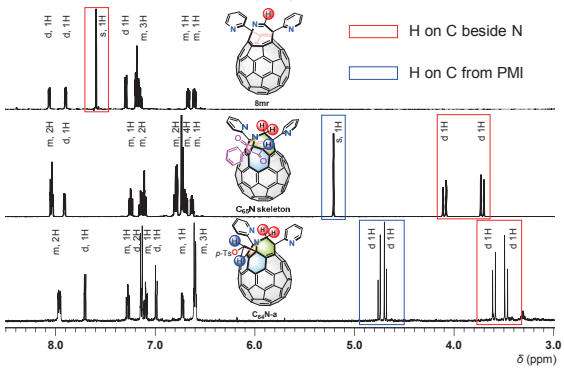

Alteration of cyclized reagents

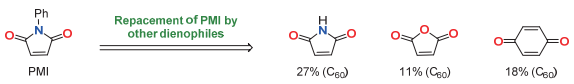

Only C_{60} without the formation of $C_{65}N$ skeletons

Plausible mechanism

Formation of $C_{65}N$ skeleton (M06-2X/6-31G(d,p))

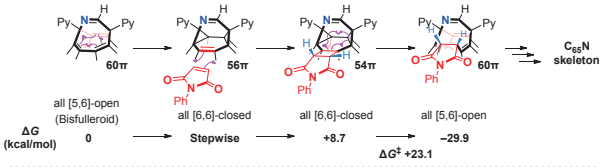

Formation of C_{60}

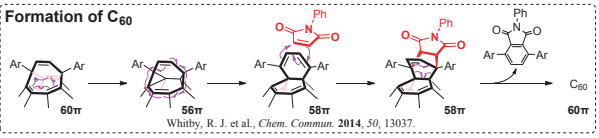

Whitby, R. J. et al., *Chem. Commun.* **2014**, *50*, 13037.

Cage-expansion to $C_{70}N_2$ skeletons

Cage-expansion with Bis-8mrs

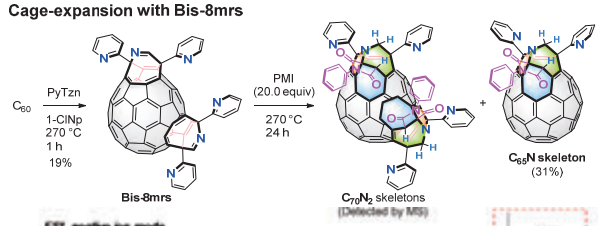

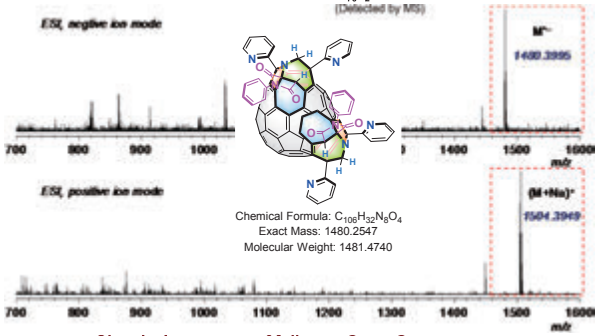

Chemical expansion of fullerene C_{60} to $C_{70}N_2$ skeletons

Dynamic Behavior of a Single *but* Hydrogen-bonded Water Molecule inside a Hydroxy Open-Cage Fullerene C_{60} Derivative

○Shota Hasegawa, Yoshifumi Hashikawa, Yasujiro Murata
Institute for Chemical Research, Kyoto University, Uji, Kyoto 611-0011, Japan

Introduction

H_2O molecule

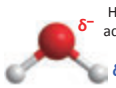

Studies on H-bonded H_2O are important
- protein foldings, drug delivery, catalyst…

Theoretical studies only, due to multiple H-bonds

Our approaches

$H_2O@C_{60}$
H_2O w/o H-bondings:
Murata, Y. et al., *Science* **2011**, *333*, 613–616.

$(H_2O)_2@C_{70}$
Hydrate cluster:
Murata, Y. et al., *Nat. Chem.* **2016**, *8*, 435–441.

H_2O molecule inside hydrophobic fullerene cage

⬇

Isolated H_2O molecule or H-bond without any interaction

This work & Summary

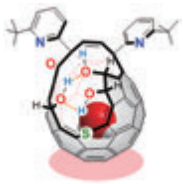

- *H-bonded single H_2O molecule*
- *Dynamics of the encapsulated H_2O*
- *Less acidic and less basic H_2O*

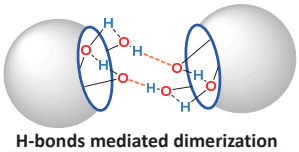

H-bonds mediated dimerization

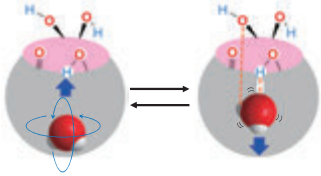

Switchable H-bonded H_2O molecule

Results and discussion

Synthesis

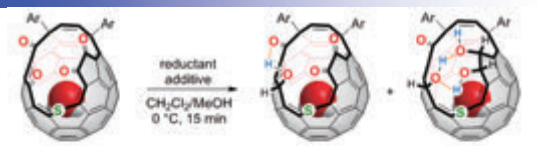

entry	reductant (equiv)	additive (equiv)	$H_2O@2$ (%)[a]	$H_2O@3$ (%)[a]
1[b]	BH_3•THF (1.20)	none	81	–
2	$NaBH_4$ (0.40)	none	47	–
3	$NaBH_4$ (1.00)	none	27	–
4	$NaBH_4$ (1.00)	$CeCl_3$ (10.0)	56	–
5	$NaBH_4$ (2.00)	$CeCl_3$ (10.0)	65	–
6	$NaBH_4$ (10.0)	$CeCl_3$ (10.0)	9	75

[a]Isolated yields. [b]The reaction was conducted at −78 °C.

H-bonded H_2O in the solid state

X-ray crystal $(H_2O)_{1.38}(C_{82}H_{32}N_2O_4S)_2$•NiOEP•$(C_6H_6)_2$
P-1, triclinic, R_1 = 6.22%, wR_2 = 18.04%

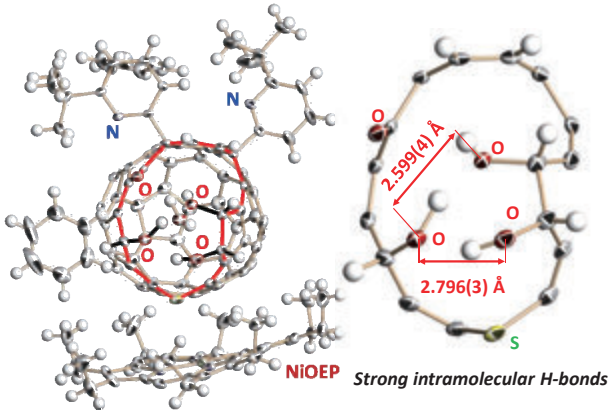

Strong intramolecular H-bonds

X-ray crystal $(H_2O)_{2.01}(C_{82}H_{32}N_2O_4S)_2$•$(CDCl_3)_5$
$P2_1/c$, monoclinic, R_1 = 15.77%, wR_2 = 45.34%

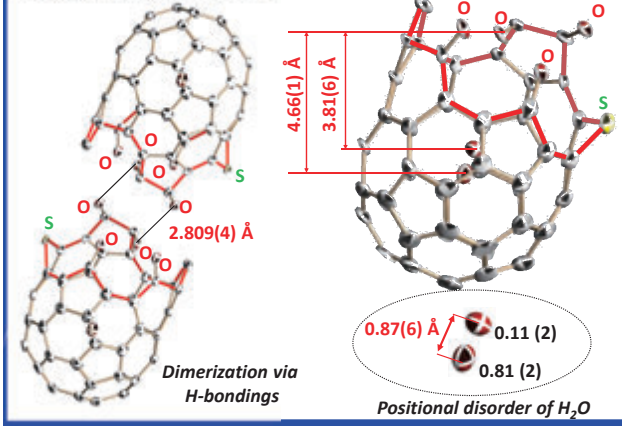

Dimerization via H-bondings

Positional disorder of H_2O

Dimerization behavior

^{1}H NMR ($CDCl_3$, 500 MHz, 300 K)

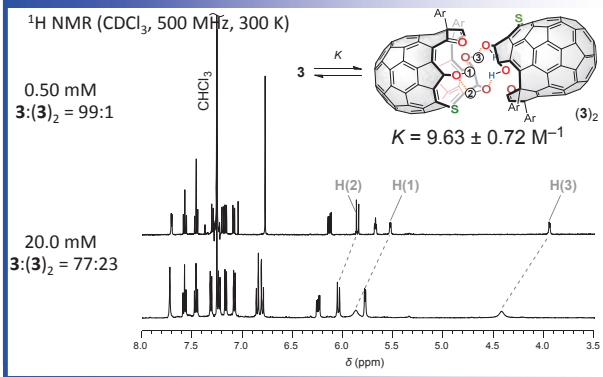

Dynamic behavior

^{1}H NMR (ODCB-d_4, 500 MHz, 260-360 K)

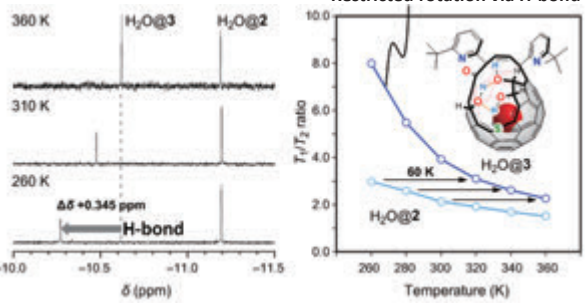

DFT calculations (B3LYP-D3/6-31G(d,P))

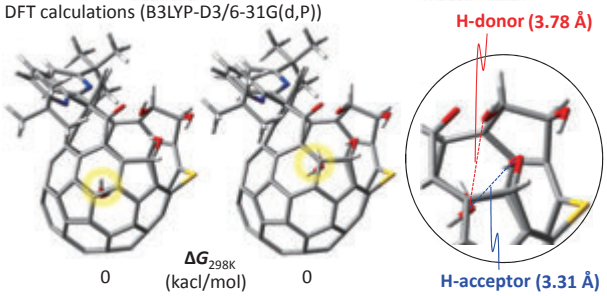

H-D exchange

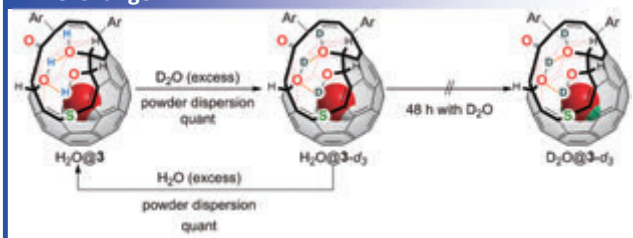

The encapsulated H_2O: less acidic and less basic than bulk water

Magnetic iron oxide nanoparticles as green and recyclable catalysts for the selective microwave-assisted oxidation of secondary alcohols

• Francesca Pincella, Katsuhiro Isozaki, Hikaru Takaya, Masaharu Nakamura

International Research Center for Elements Science, Institute for Chemical Research, Kyoto University, Uji 611-0011
Department of Energy and Hydrocarbon Chemistry, Graduate School of Engineering, Kyoto University, Kyoto 615-8510

Concept

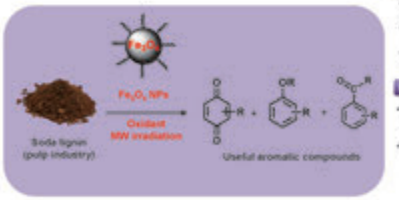

Why lignin?

- ✓ lignin is one of the main components of wood
- ✓ lignin is the most abundant aromatic material in nature
- ✓ sustainable resource, no "eat or drive" issue

Why iron oxide NPs?

- ✓ high microwave absorbing ability (local heating by electromagnetic induction)
- ✓ easy preparation, recovery and recycling of catalysts

Summary

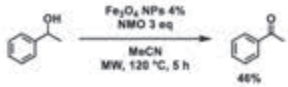

- Among various iron oxide nanoparticles, Fe_3O_4 (magnetite) is uniquely able to catalyze the oxidation of a secondary alcohol to the corresponding ketone with high selectivity and moderate yield under microwave irradiation.
- NMO was found to guarantee the highest selectivity without causing catalyst dissolution.
- Thanks to its magnetic properties, the catalyst can be easily recovered from the reaction mixture and reused multiple times.

Background

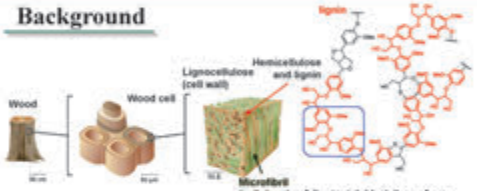

Wood consists of cellulose, hemicellulose and lignin.

Lignin makes up between 10 to 40% of the wood cell wall.

Complex with cellulose, hemicellulose and lignin

A lignin rich black liquor from pulp industry is mostly burned
World total: 600 million ton/year
Japan total: 70 million ton/year

A direct transformation of plant biomass to useful aromatic compounds is preferable:
lignin-based aromatic biorefinery

Substructure of Lignin (β-O-4 dimer)

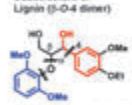

Oxidative degradation of lignin dimer unit:
1. Benzyl alcohol oxidation
2. Methoxybenzene oxidation


Chem. Asian J. 2016, 11, 1076 back cover


Org. Biomol. Chem. 2016, 14, 7466 front cover

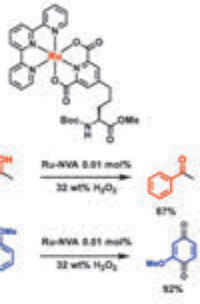

Oxidative Degradation of Wood Powder

Ru-cat 1: Ru-NVA + lignin binding peptide C416
Ru-cat 2: Ru-NVA

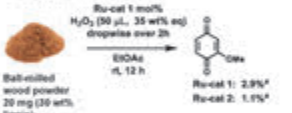

[a]Yield based on moles of monomer units of lignin.

Zul. Rep. 2016, 6, 21503
ACS Omega 2018, 3, 7483

Advantages: high yield and mild reaction conditions
Disadvantages: non-recyclable rare transition metal catalyst

Synthesis and Characterization of Fe_3O_4 NPs

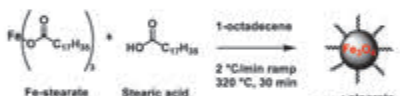

Averaged formula: $(Fe_3O_4)_{core}(stearate)_{1.08}$

XRD

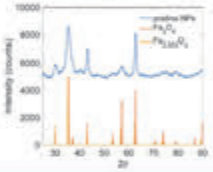

XAFS (BL14B2, SPring-8)

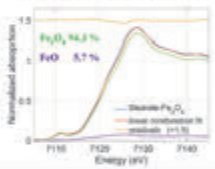

TEM

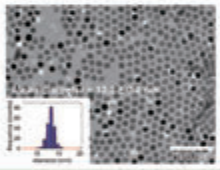

Fe_3O_4 NPs catalyzed oxidation of secondary alcohol

Catalyst optimization

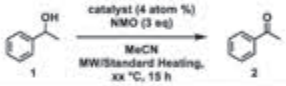

Entry	Catalyst	MW/SH	Temp. (°C)	Yield[a] (%) 2	RSM[a] (%) 1
1	Stearate-Fe_3O_4	MW	120	45.5	54.5
2	Stearate-Fe_3O_4	SH	80	0.7	>99
3	Commercial Fe_3O_4	MW	120	21	79
4	Commercial Fe_3O_4	SH	80	0.7	>99
5	Commercial Fe_2O_3	MW	120	3	97
6	Commercial Fe_2O_3	SH	80	0.6	>99
7	Commercial FeO	MW	120	0.7	>99
8	Commercial FeO	SH	80	0.7	>99
9	Commercial FeS_2[b]	MW	120	40	54

[a]Yield is calculated by ^{1}H NMR using 1,1,2,2-tetrachloroethane as an internal standard.
[b]The surface of pyrite is oxidized in air (Buckley, A.N., Woods, R. *Appl. Surf. Sci.* **1987**, *27*, 437-452).

Oxidant optimization

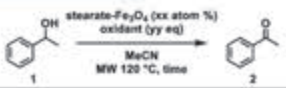

Entry	Catalyst loading (%)	Oxidant (eq)	Time	Yield[a] (%) 2	RSM[a] (%) 1
1	4	-	15 h	1	98
2	4	O_2 (1 atm)	15 h	1	98
3[b]	4	H_2O_2 (10)	15 h	34	19
4	4	Oxone (1)	5 h	6	80
5[c]	4	*m*-CPBA (1)	15 h	43	18
7[d]	4	$Pb(OAc)_4$ (1)	5 h	41	22
8	4	NMO (3)	15 h	45.5	54.5
9	0	NMO (3)	15 h	5	94

[a]^{1}H NMR yield using 1,1,2,2-tetrachloroethane as an internal standard. [b]Nanoparticles completely dissolved. [c]Nanoparticles partially dissolved, oxidant overs detected. [d]Unidentified products detected.

Catalyst recyclability

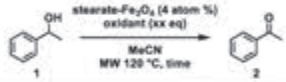

Entry	Cycle	NMO (eq)	Time	Yield[a] (%) 2	RSM[a] (%) 1
1	1	3	15 h	43	57
2	2	3	15 h	40	60
3	1	1	5 h	27[b]	73[b]
4	2	1	5 h	27[b]	73[b]
5	3	1	5 h	27	73
6	4	1	5 h	25	75
7	5	1	5 h	18	82

[a]Yield is calculated by ^{1}H NMR using 1,1,2,2-tetrachloroethane as an internal standard.
[b]Yield is calculated by ^{1}H NMR using 1,3,5-trimethoxybenzene as an internal standard.

Recycled catalyst time course

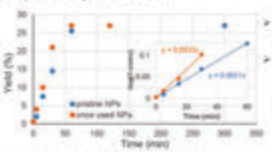

- Same final yield
- 1.8 times faster reaction rate with used catalyst

Proposed catalytic cycle

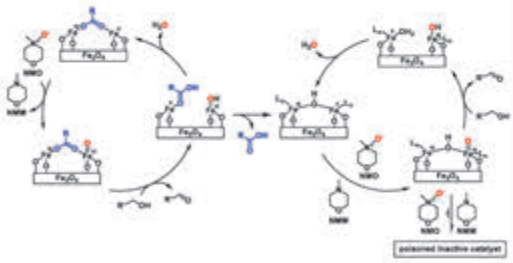

- The poisoned inactive catalyst can be easily recovered and reused multiple times after removal of the reaction media (the equilibrium shifts back to the active catalyst).
- The catalyst is fully deactivated after several cycles (>5) when phase transformation occurs from the original phase (Fe_3O_4, magnetite) to a Fe(II)-deficient oxide (γ-Fe_2O_3, maghemite).

Recycled catalyst: characterization

XRD

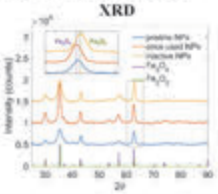

FT-IR

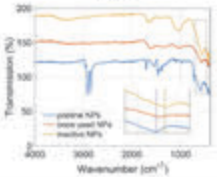

TEM

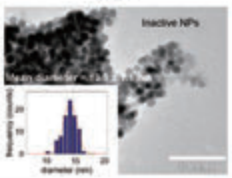

- conversion of the deactivated NPs from Fe_3O_4 to Fe_2O_3 (shift in XRD diffraction peaks and Fe-O IR peak)
- the final NPs size is 5% larger than the initial size

Light–Driven Entropically Unfavorable Coupling between *N*–methylamine and Aromatic Ketone

○Atsushi Hosokawa,[1,2] Takahiro Iwamoto,[1,2] Masaharu Nakamura[1,2]

[1]*International Research Center for Elements Science (IRCELS), Institute for Chemical Research, Kyoto University, Kyoto 611-0011*

[2]*Department of Energy and Hydrocarbon Chemistry, Graduate School of Engineering, Kyoto University, Kyoto 615-8520*

Introduction

Light–driven C–C bond formation

Thermodynamically uphill reaction
Unique reaction impossible by conventional, thermal reaction
Innovative chemical process to directly access functional molecule

·Norish–Yang Reaction (Intramolecular Reaction)

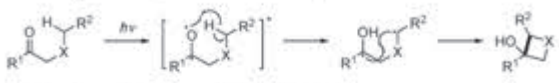

Endergonic reaction (ΔG = ca. 10 kcal/mol, $\Delta H > 0$)
Many applications in synthetic chemistry (e.g. natural product synthesis, CO_2 fixation)

1) Yang, N. C.; Yang, D. D. H. *J. Am. Chem. Soc.* **1958**, *80*, 2913.
2) Ishida, N.; Shimamoto, Y.; Murakami, M. *Angew. Chem. Int. Ed.* **2012**, *51*, 11750.

·Intermolecular Reaction between Aromatic Ketone and Aniline Derivatives

Only two examples
Photocatalyst and stoichiometric additive are necessary

1) Ding, W.; Lu, L. Q.; Liu, J.; Song, H. T.; Xiao, W. J. *J. Org. Chem.* **2016**, *81*, 7237.
2) Fava, E.; Millet, A.; Nakajima, M.; Loescher, S.; Rueping, M. *Angew. Chem. Int. Ed.* **2016**, *55*, 6776.

This Work

Endergonic reaction caused by entropy–loss ($\Delta G > 0$, $\Delta S > 0$)
Catalyst–free # Scalable (>10 g) # Chemoselective

1. Optimization of Base

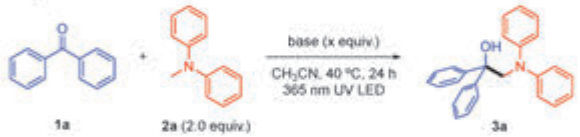

1a **2a** (2.0 equiv.) **3a**

entry	base (x equiv.)	yield (%)[a]	conv. (%)[a]
1	none	7	100
2	LiO*t*Bu (0.2)	73	100
3	NaO*t*Bu (0.2)	80	98
4	NaO*t*Bu (0.5)	57	87
5	NaO*t*Bu (1.0)	53	94
6[b]	NaO*t*Bu (0.2)	N.D.	10

[a]Determined by ^{1}H NMR. [b]Without light irradiation.

2. Substrate Scope

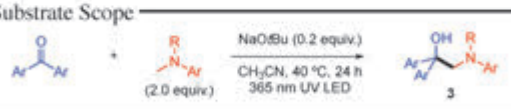

(2.0 equiv.) **3**

~scope of amines~

3b(R^1 = Me, R^2 = Me): 84%[a]
3c(R^1 = F, R^2 = H): 69%
3d(R = H): 74%
3e(R = Br): 69%
3f(R = CO_2Et): 51%
3g(R = Bpin): 71%
3h: 45%
3i: 55%[b]

~scope of ketones~

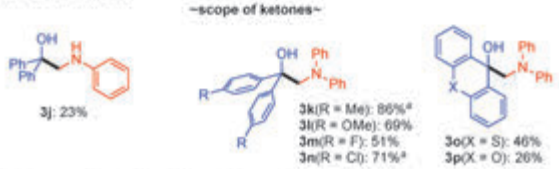

3j: 23%
3k(R = Me): 86%[a]
3l(R = OMe): 69%
3m(R = F): 51%
3n(R = Cl): 71%[a]
3o(X = S): 46%
3p(X = O): 26%

[a]LiO*t*Bu was used as a base. [b]Ketone (0.3 mmol) was used. Reaction was performed at rt.

3. Thermodynamics (DFT Calculation)

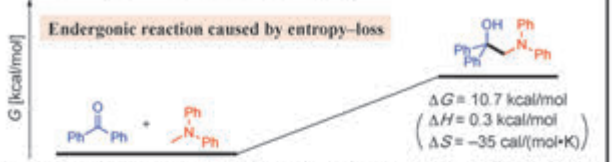

B3LYP/6-311++G(d,p) level of theory with SMD solvent model (solvent = CH_3CN) at 298.15 K
Translational entropy is corrected by Whitesides's model.

Mammen, M.; Shakhnovich, E. I.; Deutch, J. M.; Whitesides, G. M. *J. Org. Chem.* **1998**, *63*, 3821.

4. Synthetic Application

a) Large scale synthesis

(48 mmol) (2.0 equiv.) 76% (11.0 g)

b) Multi–coupling

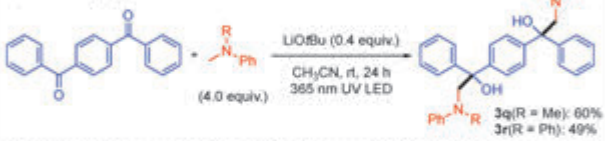

(4.0 equiv.) **3q**(R = Me): 60%
3r(R = Ph): 49%

c) Chemoselective coupling at *N*–methyl group

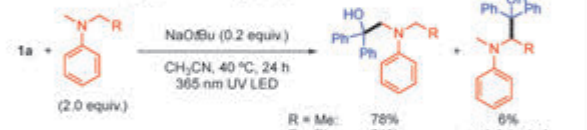

(2.0 equiv.)
R = Me: 78%
R = Ph: 81%
6% not detected

·Plausible mechanism of selective coupling at *N*–methyl group

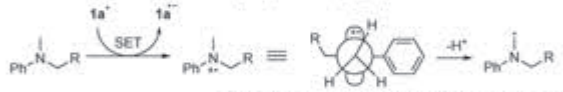

Lewis, F. D.; Ho, T. I.; Simpson, J. T. *J. Org. Chem.* **1981**, *46*, 1077.

5. Synthesis of π–Conjugated Enamines

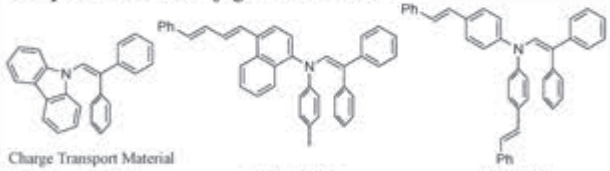

Charge Transport Material
Jankauskasu, V. et al. *Synth. Met.* **2008**, *158*, 462.

Photorecepter
Patent No.; JP 2011095476

Xerography
Patent No.; JP 2018115127

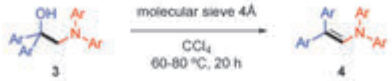

3 **4**

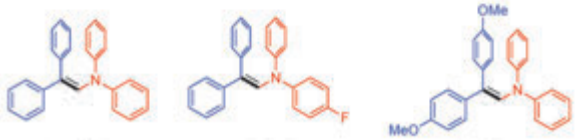

4a: 80% **4b**: 78% **4c**: 67%

Summary

Intermolecular coupling between *N*-methylamine and aromatic ketone was achieved.
This is thermodynamically uphill reaction caused by entropy-loss.
This reaction enables a novel synthetic route to access π–conjugated enamines.

Synthetic Resolution of Wood Lignin by Iron-Catalyzed Oxidation Reaction

○Takafumi Shanoh,[1),2)] Hikaru Takaya,[1),2)] Yuuya Nakatani,[1),3)] Masato Ito,[4)] Masaharu Nakamura[1),2)]

[1)]Institute for Chemical Research, Kyoto University, Japan, [2)]Department of Energy and Hydrocarbon Chemistry, Graduate School of Engineering, Kyoto University, Japan [3)]Faculty of Engineering, Kyoto University, Japan, [4)]Institute for Materials Chemistry and Engineering, Kyushu University, Japan

Introduction: Lignin

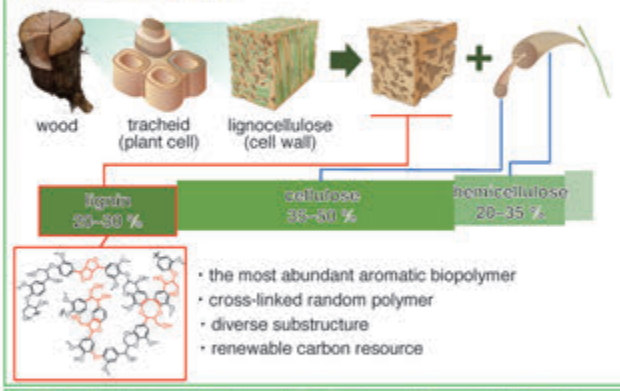

- the most abundant aromatic biopolymer
- cross-linked random polymer
- diverse substructure
- renewable carbon resource

Introduction: Enzymatic Depolymerization of Lignin in Nature

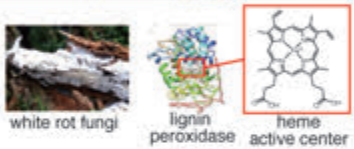

lignin —*degradation*→ CO_2, HCO_2H, organic acids

Horsfall, L. *et al. Front. Biol.* **2014**, *9*, 448–471.

Iron-Catalyzed Depolymerization of Lignin

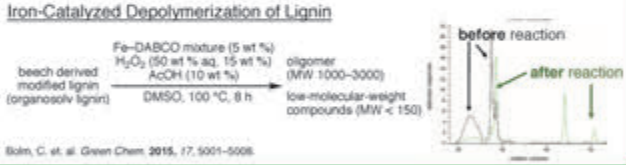

Bolm, C. *et. al. Green Chem.* **2015**, *17*, 5001–5008.

This Work: Iron-Catalyzed Oxidation of Benzylic Alcohols

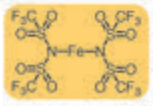

$Fe(NTf_2)_2$ catalyst

- Easy preparation from commercially available compounds
- Highly robust under oxidative condition
- Eco-friendly & the most abundant metal on earth

Optimization

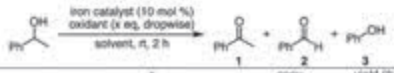

entry	iron catalyst	oxidant	x (eq)	solvent	conv. (%)	yield (%) 1	2	3
1	$Fe(NTf_2)_2$	H_2O_2[a]	6	EtOAc	84	64	<1	15
2	$Fe(OTf)_2$	H_2O_2[a]	6	EtOAc	86	57	<1	15
3	$FeCl_2{\cdot}4H_2O$	H_2O_2[a]	6	EtOAc	63	29	<1	3
4	$Fe(NTf_2)_2$	$tBuOOH$[b]	6	EtOAc	84	39	<1	13
5	$Fe(NTf_2)_2$	mCPBA[c]	1	EtOAc	74	36	1	nd
6	$Fe(NTf_2)_2$	H_2O_2[a]	6	CH_2Cl_2/CH_3CN (1/1)	86	50	1	10
7	$Fe(NTf_2)_2$	H_2O_2[a]	6	CH_2Cl_2	56	20	1	8
8[d]	$Fe(NTf_2)_2$	H_2O_2[a]	6	H_2O	97	5	<1	13

[a]Used in 35 wt % aqueous solution. [b]Used in 70 wt % aqueous solution. [c]added in one portion. [d]Black precipitate was formed.

Substrate Scope

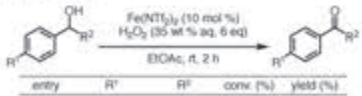

entry	R^1	R^2	conv. (%)	yield (%)
1	H	Me	92	61
2	CF_3	Me	69	42
3	Cl	Me	72	60
4	OMe	Me	>99	28
5	H	Ph	>99	>99

$Fe(NTf_2)_2$ vs Fenton Reaction

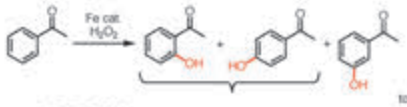

				total yield
$Fe(N(SO_2CF_3)_2)_2$	1	:	0	trace
Fenton reaction[a] +OH	2 : <0.1 : 3			4.6 %

[a]Tatsumi, S. *et al. J. Soc. Chem. Ind. Japan* **1961**, *64*, 463–466.

Iron-Catalyzed Oxidative Cleavage of β-O-4 Linkage

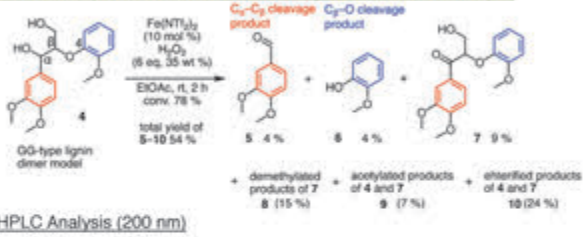

UHPLC Analysis (200 nm)

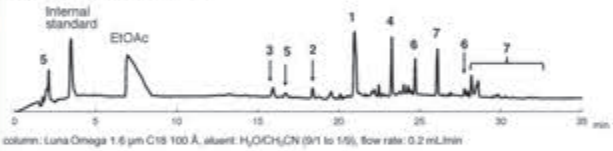

column: Luna Omega 1.6 μm C18 100 Å, eluant: H_2O/CH_3CN (9/1 to 1/9), flow rate: 0.2 mL/min

Mechanism of C_α–C_β, C_β–O Cleavage, Demethylation

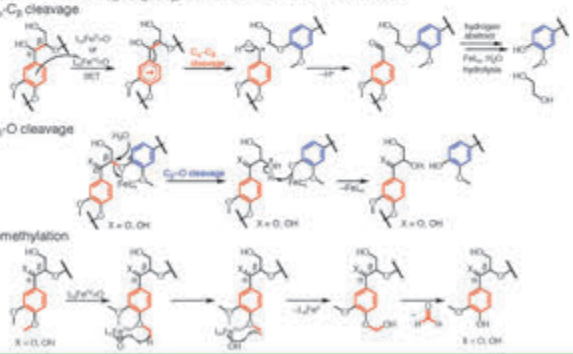

Iron-Catalyzed Depolymerization of Soda Lignin

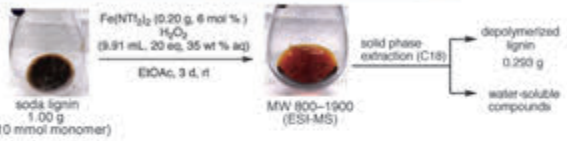

GPC Analysis

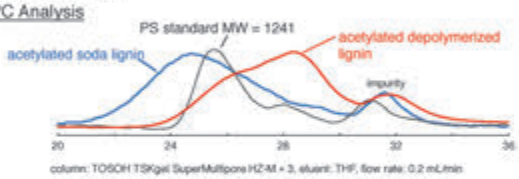

column: TOSOH TSKgel SuperMultipore HZ-M × 3, eluant: THF, flow rate: 0.2 mL/min

Iron-Catalyzed Delignification of Wood Powder

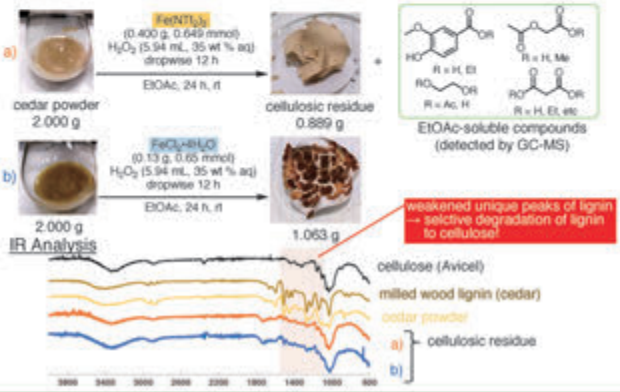

Crystal structures and properties of Ag-Bi-I compounds

Anucha Koedtruad, Taketo Handa, Tomoya Nakamura, Takashi Saito, Daisuke Kan, Yoshihiko Kanemitsu, Atsushi Wakamiya, and Yuichi Shimakawa

Institute for Chemical Research, Kyoto University, Uji, Kyoto 611-0011, Japan

Introduction

Solar cells

Main components:
1) Solar absorber layers
2) Hole transport layers (HTL)
3) Electron transport layers (ETL)

Working principle:
Photons captured by absorber materials activate electrons in valence bands to conduction bands producing electrons and holes. The charges then are separated: Electrons are injected into and transported through the ETL layer to an electrode, while positive charge holes move to the HTL layer and a counter electrode.

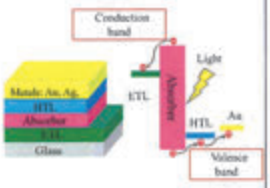

A solar cell device and a working principle

The key properties of solar absorbers:
suitable band gap (1.1 - 1.55 eV), strong solar absorption, high charge carrier mobilities, close band alignment with HTL and ETL, high stability and non-toxicity

Ag-Bi-I

Ag-Bi-I compounds were reported to be used as solar absorbers. The compounds are stable and non-toxicity.
- $AgBiI_4$ ($Ag_{0.5}Bi_{0.5}I_2$) and $AgBi_2I_7$ ($Ag_{0.29}Bi_{0.57}I_2$) with defect-spinel-type structures
- Ag_3BiI_6 ($Ag_{0.43}Bi_{0.14}I_2$) and Ag_2BiI_5 ($AgBi_{0.33}I_2$) with $CdCl_2$-type structures


$CdCl_2$-type structure

Problems at the current stage:
- It was difficult to obtain single phase samples.
- Actual chemical compositions for the compounds were not revealed.
- Detailed crystal structures and structure-property relations were not clarified.

Aims of the research

- Synthesis of single phase of Ag-Bi-I compounds
- Analysis of chemical compositions and detailed crystal structures
- Evaluation of optical and electrical properties and the structure-property relations


Defect-spinel-type structure

Reference: *Chem Commun.* **2017**, *53*, 20 – 44.

Experiments

Synthesis by solid state reaction

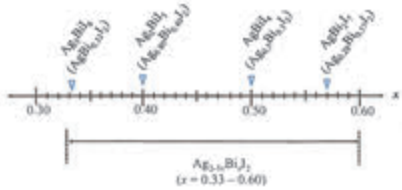

Compounds with general formula $Ag_{2-3x}Bi_xI_2$ have been prepared. The compositions were varied with $0.33 \le x \le 0.60$ to cover the range of compositions of the previously reported compounds

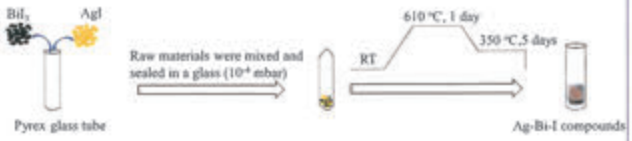

Materials characterization

- Phase identification by XRD
- Structure analysis with synchrotron XRD data
- Measurement of Valence band energy levels by photoelectron spectroscopy
- Measurement of band gap by UV-Vis spectroscopy
- Measurement of electrical conductivity for transport property analysis by AC 2-probe technique

Results and discussion

Synchrotron X-ray diffraction and structural refinement

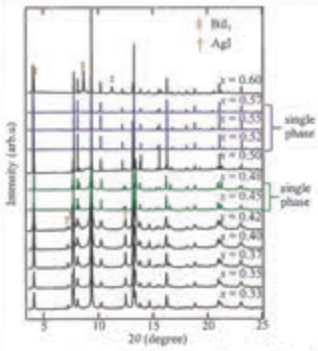

Synchrotron X-ray diffraction spectra of $Ag_{2-3x}Bi_xI_2$

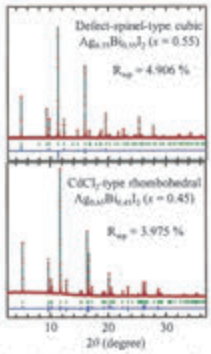

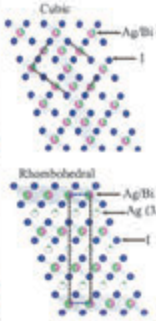

Examples of structural refinement of samples with cubic and rhombohedral structures

The structure analysis of $Ag_{2-3x}Bi_xI_2$ (x = 0.33 – 0.60) with synchrotron X-ray diffraction data reveals two distinct phases: the defect-spinel-type cubic and the $CdCl_2$-type rhombohedral structures.

Atom	Site	Occupancy
Bi	16c (0 0 0)	0.5558(5)
Ag	16c (0 0 0)	0.3537(5)
I	32e (x x x) x =0.25248(4)	1.000

The cubic structure, $Fd\bar{3}m$ space group
Single phase compositions : $x = 0.52 – 0.57$
The phase is obtained at the Bi-rich compositions. The structure consists of a cubic close-packed I-ion sublattice. The Ag and Bi atoms partially occupy at the octahedral 16c sites, giving cation deficiency.

Atom	Site	Occupancy
Bi	3a (0 0 0)	0.431(2)
Ag1	3a (0 0 0)	0.569(2)
I	6c (0 0 z) z =0.24827(5)	1.000
Ag2	3b (0 0 1/2)	0.081(2)

The rhombohedral structure, $R\bar{3}m$ space group
Single phase compositions : $x = 0.45 – 0.48$
The phase is obtained at the Ag-rich compositions. The structure consists of the cubic close-packed I-ion sublattice. The Ag and Bi atoms fully occupy at the octahedral 3a sites, and additional Ag atoms are located at an interstitial 3b site between the octahedral layers.

Valence band level (VB) measurements

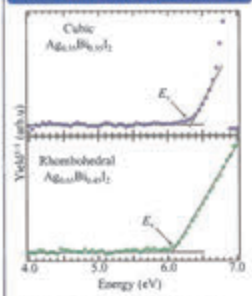

Photoelectron spectra of the samples

Band gap (Eg) measurement

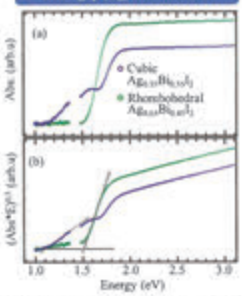

Absorption spectra (a) and Tauc plots (b) of the samples

Conductivity measurement

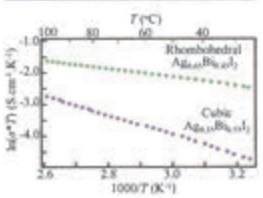

Arrhenius plots of AC electrical conductivity of the samples

Samples	Valence band level (eV)	Indirect band gap (eV)	Activation energy (kJ/mol)
Rhombohedral			
$Ag_{0.55}Bi_{0.45}I_2$ (x = 0.45)	-6.12 ± 0.03	1.50	10.89
$Ag_{0.52}Bi_{0.48}I_2$ (x = 0.48)	-6.13 ± 0.04	1.53	15.41
Cubic			
$Ag_{0.48}Bi_{0.52}I_2$ (x = 0.52)	-6.38 ± 0.01	1.08	28.32
$Ag_{0.45}Bi_{0.55}I_2$ (x = 0.55)	-6.36 ± 0.04	1.11	25.77
$Ag_{0.43}Bi_{0.57}I_2$ (x = 0.57)	-6.41 ± 0.04	1.10	27.21

The rhombohedral structure compounds have shallower valence band energies, larger indirect band gap energies, and higher electrical conductivity with lower activation energy (E_a) than the cubic structure compounds. The distinct properties result from the additional Ag occupation in the rhombohedral phase and the deficiencies of the octahedral site in the cubic phase.

Conclusions

- $Ag_{2-3x}Bi_xI_2$ (x = 0.33 – 0.60) compounds have been prepared by solid state reaction.
- The Ag-rich compositions yielded the rhombohedral phase and the single phase was obtained in the composition range of $0.45 \le x \le 0.48$, while the Bi-rich compositions yielded the cubic phase and the single phase was obtained with $0.52 \le x \le 0.57$.
- The I atoms consisted of the cubic close-packed sublattice for both structures, and the Ag and Bi atoms of the rhombohedral phase fully occupied octahedral sites while those of the cubic phase partially occupied the octahedral sites, giving cation deficiency (defect-spinel structure).
- The rhombohedral structure compounds showed shallower valence band energies, larger band gaps, and higher electrical conductivity (lower E_a) than the cubic structure compounds. The defect structures played important roles in the distinct properties.

Nanoscale Oxygen Dynamics in epitaxial $SrFeO_{2.5+\delta}$ thin films

Yooun Heo[1,*], Daisuke Kan[1], Yuichi Shimakawa[1,2]
[1]Institute of Chemical Research, Kyoto University, Gokasho, Uji, Kyoto 611-0011, Japan
[2]Integrated Research Consortium on Chemical Sciences

*Email:heo.yooun.56x@scl.kyoto-u.ac.jp

Kyoto University | Institute for Chemical Research | Shimakawa Group

Introduction

- Oxygen off-stoichiometry in perovskite (PV) has been well-known to strongly influence their structural and physical properties
- The off-stoichiometry provides nanoscale oxygen dynamics—including oxygen ion incorporation and movements during redox reactions—resulting in emergence of functionalities such as fast redox reactions and resistive switching
- A thorough understanding of the local oxygen ion dynamics in oxides and their link with functionalities is still lacking

Objectives

- Evaluation of nanoscale oxygen dynamics and redox reactions induced by air-annealing and electric field
- Fabrication of epitaxial $SrFeO_{2.5}$ (SFO2.5) thin films on Nb-$SrTiO_3$ substrate by pulsed laser deposition and oxidation process for SrFeO2.5+δ (SFO2.5+δ) samples by air-annealing at 100-600 °C
- Characterization of structures and local conduction properties of oxidized $SrFeO_{2.5+\delta}$ by X-ray diffraction and conduction AFM (c-AFM)

Results and Discussion

Structural characterization of as-grown $SrFeO_{2.5}$ film and a film air-annealed at 600 °C

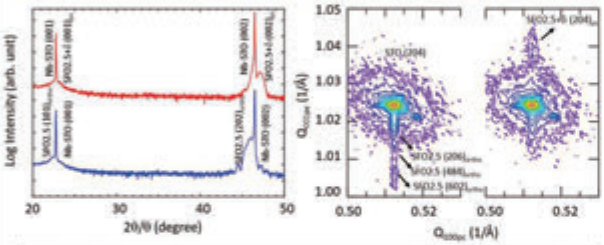

2θ-θ profile and the reciprocal spacing mapping indicate the air-annealing-induced shrinkage of the out-of-plane lattice while the in-plane lattice constant remain unchanged and fixed by the substrate. The air-annealing results in oxygen incorporation into the brownmillerite (BM) structure and as a result the annealed film has the perovskite (PV)-like structure.

Oxygen incorporation-induced evolution of structures and electrical conduction in SrFeO2.5+δ

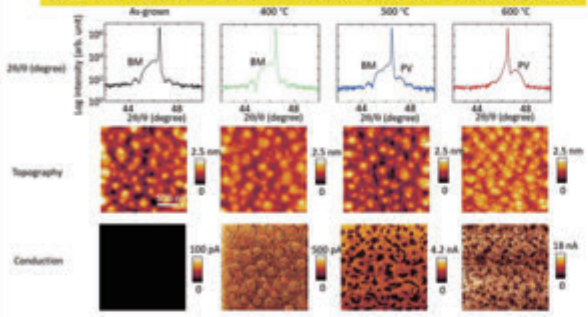

The oxidation-induced structural evolution from the BM to PV structure occurs locally, not homogeneously in the entire film, and that the PV phase (bright) is more conducting than the BM phase (dark).

Local conductions due to oxygen dynamics in SrFeO2.5+δ

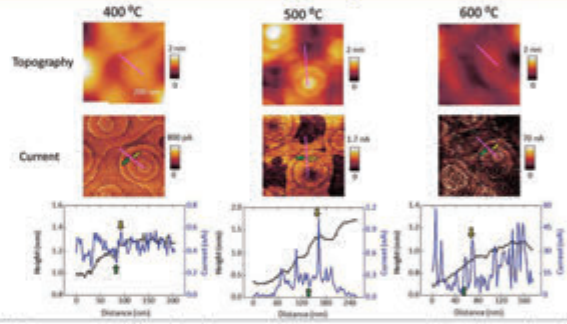

Enhancement of the local current at terraces near outer step edges is clearly seen indicating that the oxygen ions are preferably introduced in these local regions and diffused into the films.

Electric-field-dependent local conduction in SrFeO2.5+δ

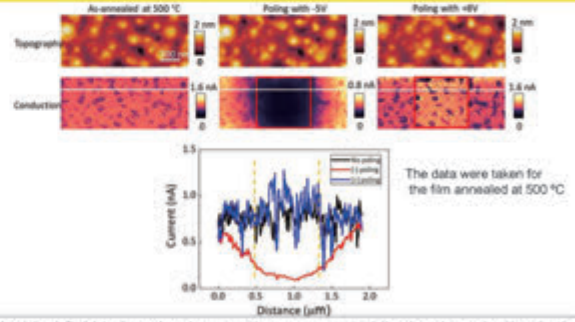

The data were taken for the film annealed at 500 °C

Electrical-field-induced redox reactions can control the local conduction in the SFO2.5+δ film. Importantly, the electric-field-induced oxidation and related oxygen incorporation preferentially occurs in the local terraces near the step edges, as do the air-annealing-induced oxidation and incorporation of oxygen ions involved.

Conclusions

- We investigate local electrical conduction associated with the oxidation of as-grown BM SFO2.5 thin films, revealing the significance of nanoscale oxygen dynamics and associated on the redox reactions in SFO2.5 films.
- The BM-to-PV structural changes due to air-annealing and oxidizing the film enhance conduction only in the terraces near the outer step edges.
- The oxidation proceeds by preferential incorporation of oxygen in the local regions of the terraces and diffusion of that oxygen into the film
- The local conduction in the film can be controlled by electric-field-induced redox reactions.

Novel Hexagonal Perovskite $Ba_4Fe_3NiO_{12}$ Containing Tetravalent Fe and Ni Ions

○Zhenhong TAN・Takashi SAITO・Fabio DENIS ROMERO・Midori AMANO PATINO・Masato GOTO
・Yuichi SHIMAKAWA（*Institute for Chemical Research*, Kyoto University）

Introduction

・Unusual high-valence Fe-/ Ni-containing perovskite oxides

$CaFe^{4+}O_3$ Fe^{4+}-containing perovskite oxides [1-4]

$BaFeO_{3-\delta}$ $BaFe^{3+}_{1/3}Fe^{(4+\sigma)+}_{2/3}O_{3-\delta}$

$SrFe^{4+}O_3$

Ni^{4+}-containing perovskite oxides [5,6]

$BaNi^{4+}O_3$ $SrFe_{0.5}Ni_{0.5}{}^{4+}O_3$

The solid compounds containing unusual high-valence Fe and Ni are rare. The purpose of the research is to investigate new perovskite oxides that contain those unusual high-valence ions in a Ba-Fe-Ni solid solution system.

[1] M. Takano, *et al. Mat. Res. Bull.* **12**, 923 (1977) [2] P. K. Gallagher, *et al. The Journal of Chemical Physics.* **41**, 2429(1964) [3] P. K. Gallagher, *et al. The Journal of Chemical Physics.* **43**, 516(1965) [4] S. Mori, *J. Am. Ceram. Soc.*, **49**, 600(1966) [5] Y. Takeda, *et al. Acta Crystallogr. B*, **32**, 2464(1976) [6] H. Seki, *et al. Angewandte Chemie International Edition*, **55**, 1360(2016)

・Hexagonal perovskites and related structures [7]

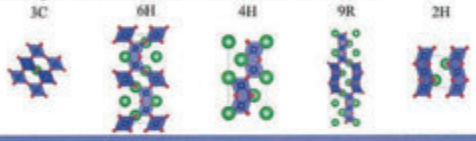

Stacking sequence	ccc...	cchcch...	chch...	chhchh...	hhh...
Octahedra connection	corner sharing	face sharing corner sharing	face sharing corner sharing	face sharing corner sharing	face sharing

[7] The Chemical Society of Japan, *Perovskite-Related Compounds: Storehouse of Functions*. 1997, pp. 11–13.

Experimental Details(High pressure synthesis)

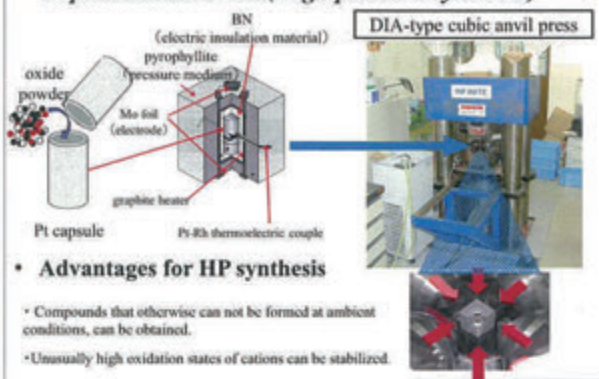

・ **Advantages for HP synthesis**

・Compounds that otherwise can not be formed at ambient conditions, can be obtained.

・Unusually high oxidation states of cations can be stabilized.

Synthesis conditions
Pressure：～ 10GPa
Temperature：～ 1500℃

・ **Preparation**

・Synthesis of precursors: $BaNiO_{2.81}$ and $BaFeO_{2.67}$

$BaNiO_{2.81}$: A mixture of stoichiometric $BaCO_3$ and NiO was calcinated in O_2 at 1000 ℃ for 12 hours. The oxygen content was determined by thermogravimetry.

$BaFeO_{2.67}$: A mixture of stoichiometric $BaCO_3$ and Fe_2O_3 was calcinated in O_2 at 1000 ℃ for 12 hours. The oxygen content was determined by iodometric titration.

・High pressure synthesis of $BaFe_xNi_{1-x}O_3$

The precursors were mixed [(1-x)$BaNiO_{2.81}$ + x$BaFeO_{2.67}$ + $KClO_4$] (x = 0, 0.1, 0.2, 0.5, 0.75, 0.8, 0.9 and 1), sealed in a Pt capsule, then treated under 8 GPa at 1000 ℃ for 30 min, and quenched to room temperature. The obtained products were washed by distilled water.

Results and discussion

・ **XRD patterns of $BaFe_xNi_{1-x}O_3$**

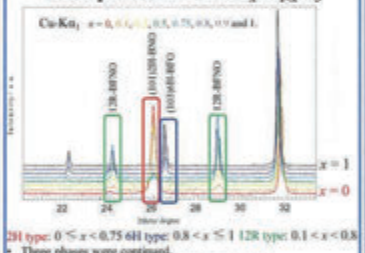

2H type: $0 \le x < 0.75$ 6H type: $0.8 < x \le 1$ 12R type: $0.1 < x < 0.8$

- Three phases were continued.
- 12R-type single phase was obtained at $x = 0.75$.

・ **Structural analyses of $BaNiO_3$ and $BaFeO_3$**

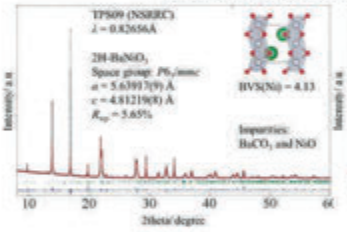

$BaNi^{4+}O_3$

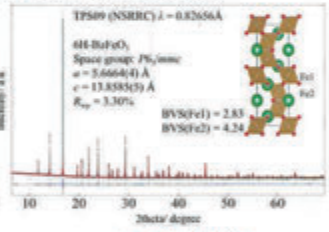

$BaFe^{3+}_{1/3}Fe^{(4+\sigma)+}_{2/3}O_3$

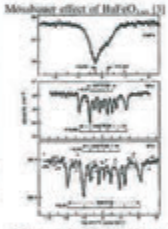

BS(Fe1) = +0.24 (RT) and +0.41 (4 K)
BS(Fe2) = -0.29 (RT) and -0.35 (4 K)

・ **Phase diagram of $BaFe_xNi_{1-x}O_3$**

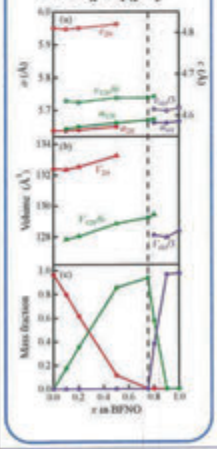

・ **Structural analysis of $Ba_4Fe_3NiO_{11.5}$**

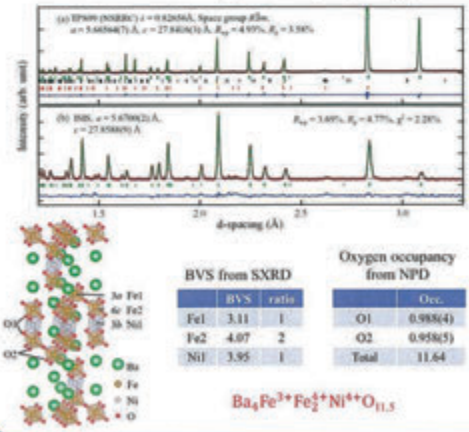

BVS from SXRD

	BVS	ratio
Fe1	3.11	1
Fe2	4.07	2
Ni1	3.95	1

Oxygen occupancy from NPD

	Occ.
O1	0.988(4)
O2	0.958(5)
Total	11.64

$Ba_4Fe^{3+}Fe^{4+}_2Ni^{4+}O_{11.5}$

・ **Mössbauer effect of $Ba_4Fe_3NiO_{11.5}$**

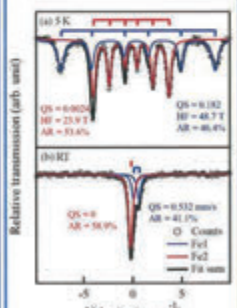

	IS (mm/s, RT)	IS (mm/s, 5 K)
Fe1	+0.354	+0.473
Fe2	-0.220	-0.145

・ **Magnetic properties of $Ba_4Fe_3NiO_{11.5}$**

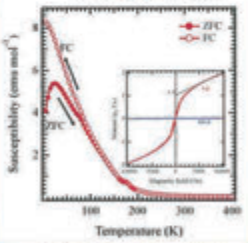

Magnetic transition at about 200 K
Ferromagnetism or weak ferromagnetism

In BFNO75: $V[(Ni^{4+}O_6)^{8-}]$ = 9.089 Å^3
In $BaNiO_3$: $V[(Ni^{4+}O_6)^{8-}]$ = 8.824 Å^3

Ni^{4+} is in low-spin $3d^6$ configuration. The weak ferromagnetism seems to originate from antiferro-(or ferri-)magnetic coupling between Fe^{3+} and Fe^{4+} spins.

Conclusions

- A new 12R-type perovskite oxide $Ba_4Fe_3NiO_{11.5}$ has been synthesized by high-pressure high-temperature technique.
- The compound contains unusual high-valence Fe and Ni ions ($Ba_4Fe^{3+}Fe^{4+}_2Ni^{4+}O_{11.5}$).
- $Ba_4Fe_3NiO_{11.5}$ shows a ferromagnetic-like behavior below about 200 K with small magnetization.
- Ni^{4+} is suggested to have low-spin electron configuration. The observed week ferromagnetism seems to originate from coupling between Fe^{3+} and Fe^{4+} spins.

Directional electron transfer coupled spin-crossover in the crystals of [FeCo] di-nuclear complexes facilitating ultrafast polarization switching

Pritam Sadhukhan, Shengqun Su, Shinji kanegawa, Osamu Sato*

Institute for Materials Chemistry and Engineering, Kyushu University, 744 Motooka, Nishi-ku, Fukuoka 819-0395, Japan.

Research Motive

To develop functional magnetic materials to obtain thermally induced phase transition from nonpolar to polar structure via electron transfer resulting polarization switching at a crystalline level which can be widely used in pyroelectric sensors & memory devices.

Introduction

Polarization switching

Ion displacement

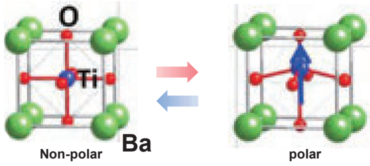

D. Fu et al. Intech DOI: 10.5772/61017
Ferroelectric materials – Synthesis & characterization

Charge transfer in molecules

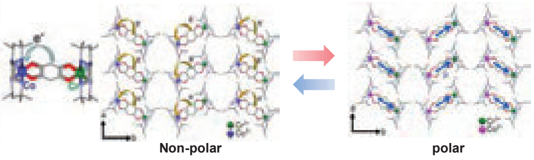

S. Kanegawa, *J. Am. Chem. Soc.* **2016**, *138*, 14170-14173.

Background

Valance tautomerism

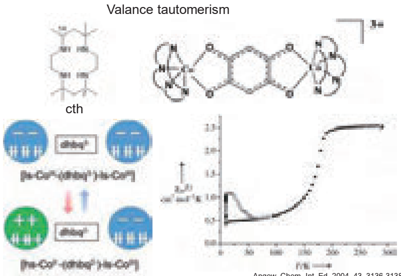

Angew. Chem. Int. Ed. 2004, 43, 3136-3138

Result & discussion

Synthesis of [(Fe(*RR*-cth))(Co(*SS*-cth))(*μ*-dhbq)](PF$_6$)$_3$

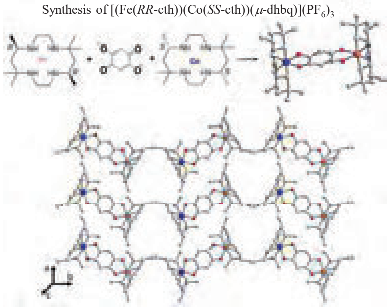

Polarization direction control: chiral methodology

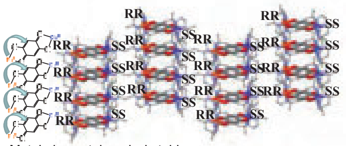

Metal elemental analysis table:

Unit: mass%

	Co	Fe
1st analysis	4.72	4.49
2nd analysis	4.71	4.47
Average value	4.72	4.48

The composition ratio:

	Co	Fe
1st analysis	0.998	1
2nd analysis	0.999	1
Average value	0.998	1

Crystal data:

	[(Fe(SS-cth))(Co(RR-cth))(dhbq)](PF$_6$)$_3$	
Empirical Formula	$C_{38}H_{74}CoF_{18}FeN_8O_4P_3$	$C_{38}H_{74}CoF_{18}FeN_8O_4P_3$
Formula Weight	1256.73	1256.73
temp(K)	40	130
Crystal System	monoclinic	monoclinic
Lattice Type	Primitive	Primitive
Space group	$P2_1$(#4)	$P2_1$(#4)
a(Å)	8.8092(5)	8.8881(7)
b(Å)	29.7189(16)	30.327(2)
c(Å)	10.1576(6)	10.1858(8)
α(deg.)	90	90
β(deg.)	110.121(8)	110.125(8)
γ(deg.)	90	90
V (Å^3)	2497.0(3)	2578.0(4)
Z value	2	2
D_{calc}(g/cm^3)	1.671	1.619
radiation	Sr(l = 0.70070 Å)	Sr(l = 0.70070 Å)
R_1 (I>2.00σ(I))	0.0557	0.0868
wR_2 (all)	0.1457	0.2321
GOF	1.073	1.066
Frack parameter	0.05(3)	0.02(3)

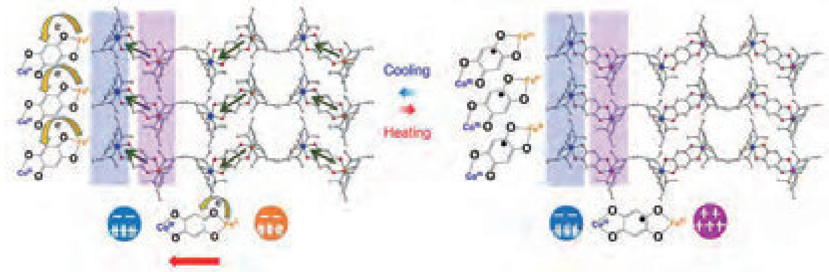

Magnetic susceptibility data

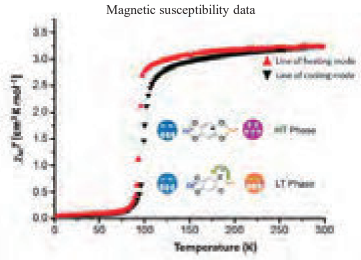

Variable temperature FT-IR spectrum

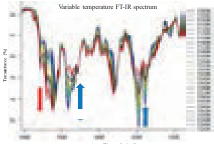

- CO stretching vibrations for dhbq^{2-} : **1470 cm^{-1}** & **1290 cm^{-1}**
- CO stretching vibrations for dhbq^{3-} : **1525 cm^{-1}**

Variable temperature Raman spectrum

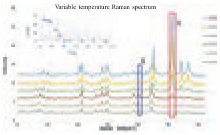

- [Fe^{II} –O] stretching frequency band : **567 cm^{-1}**
- Shift of **500 cm^{-1}** band (Fe^{II}-O) to **490 cm^{-1}** band (Fe^{III}-O) with increasing temperature

Mass spectroscopy data in acetone

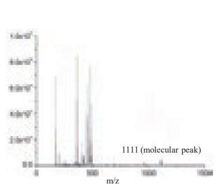

Circular dichromism spectra in acetone

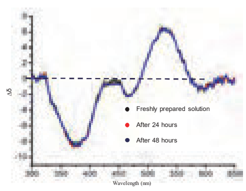

Pyroelectric data

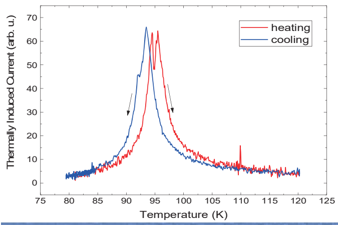

Selected bond length table

	[(Fe(SS-cth))(Co(RR-cth))(dhbq)](PF6)$_3$		[(Fe(RR-cth))(Co(SS-cth))(dhbq)](PF6)$_3$	
	40 K	130 K	40 K	130 K
Fe-O(Å)	1.898(7)	2.015(7)	1.886(16)	2.017(9)
	1.900(7)	2.013(6)	1.848(15)	2.011(8)
Fe-N(Å)	2.058(8)	2.158(9)	2.028(17)	2.148(11)
	2.032(8)	2.147(9)	2.014(19)	2.131(10)
	2.054(9)	2.168(9)	1.950(18)	2.147(11)
	2.005(8)	2.139(8)	2.062(18)	2.138(11)
Co-O(Å)	1.897(7)	1.889(7)	1.878(16)	1.894(9)
	1.892(7)	1.892(7)	1.908(16)	1.888(8)
Co-N(Å)	2.025(9)	2.030(10)	1.99(2)	2.016(12)
	2.024(8)	1.964(8)	2.059(18)	1.987(12)
	2.012(9)	2.026(10)	1.996(18)	1.972(10)
	1.986(8)	2.005(9)	2.00(2)	2.027(12)

Temperature dependent X-ray absorption spectroscopy data

Fe pre-edge XAS data

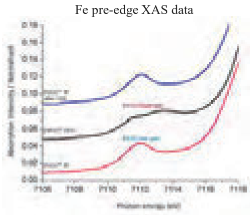

Fe K-edge & Co K-edge XAS data

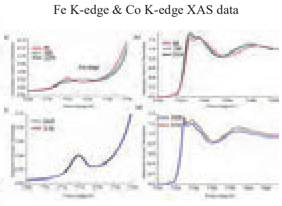

Conclusion

- A dinuclear complex [{Fe(RR-cth)}{Co(SS-cth)}(dhbq)](PF$_6$)$_3$ is synthesized by chirality-assisted methodology that played an important role in the polarization switching at the crystalline level.
- Charge transfer coupled gradual thermal spin-crossover was found at 85 K with thermal hysteresis.
- There is certain possibility to obtain valence tautomeric transition by substituting the metal ion with another paramagnetic metal (3d or 4d) to achieve switching with different electronic ground state.

Tetrahydrofuran-Triggered Magnetic Coupled with Vapochromism Switching in a Cobalt(II)-Based Single-Ion Magnet

Sheng-Qun Su, Shu-Qi Wu, Shinji Kanegawa, Osamu Sato

Institute for Materials Chemistry and Engineering, Kyushu University, and IRCCS

Control of Magnetic Property

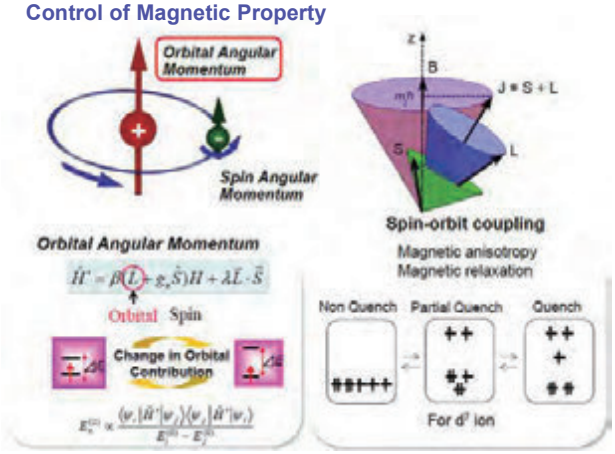

orbital …… coordination number …… spin

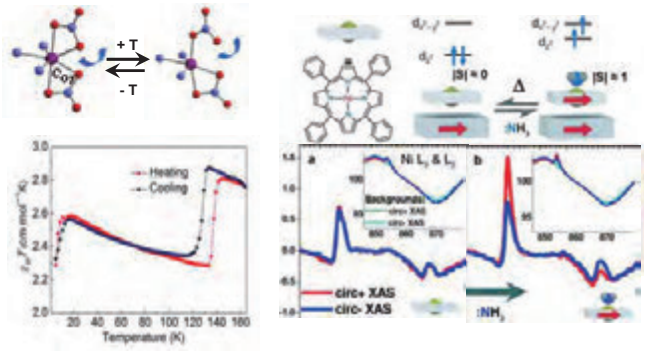

Su S.-Q. et.al

Angew Chem Int Ed. 52, 4568-4671 (2013)

Results and Discussion

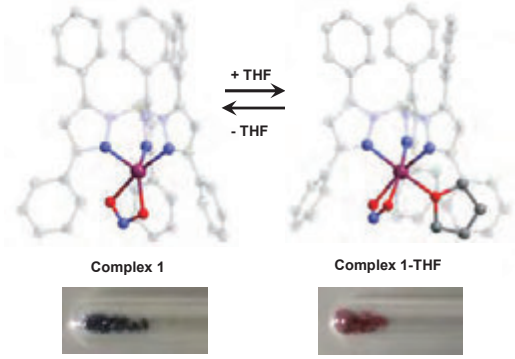

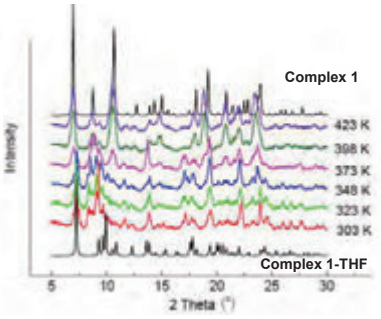

The variable temperature powder X-ray diffraction data

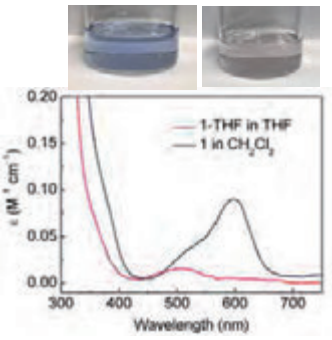

UV-Vis spectra of solution samples

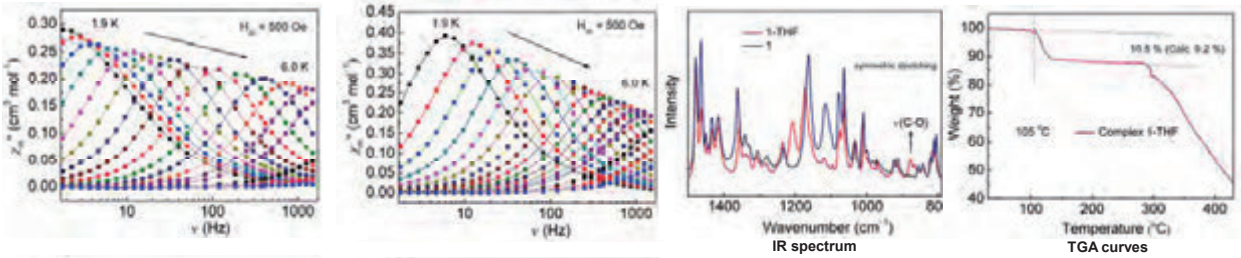

IR spectrum

TGA curves

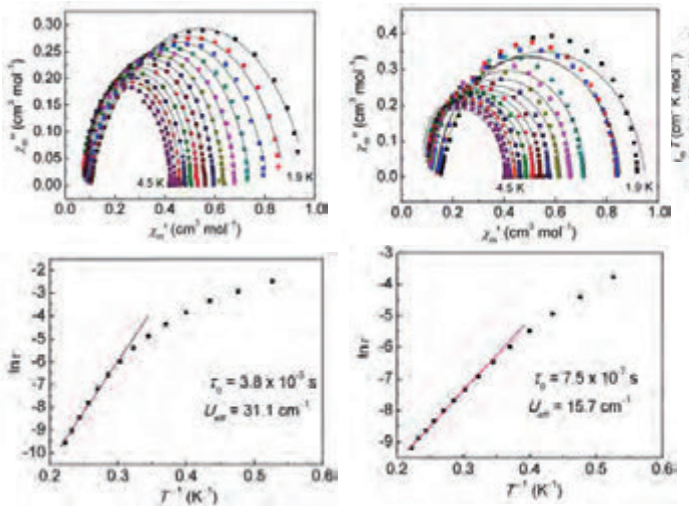

The static magnetic properties

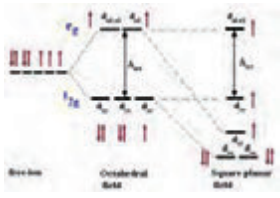

Energy level of the d-orbitals

The dynamic magnetic properties of complexes 1 (left) and complex 1-THF (right).

Conclusion

Key words

- single-ion magnet
- coordination number
- magnetic momentum
- orbital angular momentum
- relaxation time
- vaporchromism

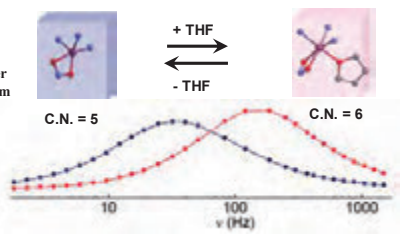

Aldol Reaction Type C–C Bond Formation Catalyzed by a Mononuclear Copper(II)-Superoxide Complex

○ Tsukasa ABE, Yuta HORI, Yoshihito SHIOTA, Kazunari YOSHIZAWA

Institute for Materials Chemistry and Engineering, Kyushu University, 744 Motooka, Nishi-ku, Fukuoka, Japan

Copper Active-Oxygen Complexes

Abstract

A mononuclear copper(II)-superoxide complex supported by a N-[(2-pyridyl)methyl]-1,5-diazacyclooctane tridentate ligand (L^{Pym}), generated in acetone at low temperature (e.g. –95 °C), has been demonstrated to induce catalytic C–C bond formation reaction between carbonyl compounds (substrate) and the solvent molecule (acetone), giving β-hydroxy-ketones (aldol). Kinetic and spectroscopic studies have indicated that nucleophilic addition of the superoxide species to the carbonyl carbon of the substrate is involved as an initial step of the C–C bond formation reaction. Mechanistic details have been further evaluated by DFT calculation studies. *Communications Chemistry* accepted.

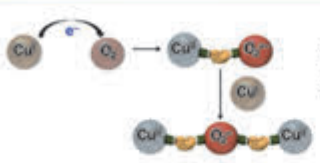

Key reactive intermediates in catalytic oxidation reaction and biological oxidation reaction

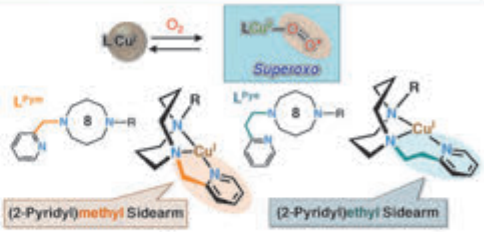

Catalytic oxidation process

Alkane oxygenation

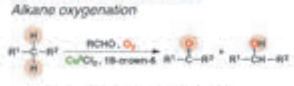

Alcohol oxidation

Biological oxidation process

Methane monooxygenase (pMMO)

Dopamine β-monooxygenase (DβM)

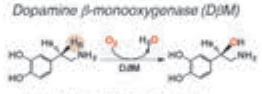

Reactivity of Copper(II)-Superoxide Complexes

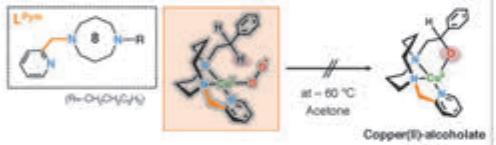

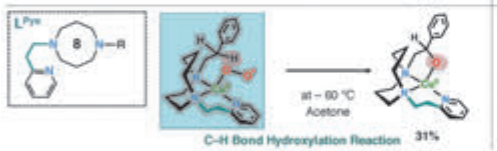

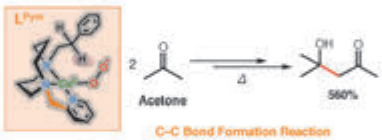

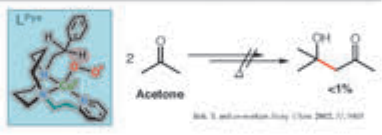

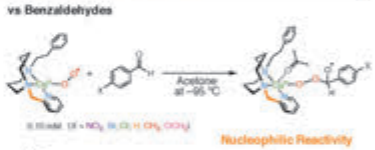

Energy Profile for the C–C Bond Formation by the Reaction of Copper(II)-Superoxide Complex with Benzaldehyde

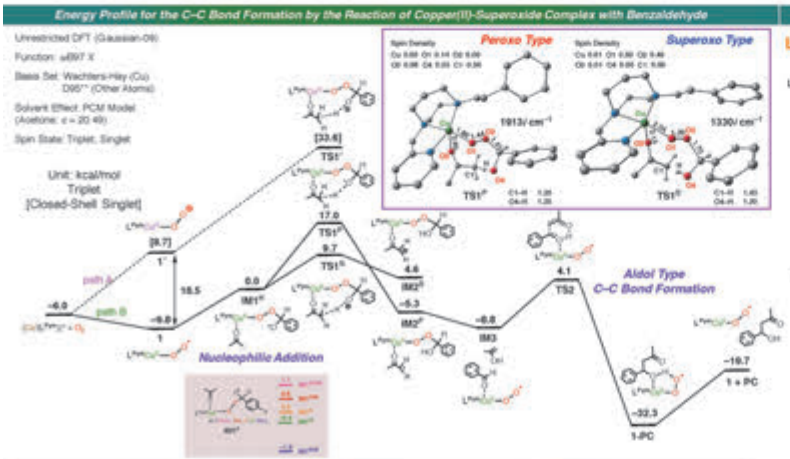

Ligand Effect on the Reactivity

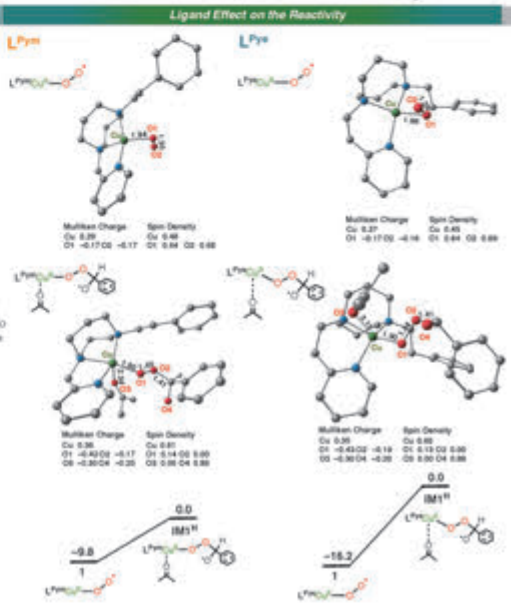

Summary

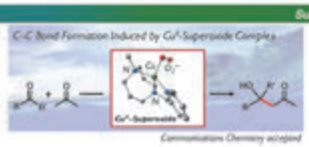

- Superoxide complex can induce the catalytic the C–C bond formation reaction.
- The present results unambiguously demonstrate that there is an unprecedented catalytic role of transition-metal superoxide species in such C–C bond formation reactions.

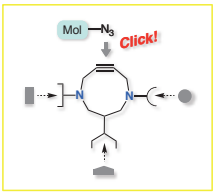

Development and Application of Multi-molecule Connectable DACN

Yuuya Kawasaki, Yuuki Seto, Shintarou Kawahara, Kazunobu Igawa, Katsuhiko Tomooka

Institute for Materials Chemistry and Engineering, and IRCCS Kyushu University

Background

Evolution of Huisgen Reaction Device

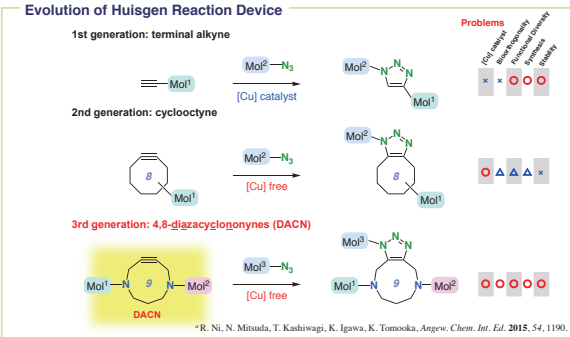

[a] R. Ni, N. Mitsuda, T. Kashiwagi, K. Igawa, K. Tomooka, *Angew. Chem. Int. Ed.* **2015**, *54*, 1190.

DACN Derived Multi-Molecule Connector

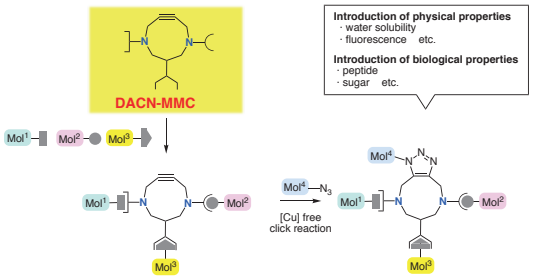

Result

Synthesis of DACN

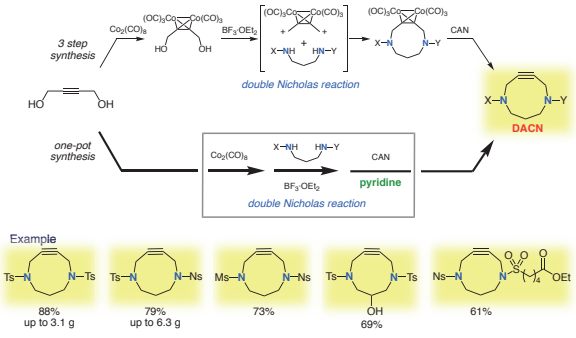

K. Igawa, S. Aoyama, Y. Kawasaki, T. Kashiwagi, Y. Seto, R. Ni, N. Mitsuda, K. Tomooka, *Synlett* **2017**, *28*, 2110.

Reactivity of DACN

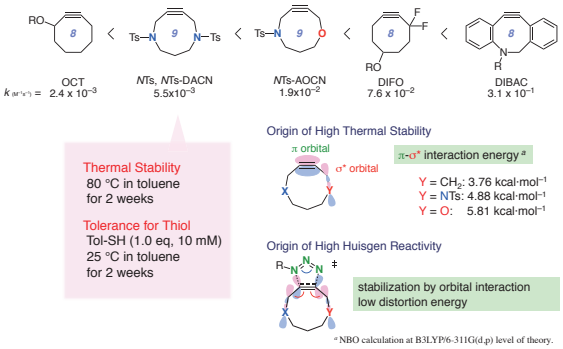

[a] NBO calculation at B3LYP/6-311G(d,p) level of theory.

Design and Concept of DACN-MMC

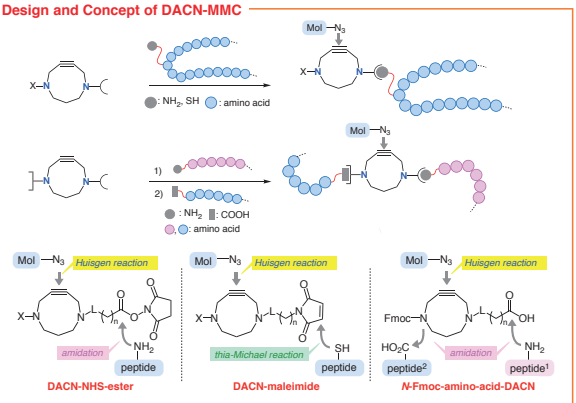

DACN-NHS ester

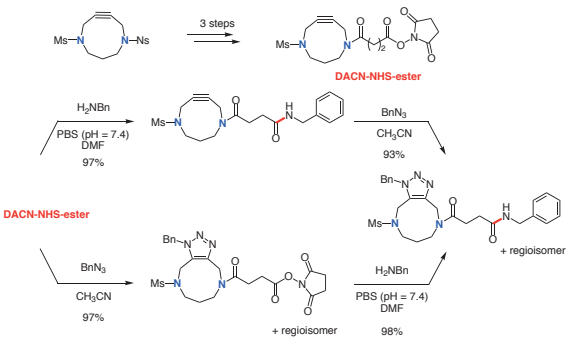

DACN-maleimide

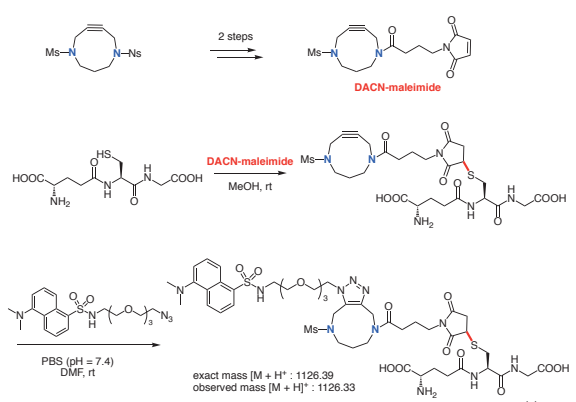

N-Fmoc Amino Acid DACN

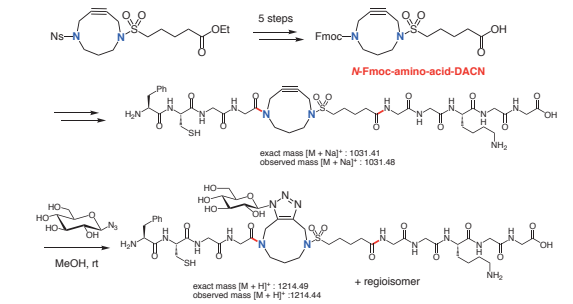

In Progress

Synthesis of Iptycenes Using Ynolate-Aryne Triple Cycloaddition

○Takayuki Iwata,[1] Takuto Fukami,[2] Tatsuro Yoshinaga,[2] Takumi Fujiwara,[2] Mitsuru Shindo[1]

([1]Institute for Materials Chemistry and Engineering, Kyushu University
[2]Interdisciplinary Graduate School of Engineering Sciences, Kyushu University)

Introduction

anthracenes + benzynes —Diels-Alder reaction→ triptycene

Triptycene
D_{3h} symmetry
Rigid three-dimentional molecule
Firstly synthesized by Bartlett
Usually synthesized by DA reaction

P. D. Bartlett, *et al.*, *J. Am. Chem. Soc.* **1942**, *64*, 2649.
G. Wittig, *et al.*, *Angew. Chem.* **1956**, *68*, 40.

ynolate-aryne triple cycloaddition reaction

Umezu, S.; Gomes, G. B.; Yoshinaga, T.; Sakae, M.; Matsumoto, K.; Iwata, T. Alabugin, I.; Shindo, M. *Angew. Chem. Int. Ed.*, **2017**, *56*, 1296.

ynolates + benzynes (X = H, OMe) → X = H: 37-69%, X = OMe: 27-52%

"[2+2]" → Dewar anthracene → "[2+2]" → anthracene → [4+2]

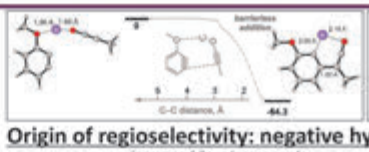

Origin of regioselectivity: negative hyperconjugation

hyperconjugation in benzyne

increased δ+ = larger angle

Structural and electronic distortion → Electronically favorable TS → More stable carbanion → meta-substituted product

importance of negative hyperconjugation → $\sigma^*_{C\text{-}X}$

This work

- Synthesis of silyl triptycenes was investigated utilizing the ynolate-aryne triple cycloaddition reaction.
- Synthesis of iptycenes was also investigated using triptycynes.

Results

1. Synthesis of distorted silyl triptycenes

ynolates —sec-BuLi (5.0 eq), THF, 0 °C, 1 h→ dihedral angle / Si-O distance

t-BuLi (4.0 eq), THF, -78 °C to 0 °C

Shindo, M. *et al.*, Org. Synth. **2007**, *84*, 11.

	dihedral angle	Si-O distance	yield
Me_3Si	21.7° 21.7° 21.7°	3.08 Å 3.08 Å 3.08 Å	y. 42%
$EtMe_2Si$	19.1° 19.4° 23.6°	3.07 Å 3.19 Å 3.08 Å	y. 48%
$PhMe_2Si$	21.0° 24.4° 26.8°	3.05 Å 3.11 Å 3.12 Å	y. 10%
t-$BuMe_2Si$	14.9° 20.2° 32.7°	3.29 Å 3.29 Å 3.29 Å	y. 50%
Ph_2MeSi	12.2° 15.9° 18.2°	3.19 Å 3.14 Å 3.13 Å	y. 21%
Et_3Si	18.4° 30.7° 31.9°	3.29 Å 3.19 Å 3.08 Å	y. 52%
i-Pr_3Si	30.2° 34.0° 35.4°	3.22 Å 3.20 Å 3.25 Å	y. 2%

$Si(i\text{-}Pr)_3$ highly distorted

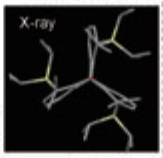

*Sum of Van der Waals radius 1.52 Å (O) + 2.10 Å (Si)= 3.62 Å

2. Synthesis of tiptycenes using anthrone

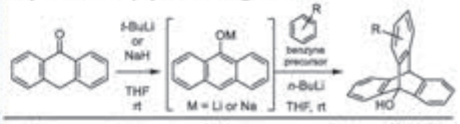

entry	precursor	triptycene	base	Yield (%)
1			*t*-BuLi	64
2			NaH	36
3			*t*-BuLi	61
4			NaH	71
5			*t*-BuLi	52
6			NaH	62
7			*t*-BuLi	62
8			NaH	73

3. Synthesis of pentiptycene using anthrone

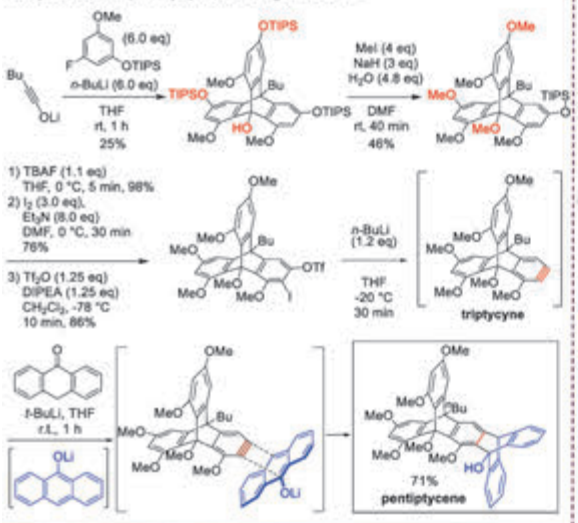

4. Synthesis of iptycene using ynolate

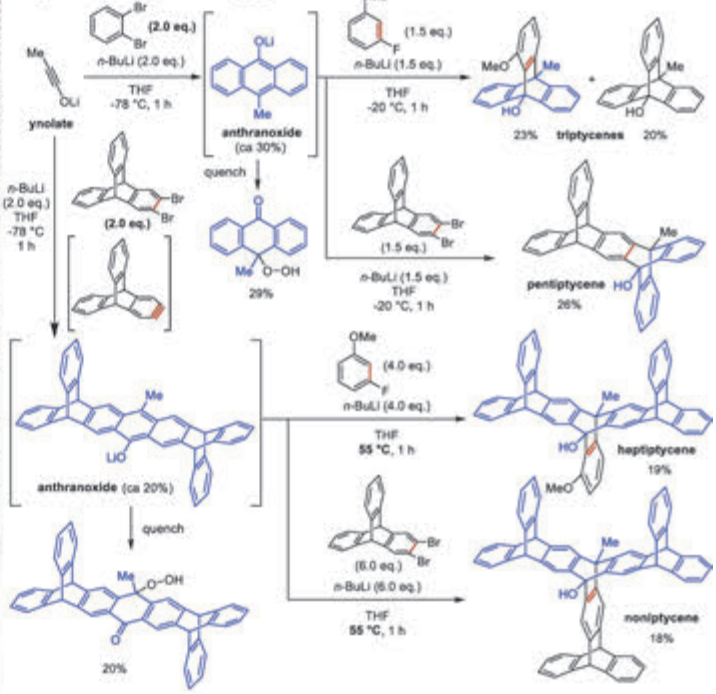

Conclusion

- Distorted silyl triptycenes were obtained.
- Iptycenes were also successfully synthesized using triptycynes and anthranoxide which was prepared from (1) anthrone or (2) ynolate and arynes.

Polarity Switching Crystals Prepared by Pseudo-racemic Crystallization

(IMCE, Kyushu Univ.)Shinji Kanegawa and Osamu Sato
E-mail: kanegawa@cm.kyushu-u.ac.jp

IMCE

Introductions

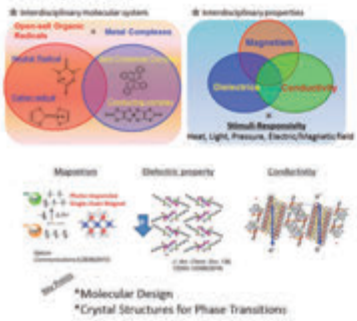

*Molecular Design
*Crystal Structures for Phase Transitions

Functional Inorganic Metal Oxides

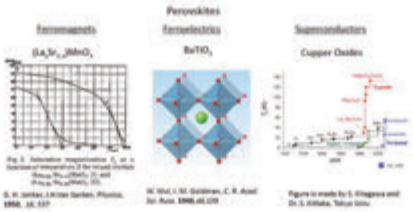

A variety of physical properties in the same(similar) structure

Kinds of Metal, Ratio of Metals → Properties, Transition temperature
Simple preparation → Improvement in short time

Advantages and Disadvantages of Molecular-Based Materials

Advantages

* Light weight, Flexible, Soluble and Environment-friendly
* Flexible molecular design, Systematic study
* Fine tuning in molecular structure and physical properties

Double-edged Sword

Difficulties

*Long and complicated synthetic route
*Small structure change results totally different crystal structures
* Polymorphism

Symmetric vs. Asymmetric

Wallach's rule

"Racemic crystals tend to be more dense than their chiral counterparts"

Wallach, O. Liebigs Ann. Chem. 1895, 286, 90

In other words...
Racemic structure is more preferred than enantiopure structures in chiral systems

Strategy

To develop molecular-based functional materials

*Metal exchange in a structures(Advantage of Inorganic oxide)

*Chirality is adopted as a key factor (Character of Molecules)

Chirality-assisted Crystal Formation

*Different Metal centers
*Pseudo-centrosymmetric Crystal Growth

Preparations

Crystal Structure of *rac*-Complexes

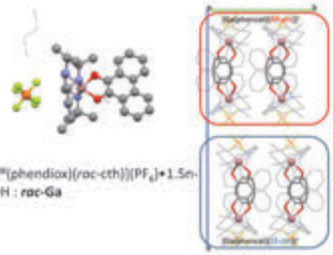

[Ga^{III}(phendiox)(*rac*-cth)](PF$_6$)•1.5*n*-PrOH : ***rac*-Ga**

Table Crystalographical Parameter

	rac-Co	*rac*-Zn	*rac*-Ga
Empirical Formula	$C_{34}H_{54}N_6O_4P_2F_{12}$ Co•1.5*n*-PrOH	$C_{34}H_{54}N_6O_4P_2F_{12}$ Zn•1.5*n*-PrOH	$C_{34}H_{54}N_6O_4P_2F_{12}$ Ga•1.5*n*-PrOH
Formula Weight	786.33	791.33	796.32
temp (K)	123 K	123 K	123 K
Crystal System	monoclinic	monoclinic	monoclinic
Lattice Type	C-centered	C-centered	C-centered
Space group	C2/c (#15)	C2/c (#15)	C2/c (#15)
a (Å)	20.214(4)	20.292(2)	20.334(4)
b (Å)	12.664(3)	12.734(1)	12.665(2)
c (Å)	29.190(6)	29.147(3)	29.192(6)
α (deg.)	90	90	90
b (deg.)	101.155(3)	99.765(3)	100.603(3)
g (deg.)	90	90	90
V (Å^3)	7311(3)	7412.7(9)	7380(3)
Z value	8	8	8
radiation	MoKa (l = 0.71075 Å)	MoKa (l = 0.71075 Å)	MoKa (l = 0.71075 Å)
R_1 (I > 2.00σ(I))	0.0909	0.0671	0.0667
wR_2 (all)	0.2399	0.1713	0.1876

Table Selected Bond lengths

	rac-Co	*rac*-Ga	*rac*-Zn
temperature	123 K	123 K	123 K
M-O (Å)	1.914	1.918	2.126
	1.905	1.938	2.132
M-N (Å)	2.018	2.126	2.196
	2.026	2.132	2.147
	2.037	2.134	2.168
	2.056	2.196	2.219
C-O (Å)	1.344	1.359	1.278
	1.350	1.368	1.269
C-C (Å)	1.364	1.372	1.440
	1.450	1.433	1.452
	1.408	1.423	1.406
	1.466	1.452	1.470
	1.427	1.423	1.411
	1.450	1.430	1.450

Magnetic Properties of *rac*-Complexes

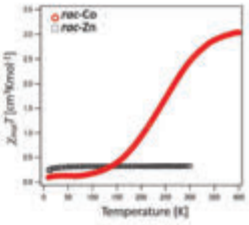

rac-Ga was diamagnetic

IR Spectra

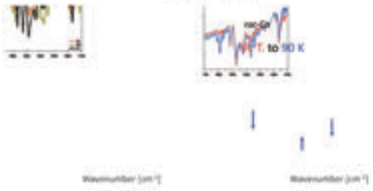

Electronic states

***rac*-Co**: [Co^{III}(phencat)]$^+$ at LT, [Co^{II}(phensq)]$^+$ at HT
***rac*-Ga**: [Ga^{III}(phencat)]$^+$
***rac*-Zn**: [Zn^{II}(phensq)]$^+$

DFT Calculations; Dipole Moments

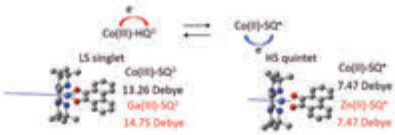

Crystal Structure of *Pseudo*-racemic Complexes

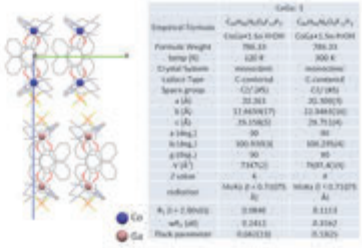

Magnetic Properties of *Pseudo*-racemic Complexes

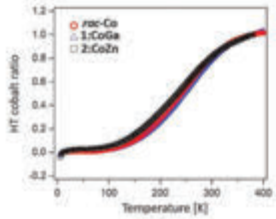

Expected Polarity Switching

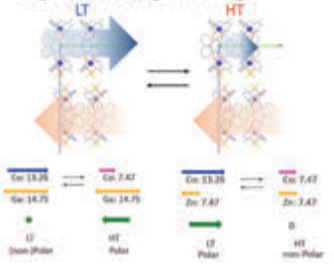

Summary

To develop molecular-based functional materials

*Metal exchange methods

*Chirality is adopted as a key factor

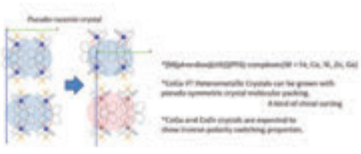

スピン転移とプロトン移動が協奏する鉄二価錯体における光誘起プロトン移動

○中西 匠、佐藤 治（九大先導研）

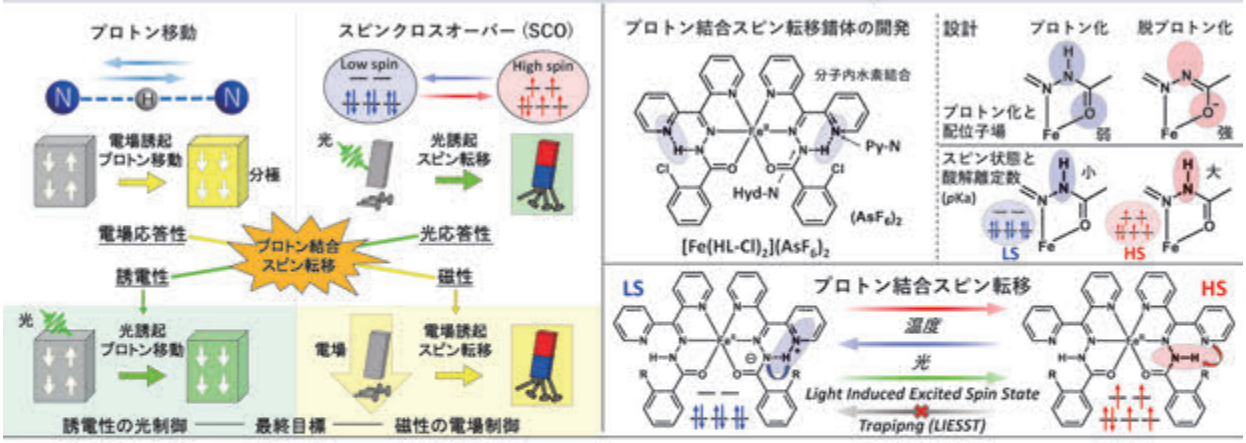

Experiment

Synthesis $2HL\text{-}Cl + FeCl_2 \cdot 4H_2O + 2LiAsF_6 \xrightarrow{MeOH,\ N_2} [Fe(HL\text{-}Cl)_2](AsF_6)_2$

Magnetic Property

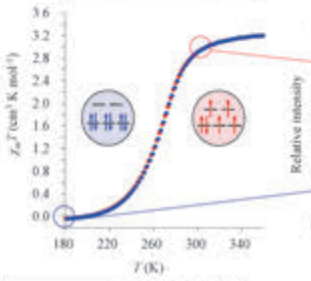

Mössbauer Spectra

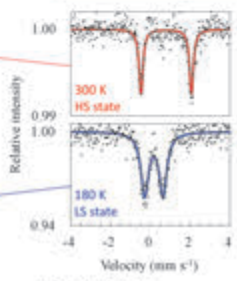

Crystal Structure

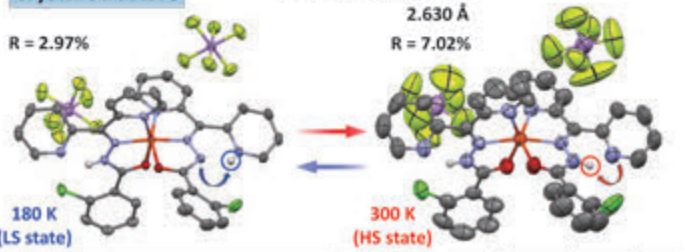

		Coordination angles centered on Py-N and Hyd-N (°)		Proton position
		Py-N	Hyd-N	
350 K	HL-Cl(A)	118.0(7)	114.5(5)	Hyd-N
	HL-Cl(B)	117.3(6)	115.0(5)	Hyd-N
180 K	HL-Cl(A)	123.5(2)	108.1(2)	Py-N
	HL-Cl(B)	118.0(2)	113.2(2)	Hyd-N

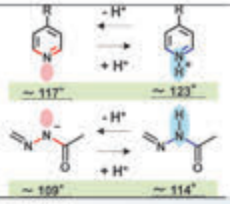

IR Spectra

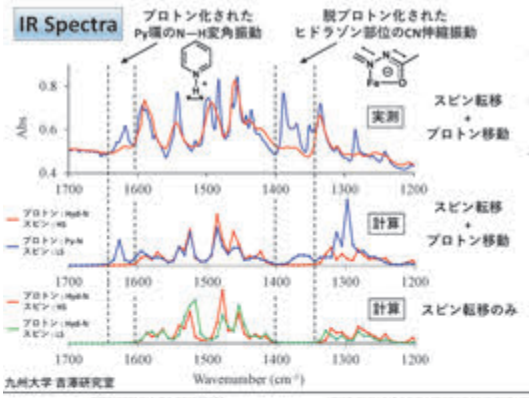

温度誘起SCOと連動した分子内プロトン移動

LIESST effect

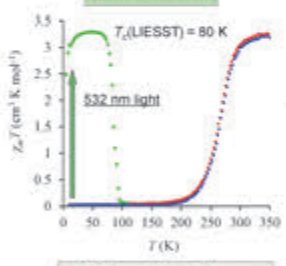

Crystal Structures before and after irradiation

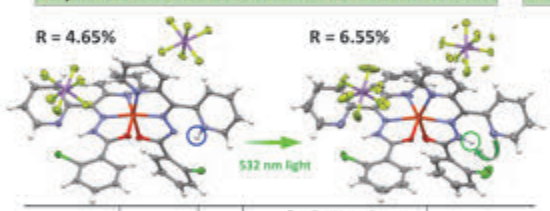

	Fe—N distance (Å)	Spin state	Coordination angles centered on Py-N and Hyd-N in HL-Cl(A) (°)		Proton position in HL-Cl(A)
			Py-N	Hyd-N	
Before irradiation	1.872	LS	123.4(4)	108.1(3)	Py-N
After irradiation	2.119	HS	118.4(7)	114.2(5)	Hyd-N

Timescale of light-induced proton transfer

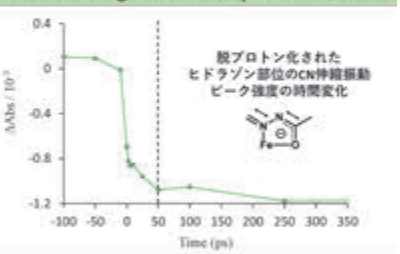

IR Spectra before and after irradiation

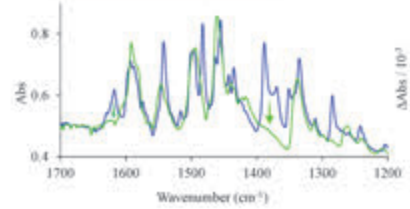

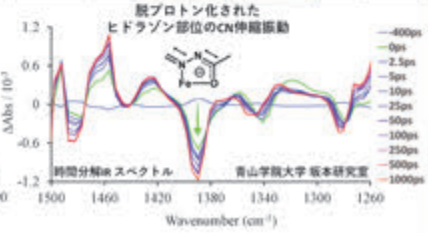

Conclusion

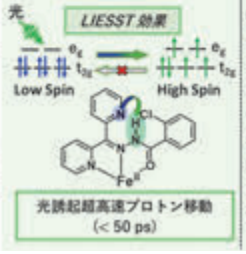

LIESSTと連動した超高速光誘起プロトン移動と、プロトン移動後の状態のトラッピングに成功した。今後は、光誘起プロトン移動を利用した分極の光制御や、電場誘起プロトン移動を利用した磁性の電場制御の実現を目指す。

Regioselective Oxidation of Aliphatic Ketones on ZnO Single-Crystal Nanowires

○Takuro Hosomi,[1] Akihide Inoue,[2] Kazuki Nagashima,[1, 2] Tsunaki Takahashi,[1] Nobutaka Shioya,[3] Takafumi Shimoaka,[3] Guozhu Zhang,[1] Masaki Kanai,[1] Takeshi Hasegawa,[3] Takeshi Yanagida[1, 2] ([1] Institute for Materials Chemistry and Engineering, Kyushu University; [2] Interdisciplinary Graduate School of Engineering Sciences, Kyushu University; [3] Division of Environmental Chemistry, Institute for Chemical Research, Kyoto University)

本研究の着眼点

ひろく普及している物理センサ（光・音・力）
実用化が進まない化学センサ（分子）

物質・分子の「選択」の難しさ

一般的なガス分子センサ

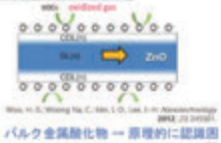

バルク金属酸化物 ⇒ 原理的に認識困難

単結晶ナノ金属酸化物材料

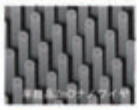

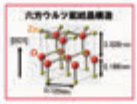

高い単結晶性のナノレベルで精緻に制御された構造

単結晶ナノ金属酸化物材料は、有機分子を精緻に識別できるか？

ZnOナノワイヤの作製方法と評価

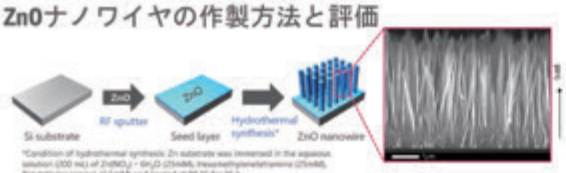

ZnOナノワイヤの分子認識能評価

分子の吸着と脱離温度の解析

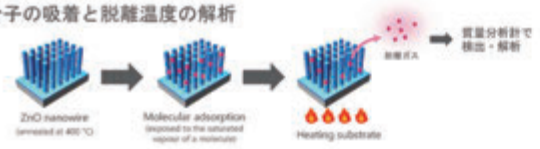

吸着させた分子種

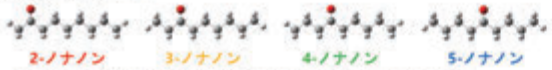

カルボニル基の位置のみが異なる４つの長鎖ケトン ⇒ 識別難易度きわめて高い

吸着させた分子種

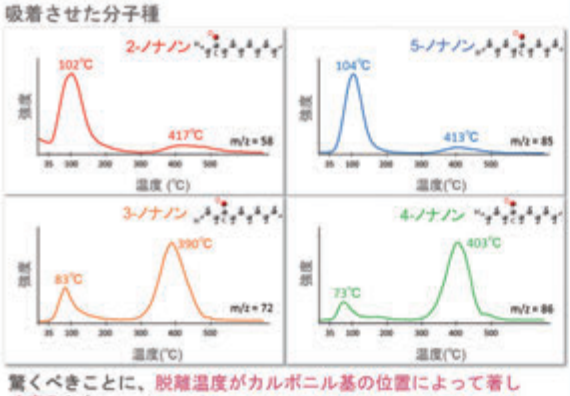

驚くべきことに、脱離温度がカルボニル基の位置によって著しく変化した

⇒ 何が起きたのか？

ナノワイヤ表面で何が起きたのか？

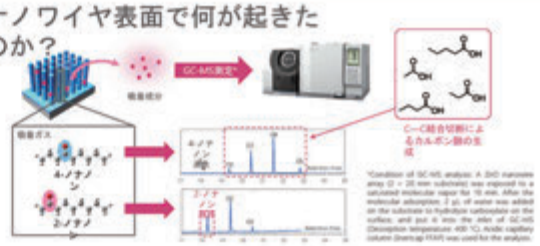

脱離温度が高いケトンにおいて、カルボン酸への酸化反応が著しく加速されていた

酸化反応が脱離温度に与える影響

赤外分光測定を用いてナノワイヤ表面の分子の吸着状態を観察

ZnOナノワイヤ上におけるノナノンのFT-IRスペクトル

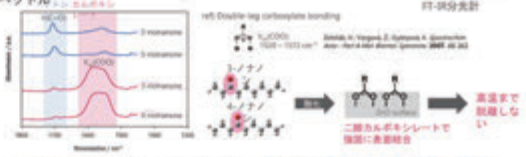

脱離温度が高いケトンにおいては、選択的にZnOへの強固なカルボキシレート結合が形成されていた

何を「選択」しているのか？

炭素鎖長を変えたケトンで酸化反応の分子選択性のルールを調査

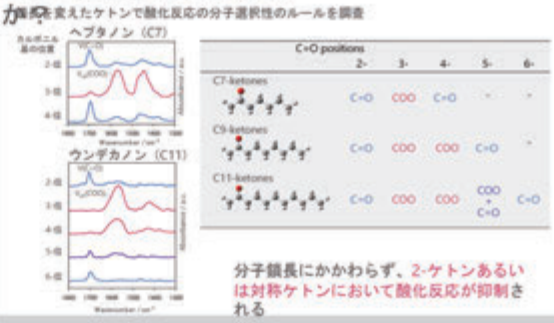

分子鎖長にかかわらず、2-ケトンあるいは対称ケトンにおいて酸化反応が抑制される

分子選択性の由来は何か？

官能基の影響

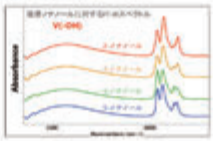

アルコールでは選択性なし

露出結晶面の影響

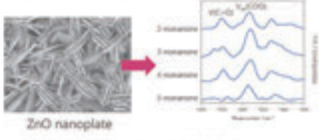

c面ZnO上では選択性なし

分子認識のメカニズムにおいて、ZnO単結晶のm面とケトンとの相互作用が重要である

まとめ

- ZnOナノワイヤに対するケトン分子の吸着の強さは、C=O基の位置によって著しく異なる
- C–C結合開裂を伴う酸化・カルボキシレート形成が、強い吸着の源である
- C7, C9, C11いずれのケトンでも選択性は発現し、2-ケトンおよび対称ケトンにおいて酸化が抑制される
- この分子認識にはナノワイヤ側面のm面の存在が重要である

Theoretical Study of H_2O Oxidation by A Half-Sandwich Iridium Complex

KYUSHU UNIVERSITY

O Kei Ikeda[1], Yuta Hori[2], Yoshihito Shiota[2], M. Haris Mahyuddin[2], Aleksandar Staykov[3], Takahiro Matsumoto[1,3,4], Kazunari Yoshizawa[2], Seiji Ogo[1,3,4]

([1]Graduate School of Engineering, Kyushu University, [2]IMCE, Kyushu University, [3]I²CNER, Kyushu University, [4]Center for Small Molecule Energy, Kyushu University)

1. Introduction

Ogo *et. al.* synthesize an half-sandwich iridium complex which has abilities of oxidation both H_2 and H_2O molecules

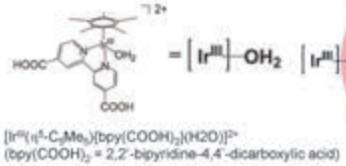

$[Ir^{III}(\eta^5\text{-}C_5Me_5)\{bpy(COOH)_2\}(H2O)]^{2+}$
($bpy(COOH)_2$ = 2,2'-bipyridine-4,4'-dicarboxylic acid)

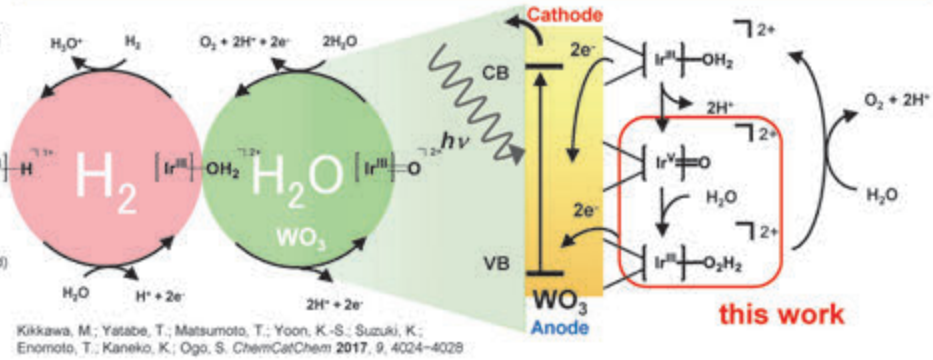

Kikkawa, M.; Yatabe, T.; Matsumoto, T.; Yoon, K.-S.; Suzuki, K.; Enomoto, T.; Kaneko, K.; Ogo, S. *ChemCatChem* **2017**, *9*, 4024–4028

2. Method

DFT Calculation

- Program
  Gaussian16 RevA.03
- Basis Set
  SDD (Ir) TZVP (others)
- Functional
  B3LYP-D3
- Solvent
  Water (PCM: ε = 78.39)
- Zero-point energy correction

3. Electronic structures of Ir=O species

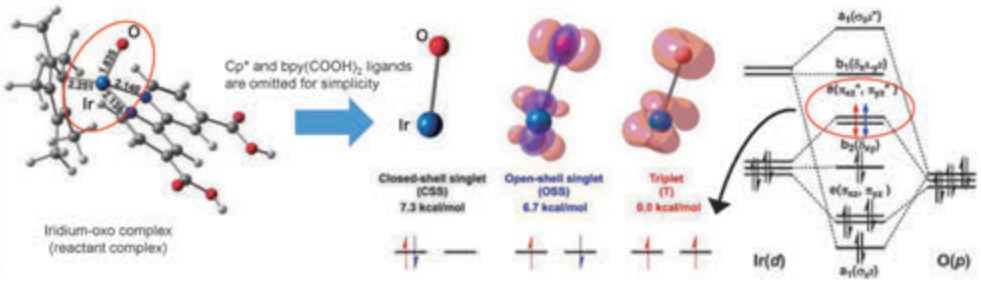

Iridium-oxo complex (reactant complex)

4. Reaction path

ROC (Radical Oxo Coupling) mechanism

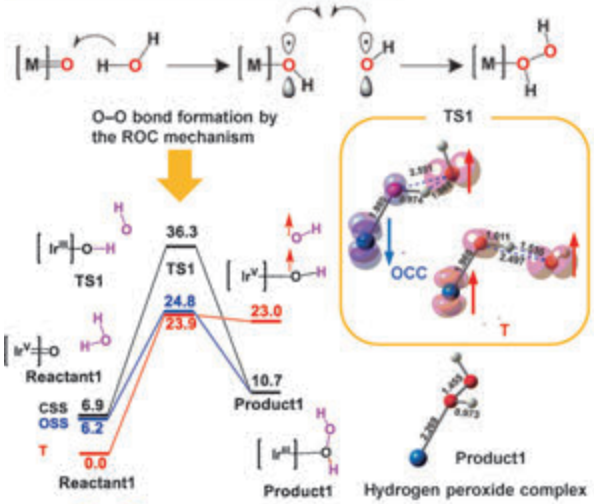

WNA (Water Nucleophilic Attack) mechanism

ΔE (kcal/mol)
Bond length are in Å

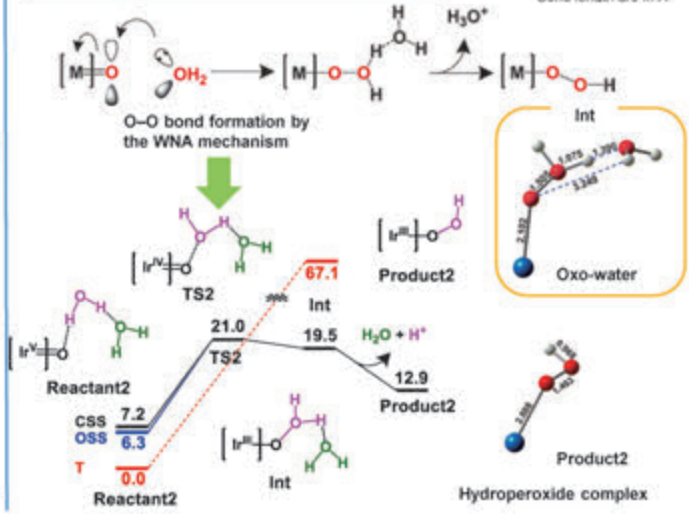

5. Summary

- Iridium-oxo species have three possible spin states (triplet, open-shell singlet, and closed-shell singlet states) caused by the two-degenerate π^* orbitals between the Ir-5d and O-2p.
- In the ROC mechanism, H_2O oxidation reaction by iridium-oxo complex proceeds in the open-shell singlet state.
- In the WNA mechanism, iridium-oxo complex react with a H2O molecules to form the hydroperoxide complex through the oxo-water complex, where the deprotonation reaction occurs.
- The WNA mechanism is energetically favored than the ROC mechanism.

Robust Nanowire-Nanocellulose Composite Network Structure for One-time Use Disposable Paper Molecular Sensor

[1]IMCE Kyushu Univ. [2]ISIR Osaka Univ.

K. Nagashima[1], H. Koga[2], T. Takahashi[1], M. Nogi[2], T. Yanagida[1]

Introduction

Chemical data collection via molecular recognition electronics is interesting !!

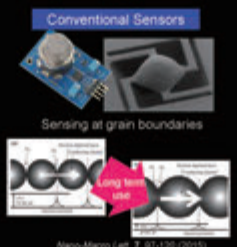

Deterioration of sensing performance due to morphological change of grain boundaries

Approach in this study

Disposable Nanopaper Sensor

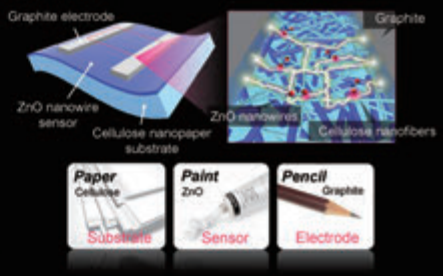

Experiment

1. Hydrothermal growth of ZnO nanowires

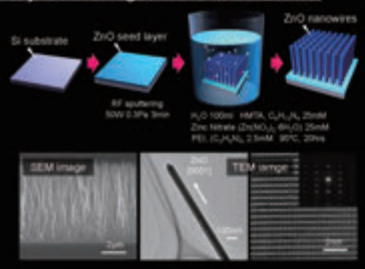

2. Fabrication of nanopaper sensor

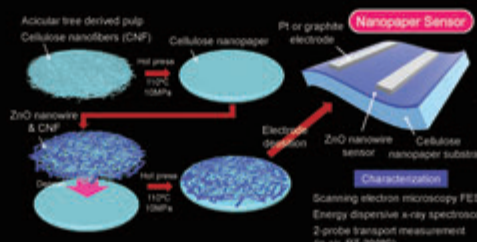

Scanning electron microscopy FESEM 30kV
Energy dispersive x-ray spectroscopy EDS
2-probe transport measurement (in air, RT-200°C)

Wear resistance of nanopaper sensor

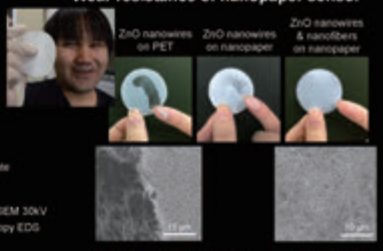

Drastically improved wear resistance by robust nanowire-nanofiber networks

Results & Discussion

Structure/Composition of Nanopaper Sensor

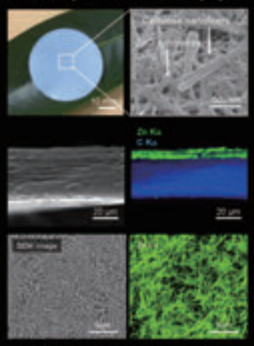

Localized nanowire network on surface

Molecular Sensing by Nanopaper Sensor

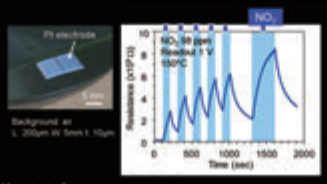

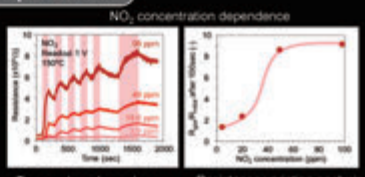

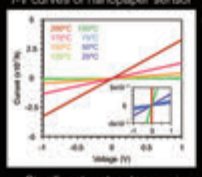

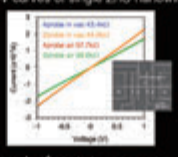

Significant molecular sensing property of nanopaper sensor

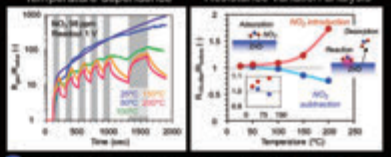

① Low temperature: Adsorption dominant → Larger gain

② High temperature: Reaction/Desorption dominant → Quick response

Nanopaper Sensor with Graphite Electrode

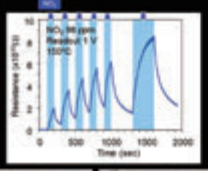

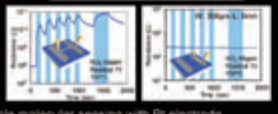

Comparable molecular sensing with Pt electrode

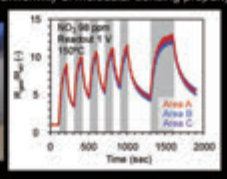

Usability as paper / In-plane uniformity of sensor property

Flammability of nanopaper sensor

Disposable nanopaper-based molecular sensor was demonstrated

Summary

We successfully demonstrated inexpensive disposable nanopaper molecular sensor composed of metal oxide nanowires, cellulose nanofibers and graphite electrodes.

Regioselective Trifluoromethylthiolation of *N*-Heteroaromatic Compounds

Takeru Torigoe, Ryuhei Muta, Yoichiro Kuninobu

Institute for Materials Chemistry and Engineering,
Kyushu University, 6-1 Kasugakoen, Kasuga-shi, Fukuoka 816-8580, Japan

Introduction

Fluorine

- The Second Smallest Atom
- The Highest Electronegativity
- Strong C–F Bond

· Mimic effect, block effect
· Repellency, heat resistance

An Example of Pharmaceuticals Containing -SCF_3 group

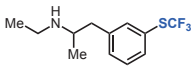

Triflorex
(anorectic drug)

Representative Method to Prepare Ar–SCF_3

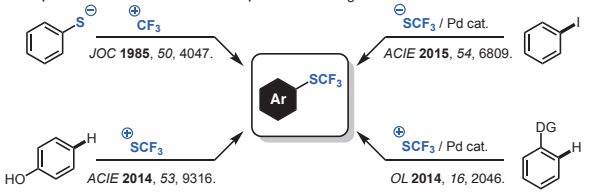

Previous Work

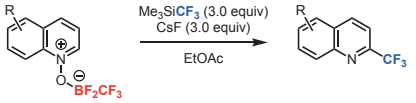

Nishida, T.; Ida, H.; Kuninobu, Y.; Kanai, M. *Nat. Commun.* **2014**, *5*, 3387.

This Work

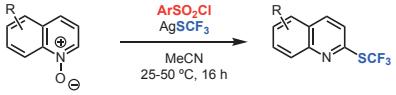

Selectivity: >20:1
up to 90 % yield

Reaction of Quinoline N-Oxide

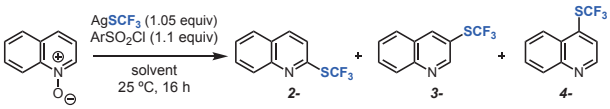

entry	solvent	$ArSO_2Cl$	total yield (%)	ratio 2-	3-	4-
1	EtOAc	-	<5	-	-	-
2	EtOAc	*o*-NsCl	63	68	11	21
3	DMF	*o*-NsCl	33	>99	0	<1
4	CH_2Cl_2	*o*-NsCl	38	87	8	5
5	Toluene	*o*-NsCl	28	68	14	18
6	THF	*o*-NsCl	27	74	<1	26
7	MeCN	*o*-NsCl	82	66	11	23
8	MeCN	*p*-NsCl	68	63	13	24
9	MeCN	TsCl	41	24	37	39
10	MeCN	TfCl	<5	-	-	-
11	MeCN	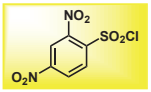	94	96	<1	4
12	MeCN	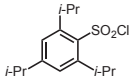	64	36	19	45

Gram-scale reaction

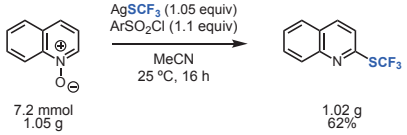

Scope of Substrate

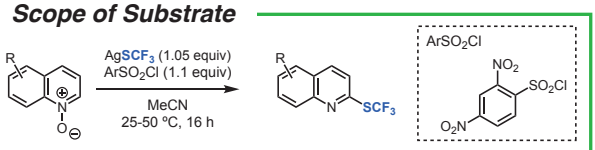

Product / isolated yield

R	yield
Me	73%
F	75%
Cl	82%
Br	77%
I	71%
CO_2Me	58%

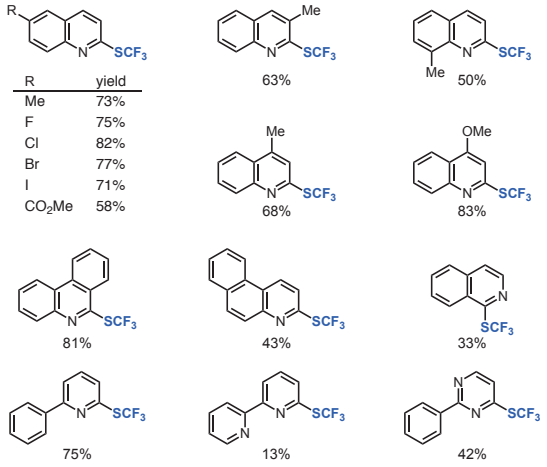

Reaction of Quinidine Derivative

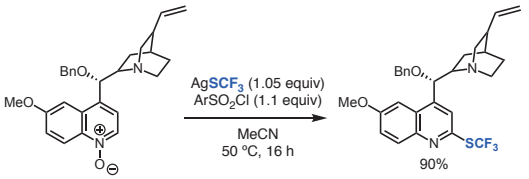

Conversion into -SO_2CF_3

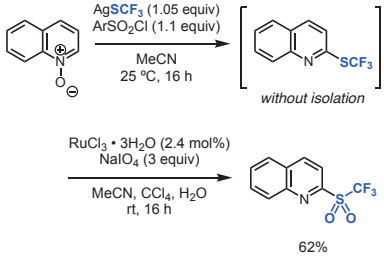

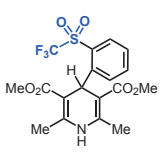

Nifedipin analog
(hypotensive agent)

Possible Mechanism

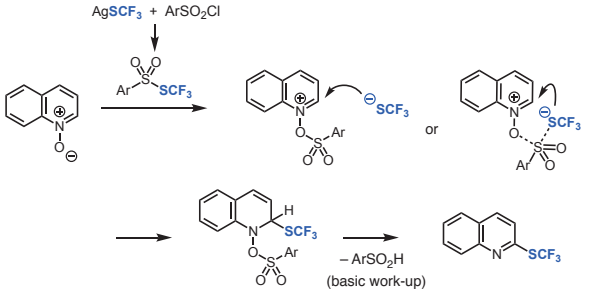

Effects of Electron-Phonon Coupling on Quantum Interference in Polyenes

KYUSHU UNIVERSITY

(IMCE, Kyushu Univ.)○Yuta Tsuji, Kazunari Yoshizawa

Quantum Interference (QI)

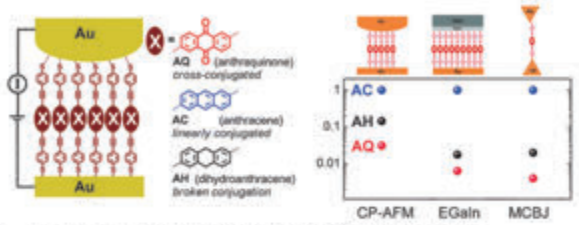

- three molecular wires with different conjugation patterns
- linearly conjugated AC → highest, cross-conjugated AQ → lowest (QI)
- this trend does not depend on the methodology
- wave nature of transferred electrons

(1) Guédon et al. Nat. Nanotechnol. 7, **2012**, 7, 305. (2) Aradhya et al. *Nat. Nanotechnol.* **2013**, *8*, 399.
(3) Valkenier et al. *Phys. Chem. Chem. Phys.* **2014**, *16*, 653.

Non-Equilibrium Green's Function (NEGF) Method for Elastic Transport

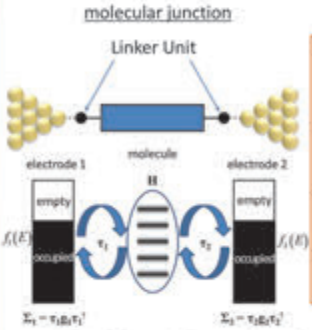

Conductance

$$g = \frac{2e^2}{h} T(E_F)$$

Green's function

$$\mathbf{G} = [(E + i\eta)\mathbf{I} - \mathbf{H} - \boldsymbol{\Sigma}_1 - \boldsymbol{\Sigma}_2]^{-1}$$

Transmission function

$$T(E) = \mathrm{tr}[\boldsymbol{\Gamma}_1 \mathbf{G} \boldsymbol{\Gamma}_2 \mathbf{G}^\dagger]$$

Broadening function

$$\boldsymbol{\Gamma}_{1(2)} = i\left[\boldsymbol{\Sigma}_{1(2)} - \boldsymbol{\Sigma}_{1(2)}^\dagger\right] = 2\pi\rho_{1(2)}\boldsymbol{\tau}_{1(2)}\boldsymbol{\tau}_{1(2)}^\dagger$$

Datta, S. *Quantum Transport : Atom to Transistor*. Cambridge University Press, (2005).

Elastic Transport vs. Inelastic Transport

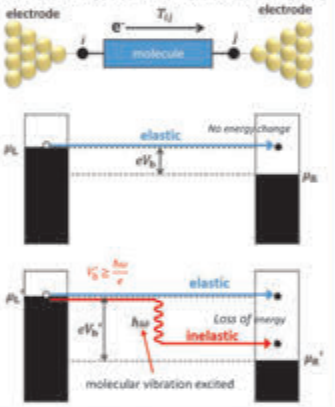

Effects of QI on Inelastic Transport

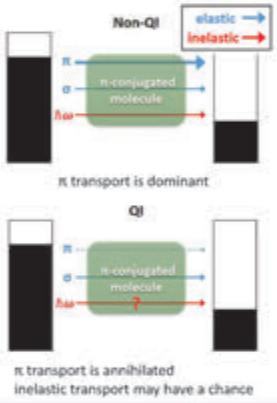

Theoretical Background

Self-Consistent Born Approximation (SCBA) & Lowest Order Expansion (LOE)

Inelastic current

$$I_{in}(V_b, \lambda) = I^{Sym}(V_b, \hbar\omega_\lambda, T, \{n_\lambda\})\mathcal{T}^{Sym}(V_b, \lambda) + I^{Asym}(V_b, \hbar\omega_\lambda, T)\mathcal{T}^{Asym}(V_b, \lambda)$$

Inelastic transmission functions

$$\mathcal{T}^{Sym}(V_b, \lambda) = \mathrm{Tr}\left[\mathbf{G}^\dagger \boldsymbol{\Gamma}_L \mathbf{G}\left\{\mathbf{M}_\lambda \mathbf{G} \boldsymbol{\Gamma}_R \mathbf{G}^\dagger \mathbf{M}_\lambda + \frac{i}{2}\left(\boldsymbol{\Gamma}_R \mathbf{G}^\dagger \mathbf{M}_\lambda \mathbf{A} \mathbf{M}_\lambda - \mathrm{H.c.}\right)\right\}\right]$$

$$\mathcal{T}^{Asym}(V_b, \lambda) = \mathrm{Tr}\left[\mathbf{G}^\dagger \boldsymbol{\Gamma}_L \mathbf{G}\left[\boldsymbol{\Gamma}_R \mathbf{G}^\dagger \mathbf{M}_\lambda \mathbf{G}(\boldsymbol{\Gamma}_R - \boldsymbol{\Gamma}_L)\mathbf{G}^\dagger \mathbf{M}_\lambda + \mathrm{H.c.}\right]\right]$$

electrode attachment

$$\boldsymbol{\Gamma}_L \mathbf{G} \boldsymbol{\Gamma}_R = \gamma_L \gamma_R \left|G_{i,j}\right|^2 \left|\right\rangle\left\langle\right|$$

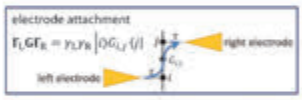

If QI happens, $G_{i,j} = 0$, and hence $\boldsymbol{\Gamma}_L \mathbf{G} \boldsymbol{\Gamma}_R = \mathbf{0}$

$$\mathcal{T}^{Sym}(V_b, \lambda) \to \mathrm{Tr}\left[\boldsymbol{\Gamma}_L \mathbf{G} \mathbf{M}_\lambda \mathbf{G} \boldsymbol{\Gamma}_R \mathbf{G}^\dagger \mathbf{M}_\lambda \mathbf{G}^\dagger\right] = \gamma_L \gamma_R \left|(G_M)_{i,j}\right|^2$$

$$\mathcal{T}^{Asym}(V_b, \lambda) \to 0 \qquad (\mathbf{G}_M = \mathbf{G}\mathbf{M}_\lambda\mathbf{G})$$

$\mathbf{M}_\lambda$: electron-phonon coupling matrix for phonon mode λ

$$M_{i,j}^{(\lambda)} = \sum_\beta \left\langle i \left| \frac{\partial \hat{H}}{\partial Q_\lambda} \right| j \right\rangle_{Q_0} v_\beta^{(\lambda)} \sqrt{\frac{\hbar}{2M_\beta \omega_\lambda}}$$

Whether the matrix element of the G_M matrix becomes 0 or not determines whether the inelastic transport survives or perishes.

[1] T. Frederiksen, M. Paulsson, M. Brandbyge, and A.-P. Jauho, Phys. Rev. B **75**, 205413 (2007).
[2] R. Sobrino and T. Novotný, J. Chem. Phys. **146**, 174114 (2017).

The Model

Linear Polyene

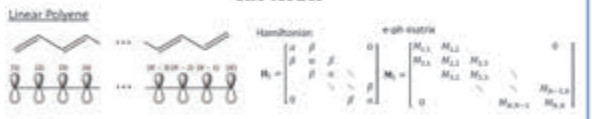

Cyclic Polyene

Green's Function

Green's function at the Fermi level ($E = 0$)

$$\mathbf{G}^{(0)}(E_F) = -\mathbf{H}^{-1}$$

Linear Polyene

$$G_{i,j} = \frac{(-1)^{\frac{i+j-\alpha}{2}}}{t}\left[1 + (-1)^{i-j}\right]\left[1 - (-1)^{i+j}\right]|i| < |j|$$

$$G_{i,j} = \frac{(-1)^{\frac{i+j-\alpha}{2}}}{t}\left[1 + (-1)^{i-j}\right]\left[1 - (-1)^{i+j}\right]|i| > |j|$$

α, β	$G_{i,j}$, $\lvert i\rvert < \lvert j\rvert$	$G_{i,j}$, $\lvert i\rvert > \lvert j\rvert$
(odd, odd)	0	0
(odd, even)	$(-1)^{\frac{i+j-1}{2}}$	0
(even, odd)	0	$(-1)^{\frac{i+j-1}{2}}$
(even, even)	0	0

Cyclic Polyene

$$G_{i,j} = \frac{(-1)^{\frac{i-j-2}{2}}}{t}\left[1 - (-1)^{i-j}\right]|i| < |j|$$

$$G_{i,j} = \frac{(-1)^{\frac{i-j-2}{2}}}{t}\left[1 - (-1)^{i-j}\right]|i| > |j|$$

$\lvert i\rvert$	$G_{i,j}$, $\lvert i\rvert < \lvert j\rvert$
odd	0
even	$\frac{(-1)^{\frac{i-j}{2}}}{2}$

0 means a QI case

R. Movassagh, G. Strang, Y. Tsuji, and R. Hoffmann, J. Math. Phys. **58**, 033505 (2017).

An Example

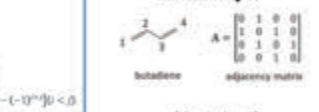

$$\mathbf{A}^{-1} = \begin{bmatrix} 0 & 1 & 0 & -1 \\ 1 & 0 & 0 & 0 \\ 0 & 0 & 0 & 1 \\ -1 & 0 & 1 & 0 \end{bmatrix}$$

inverse matrix

$$\mathbf{M} = \begin{bmatrix} M_{1,1} & M_{1,2} & 0 & 0 \\ M_{2,1} & M_{2,2} & M_{2,3} & 0 \\ 0 & M_{3,2} & M_{3,3} & M_{3,4} \\ 0 & 0 & M_{4,3} & M_{4,4} \end{bmatrix}$$

electron-phonon coupling

Closed Forms for the Inelastic Current Contribution

Possible electrode-connection modes where QI happens ($i < j$)

Linear Polyene

Case A: i and j are odd

$$(GMG)_{2p-1,2r-1} = (-1)^{p+r}\sum_{s=p}^{r-1} M_{2s,2s}$$

Case B: i is even and j is odd

$$(GMG)_{2p,2r-1} = 0$$

Case C: i and j are even

$$(GMG)_{2p,2r} = (-1)^{p+r}\sum_{q=1}^{r} M_{2q-1,2q-1}$$

Cyclic Polyene

Case A: i is 1 and j is odd

$$(GMG)_{1,2q+1} = \frac{(-1)^q}{4}\left[-\sum_{p=1}^{q} M_{2p,2p} + \sum_{p=q+1}^{N/2} M_{2p,2p}\right]$$

all sites in cyclic polyenes are equivalent due to symmetry without loss of generality, we can set i to 1, and j varies

Applications of the Closed Forms

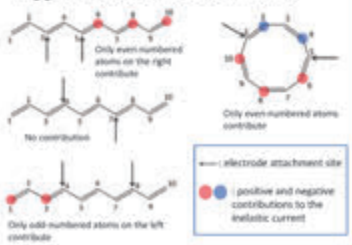

A Selection Rule for Inelastic Current

Starring Procedure of Alternant Hydrocarbons

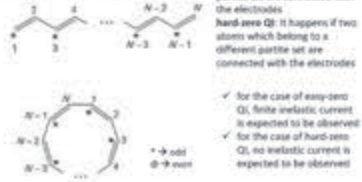

easy-zero QI: It happens if two atoms which belong to the same partite set are connected with the electrodes

hard-zero QI: It happens if two atoms which belong to a different partite set are connected with the electrodes

- ✓ for the case of easy-zero QI, finite inelastic current is expected to be observed
- ✓ for the case of hard-zero QI, no inelastic current is expected to be observed

Conclusions

- ✓ We obtained a closed-form expression for the inelastic transmission through polyenes which show destructive quantum interference (QI).
- ✓ We deduced some interesting selection rules for the atoms which may contribute to the inelastic current on the basis of the parity of their label number.
- ✓ We proved that if the electrode-attachment atoms are both starred or both unstarred, the elastic π transport will be annihilated due to QI but the inelastic current will be persistent.
- ✓ If a starred atom and an unstarred atom are connected with the electrodes, QI is expected to occur in certain circumstances (not always), and the inelastic current can be expected to vanish. And this does not happen in the case of cyclic polyenes.

Tsuji, Y.; Yoshizawa, K. J. Chem. Phys. **149**, 134115 (2018).

Reverse Atom Transfer Radical Polymerization of St and MMA by $(Me_3TACN)FeX_3$ (X = Cl, Br)

Atsushi Tahara,[1] Yuto Ii,[2] Mitsunobu Kawamura,[1] Yusuke Sunada,[3] Hideo Nagashima[1]

[1]*Institute for Materials Chemistry and Engineering, Kyushu University, Kasuga, Fukuoka 816-8580*
[2]*Interdisciplinary Graduate School of Engineering Sciences, Kyushu University, Kasuga, Fukuoka 816-8580*
[3]*Institute of Industrial Science, The University of Tokyo, Meguro, Tokyo 153-8505*

九州大学 KYUSHU UNIVERSITY

Introduction

Atom Transfer Radical Polymerization (ATRP)

Highly-controlled ATRP shows...
- Narrow Molecular Weight Distribution.
- Functionalization by changing Monomer / Initiator
- Block Copolymerization. (Late Stage Functionalization)

Problem is ...
- Control of Radical Density.
- Efficient Removal of Metal Residue.
- Reusability of the Catalysts.
- Stability of the Catalyst Precursor

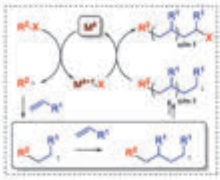

Reverse ATRP

Highly-controlled Reverse ATRP shows...
- Same Performances as Normal ATRP.
- High Stability of the Catalyst Precursor (even toward air and moisture)

Problem is ...
- Control of Radical Density.
- Substrate Scope
- Efficient Removal of Metal Residue.
- Reusability of the Catalysts.
- Stoichiometric Amount of Metals (will be solved by ICAR or AGET-ATRP)

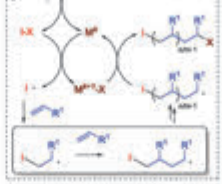

Previous Work : ATRP catalyzed by a series of $(R_3TACN)FeX_2$

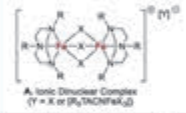

A. Ionic Dinuclear Complex ($Y = X$ or $[R_3TACNFeX_4]$)
B. Neutral Mononuclear Complex
C. Neutral Mononuclear Complex (stabilized by L)

R : sterically small (Me)
- Easy to separate metal with MeOH
- Low controllability (only St)

R : sterically bulky (Pr)
- High controllability (St, MMA, BA)
- Difficult to separate metal

R : sterically small (Me)
- Easy to separate metal with MeOH
- High controllability (St, MMA, BA)
- Commercially available ligand
- Low stability toward air, moisture

R : sterically medium (n-C_6H_{13}) ... both A and B
- Easy to separate metal with MeOH
- High controllability (St, MMA, BA)
- Commercially non-available ligand

All Fe(II) complexes are instable toward air, moisture

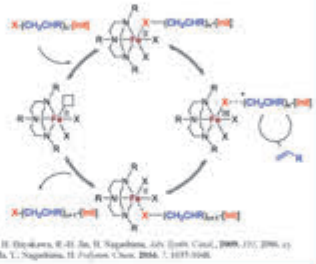

This Work

- ✓Iron catalysts for highly controlled reverse ATRP were synthesized
- ✓Reverse ATRP of St, MMA was achieved
- ✓Reusability of catalysts was performed
- ✓Lowering catalyst loading was achieved by ICAR-ATRP.

Result (1)

Syntheses of $Me_3TACNFeX_3$ complexes

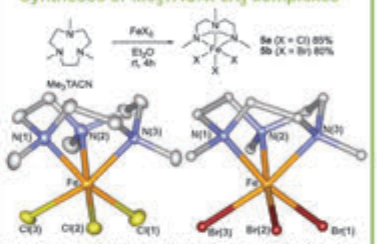

5a (X = Cl) 85%
5b (X = Br) 80%

Molecular structure of **5a** [$P2_1/n$ (#14)]
$R_1 = 0.0431$, $wR_2 = 0.1142$

Molecular structure of **5b** [$P2_1/n$ (#14)]
$R_1 = 0.0425$, $wR_2 = 0.0747$

^1H NMR : no signals
m.p. 180–200°C
Anal. Calcd for $C_9H_{21}N_3Cl_3Fe$
C 32.42, H 6.35, N 12.60;
found: C 33.27, H 6.66, N 12.20

^1H NMR : no signals
m.p. 180–200°C
Anal. Calcd for $C_9H_{21}N_3Cl_3Fe$
C 23.16, H 4.53, N 9.00;
found: C 23.18, H 4.56, N 9.00

Result (2)

[1] Reverse ATRP of St, MMA, BA catalyzed by 5

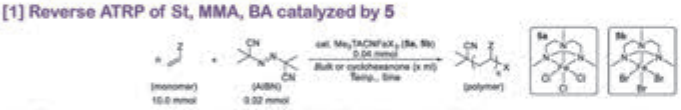

(monomer) 10.0 mmol
(AIBN) 0.02 mmol
cat. $Me_3TACNFeX_3$ (**5a**, **5b**) 0.04 mmol
Bulk or cyclohexanone (x ml)
Temp., time
(polymer)

X = Cl (**5a**)[a]

Monomer : cat. : AIBN = 250 : 1 : 0.5

Entry	Monomer	Solvent (X ml)	Temp. (°C)	Time (h)	Conv. (%)[b]	M_n	M_n(calc.)	M_w/M_n
1	Styrene (St)	Bulk	100	72	>99	29100	26000	1.28
2		1 ml	100	72	>99	26700	26000	1.18
3		1 ml	120	48	>95	23490	24700	1.19
4	Methyl methacrylate (MMA)	Bulk	100	48	>99	37000	25000	1.59
5		1 ml			>99	33000	25000	1.24
6		2 ml			95	25900	22500	1.30
7		5 ml			93	21800	21500	1.27
8	n-Butyl acrylate (BA)	Bulk	100	24	88	41900	27500	4.07
9		1 ml		24	54	27300	19200	1.86
10		5 ml		48	20	7560	6400	1.95

[a]All reactions were performed with [monomer] : [catalyst] : [AIBN] ratio of 250 : 0.5 : 1
[b]Determined by ^1H NMR using a benzyl methyl ether as an internal standard

X = Br (**5b**)[a]

Monomer : cat. : AIBN = 250 : 1 : 0.5

Entry	Monomer	Solvent (X ml)	Temp. (°C)	Time (h)	Conv. (%)[b]	M_n	M_n(calc.)	M_w/M_n
1	Styrene (St)	Bulk	100	72	88	39000	26000	1.50
2		1 ml			91	31800	26000	1.21
3	Methyl methacrylate (MMA)	Bulk	70	48	75	58600	22800	1.60
4		1 ml	80		88	29000	22000	1.30
5		2 ml	60		76	27300	19000	1.33
6	n-Butyl acrylate (BA)	Bulk	80	na	48	–	15400	–
7		1 ml			68	7010	20800	1.55
8		5 ml			45	3230	14400	1.58

[a]All reactions were performed with [monomer] : [catalyst] : [AIBN] ratio of 250 : 0.5 : 1
[b]Determined by ^1H NMR using a benzyl methyl ether as an internal standard

[2] Removal of Catalysts and its reusability

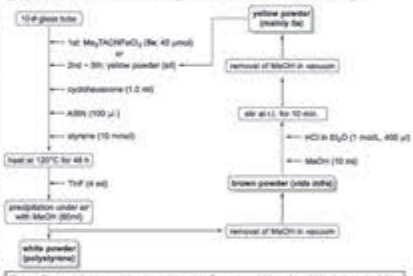

Entry	St : cat. : Initiator	Number of times	Conv.[a]	M_n(exp.)	M_n(calc.)	M_w/M_n
1	250 : 1 : 0.5	1	>99%	26300	26000	1.24
2		2	92%	23700	23900	1.20
3		3	98%	25000	25500	1.29
4		4	95%	23919	24700	1.33
5		5	95%	22588	24700	1.28

Ideal M_n and narrow PDI was achieved on each steps

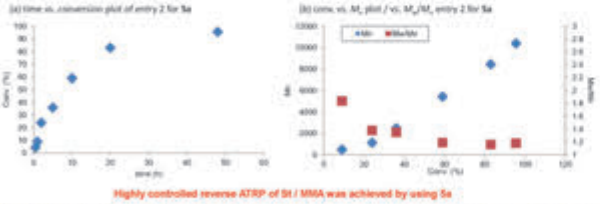

Highly controlled reverse ATRP of St / MMA was achieved by using **5a**

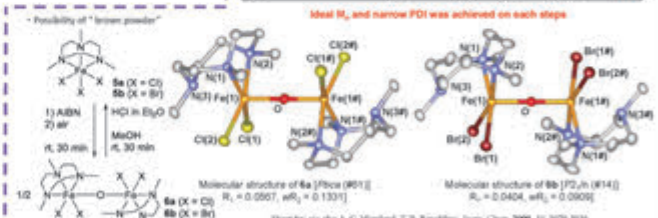

Molecular structure of **6a** [Pbca (#61)]
$R_1 = 0.0567$, $wR_2 = 0.1331$

Molecular structure of **6b** [$P2_1/n$ (#14)]
$R_1 = 0.0404$, $wR_2 = 0.0809$

[3] ICAR-ATRP of St, MMA by 5a, 5b

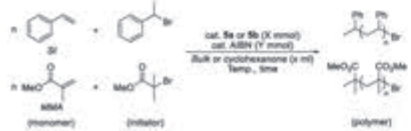

(monomer) 10.0 mmol
(initiator) 0.04 mmol
cat. **5a** or **5b** (X mmol)
cat. AIBN (Y mmol)
Bulk or cyclohexanone (x ml)
Temp., time
(polymer)

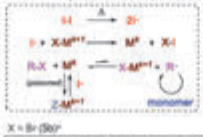

ICAR-ATRP (Initiators for Continuous Activator Regeneration ATRP)

- Low valent M^n is generated from $X\text{-}M^{n+1}$ and R-X
- Low valent M^n is reacted with initiator R-X
- When low valent M^n is poisoned into $Z\text{-}M^{n+1}$, it reduces it into M^n
- => Low reaction temperature is ideal

J. Granada, K. Matyjaszewski, *Macromolecules*, **2001**, *34*, 7664.

X = Cl (**5a**)[a]

Ent ry	Mono mer	Monomer : Initiator : **5a** : AIBN	Solvent (X ml)	Temp. (°C)	Time (h)	Conv. (%)[b]	M_n (exp.)	M_n (calc.)	M_w/M_n
1	St	250 : 1 : 0.05 : 0.025	Bulk	100	24	98	21900	25480	1.27
2			Bulk	120	24	97	21000	25200	1.31
3			1 ml	100	48	70	17700	18200	1.29
4			1 ml	120	48	71	16900	18460	1.30
5	MMA	250 : 1 : 0.1 : 0.05	1 ml	60	24	38	28400	25600	1.73

[a]Determined by ^1H NMR using a benzyl methyl ether as an internal standard

Highly controlled ICAR-ATRP of St was achieved by using **5a**

X = Br (**5b**)[a]

Ent ry	Mono mer	Monomer : Initiator : **5b** : AIBN	Solvent (X ml)	Temp. (°C)	Time (h)	Conv. (%)[b]	M_n (exp.)	M_n (calc.)	M_w/M_n
1	St	250 : 1 : 0.05 : 0.025	Bulk	100	72	51	14700	13300	1.26
2			Bulk	120	72	33	8800	8600	1.50
3			250 : 1 : 0.1 : 0.1	1 ml	60	24	95	25800	24700	1.45
4		250 : 1 : 0.1 : 0.05	1 ml	60	24	85	23500	22100	1.31
5	MMA	250 : 1 : 0.05 : 0.05	1 ml	60	24	80	24100	20000	1.39
6		250 : 1 : 0.05 : 0.025	1 ml	60	24	85	25200	22100	1.36
7		250 : 1 : 0.05 : 0.025	1 ml	60	48	96	33100	24000	1.29

[a]Determined by ^1H NMR using a benzyl methyl ether as an internal standard

Highly controlled ICAR-ATRP of MMA was achieved by using **5b**

[4] AGET-ATRP of MMA by 5a, 5b

(monomer) 10.0 mmol
(initiator) 0.04 mmol
cat. **5a** or **5b** (40 μmol)
Reductant (400 μmol)
Bulk or cyclohexanone (x ml)
Temp., time
(polymer)

AGET-ATRP (Activators Generated by Electron Transfer ATRP)

- R-M^{n+1} is reduced into M^n
- Low valent M^n is reacted with initiator R-X
- => Nhg reaction temperature is ideal

Entry	Cat.	Reductant	Solvent (X ml)	Temp. (°C)	Time (h)	Conv. (%)	M_n (exp.)	M_n (calc.)	M_w/M_n
1	**5a**	Ascorbic acid	1 ml	100	48	53	30500	13500	1.58
2	**5b**		1 ml	100	48	65	18500	16300	1.49
3	**5a**	Zn powder	1 ml	100	48	90	41400	20000	1.89
4	**5b**		1 ml	100	48	80	34400	22500	1.91
5	**5a**	Fe powder	1 ml	100	48	90	27800	23400	1.32
6	**5b**		1 ml	100	48	70	19600	18200	1.30

[a]Determined by ^1H NMR using a benzyl methyl ether as an internal standard

Highly controlled AGET-ATRP of MMA was achieved when using Fe powder

Theoretical study of proton-coupled spin crossover Fe(II) complexes

Yuta Hori, Takumi Nakanishi, Yoshihito Shiota, Osamu Sato, Kazunari Yoshizawa
(Institute for Materials Chemistry and Engineering and IRCCS, Kyushu University)

Introduction

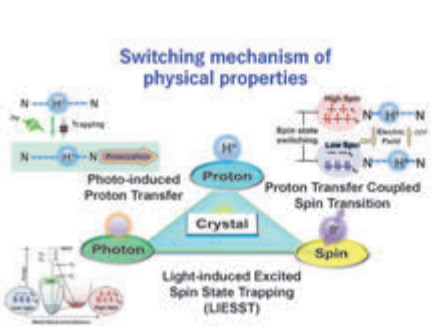

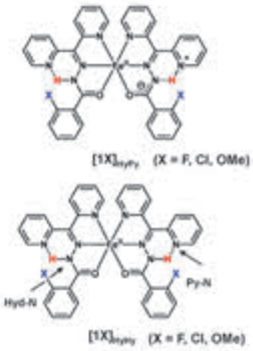

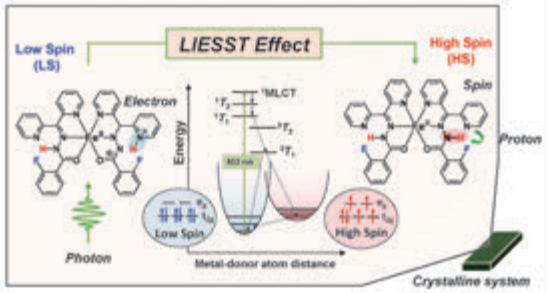

Aim of this study

We investigate reaction paths for proton-coupled spin transition in Fe(II) complex using DFT.

Computational method

Functional	UB3LYP* (E_x^{HF}: 15%)
Basis Set	6-311+G**
Spin Multiplicity	Singlet, Quintet
Program	Gaussian 09

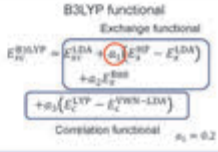

Results and Discussion

Optimized Structures

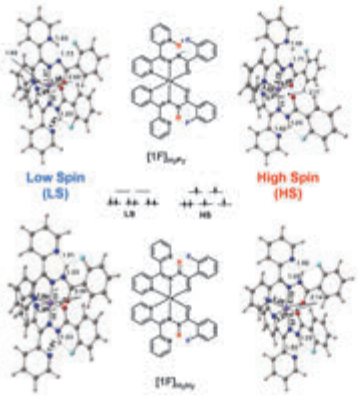

Intramolecular proton transfer

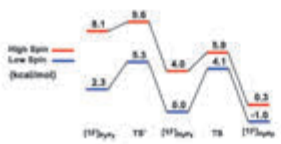

IR spectroscopic results

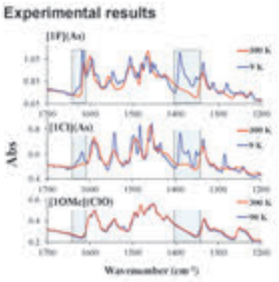

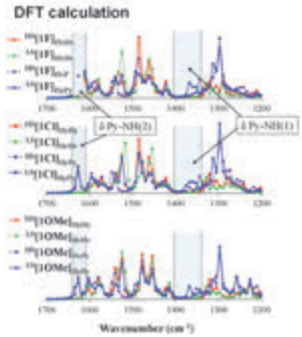

$\chi_m T$–T polots

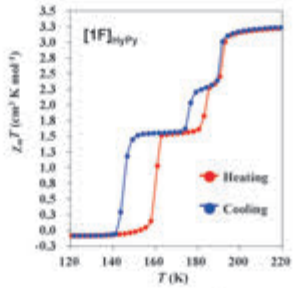

substituent effect

Complex	Initial (Low spin)	Final (High spin)	ΔE
[1F]	$[1F]_{HyPy}$	$[1F]_{HyPy}$	4.0
		$[1F]_{HyHy}$	0.3
	$[1F]_{HyHy}$	$[1F]_{HyPy}$	5.0
		$[1F]_{HyHy}$	1.3

Complex	Initial (Low spin)	Final (High spin)	ΔE
[1Cl]	$[1Cl]_{HyPy}$	$[1Cl]_{HyPy}$	4.4
		$[1Cl]_{HyHy}$	1.0
	$[1Cl]_{HyHy}$	$[1Cl]_{HyPy}$	4.9
		$[1Cl]_{HyHy}$	1.5

Complex	Initial (Low spin)	Final (High spin)	ΔE
[1OMe]	$[1OMe]_{HyPy}$	$[1OMe]_{HyPy}$	4.6
		$[1OMe]_{HyHy}$	−3.6
	$[1OMe]_{HyHy}$	$[1OMe]_{HyPy}$	10.2
		$[1OMe]_{HyHy}$	2.0

【Reference】

[1] T. Nakanishi, Y. Hori, H. Sato, S. Wu, A. Okazawa, N. Kojima, T. Yamamoto, Y. Einaga, S. Hayami, Y. Horie, H. Okajima, A. Sakamoto, Y. Shiota, K. Yoshizawa, O. Sato, in submitted.

【Acknowledgements】

- 統合物質創製化学研究推進機構(IRCCS)、融合創発研究「理論的解析を軸とした新規プロトン移動型スピン制御材料の開発」堀優太、中西匠、水野元博
- KAKENHI Grant number 17H06928 from Japan Society for the Promotion of Science (JSPS)
- Research Institute for Information Technology, Kyushu University.

Photochemical Isomerization Approach to Planar Chiral Medium-sized Cyclic Molecules

Yuki Yoshida, Kouhei Machida, Mariko Okamoto, Yusuke Ano, Kazunobu Igawa, and Katsuhiko Tomooka

Institute for Materials Chemistry and Engineering, and IRCCS, Kyushu University

Background

Our Chemistry about Planar Chiral Medium-sized Cyclic Molecules

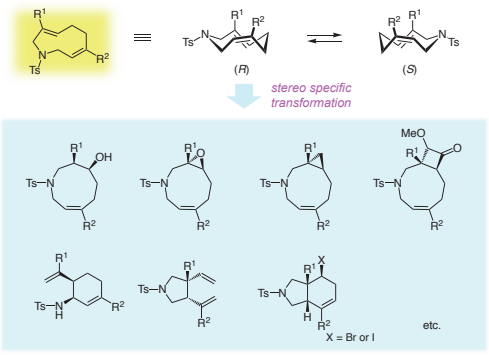

Synthetic Approach for Planar Chiral Medium-sized Cyclic Molecules

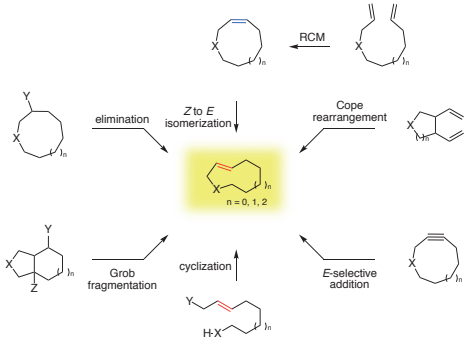

Result

This Work

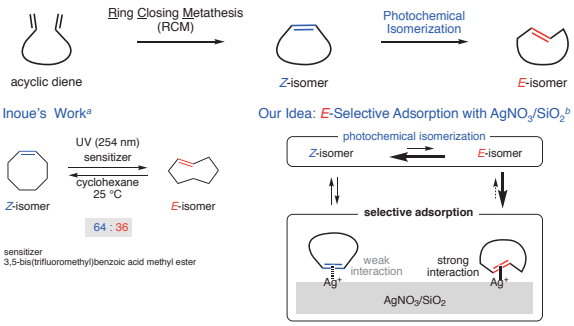

a) N. Yamasaki, Y. Inoue, T. Yokoyama, A. Tai, *J. Photochem. Photobiol., A: Chem.* **1989**, *48*, 465.
b) Related report : Fox and colleagues reported the efficient photochemical *Z* to *E* isomerization of medium-sized cyclic molecules with continuous circulation of a reaction mixture pumped through a packed column of $AgNO_3/SiO_2$: M. Royzen, G. P. A. Yap, J. M. Fox, *J. Am. Chem. Soc.* **2008**, *130*, 3760. M. Royzen, M. T. Taylor, A. DeAngelis, J. M. Fox, *Chem. Sci.* **2011**, *2*, 2162.

Optimization of Photo Isomerization

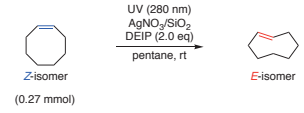

Entry	$AgNO_3/SiO_2$ $AgNO_3$-content [wt%]	$AgNO_3/SiO_2$ amount [mg]	time [h]	*E*/*Z*	(yield)[a]
1	–	none	42	23 : 77	(87%)
2	5	400	42	75 : 25	(81%)
3	10	400	42	93 : 7	(81%)
4	20	400	42	77 : 23	(73%)
5	10	500	42	97 : 3	(88%)
6	10	500	24	67 : 33	(72%)

a) Combined yields of (*E*) and (*Z*). Determined by GC analysis.

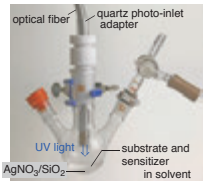

Synthesis of Planar Chiral Orthocyclophene

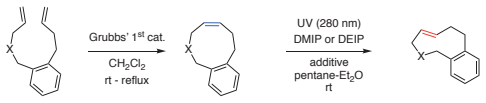

		additive	*E*/*Z* (yield)[b]
a	X = $C(SO_2Ph)_2$ (quant)	none	22 : 78 (quant)[c]
		$AgNO_3/SiO_2$	89 : 11 (88%)[c]
	X = CH_2 (68%)	none	26 : 74 (81%)[d]
		$AgNO_3/SiO_2$	64 : 36 (67%)[d]
	X = NTs (21%)	none	31 : 69 (79%)
		$AgNO_3/SiO_2$	74 : 26 (88%)[d]

a) Mg, MeOH, rt, 92%. *b*) Combined yield of (*E*) + (*Z*). Determined by ^1H NMR analysis.
c) K. Igawa, K. Machida, K. Noguchi, K. Uehara, K. Tomooka, *J. Org. Chem.* **2016**, *81*, 11587.
d) K. Machida, Y. Yoshida, K. Igawa, K. Tomooka, *Chem. Lett.* **2018**, *47*, 186.

Synthesis of Planar Chiral Dialkoxysilane

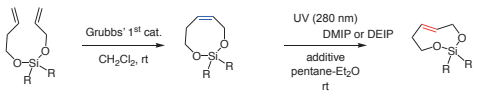

	additive	*E*/*Z* (yield)[a]
R = *t*-Bu (72%)	none	25 : 75 (94%)[b]
	$AgNO_3/SiO_2$	89 : 11 (61%)[c]
R = Ph (87%)	none	33 : 67 (99%)[b]
	$AgNO_3/SiO_2$	>98 : <2 (48%)[c]

a) Combined isolated yield of (*E*) + (*Z*).
b) K. Tomooka, S. Miyasaka, S. Motomura, K. Igawa, *Chem. Eur. J.* **2014**, *20*, 7598.
c) K. Machida, Y. Yoshida, K. Igawa, K. Tomooka, *Chem. Lett.* **2018**, *47*, 186.

Stereochemical Behavior of Planar Chiral Medium-sized Cyclic Molecules

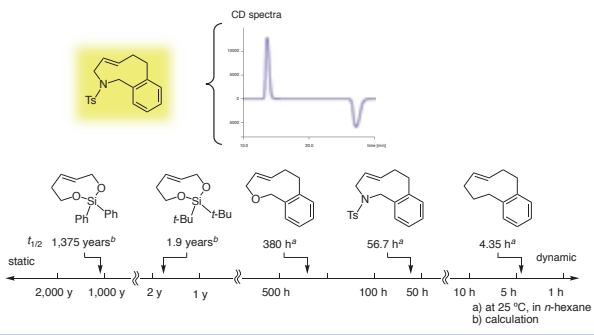

Summary

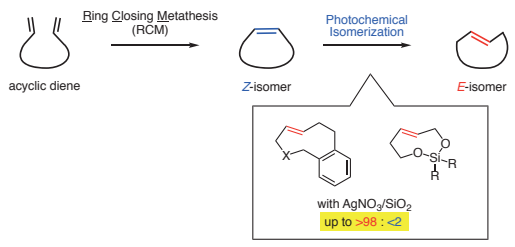

IRCCS 統合物質創製化学研究推進機構

阿波賀邦夫　**エネルギー・資源研究プラットホーム**
〒464-8602　名古屋市千種区不老町 名古屋大学大学院理学研究科
TEL 052-789-2291　FAX 052-789-5947

中野　環　**新反応・新触媒研究プラットホーム**
〒001-0021　北海道札幌市北区北 21 条西 10 丁目 北海道大学触媒科学研究所
TEL 011-706-9155　FAX 011-706-9156

島川祐一　**マテリアル研究プラットホーム**
〒611-0011　京都府宇治市五ヶ庄 京都大学化学研究所附属元素科学国際研究センター
TEL 0774-38-3110　FAX 0774-38-3118

吉澤一成　**ケムバイオ研究プラットホーム**
〒819-0395　福岡市西区元岡 744 九州大学先導物質化学研究所
TEL 092-802-2529　FAX 092-802-2528

機構事務室
〒464-8602　名古屋市千種区不老町 名古屋大学物質科学国際研究センター
TEL 052-789-5907　FAX 052-789-5900

IRCCS, Integrated Research Consortium on Chemical Sciences